

Novel binders derived from an albumin-binding domain scaffold targeting human prostate secretory protein 94 (PSP94)

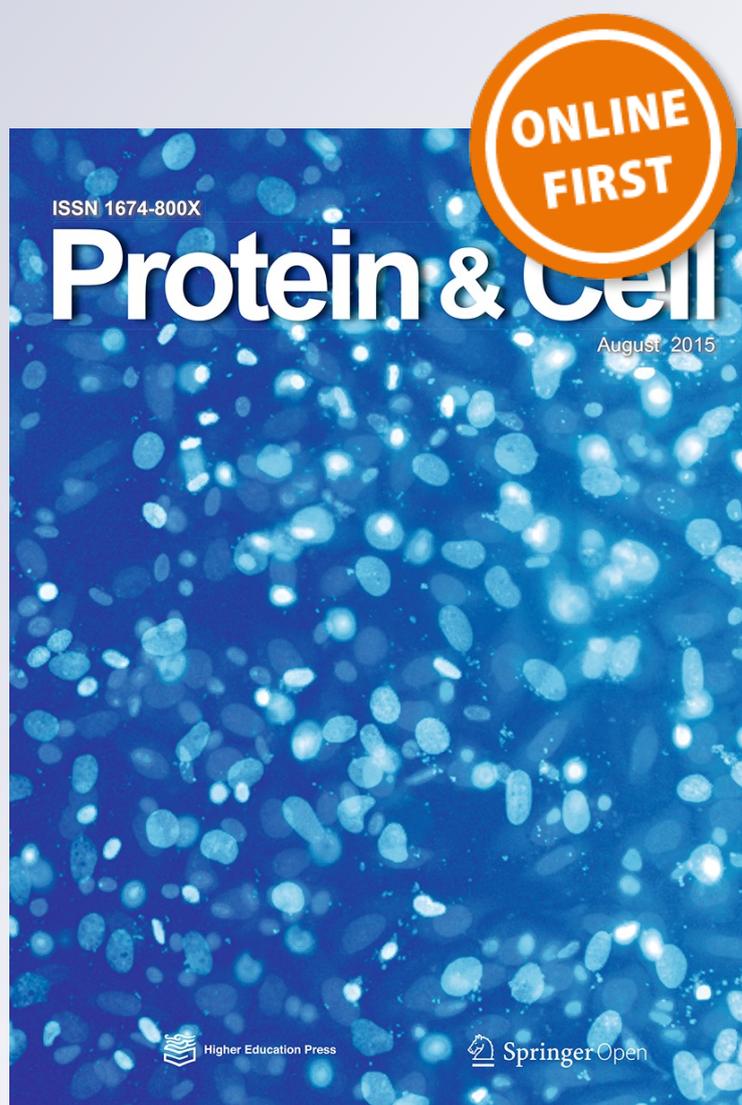
**Lucie Marečková, Hana Petroková,
Radim Osička, Milan Kuchař & Petr
Malý**

Protein & Cell

ISSN 1674-800X

Protein Cell

DOI 10.1007/s13238-015-0194-9



Your article is published under the Creative Commons Attribution license which allows users to read, copy, distribute and make derivative works, as long as the author of the original work is cited. You may self-archive this article on your own website, an institutional repository or funder's repository and make it publicly available immediately.

LETTER

Novel binders derived from an albumin-binding domain scaffold targeting human prostate secretory protein 94 (PSP94)

Dear Editor,

Prostate secretory protein 94 (PSP94), also known as β -microseminoprotein, is a product of the *MSMB* gene and one of the most abundant proteins found in human seminal plasma (Anklesaria et al., 2013). This small cysteine-rich non-glycosylated protein is considered to be involved in regulation of many biological processes including male reproduction. It has been observed that PSP94 and its porcine homologue inhibit acrosomal reaction, sperm motility, and maintain the sperm environment (Anahi Franchi et al., 2008; Manaskova-Postlerova et al., 2011).

Despite of its possible role in reproduction, recently it has been proposed its association with development of prostate cancer (PC). It has been demonstrated that PSP94 suppresses tumor growth and reduces proliferation of some cancer cells by inducing apoptosis. This action is suggested to be regulated via binding to cell-surface receptors (Yang et al., 1998; Annabi et al., 2006). Moreover, the large genome-wide association studies showed that decreased expression of PSP94 caused by the rs10993994 single nucleotide polymorphism is associated with an increased risk of developing prostate cancer, suggesting a protective role of PSP94 in PC incidence (Lou et al., 2009; FitzGerald et al., 2013).

Currently, the clinically validated test for PC diagnosis relies on detection of serum level of prostate-specific antigen (PSA, human kallikrein-3) using monoclonal antibody-based ELISA kit but this examination, yet widely used, fails to predict early stages of PC development and, in addition, does not distinguish precisely between malign form of PC and benign prostate hyperplasia. Due to lack of this specificity many patients have to undergo unnecessary prostate tissue biopsy (Lazzeri et al., 2012). To overcome this drawback, a larger set of PC biomarkers has been suggested to improve early prediction of PC, to identify recurrent stages of malignancy after the prostatectomy and treatment, and to more precisely correlate serum-level oncomarkers with a histological Gleason scoring. Therefore, novel and more complex tools for improved PC diagnosis, including multifactorial biosensors or ELISA sets, are being required (Mhatre et al., 2014).

Many studies have suggested that PSP94 could be a useful biomarker for PC diagnosis and prognosis (Nam et al., 2006; Reeves et al., 2006; Velonas et al., 2013). The estimation of bound/free PSP94 has been suggested as an independent prognostic marker following radical prostatectomy that can predict time to recurrence of PC (Reeves et al., 2006). The measurement of PSP94 levels was able to identify patients with high-grade disease among a subset of patients in whom tests of PSA or free/total PSA were least informative (Nam et al., 2006; Mhatre et al., 2014).

Artificial binding proteins derived from small protein domain scaffolds represent a valuable non-immunoglobulin alternative for the construction of novel bio-sensing devices. Engineered small, stable, robust, and soluble proteins with a sufficient thermal and hydrodynamic stability and without disulphide bonds can be produced in a mass amount in bacteria and easily modified by gene-fusion approaches. In addition, they are amenable to rational improvement or *ab initio* design and suitable for high-throughput selection and diagnostic procedures (Gilbreth and Koide, 2012).

Recently we have demonstrated that a high-complex combinatorial library derived from three-helix bundle of albumin-binding domain (ABD) of streptococcal protein G can be used for development of sub-to-nanomolar affinity binders of human interferon gamma (Ahmad et al., 2012) or for novel IL-23 receptor antagonists with a promising anti-inflammatory potential (Kuchar et al., 2014). Therefore, we used this ABD scaffold-derived library to generate unique binders of human PSP94. In combination with five campaigns of ribosome display selection we generated a collection of 35 PSP94-binding clones called PAB binders, representing 29 unique sequence variants (Fig. 1A). These variants in the form of fusion proteins, carrying 46 amino acid residue-long ABD sequence linked to a helical 305 amino acid ToIA spacer protein with an installed C-terminal AviTag consensus, were further characterized. PAB clones were tested for the production of bacterial proteins after transformation of *E. coli* host cells and protein production in cell lysates. After the verification of binding function in ELISA in combination with Western blot analysis, we selected most promising candidates for more detailed characterization.

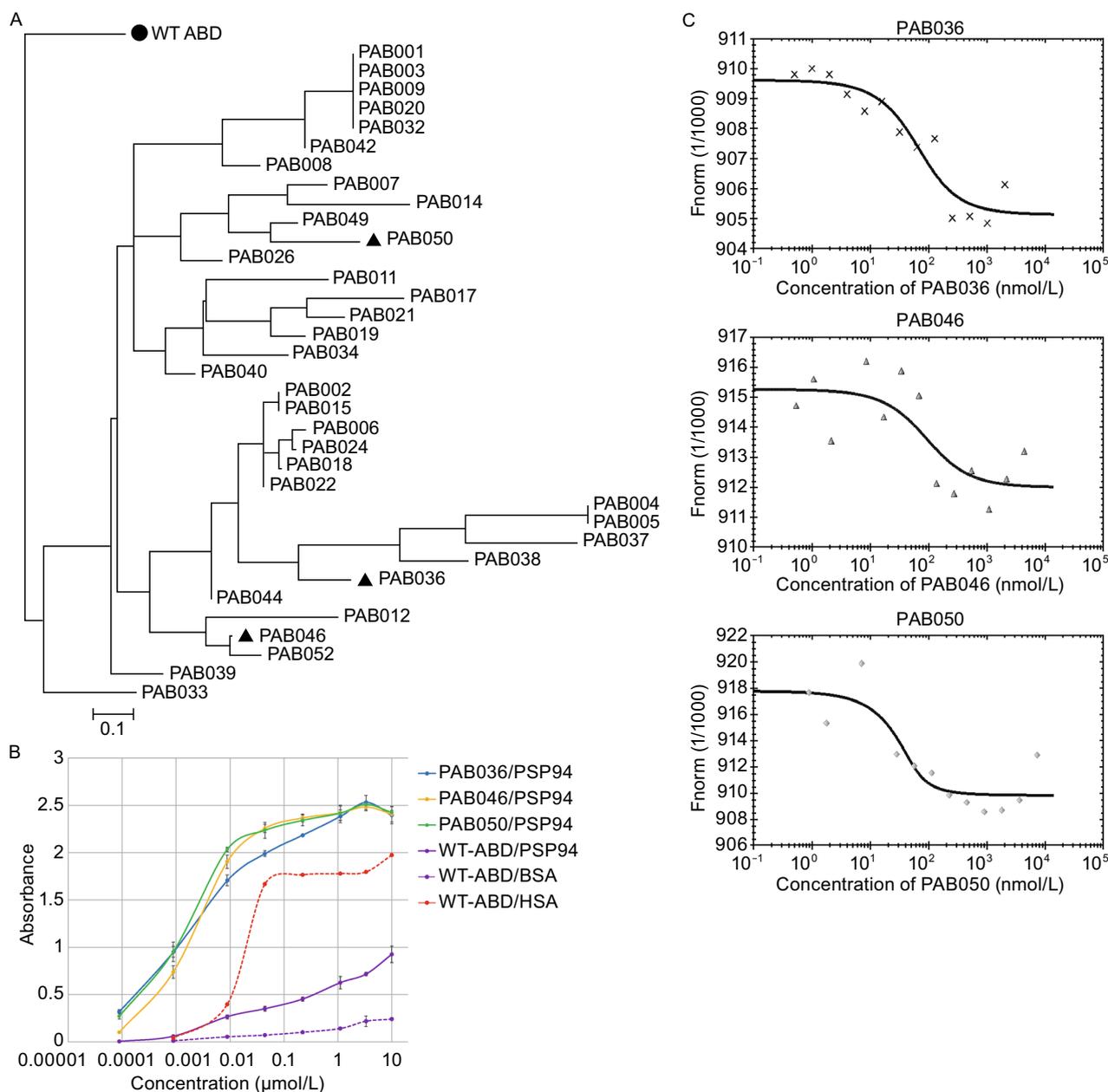


Figure 1. Generation of PAB variants and their binding to recombinant HisTag-PSP94. (A) Similarity tree of polypeptide sequences of the selected PAB binders. Analysis of a collection of 35 PAB binders obtained by ribosome display selection identified 29 unique sequence variants. For the analysis, randomized sequences between residues 20 and 46 were compared, as the N-terminal amino acid positions 1–19 were non-mutated. The sequence of the parental ABD wild-type domain (●) was used as a root of the tree. PAB variants selected for more detailed analysis are highlighted as triangles. (B) Binding of PAB variants to recombinant HisTag-PSP94 assessed by ELISA. Serially-diluted PAB variants in the form of biotinylated HisTag-PAB-TolA-AviTag fusion proteins were applied to a Polysorp microtiter plate coated with 10 $\mu\text{g/mL}$ of recombinant HisTag-PSP94. WT-ABD indicates the parental wild-type ABD-TolA-AviTag protein as a non-mutated control with the natural affinity to HSA. The binding was detected by Streptavidin-HRP conjugate. The error bars represent the standard deviation from the three measurements. (C) The binding affinity of PAB variants to the fluorescently-labeled recombinant HisTag-PSP94 measured by microscale thermophoresis. Thermophoresis + T-jump data shown as binding curves were evaluated by a NanoTemper software and calculated K_d values for PAB036, PAB046, and PAB050 variants were 40 ± 6 nmol/L, 49 ± 10 nmol/L, and 10 ± 3 nmol/L, respectively.

Purified recombinant proteins of these PAB variants confirmed binding to immobilized His-PSP94 bacterial protein in ELISA using detection with streptavidin-HRP conjugate (Fig. 1B). We also verified that these selected protein variants do not substantially bind to coated BSA protein (data not shown). To further confirm that these PAB clones bind to human PSP94 protein, we used another ELISA sandwich layout in which *in vivo* biotinylated PAB clones were immobilized to a coated streptavidin and binding of His-PSP94 was detected by anti-PSP94 antibody followed by a secondary IgG-HRP conjugate (results not shown).

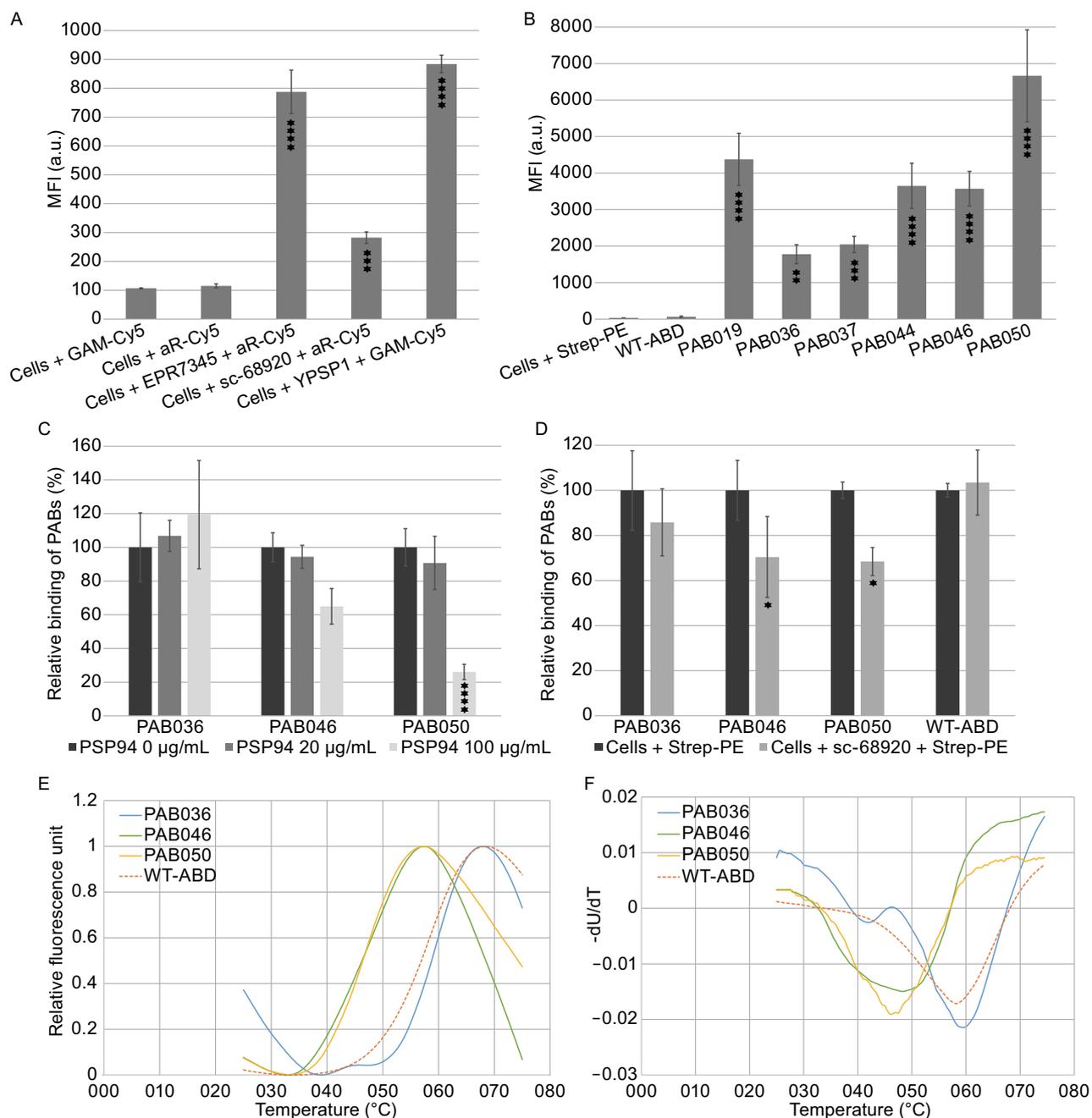
To estimate the binding affinity of the particular PAB variants in solution, we used microscale thermophoresis (MST) with a fluorescently-labelled HisTag-PSP94 and measured interactions with PAB036, PAB046, and PAB050 variants. In the Fig. 1C, binding curves obtained for all selected PAB variants are shown, representing one of the performed experiments. Using a commercial software, K_d constants measured for all three PAB variants were estimated to be 40 ± 6 nmol/L and 72 ± 25 for PAB036, 49 ± 10 nmol/L for PAB046, and 10 ± 3 , 12 ± 3 and 21 ± 8 nmol/L (an average value 14 nmol/L) for PAB050.

To corroborate whether PAB binders are capable of binding to a native human target, we used LNCaP prostate cancer cell line formerly described to secrete and cell-surface express the PSP94 protein (Yang et al., 1998). To verify this expected positivity, we used flow cytometry to assay the binding of two monoclonal and one polyclonal anti-PSP94 antibodies. As demonstrated in the Fig. 2A, all three anti-PSP94 antibodies substantially bind to LNCaP cells while the presence of the only secondary Cy-5-conjugated IgGs remains to be negative. Statistical significance of the positive binding in comparison to the binding of the corresponding secondary antibody only was verified by ANOVA and is shown by asterisks. This result suggests that LNCaP cells capture a part of the secreted PSP94 by an autologous membrane receptor and can be, therefore, used for the investigation of binding of PAB clones to the membrane-bound PSP94. The possibility of the attachment of the PSP94 to cell surface via interactions with a membrane receptor has been already suggested (Annabi et al., 2006). Results of binding of all used anti-PSP94 antibodies to cell surface-bound PSP94 were further supported by intracellular binding of these antibodies to LNCaP cells with permeabilized membranes (results not shown). In the further experiment, *in vivo* biotinylated PAB variants in the form of PAB-TolA-AviTag fusion proteins were tested by flow cytometry for the ability to bind to PSP94-expressing LNCaP cells. The ABD-wild-type protein corresponding to the parental non-randomized ABD scaffold was used as a control to exclude the possibility that non-randomized residues of the ABD bundle could mediate high-affinity interactions with prostate cancer cells. In addition, presence of TolA fusion moiety, identical between PAB variants and the ABD wild-type control, should exclude that ABD-unrelated TolA sequences mediate or substantially contribute to cell-surface binding. As

demonstrated in the Fig. 2B, several PAB variants bind to LNCaP cells, as detected by streptavidin-PE conjugate. Statistical significance of binding for each PAB variant compared to the binding of parental wild-type ABD-TolA control is provided by ANOVA and shown by asterisks. We also investigated binding of PAB clones to permeabilized LNCaP cells and results are in correlation with intact cells staining (data not shown). Interestingly, PAB036 variant, binding well to the bacterial PSP94 in ELISA, and substantially also to the intracellular LNCaP cell product (not shown), exhibited weaker cell-membrane binding compared to the other PAB variants. It is possible that this clone recognizes a different binding surface of the PSP94 in comparison to the other binders and that this membrane PSP94, bound in an oriented way to its cognate cell-surface receptor, is sterically hindered and, thus, partially unapproachable for a full PAB036 recognition. This is supported by a strong binding in the case of a free accessible PSP94 (data not shown). Based on the result of this binding assay, we selected PAB036, PAB046, and PAB050 variants as the most promising candidates for further characterization. The amino acid sequences between residues 20 and 46 of these three variants are as follows: PAB036: **WYKNGINPAHRV**RVWK-**GRIDAILARLP**; PAB046: **RYKNAINRAPAV**WWWKRLIDAI-**LAALP**; PAB050: **LYKNHINTAWRVA**AVKRAIDLILASLP, all presented with the indicated positions of the 11 randomized residues. Parental non-randomized WT-ABD full-length sequence (46 amino acids of the full ABD scaffold) is LAEAKVLANRELDKYGVSDYYKLNINNAKTVEGVKALIDEILAALP with the marked mutable positions.

To verify whether recombinant bacterial human PSP94 competes with cell-bound PSP94, we performed cell-surface competition binding assay in which PAB036, PAB046, and PAB050 variants were mixed with an increasing concentration of the recombinant PSP94 protein and were left bound to LNCaP cells for 30 min. The results of repeated experiments shown in the Fig. 2C indicate that increasing concentrations of the PSP94 protein inhibited binding of the PAB046 and PAB050 variants to the cells. While the concentration 20 μ g/mL decreased binding of both these PAB proteins only by 5%–10%, concentration of 100 μ g/mL inhibited this binding substantially by 35% for PAB046 and by 74% for PAB050. Contrary that, PAB036 variant did not exhibit any inhibitory effect. Statistical evaluation by ANOVA was performed and indicated by asterisks.

As an important proof of specificity of PAB binders, we performed cell-surface competition binding assay using LNCaP cells. We first tested whether monoclonal antibody YPSP-1 inhibits binding of PAB variants to LNCaP cells by flow cytometry. Our data demonstrated that this monoclonal antibody did not compete with PAB036, PAB046, and PAB050 variants for binding to LNCaP cells (data not shown), suggesting that an interacting epitope differs from those recognized by the particular PAB binders. We also tested the ability of polyclonal antibody sc-68920 to inhibit binding of PAB variants to the same cells and found that this



antibody is able to suppress the PAB binding. We used it, therefore, in cell-surface competition binding assay to demonstrate the specificity of used PAB binders for cell-bound PSP94 recognition on LNCaP cells. As shown in Fig. 2D, a dose of 4 micrograms of sc-68920 suppressed the binding of PAB046 and PAB050 by 30% compared to the control non-inhibited PAB variants (100%) and this decrease is statistically significant as verified by ANOVA (indicated by

asterisks). On the other hand, inhibition of PAB036 binding was only about 15%. ABD-WT-ToIA protein was used as a non-inhibiting ABD control in this flow cytometry test. To investigate what is the impact of ABD scaffold randomization on PAB binder's stability, we measured thermal stability of PAB036, PAB046, and PAB050 variants using thermal shift assay (TSA). Temperature melting points (T_m) measured in 300 mmol/L NaCl, 50 mmol/L Tris buffer, pH 8, are 59.6°C for

Figure 2. Binding of PAB variants to prostate cancer LNCaP cells analyzed by flow cytometry and tests of their thermal stability.

(A) Detection of PSP94 on cell-surface of prostate cancer LNCaP cells using anti-PSP94 antibodies: monoclonal EPR7345, polyclonal sc-68920, and monoclonal YPSP-1. (B) Binding of PAB-Tola-Avitag variants to LNCaP cells. Soluble PAB proteins purified as *in vivo* biotinylated HisTag-PAB-Tola-AviTag fusion products were added to cells and the binding was detected by streptavidin-PE conjugate. WT-ABD indicates parental non-mutated ABD wild-type as a control. (C) Competition of recombinant HisTag-PSP94 with the selected PAB variants for binding to LNCaP cells. The graphical representation of binding of *in vivo* biotinylated PAB-Tola-Avitag variants to LNCaP cells in the presence of increased concentrations of recombinant HisTag-PSP94 is shown, as detected by streptavidin-PE conjugate. The fluorescent intensities of bound PAB clones to LNCaP cells in the absence of recombinant PSP94 were taken as 100% and the averaged values of the three experiments are shown with standard deviations. (D) Competition of rabbit polyclonal antibody sc-68920 with PAB variants for binding to membrane-bound PSP94 on LNCaP cells. Cells were incubated with (80 µg/mL) or without (control) sc-68920 antibody for 15 min on ice, then PAB binders at concentration 10 µg/mL were added and left to incubate for 30 min. Binding of PAB variants was detected by streptavidin-PE conjugate. In all flow cytometry binding tests (A–D), results are expressed as the arithmetic mean ± standard deviation of the mean. Statistical analysis was done using one-way ANOVA followed by Dunnett's post-test, comparing all the samples with the control. GraphPad Prism 6.0 (GraphPad Software) was used to perform statistical analysis. Significant differences are indicated by asterisks (*, $P < 0.05$; **, $P < 0.01$; ***, $P < 0.001$; ****, $P < 0.0001$). (E) Thermal melting fluorescence curves of PAB binders and parental non-mutated ABD wild-type (WT-ABD) control. (F) First derivative of fluorescence versus temperature of curves shown in the panel (E). The melting point is given as the lowest point of the curve. All measurements were done in duplicate (PAB046) or in triplicates (PAB036, PAB050, WT-ABD) and averaged.

PAB036, 48.5°C for PAB046, and 46.0°C for PAB050 (Fig. 2E and 2F). T_m value for parental non-randomized wild-type ABD is 58.0°C. These data indicate that particular mutations in each of variants can strongly affect the protein stability. While in the case of PAB036 variant the amino acid alterations slightly improved the original scaffold stability, thermal stability of PAB046 as well as PAB050 was significantly decreased.

Electronic supplementary material The online version of this article (doi:10.1007/s13238-015-0194-9) contains supplementary material, which is available to authorized users.

Collectively, we present the generation and characterization of unique protein binders of human prostate cancer oncomarker that can be useful as alternatives to monoclonal antibodies for detection of MSMB in studies of fertilization and, with possible modifications using gene-fusion or affinity maturation approaches, they could serve as novel capture proteins for improved prostate cancer diagnostics.

FOOTNOTES

We thank Petra Kadlčáková and Michal Malý for technical support and Dr. C. Bařínka for providing prostate cancer cell lines. This study was supported by the grants No. FR-TI4/667 of the Ministry of Industry and Trade of the Czech Republic and No. GAP302/11/0580 from the Czech Science Foundation, by BIOCEV CZ.1.05/1.1.00/02.0109 from the ERDF and by the institutional research support #RVO: 86652036.

Lucie Marečková, Hana Petroková, Radim Osička, Milan Kuchař, and Petr Malý declare that they have no conflict of interest. This article does not contain any studies with human or animal subjects performed by the any of the authors.

Lucie Marečková¹, Hana Petroková¹, Radim Osička², Milan Kuchař¹, Petr Malý¹✉

¹ Institute of Biotechnology, Czech Academy of Sciences, v. v. i., Vídeňská 1083, 142 20 Prague, Czech Republic

² Institute of Microbiology, Czech Academy of Sciences, v. v. i., Vídeňská 1083, 142 20 Prague, Czech Republic

✉ Correspondence: petr.maly@ibt.cas.cz (P. Malý)

OPEN ACCESS

This article is distributed under the terms of the Creative Commons Attribution 4.0 International License (<http://creativecommons.org/licenses/by/4.0/>), which permits unrestricted use, distribution, and reproduction in any medium, provided you give appropriate credit to the original author(s) and the source, provide a link to the Creative Commons license, and indicate if changes were made.

REFERENCES

- Ahmad JN, Li J, Biedermannova L, Kuchar M, Sipova H, Semradtova A, Cerny J, Petrokova H, Mikulecky P, Polinek J et al (2012) Novel high-affinity binders of human interferon gamma derived from albumin-binding domain of protein G. *Proteins* 80 (3):774–789
- Anahi Franchi N, Avendano C, Molina RI, Tissera AD, Maldonado CA, Oehninger S, Coronel CE (2008) β -Microseminoprotein in human spermatozoa and its potential role in male fertility. *Reproduction* 136(2):157–166
- Anklesaria JH, Jagtap DD, Pathak BR, Kadam KM, Joseph S, Mahale SD (2013) Prostate Secretory Protein of 94 amino acids (PSP94) binds to prostatic acid phosphatase (PAP) in human seminal plasma. *PLoS One* 8(3):e58631
- Annabi B, Currie JC, Bouzegrane M, Dulude H, Daigneault L, Garde S, Rabbani SA, Panchal C, Wu JJ, Beliveau R (2006) Contribution of the 37-kDa laminin receptor precursor in the anti-

- metastatic PSP94-derived peptide PCK3145 cell surface binding. *Biochem Biophys Res Commun* 346(1):358–366
- FitzGerald LM, Zhang X, Kolb S, Kwon EM, Liew YC, Hurtado-Coll A, Knudsen BS, Ostrander EA, Stanford JL (2013) Investigation of the relationship between prostate cancer and MSMB and NCOA4 genetic variants and protein expression. *Hum Mutat* 34(1):149–156
- Gilbreth RN, Koide S (2012) Structural insights for engineering binding proteins based on non-antibody scaffolds. *Curr Opin Struct Biol* 22(4):413–420
- Kuchar M, Vankova L, Petrokova H, Cerny J, Osicka R, Pelak O, Sipova H, Schneider B, Homola J, Sebo P et al (2014) Human interleukin-23 receptor antagonists derived from an albumin-binding domain scaffold inhibit IL-23-dependent ex vivo expansion of IL-17-producing T-cells. *Proteins* 82(6):975–989
- Lazzeri M, Briganti A, Scattoni V, Lughezzani G, Larcher A, Gadda GM, Lista G, Cestari A, Buffi N, Bini V et al (2012) Serum index test %[-2]proPSA and Prostate Health Index are more accurate than prostate specific antigen and %fPSA in predicting a positive repeat prostate biopsy. *J Urol* 188(4):1137–1143
- Lou H, Yeager M, Li H, Bosquet JG, Hayes RB, Orr N, Yu K, Hutchinson A, Jacobs KB, Kraft P et al (2009) Fine mapping and functional analysis of a common variant in MSMB on chromosome 10q11.2 associated with prostate cancer susceptibility. *Proc Natl Acad Sci USA* 106(19):7933–7938
- Manaskova-Postlerova P, Davidova N, Sulc M, Philimonenko A, Hozak P, Jonakova V (2011) Reproductive tissue expression and sperm localization of porcine beta-microseminoprotein. *Cell Tissue Res* 344(2):341–353
- Mhatre DR, Mahale SD, Khatkhatay MI, Desai SS, Jagtap DD, Dhabalia JV, Tongaonkar HB, Desai MP, Dandekar SP, Varadkar AM (2014) Development of an ELISA for sPSP94 and utility of the sPSP94/sPSA ratio as a diagnostic indicator to differentiate between benign prostatic hyperplasia and prostate cancer. *Clin Chim Acta* 436:256–262
- Nam RK, Reeves JR, Toi A, Dulude H, Trachtenberg J, Emami M, Daigneault L, Panchal C, Sugar L, Jewett MA et al (2006) A novel serum marker, total prostate secretory protein of 94 amino acids, improves prostate cancer detection and helps identify high grade cancers at diagnosis. *J Urol* 175(4):1291–1297
- Reeves JR, Dulude H, Panchal C, Daigneault L, Ramnani DM (2006) Prognostic value of prostate secretory protein of 94 amino acids and its binding protein after radical prostatectomy. *Clin Cancer Res* 12(20 Pt 1):6018–6022
- Velonas VM, Woo HH, Remedios CG, Assinder SJ (2013) Current status of biomarkers for prostate cancer. *Int J Mol Sci* 14(6):11034–11060
- Yang JP, Finkelman MA, Clarke MW (1998) Detection of PSP94 and its specific binding sites in the prostate adenocarcinoma cell line LNCaP. *J Urol* 160(6 Pt 1):2240–2244

RESEARCH ARTICLE

Development of Recombinant *Lactococcus lactis* Displaying Albumin-Binding Domain Variants against Shiga Toxin 1 B Subunit

Petra Zadavec^{1,2}, Lucie Marečková³, Hana Petroková³, Vesna Hodnik^{4,5}, Milica Perišić Nanut¹, Gregor Anderluh^{4,5}, Borut Štrukelj^{1,2}, Petr Malý³, Aleš Berlec^{1*}

1 Department of Biotechnology, Jožef Stefan Institute, Jamova 39, SI-1000, Ljubljana, Slovenia, **2** The Chair of Pharmaceutical Biology, Faculty of Pharmacy, University of Ljubljana, Aškerčeva 7, SI-1000, Ljubljana, Slovenia, **3** Laboratory of Ligand Engineering, Institute of Biotechnology CAS, v. v. i., BIOCEV Research Center, Průmyslová 595, 252 50, Vestec, Czech Republic, **4** Department of Biology, Biotechnical Faculty, University of Ljubljana, Jamnikarjeva 101, 1000, Ljubljana, Slovenia, **5** National Institute of Chemistry, Hajdrihova 19, 1000, Ljubljana, Slovenia

* ales.berlec@ijs.si



OPEN ACCESS

Citation: Zadavec P, Marečková L, Petroková H, Hodnik V, Perišić Nanut M, Anderluh G, et al. (2016) Development of Recombinant *Lactococcus lactis* Displaying Albumin-Binding Domain Variants against Shiga Toxin 1 B Subunit. PLoS ONE 11(9): e0162625. doi:10.1371/journal.pone.0162625

Editor: Oscar P. Kuipers, University of Groningen, NETHERLANDS

Received: June 17, 2016

Accepted: August 25, 2016

Published: September 8, 2016

Copyright: © 2016 Zadavec et al. This is an open access article distributed under the terms of the [Creative Commons Attribution License](https://creativecommons.org/licenses/by/4.0/), which permits unrestricted use, distribution, and reproduction in any medium, provided the original author and source are credited.

Data Availability Statement: All relevant data are within the paper.

Funding: This work was supported by Slovenian Research Agency grant P4-0127, by Slovene human resources development and scholarship fund, by Bilateral mobility project between Academy of Sciences of the Czech Republic and Slovenian Academy of Sciences and Arts (No. SAZU-16-01) and by BIOCEV CZ.1.05/1.1.00/02.0109 from the ERDF and the institutional research concept RVO: 86652036.

Abstract

Infections with shiga toxin-producing bacteria, like enterohemorrhagic *Escherichia coli* and *Shigella dysenteriae*, represent a serious medical problem. No specific and effective treatment is available for patients with these infections, creating a need for the development of new therapies. Recombinant lactic acid bacterium *Lactococcus lactis* was engineered to bind Shiga toxin by displaying novel designed albumin binding domains (ABD) against Shiga toxin 1 B subunit (Stx1B) on their surface. Functional recombinant Stx1B was produced in *Escherichia coli* and used as a target for selection of 17 different ABD variants (named S1B) from the ABD scaffold-derived high-complex combinatorial library in combination with a five-round ribosome display. Two most promising S1Bs (S1B22 and S1B26) were characterized into more details by ELISA, surface plasmon resonance and microscale thermophoresis. Addition of S1Bs changed the subcellular distribution of Stx1B, completely eliminating it from Golgi apparatus most likely by interfering with its retrograde transport. All ABD variants were successfully displayed on the surface of *L. lactis* by fusing to the Usp45 secretion signal and to the peptidoglycan-binding C terminus of AcmA. Binding of Stx1B by engineered lactococcal cells was confirmed using flow cytometry and whole cell ELISA. Lactic acid bacteria prepared in this study are potentially useful for the removal of Shiga toxin from human intestine.

Introduction

Infections with Shiga toxin (Stx)-producing bacteria, such as Stx-producing *Escherichia coli* (STEC) and *Shigella dysenteriae*, cause diarrhea and hemorrhagic colitis in human, and may further develop into a life-threatening hemolytic uremic syndrome (HUS), characterized by microangiopathic hemolytic anemia, thrombocytopenia, and acute renal failure [1, 2]. Shiga

Competing Interests: The authors have declared that no competing interests exist.

toxin, the major virulence factor of STEC, can be produced as Stx1 variants (Stx1 and Stx1c), Stx2 variants (Stx2, Stx2c, Stx2d, Stx2e, Stx2f) or both variants in different combinations [3]. Stx produced by *S. dysenteriae* is almost identical to Stx1 produced by *E. coli*. All members of Stx family are composed of monomeric enzymatically active A subunit (StxA), which is non-covalently attached to pentameric B subunit (StxB). The latter is responsible for binding to globotriaosylceramide receptor (Gb₃) on the cell surface, or to globotetraosylceramide (Gb₄) receptor in the case of Stx2e [3].

Human infection with STEC is mainly associated with ingestion of contaminated food, and can quickly spread among humans causing massive outbreaks of STEC diseases. After ingestion, STEC pass through gastrointestinal (GI) tract, where they colonize the lower GI tract and release Stx into the gut lumen [1]. Stx is absorbed by the intestinal epithelium into the blood circulation and targets tissues expressing Gb₃ receptor [4]. Once bound, the toxin is very effectively internalized into the cells by endocytosis and transported through the retrograde pathway, whereby active A subunit is cleaved by furin and translocated to cytosol, where it functions as a highly specific N-glycosidase, inhibiting protein synthesis and causing cell death [5, 6].

Currently, there is no specific treatment for patients with developed HUS. Recommended management relies on supportive therapy that includes fluid and electrolyte balance, nutritional support, management of hypertension and renal transplantation [4]. Because the conventional antibiotic treatment of STEC infections increases the risk of developing HUS by induction of Stx expression and toxin release into the gut, there is a need for the development of new therapies. Various potential therapeutic strategies are currently under development, and include compounds directed against STEC, Stx receptor analogues, receptor synthesis inhibitors, antitoxin antibodies, inhibitors of toxin transport, processing and function, natural products and also novel antimicrobial therapies (reviewed in [7, 8]). Monoclonal antibodies against Stx1 and Stx2 are currently furthest in development [7].

As an alternative to conventional monoclonal antibodies, more than 20 different types of small single-domain non-immunoglobulin (non-Ig) scaffolds are being used to produce binding proteins against more than a hundred different targets [9]. Compared to antibodies, engineered non-Ig scaffolds are stable, robust and soluble monomeric proteins, that lack disulfide bonds, are easily and inexpensively produced in large amounts in bacteria, exhibit effective tissue penetration, rapid distribution and elimination, can be easily modified by conjugation or gene fusion technology and can exert multivalency or multispecificity [9, 10]. Among them, a highly complex combinatorial library, derived from the three-helix bundle of the albumin-binding domain (ABD) scaffold of streptococcal protein G has been used successfully for the selection of human interferon gamma binders [11], interleukin (IL)-23 receptor antagonist [12] and binders of human prostate secretory protein 94 (PSP94) [13]. In this work we applied the ABD scaffold library for the selection of unique binders of Stx1B.

Probiotics, including *E. coli* Nissle 1917 [14], *E. coli* 1307 [15], and several *Lactobacillus* strains [16] were reported as effective inhibitors of growth of STEC. Lactic acid bacteria (LAB) are often used as probiotics and are, because of their safety, also considered for genetic engineering and delivery of therapeutic proteins to the human intestine. We have previously demonstrated effective display of two non-Ig scaffolds, Affibodies [17] and DARPins [18], on the surface of recombinant or nonrecombinant lactic acid bacteria (LAB), by using the C terminal part of the lactococcal AcmA protein (cA) containing the lysine motif (LysM) domain as the cell wall anchor [19–22]. Engineered probiotic LAB with surface displayed Stx-binding protein could be a promising candidate for treating infections caused by STEC or *S. dysenteriae*. A similar approach has already been used in the development of recombinant *E. coli* bacteria with an engineered oligosaccharide biosynthesis pathway that resulted in the production of Stx receptor mimic on the bacterial surface [23, 24].

The goal of the present study was to engineer recombinant LAB *Lactococcus lactis* capable of binding Stx1B, by displaying binding proteins against Stx1B on the surface of *L. lactis*. We chose StxB as a target for selecting binding proteins against Stx, because it is capable of binding to the receptor and is not toxic by itself. We have expressed, purified and characterized recombinant Stx1B, and used it for the development of ABD-derived binding proteins S1Bs against Stx1B. S1Bs were biochemically, biophysically and functionally characterized, displayed on the surface of *L. lactis* and their ability to bind Stx1B was confirmed.

Materials and Methods

Bacterial strains, media and culture conditions

The bacterial strains used in this study are listed in [Table 1](#). *E. coli* strains DH5 α , BL21 (DE3) and BL21 (DE3) BirA were grown at 37°C, unless otherwise stated, with aeration in lysogeny

Table 1. Strains, plasmids, gene and primers used in this study.

Strain, plasmid, gene or primer	Relevant features or sequence (5'– 3')	Reference
Strains		
<i>E. coli</i>		
DH5 α	endA1 glnV44 thi-1 recA1 relA1 gyrA96 deoR F- Φ 80dlacZ Δ M15 Δ (lacZYA-argF)U169, hsdR17(rK- mK+), λ -	Invitrogen
BL21 (DE3)	F-ompT gal dcm lon hsdSB (rB- mB-) λ (DE3)	Novagen
BL21 (DE3) BirA	BL21 (DE3) with biotin ligase gene	Novagen
<i>L. lactis</i> NZ9000	MG1363 nisRK Δ pepN	[28–31]
Plasmids		
pET28b(+)	Kanr, <i>E. coli</i> expression vector	Novagen
pNZ8148	pSH71 derivative, PnisA, Cmr, nisin-controlled expression	[28–31]
pSDLBA3b	pNZ8148 containing gene fusion of spUsp-LEIS, b-dom and cA	[17]
pET28-Stx1B	pET28b containing Stx1B gene	This work
pET28- H6-TolA-Avi	pET28b containing tolA gene with AviTag on C-terminus	[12]
pET28-H6-S1Bx-TolA-Avi	pET28b containing gene fusion of different variants of S1B clones with TolA and AviTag	This work
pET28-H6-ABDwt-TolA-Avi	pET28b containing gene fusion of ABDwt with TolA and AviTag	
pSD-S1B22	pNZ8148 containing gene fusion of Usp45 signal peptide, S1B22 and cA	This work
pSD-S1B26	pNZ8148 containing gene fusion of Usp45 signal peptide, S1B26 and cA	This work
pSD-ABDwt	pNZ8148 containing gene fusion of Usp45 signal peptide, ABDwt and cA	This work
pSD-H6-ABDwt	pNZ8148 containing gene fusion of Usp45 signal peptide, H6 tag, ABDwt and cA	This work
Gene		
Stx1B	CCATGGCAAAAAAACATTATTAATAGCTGCATCGCTTTCATTTTTTTCAGCAAGTGCCTGGCGACGCCTGAT TGTGTAACGGAAAGGTGGAGTATACAAAATATAATGATGACGATACCTTTACAGTTAAAGTGGGTGATAAAGA ATTATTTACCAACAGATGGAATCTTCAGTCTCTTCTTCAGTGCGCAAATTACGGGGATGACTGTAACCATTA AAAC TAATGCCTGT CAT AATGGAGGGGATT CAGCGAAGTTATTTTTCGTCTCGAG	This work
Primer		
setB-rev	ACCGCGGATCCAGGTAA	[11, 12]
EWT5-ABDforN1	TTCTCCATGGGTATGAGAGGATCGCATCACCATCACCATCACCTGGCGGAAGCTAAAGTCTTAGCTAAC	[13]
EWT5-ABDforN2	TTCTCCATGGGCAGCAGCCATCACCATCACCATCACCTGGCGGAAGCTAAAGTCTTAGCTAAC	[13]
ABD-F	GGATCCCTGGCGGAAGCTAAAGTC	This work
S1B22-R	GAATTCAGGTAAACGAGCTAAAATAGCATCTATC	This work
S1B26-R	GAATTCAGGTAAACGAGCTAAAATCCAATC	This work
ABDwt-R	GAATTCAGGTAAATGCAGCTAAAATTTTCATCTATC	This work
ABDH6-F	AGGATCCCATCACCATCACCATCAC	This work

doi:10.1371/journal.pone.0162625.t001

broth (LB) medium supplemented with 50 µg/mL kanamycin. *L. lactis* NZ9000 was grown in M-17 medium (Merck) supplemented with 0.5% glucose (GM-17) and 10 µg/mL of chloramphenicol at 30°C without aeration.

Preparation of recombinant Stx1B subunit

A gene for Stx1B was designed (Table 1), synthesized *de novo* by ATG Biosynthetics (Merzhausen, Germany) and cloned to plasmid pET28b using NcoI/XhoI restriction sites, yielding pET28-Stx1B. Overnight culture of *E. coli* BL21 (DE3) harboring plasmid pET28-Stx1B was diluted (1:100) in 1 L of fresh LB medium and grown to optical density $A_{600} = 3.5\text{--}4.0$. Expression of fusion protein Stx1B with hexa-histidine (H6) tag was induced by addition of 1 mM isopropyl β -D-1-thiogalactopyranoside (IPTG) for 3 h at 28°C. The culture was centrifuged at $5000 \times g$ for 15 min and the pellet resuspended in 30 mL of equilibration/wash (Eq/W) buffer (50 mM NaH_2PO_4 , 300 mM NaCl, pH 7.0). The cells were lysed with a cycle of freezing and thawing, and with 3 fold 5 min sonication with a UPS200S sonifier (Hielscher, Teltow, Germany). After cell lysis, the suspension was centrifuged at $15000 \times g$ for 20 min and the supernatant stored. Inclusion bodies were dissolved in Eq/W buffers with increasing concentrations of guanidinium HCl (1M, 3M and 6M) for 6 h or overnight at 4°C, followed at each step by centrifugation and supernatant removal. Stx1B-H6 soluble in Eq/W with 6 M guanidinium HCl was isolated with BD Talon metal affinity resin (BD Biosciences) according to the manufacturer's instructions, using batch/gravity-flow column purification and imidazole elution (elution buffer: 45 mM NaH_2PO_4 , 270 mM NaCl, 5.4 M guanidinium HCl, 150 mM imidazole, pH 7.0). Fractions containing pure Stx1B were pooled and stored. We screened different refolding conditions according to [25–27]. Recombinant Stx1B was refolded by 100-fold rapid dilution in solubilization buffer (50 mM Tris-HCl with 0.5 M arginine and 0.01% Brij-35, pH 7.5).

Determination of molecular weight of Stx1B subunit

The molecular weight and oligomerization status of Stx1B were determined using analytical gel filtration chromatography (1.2×60 cm, 7 mL/h flow rate with 15 min fraction collection time) on a polyacrylamide gel Bio-Gel P-100 (Bio Rad, Hercules, USA), due to Stx1B cross-reactivity with a Superdex column (GE Healthcare), for size exclusion chromatography. Six proteins of 14.4–97 kDa (Amersham Low molecular weight Calibration Kit, GE Healthcare) were used as standards.

In vitro binding of Stx1B to globotriaosylceramide (Gb₃) receptor

Binding of Stx1B to its natural receptor Gb₃ was determined by enzyme-linked immunosorbent assay (Gb₃ ELISA) as described [32]. Receptor Gb₃ was purchased from Matreya LLC (PA, USA) and dissolved in chloroform/methanol (2:1). 100 µL of Gb₃ solution with concentration 10 µg/mL was used to coat Nunc PolySorp Strips (Thermo Fisher Scientific) overnight in laminar flow to evaporate chloroform/methanol. After washing with phosphate buffer saline with 0.05% Tween 20 (PBST) and blocking with 2% bovine serum albumin (BSA) in PBST, 100 µL of serial twofold dilutions of recombinant Stx1B in triplicate (starting with 1 µg/mL in 0.2% BSA in PBST) were added to the wells and incubated for 1 h. Bound Stx1B-H6 was detected with primary THE™ His tag Antibody (GenScript, NJ, USA) (dilution 1:2000 in 0.2% BSA in PBST) and with horseradish peroxidase (HRP)-conjugated goat anti-mouse IgG secondary antibody (Merck Millipore, Darmstadt, Germany) (dilution 1:5000 in 0.2% BSA in PBST). The color was developed by the addition of 100 µL substrate buffer (150 mM Na_2HPO_4 , 50 mM citric acid, pH 6.0) and 100 µL 3,3',5,5'-tetramethylbenzidine (TMB) substrate (Sigma-Aldrich, MO, USA) for 15 min at room temperature. The reaction was

terminated by the addition of 50 μ L 2 M H₂SO₄ and absorbances were read at 450 nm using Infinite M1000 (Tecan, Salzburg, Austria). No Stx1B was added to 0.2% BSA in PBST in control wells (zero concentration), while all the other steps were performed as described above. All samples were measured in triplicates.

Internalization of recombinant Stx1B by HeLa cells

HeLa cells (American Type Culture Collection) were grown in Dulbecco's Modified Eagle Medium (DMEM) supplemented with 10% fetal bovine serum (FBS), 1% GlutaMAX and pen-strep in 24-wells plates on coverslips. Fluorescein isothiocyanate (FITC)-labelled Stx1B (10 μ g/mL in 300 μ L of fresh medium) was added to the cells and incubated for 1 h on 37°C. The cells were then washed with PBS, fixed with 4% paraformaldehyde (PFA) in PBS for 15 min and permeabilized with 0.1% triton X-100 in PBS for 10 min. Non-specific staining was blocked with 3% BSA in PBS for 1 h. Golgi apparatus (GA) was labelled with mouse monoclonal anti-human Golgin-97 primary antibody (0.4 μ g/ml in 3% BSA for 1 h, Life Technologies, CA, USA) and with Alexa Fluor 555-conjugated donkey anti-mouse secondary antibody (1:1000 in 3% BSA for 1 h, A-31570, Life technologies). Coverslips were mounted with ProlongGold Anti-fade reagent with 4',6-diamidino-2-phenylindole (DAPI; Invitrogen). Immunostained cells were visualized with LSM-710 confocal microscope (Carl Zeiss, Germany), and images were acquired and processed using ZEN 2010 B SP1 software (Carl Zeiss).

Selection of Stx1B binders by ribosome display

The combinatorial DNA library of ABD protein was generated as described [11, 12], *in vitro* transcribed and the resulting mRNA was translated using *E. coli* extract (EasyXpress Protein Synthesis Mini Kit, QIAGEN, Germany). The translated products were used for the selection of Stx1B binders by ribosome display. Preselection of BSA binders was performed in wells coated with 3% BSA before the first round of the selection. The five rounds of ribosome display selections were performed in Maxisorp (NUNC, Denmark) microtiter plates coated with decreasing concentrations of recombinant Stx1B (round 1 and 2: 25 μ g/mL, round 3: 10 μ g/mL, round 4: 4 μ g/mL, round 5: 1 μ g/mL) and blocked with 3% BSA. All incubation and washing steps were performed as described [12] and after each round, mRNA was eluted from the bound ribosome complex with elution buffer (50 mM Tris-acetate, pH 7.5, 150 mM NaCl, 50 mM EDTA) containing 50 μ g/mL of *Sacharomyces cerevisiae* RNA. Purified RNA was transcribed into cDNA using reverse transcription with setB-rev primer (Table 1). Double-stranded DNA was produced by PCR using EWT5-ABDforN1 and setB-rev primers (Table 1) and fused with T7 promoter, RBS and truncated *tolA* sequences for the next round of *in vitro* translation. After the last round of the selection the final PCR product was amplified with EWT5-ABDforN2 (Table 1) primer instead of the EWT5-ABDforN1 primer, and cloned to pET28-H6-TolA-Avi plasmid (Table 1) via NcoI/BamHI sites, yielding pET28-H6-S1B-TolA-Avi. The resulting plasmid mixture was transformed into *E. coli* DH5 α , and plasmid DNA from randomly picked colonies was sequenced.

Sequence analysis and clustering of selected S1B binders

DNA sequencing of S1B variants was carried out by the Centre for DNA Sequencing of the Institute of Microbiology of the ASCR, v.v.i. (Prague, Czech Republic) or GATC Biotech (Constance, Germany). Amino acid sequences of selected clones were aligned and a similarity tree was constructed using Molecular Evolutionary Genetics Analysis tool (MEGA), version 6.0.6 (<http://www.megasoftware.net/>). Randomized sequences between residues 20 and 46 were compared, as the N-terminal amino acid positions 1–19 were non-randomized.

ELISA screening of Stx1B binders

S1B clones with unique (previously unreported) sequences were transformed into *E. coli* BL21 (DE3) BirA (Table 1) and expressed for 4 h in 2.5 mL cultures with the addition of 1 mM IPTG and 50 μ M D-biotin. Bacteria were pelleted at 15000 \times g for 5 min and resuspended in 0.01% PBST with 200 μ g/mL lysozyme. Cells were lysed with three cycles of freezing at -80°C and thawing at 37°C for 30 min. Cell lysate was centrifuged for 15 min and 50 μ L of supernatant was loaded to a PolySorp microtiter plate (Nunc), previously coated with 10 μ g/mL of recombinant Stx1B and blocked with 1% BSA (Carl Roth GmbH, Karlsruhe, Germany). After 1 h incubation at RT, the plate was washed five times with PBST, and ABD-binders were detected with HRP-conjugated streptavidin (1:5000 in 1% BSA/PBST). The color was developed with the addition of 0.5 mg/mL o-phenylenediamine (OPD, Sigma-Aldrich, St. Louis, USA) and 0.01% H₂O₂ in 0.1 M citrate buffer (pH 5.0) for 5 min. The reaction was stopped with the addition of 2 M H₂SO₄ and absorbance read at 492 nm. Lysate containing the wild-type albumin binding domain (ABDwt) in fusion with TolA protein was loaded to wells coated with 10 μ g/mL of human serum albumin (Abcam, Cambridge, UK) to serve as a positive control. Negative background was recorded in wells loaded with 1% BSA/ PBST without S1B-TolA lysate. All samples were measured in triplicates.

Expression and purification of selected H6-S1B-TolA-Avi variants

Selected H6-S1B-TolA-Avi variants were expressed in 200 mL cultures as described above. Cells were harvested by centrifugation at 5000 \times g for 20 min, resuspended in 10 mL binding buffer (20 mM Na-phosphate, 500 mM NaCl, 10 mM imidazole, pH 7.4) and lysed by sonication for 3 min. Lysates were centrifuged at 10000 \times g for 20 min and supernatants were kept. Fusion proteins were purified by fast protein liquid chromatography (Äkta Purifier, GE Healthcare) on 1 mL HisTrap HP columns (GE Healthcare) or BD Talon metal affinity resin (BD Biosciences, Palo Alto, USA) using batch/gravity-flow column purification and imidazole elution according to the manufacturer instructions. Eluted fractions were analyzed by SDS-PAGE, pooled and concentrated by ultrafiltration using Amicon Ultra (Merck Millipore; Darmstadt, Germany). Purified H6-S1B-TolA-Avi fusion proteins were dialyzed against PBS and used for ELISA tests, surface plasmon resonance analysis and microscale thermophoresis.

Assessment of binding of S1B variants to Stx1B by ELISA

The microtiter plate was coated overnight at 4°C with 10 μ g/mL of recombinant Stx1B in coating buffer (100 mM Na-bicarbonate/carbonate, pH 9.6). Wells were washed with PBST and blocked with 1% BSA in PBST for 2 h at RT. Serially diluted H6-S1B-TolA-Avi fusion proteins or ABDwt control in 1% BSA/PBST were loaded for 1 h. Following washing, bound S1B clones were detected with the addition of HRP-conjugated streptavidin (dilution 1:5000 in 1% BSA/PBST). The color was developed with 0.5 mg/mL OPD and 0.01% H₂O₂ in 0.1 M citrate buffer (pH 5.0) for 5 min. The reaction was stopped by the addition of 2 M H₂SO₄ and absorbance read at 492 nm. All samples were measured in triplicates.

Assessment of binding of S1B variants to Stx1B by surface plasmon resonance (SPR)

SPR measurements were performed with Biacore T100 (GE Healthcare) at 25°C. In the first setup we tested the binding of S1B variants prepared in fusion with TolA spacer protein and AviTag to Stx1B captured on a Series S sensor chip CM5 (Biacore, GE Healthcare). CM5 sensor chip was activated using Amine coupling Kit (GE Healthcare) according to the manufacturer's

instructions. For immobilization of Stx1B standard PBS buffer (137 mM NaCl, 2.7 mM KCl, 10 mM Na₂HPO₄, 1.8 mM KH₂PO₄, pH 7.4) was used as running buffer. Stx1B was diluted into 10 mM sodium acetate buffer, pH 5.0, to a final concentration of 20 µg/mL, and injected over the second flow cell. The final immobilization level was approximately 890 response units (RU). The first flow cell was empty and served as a reference cell to control the level of non-specific binding. All experiments were performed with running buffer PBS with 300 mM NaCl (300 mM NaCl, 2.7 mM KCl, 10 mM Na₂HPO₄, 1.8 mM KH₂PO₄, pH 7.4, 0.005% P20). Each compound was injected for 2 min at a flow-rate of 20 µL/min, and dissociation was monitored for 3 min. Regeneration of the sensor surface was achieved with two 30 s pulses of 50 mM NaOH. The following concentrations were used for titration: 0, 15.625, 31.25, 62.5, 125, 250, 500, 1000, 2000 nM; concentration 62.5 nM was repeated at the end of the concentration series.

In the reverse setup H6-S1B22-TolA-Avi or H6-S1B26-TolA-Avi variants were immobilized on a sensor chip CM5. CM5 sensor chip activation and immobilization of H6-S1B-TolA-Avi variants was performed as described above, except that two injections were needed to reach the final immobilization level of approximately 1100 RU. All experiments were performed with running buffer PBS with 300 mM NaCl (300 mM NaCl, 2.7 mM KCl, 10 mM Na₂HPO₄, 1.8 mM KH₂PO₄, pH 7.4, 0.005% P20). Each compound was injected for 1 min at a flow-rate of 10 µL/min, and dissociation was monitored for 60 s. Regeneration of the sensor surface was achieved with 25 mM NaOH for 6 s at a flow-rate of 20 µL/min. The following concentrations were used for titration: 62.5, 125, 250, 500, 1000, 2000, 4000 nM and the concentration of 500 nM was repeated at the end of the concentration series. Each titration was performed in triplicate. The obtained data was evaluated using Biacore T100 Evaluation software. The sensorgrams were reference and blank subtracted and the Steady State Affinity model was applied to calculate the affinity constant (K_d). The average of three repeated experiments was used for final K_d determination.

Assessment of binding of S1B variants to Stx1B by microscale thermophoresis (MST)

Purified Stx1B in PBS buffer (pH 7.4) was fluorescently labelled according to the manufacturer's instructions (L001™ Monolith NT.115 Protein Labelling Kit RED-NHS, NanoTemper Technologies GmbH, Germany). The stock solution of labelled Stx1B was diluted in PBS buffer with 300 mM NaCl and 0.1% Tween 20 to a final concentration of 10 nM. Sixteen serial dilutions of purified non-labelled S1B22 and S1B26 were prepared in standard PBS buffer, starting with concentrations of 35 µM and 45 µM, respectively. Serial dilutions of S1B variants were mixed 1:1 with a solution of 10 nM labelled Stx1B to a final volume of 20 µL per dilution. Prepared mixtures were incubated for 5 min at room temperature and centrifuged for 5 min at 15,000 g to remove any aggregates. The samples were filled into the Premium coated capillaries (NanoTemper Technologies GmbH, Germany). Measurements were carried out with the Monolith NT.115 instrument (NanoTemper Technologies GmbH) at 25°C using 90% LED power and 20% MST power. Data analysis was completed with NanoTemper analysis software using fluorescence change for K_d determination. The SDS-denaturation test was performed to confirm that the fluorescence change is the consequence of specific binding of ligand to the target and not due to loss of fluorescence caused by ligand-induced surface absorption or aggregation. The average of three repeated experiments was considered for final K_d calculation.

Fluorescence-based thermal shift assay (TSA)

The thermal stability of S1B proteins was tested in PBS and 50 mM Tris, 300 mM NaCl, pH 8.0 (T50N300) buffers with the addition of 5× Sypro Orange dye (Sigma-Aldrich, St. Luis, USA) to

the 25 μ L total volume. TSA was performed with the real-time PCR Detection System CFX touch (BIO-Rad Laboratories, Hercules, USA) according to [12]. The data were analyzed with CFX Manager Software and the melting temperatures (T_m) determined using the first derivative spectra.

Influence of S1B binders on internalization of Stx1B into HeLa cells

S1B22, S1B26 and ABDwt (final concentration 100 μ g/ml) were preincubated with Alexa Fluor 488-labelled recombinant Stx1B (Alexa Fluor 488[®] Protein Labeling Kit, Thermo Fisher Scientific, Massachusetts, USA—final concentration 5 μ g/ml) for 1 h in complete DMEM medium at 37°C. Stx1B, ABDwt, S1B22 or S1B26 were used alone as corresponding controls. Afterwards, the mixtures of protein and Alexa Fluor 488-Stx1B were added to HeLa cells grown in 24 well plates (flow cytometry) or on coverslips (fluorescence microscopy) and incubated for 1 h at 37°C. After incubation, the media were discarded and cells were washed with PBS and prepared for further analysis.

For flow cytometric analysis cells were detached by mild trypsinization (TripleSelect, Life Technologies) washed three times with PBS and measurements were performed on a BD FACS Calibur instrument (Beckton Dickinson, Franklin Lakes, NJ) as described in [18] using BD CellQuest Pro software for data acquisition and analysis (Beckton Dickinson).

For fluorescence microscopy the coverslips-grown cells were either labeled with PKH26 dye for general cell membrane labeling or stained with antibodies for GA labelling. Membrane labelling was performed with Red Fluorescent Cell Linker Kit containing PKH26 dye (Sigma-Aldrich, St. Louis, USA) following manufacturer's instructions. Afterwards, the cells were fixed with 2% PFA and washed with PBS. For labeling with antibodies cells were first fixed in 2% PFA, permeabilized with 0.1% Triton X-100 and incubated for 1 h in 3% BSA in PBS for blocking of non-specific staining. For labeling of GA primary mouse monoclonal anti-Golgin-97 (CDFX) antibody (1:100 in 3% BSA in PBS, Santa Cruz Biotechnology, Dallas, USA, sc-59820) and polyclonal Goat anti-Mouse Secondary Antibody conjugated with Alexa Fluor 633 (1:1000 in 1% BSA in PBS, Thermo Fisher Scientific, A-21052) were used. Cells were washed three times with PBS after every of the above mentioned steps. After the last washing step cells were stained with DAPI (Sigma-Aldrich, St. Louis, USA) and mounted with Prolong Gold Antifade Reagent (Life technologies). Immunostained cells were visualized with LSM-710 confocal microscope equipped with ZEN 2010 B SP1 software (Carl Zeiss).

Molecular cloning and expression of S1B-cA variants in *L. lactis*

Genes of S1B variants without TolA spacer were amplified with Phusion polymerase (New England Biolabs, Beverly, MA) using pET28-H6-S1Bx-TolA-Avi template and ABD-F primer and the corresponding S1B-R primer (Table 1). The gene for ABDwt was amplified using pET28-H6-ABDwt-TolA-Avi template and ABD-F/ABDwt-R (Table 1) primer pair, while H6 tag was added with ABDH6-F/ABDwt-R primer. All PCR fragments were ligated to pJET 1.2 cloning vector and cloned into plasmid pSDLBA3b, using BamHI and EcoRI restriction enzymes (New England Biolabs). Plasmid DNA was isolated with NucleoSpin Plasmid kit (Macherey and Nagel, Düren, Germany), with an additional lysozyme treatment for *L. lactis*. Lactococci were transformed by electroporation using a Gene Pulser II apparatus (Bio-Rad, Hercules, CA) according to MoBiTec GmbH instructions (Goettingen, Germany). Plasmids constructed in the study are listed in Table 1. S1B-cA variants were expressed in *L. lactis* NZ9000 in 10 mL cultures. Bacterial suspensions were grown to an A_{600} of 0.8, followed by induction with 25 ng/mL nisin (Fluka) for 3 h [17, 18, 33, 34]. Resulting suspensions were stored at 4°C for flow cytometric analysis or whole cell ELISA test.

Flow cytometry and whole cell ELISA

For flow cytometric analyses, 10 μL of *L. lactis* suspensions were added to Tris-buffered saline (TBS) and centrifuged. Cells were resuspended in TBS with Alexa 488-labelled recombinant Stx1B (20 $\mu\text{g}/\text{mL}$) and incubated at RT with constant shaking at 100 rpm. All washings, centrifugation steps and measurements were performed as described [18, 35].

The whole cell ELISA was carried out according to [36] with a few modifications. *L. lactis* suspension with surface-displayed S1B variant or ABDwt was centrifuged and resuspended in PBS to an A_{600} of 1.0. 750 μL of the suspensions were washed twice in PBS and incubated with 500 μL of recombinant Stx1B (20 $\mu\text{g}/\text{mL}$ in PBS) for 2 h, followed by additional washing with PBS. Bound toxin subunit was detected with the addition of 200 μL of Anti-Verotoxin I/SLT 1b (antiStx1B) primary antibody (diluted 1:20 in PBS, Abcam, Cambridge, UK) for 1 h, followed by washing and incubation with 200 μL of (HRP)-conjugated Goat anti-mouse IgG secondary antibody (diluted 1:500 in PBS, Merck Millipore, Darmstadt, Germany). All incubations were performed at RT in a tube rotator. After incubation with secondary antibody, cells were washed, first with PBS and then with substrate buffer (150 mM Na_2HPO_4 , 50 mM citric acid, pH 6.0). Cells were finally resuspended in 1 mL of substrate buffer, and 100 μL of suspensions, or 1:5 dilutions in substrate buffer, were loaded on a microtiter plate. The color was developed with the addition of 100 μL TMB substrate and the reaction stopped after 15 min by the addition of 50 μL of 2 M sulphuric acid. Absorbances were read at 450 nm.

Statistical analyses

Statistical analyses were performed with GraphPad Prism 5.0 software. Student's t test was used to compare the significance of differences between samples and control.

Results and Discussion

Production of recombinant Stx1B

Recombinant Shiga toxin 1B subunit (Stx1B) fusion protein with hexa histidine (H6) tag was produced in *E. coli* as a target for the selection of high affinity binders derived from ABD scaffold by using a novel procedure for its recombinant expression. The gene for Stx1B was synthesized and cloned to pET28b vector. Various expression conditions (growth at 37°C, 30°C and 25°C, induction at optical densities (A_{600}) 0.5, 1, 2 and 3.5–4.0) were tested. The highest total amount of Stx1B-H6 expression was achieved by growing the bacteria at 37°C to $A_{600} = 3.5$ –4.0, followed by induction with 1 mM IPTG for 3 h at 28°C. The majority of the fusion protein was produced in the form of inclusion bodies, which were dissolved in 6 M guanidinium HCl and efficiently purified with immobilized metal affinity chromatography (IMAC). We screened different refolding conditions and Stx1B-H6 was effectively solubilized by the rapid dilution method using 0.5 M arginine and 0.01% Brij-35-containing 50 mM Tris buffer, conditions similar to those reported by Oneda and Inouye [27] for another protein. The solubilized product was stored in Tris or PBS buffer for characterization.

Characterization of recombinant Stx1B

The molecular weight of recombinant Stx1B-H6 was determined by analytical gel filtration chromatography. It was eluted from calibrated column as one sharp symmetrical peak, with a molecular weight corresponding to the pentameric form of recombinant Stx1B.

The functionality of recombinant Stx1B was tested by its ability to bind to immobilized globotriosyl ceramide (Gb_3) receptor *in vitro*, and by its internalization into HeLa cells, which naturally contain Gb_3 on the surface. Strong, specific and concentration depended binding of

recombinant Stx1B to immobilized Gb₃ receptor was demonstrated with ELISA (Fig 1A). Stx1B was internalized into the HeLa cells 1 h after co-incubation and was transferred to GA where it co-localized with the GA marker Golgin-97 (Fig 1B), which is in accordance with a previous study [37]. These results showed that recombinant Stx1B was fully functional and suitable as a target for selection of novel high affinity binders.

Ribosome display selection of Stx1B binders

Smaller antibody variants, i.e. single chain variable fragments (ScFv), against Stx1B were previously selected by screening a phage display library constructed from a naïve human repertoire [38]. However, it was previously observed that, similar to antibodies themselves, ScFvs are not suitable for surface display on lactococcal cells (unpublished data), especially in comparison to non-Ig scaffolds, such as DARPins and Affibodies, possibly due to their larger size and more complex folding. To obtain novel protein binders of Shiga toxin, a highly complex combinatorial library derived from streptococcal albumin-binding domain scaffold was therefore applied.

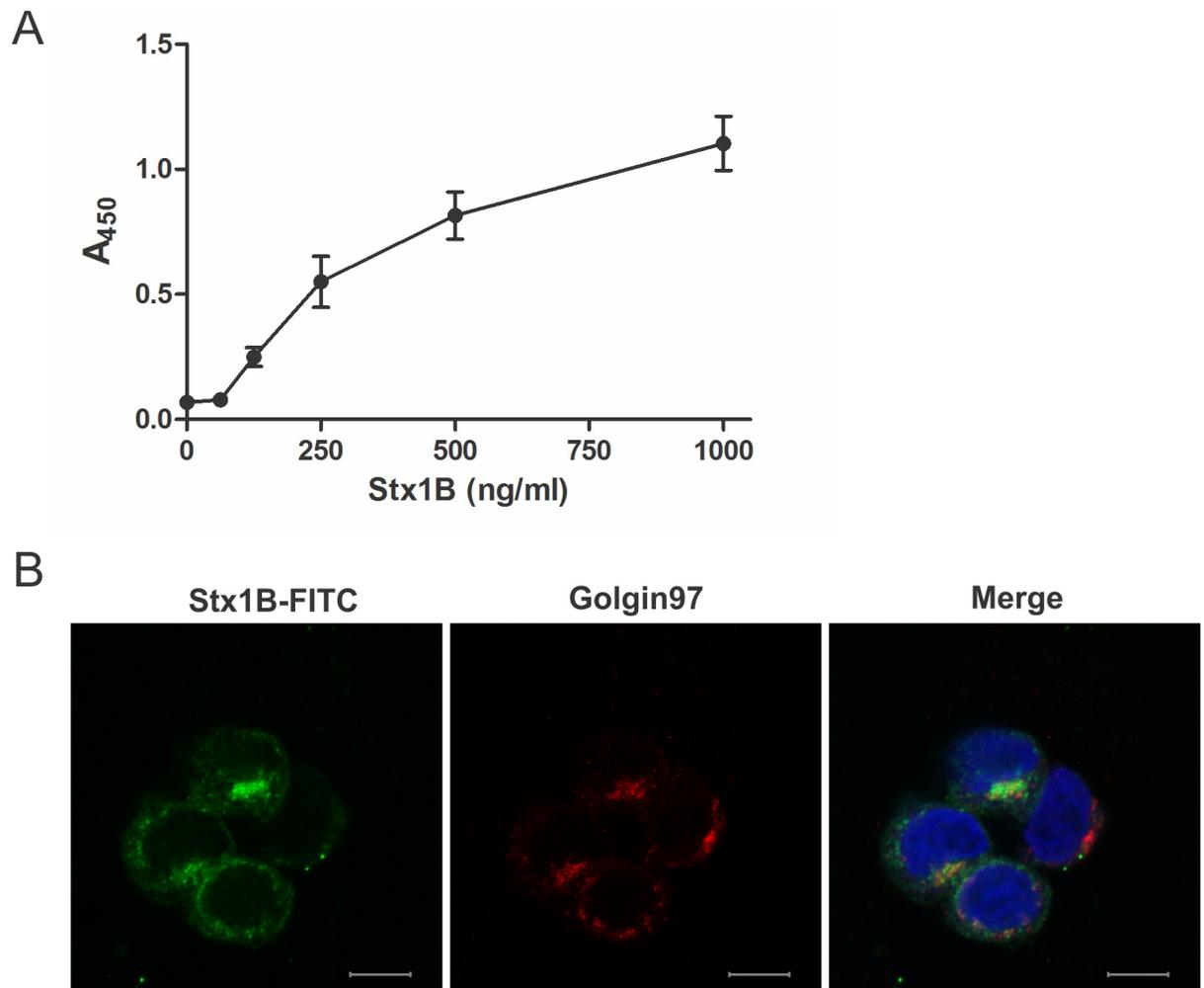


Fig 1. Ability of recombinant Stx1B to bind to Gb₃ receptor *in vitro*. (A) Binding of serially diluted Stx1B to Gb₃ as determined by ELISA using THE™ His tag antibody. A₄₅₀: Absorbance at 450 nm. Error bars denote standard deviations. (B) Internalization of FITC-labelled Stx1B into HeLa cells. Golgi apparatus was detected with mouse anti-human Golgin-97 primary antibody and Alexa Fluor 555-conjugated donkey anti-mouse secondary antibody (red). DAPI staining was used to label nuclei (blue). Bars = 10 μm.

doi:10.1371/journal.pone.0162625.g001

This has been used successfully for selecting high-affinity binders of IFN- γ [11], for development of IL-23 receptor antagonists [12] and for generation of unique binders of human prostate cancer oncomarker [13].

To select unique binders of Stx1B we used the highly-complex combinatorial ABD library [11], [12], [13] and ribosome display. Ribosome display enables the selection of binding proteins by associating ribosome-translated proteins with their parent mRNA in a complex. The mRNA-protein hybrids are selected against an immobilized ligand in multiple selection steps. The mRNA is then reverse transcribed to cDNA and its sequence amplified via PCR [39]. In the present work five cycles of ribosome display selection were performed, yielding a collection of 17 unique Stx1B-binders designated as S1B binders (Fig 2A). The identified S1B binders were produced in *E. coli* as fusion proteins with TolA spacer containing AviTag on the C-terminus and a H6 tag on the N-terminus (H6-S1B-TolA-Avi), as reported previously [11–13]. The expression level of the corresponding fusion protein was tested by SDS PAGE and the binding capacity verified by ELISA (Fig 2B). Binders S1B9, S1B22 and S1B26 with TolA-Avi and H6 fusion were selected for further analysis. The S1B28 variant showed a lower level of expression, possibly due to an unintended mutation in a non-randomized part of sequence, while S1B23 bound BSA and was therefore not Stx1B-specific. Both variants were excluded from further characterization.

Production and characterization of selected S1B binders

Selected binders in fusion with TolA-Avi and H6 were produced in *E. coli* on a large scale, purified with IMAC or HisTrap FPLC and verified on SDS-PAGE electrophoresis, where low level of expression and some proteolytic degradation of S1B9 variant were observed (Fig 3A). Stx1B was immobilized and incubated with serial dilutions of selected S1B binders, detected with HRP-streptavidin. Gradual increase of the ELISA signal confirmed binding of S1B binders to recombinant Stx1B (Fig 3B). Variant S1B26 showed the strongest binding, while binding of S1B9 variant was the weakest, which may be the consequence of degradation noted above. Sequence similarity comparison of selected binders S1B9, S1B22 and S1B26 with parental non-mutated ABDwt is presented in Fig 3C.

Based on ELISA tests and SDS PAGE analysis clones S1B22 and S1B26 were selected for further characterization of binding with surface plasmon resonance (SPR) and microscale thermophoresis (MST), and of stability with thermal shift assay (TSA).

Characterization of binding affinity of the selected S1B binders

The first setup of SPR affinity measurements included immobilization of Stx1B on the sensor chip surface and injecting S1B proteins over the surface. Binding was confirmed with different dilutions of both binders, S1B22 and S1B26. Nevertheless, we could not determine the binding constant (K_d) for tested interactions with any of the available binding models in Biacore T100 Evaluation software. This was probably due to a complex interaction between S1B variants and Stx1B, which is in pentameric form, and probably binds more than one S1B molecule. The binding mode between Stx1B and S1B binders could be investigated by structural analysis, such as molecular docking or by solving the structure of the complex. Fig 4 shows a representative response after S1B22, S1B26 and ABDwt, all in fusion with TolA-Avi and H6, were injected at 1 μ M concentration over the immobilized Stx1B. A much higher sensor response was observed with S1B22 and S1B26 than with ABDwt.

In contrast, by reversing the SPR setup, S1B22 and S1B26 in fusion with TolA-Avi and H6 were attached to the sensor chip surface and two-fold dilutions of recombinant Stx1B, starting with 4 μ M concentration, were injected over the chip surface (Fig 5A). Affinity constants were

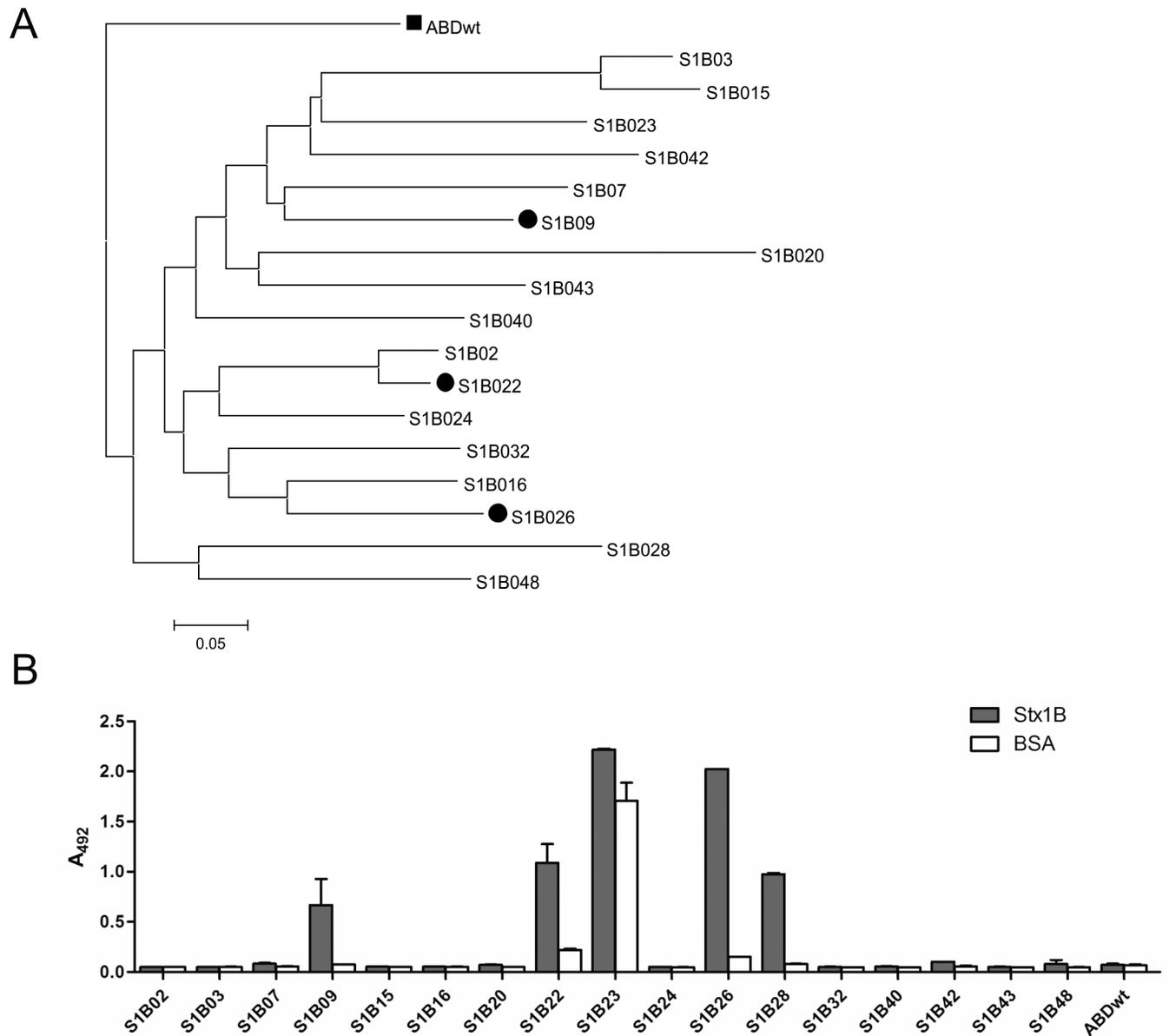


Fig 2. Sequence similarity analysis (A) and binding affinity (B) of 17 S1B binders selected after five rounds of ribosome display. A: The sequence of the parental ABD wild-type domain was used as a root of the tree and is highlighted as a square, while S1B variants selected for more detailed analysis are highlighted as circles. B: S1B binders-containing cell lysates were incubated with immobilized Stx1B (grey bars) or BSA (white bars) and detected with HRP-conjugated streptavidin. Error bars denote standard deviations.

doi:10.1371/journal.pone.0162625.g002

calculated by applying the Steady State Affinity model (Fig 5B) and the average of three experiments was considered. The binding affinity of recombinant Stx1B to S1B22 was $0.70 \pm 0.03 \mu\text{M}$ and, to S1B26, $1.00 \pm 0.09 \mu\text{M}$.

The binding affinity of S1B22 and S1B26 to fluorescently-labelled recombinant Stx1B in solution was confirmed by MST. The binding curves obtained from three repeat measurements for S1B22 and S1B26 are shown in Fig 5C. The commercial analysis software was used to plot and fit the change in initial fluorescence to yield K_d values in the micromolar range of $0.4 \pm 0.05 \mu\text{M}$ for S1B22 and $0.6 \pm 0.05 \mu\text{M}$ for S1B26.

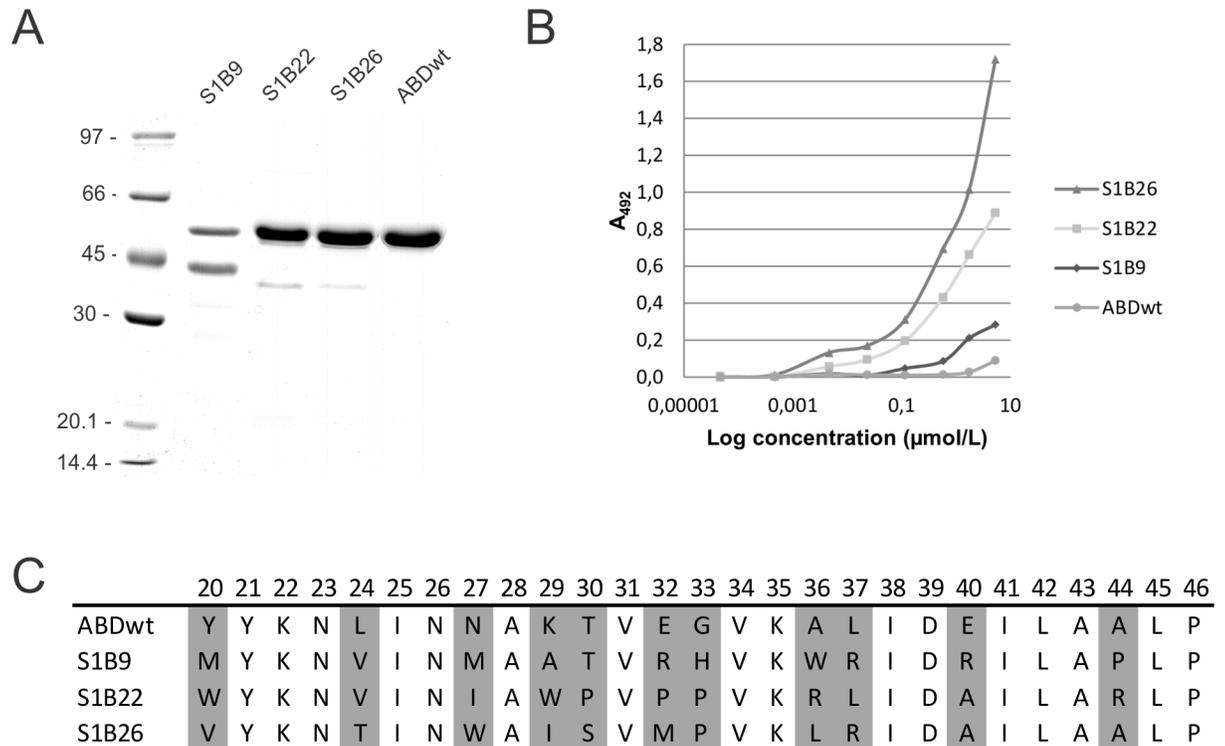


Fig 3. (A) SDS PAGE analysis of selected binders S1B9, S1B22 and S1B26 after purification from *E. coli* cell lysates, stained with Coomassie brilliant blue. (B) ELISA-determined binding of serially diluted biotinylated binders selected against immobilized recombinant Stx1B. The binding was detected by HRP-conjugated streptavidin. (C) Sequence similarity comparison of selected binders with parental non-mutated ABDwt. Randomized sequences between residues 20 and 46 were compared. Randomized positions are indicated in grey.

doi:10.1371/journal.pone.0162625.g003

Calculated affinities are lower than those reported for ScFvs against Stx1B [38]. However, the affinity of ABDs could be further improved by affinity maturation approach, in which a new combinatorial library would be constructed from the best binder sequence using error prone PCR and where the new library would be subjected to a second selection against the same target under conditions of increasing stringency [40].

Characterization of the stability of selected S1B binders

The thermal stabilities of binders S1B22 and S1B26 in fusion with TolA-Avi and H6 were investigated by the fluorescence-based thermal shift assay. The denaturation temperature (T_m) determined for binder S1B26 was 53°C in PBS buffer and 54°C in Tris-NaCl buffer. T_m for binder S1B22 could not be determined in any of the tested buffers, probably due to the presence of two tryptophanes and three prolines in the randomized part of S1B22, which are known to destabilize helical structure of proteins. The T_m value for parental wild-type ABD has been reported to be 58°C [12, 13].

Redirection of Stx1B transport in HeLa cells by selected S1B binders

S1B22 and S1B26 in fusion with TolA-Avi and H6 were tested for their ability to prevent binding of Stx1B to HeLa cells, or to interfere with retrograde transport of Stx1B to GA in HeLa cells. When fluorescently labelled Stx1B (Stx1B-Alexa Fluor 488) was mixed with S1B binders prior to incubation with HeLa cells, no decrease in mean fluorescence intensity

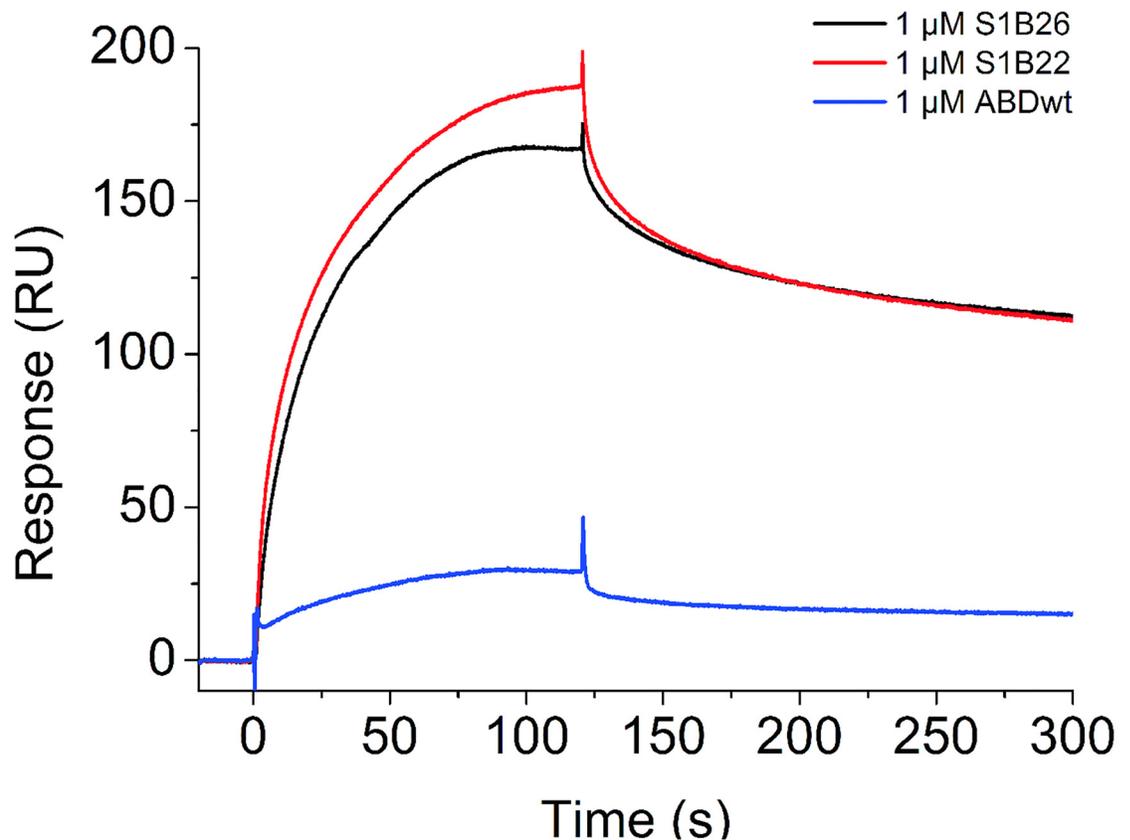


Fig 4. SPR analysis of binding of S1B22, S1B26 and ABDwt in fusion with TolA-Avi and H6 at 1 μ M concentration to immobilized recombinant Stx1B.

doi:10.1371/journal.pone.0162625.g004

(MFI) compared to the control (incubated with Stx1B-Alexa Fluor 488 alone) was observed with flow cytometry that would be consistent with inhibition of binding to HeLa cells. On the contrary, higher MFI was observed in cells incubated with mixtures of S1Bs and Stx1B-Alexa Fluor 488 (Fig 6A and 6B), indicating higher amount of bound Stx1B-Alexa Fluor 488 or different cell distribution of internalized toxin. ABDwt in fusion with TolA-Avi and H6 had no effect on internalization of Stx1B-Alexa Fluor 488 into HeLa cells (Fig 6A and 6B).

To investigate the effect of S1Bs into more details we performed fluorescence microscopy using membrane labelling marker PKH26 (Fig 6C) and marker for GA (Fig 6D). In cells incubated with Stx1B-Alexa Fluor 488 alone, or mixture of Stx1B-Alexa Fluor 488 and ABDwt, the majority of Stx1B-Alexa Fluor 488 was co-localized with the marker of GA 1 h after addition to HeLa cells (Fig 6D), as shown before with FITC-conjugated Stx1B (Fig 1B). When Stx1B-Alexa Fluor 488 was pre-incubated with S1B22 or S1B26 the distribution of Stx1B in HeLa cells was completely altered. Stx1B-Alexa Fluor 488 was partially co-localized with membrane dye, indicating localization at the cell membrane or in membrane bound vesicles, while the co-localization with the GA marker was completely lacking, indicating its absence from GA. S1B22 and S1B26 interfered with conventional internalization route of Stx1B into the HeLa cells, suggesting a possible inhibitory function of S1B variants on Stx1B retrograde transport. However, more analyses need to be performed to prove the exact mechanism of S1Bs on Stx1B trafficking.

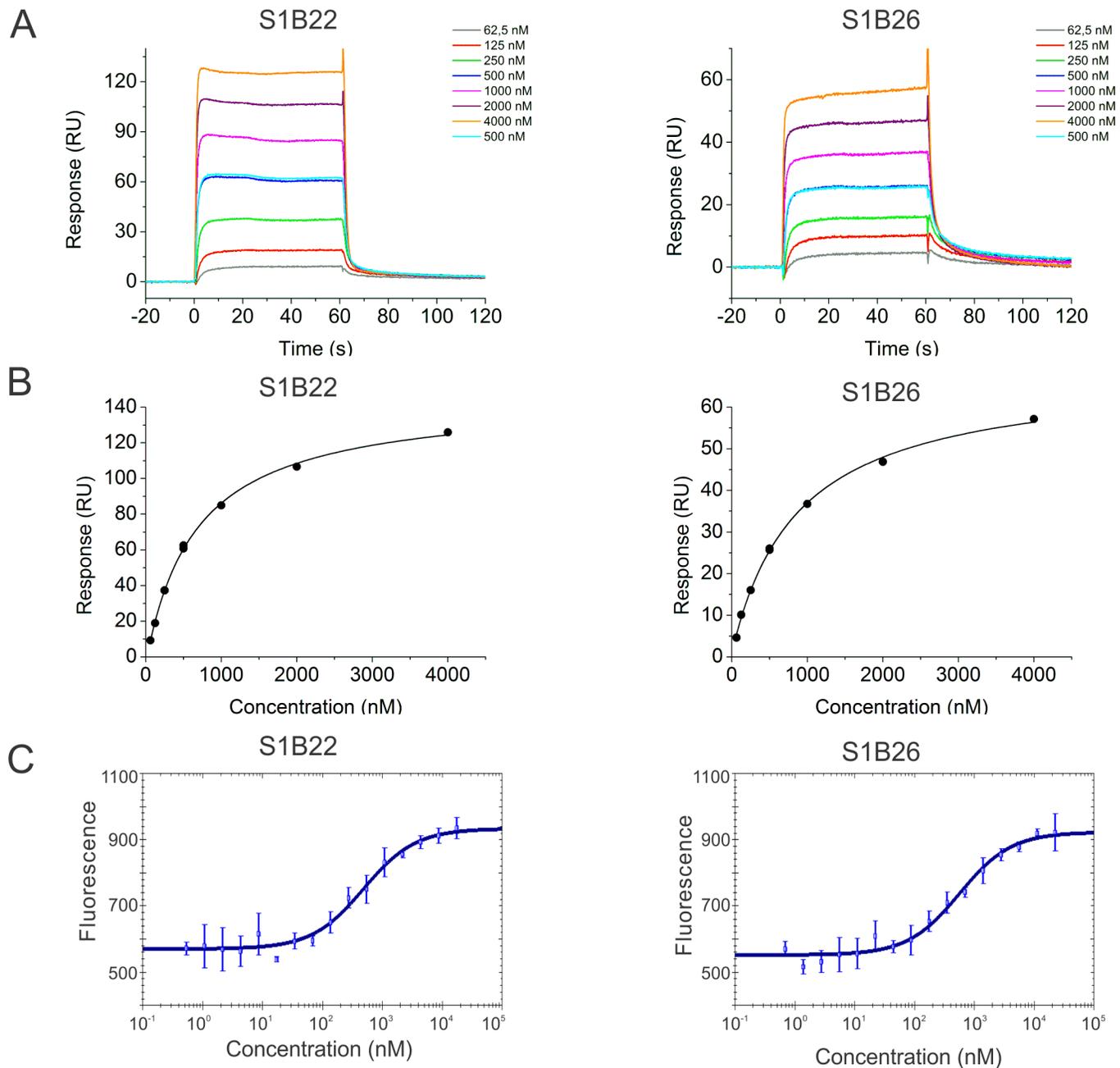


Fig 5. Determination of binding affinity of selected S1B variants to recombinant Stx1B by SPR analysis (A, B) and MST (C). (A) Recombinant Stx1B at seven different concentrations was injected over the chip surface with immobilized H6-S1B22-TolA-Avi or H6-S1B26-TolA-Avi. (B) Steady state response (obtained in (A)) was plotted against Stx1B concentration and Steady State Affinity model was applied to calculate the affinity constant. (C) Sixteen serial dilution concentrations of H6-S1B22-TolA-Avi or H6-S1B26-TolA-Avi were mixed with fluorescently labelled Stx1B at 5 nM final concentration. Fluorescence change K_d fit in NanoTemper software was used to calculate K_d . Error bars denote standard deviations.

doi:10.1371/journal.pone.0162625.g005

Expression and surface display of selected S1B binders on *L. lactis* NZ9000

Genes for S1B22, S1B26, ABDwt and H6-ABDwt without tolA spacer or tags were amplified with PCR and cloned into the plasmid pSDLBA3b [17], which had been designed for the

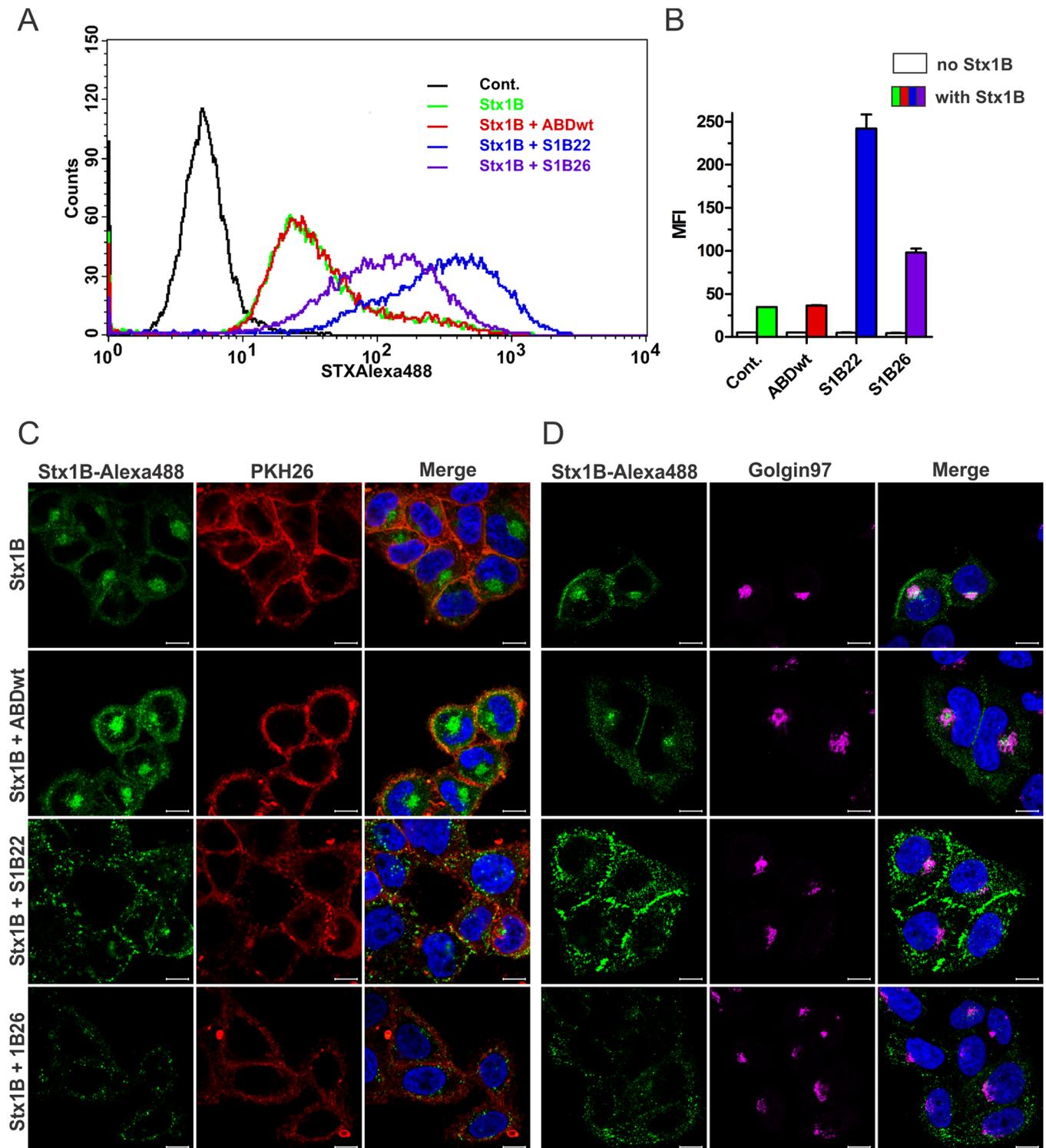


Fig 6. Influence of S1B binders on Stx1B transport into HeLa cells. A, B: Flow cytometric analysis of HeLa cells demonstrating shift in fluorescence intensity (A) and mean fluorescence intensity (MFI; B) upon 1h incubation of HeLa cells with mixtures of S1B22, S1B26 or ABDwt (all in fusion with ToIA-Avi and H6) and Alexa Fluor 488-labeled Stx1B. Cont: unstained HeLa cells. Stx1B: HeLa cells incubated with Stx1B-Alexa Fluor 488 alone. C, D: Fluorescence microscopy images of HeLa cells incubated with Alexa Fluor 488 labelled Stx1B (green) with or without pre-incubation with S1B22 and S1B26. DAPI staining (blue) was used to label nuclei. Cells were stained either with PKH26 membrane labeling dye (red; C) and Golgi apparatus was detected with mouse monoclonal Golgin-97 antibody and secondary polyclonal goat anti-mouse antibody conjugated with Alexa Fluor 633 (purple; D). Bars = 10 μ m.

doi:10.1371/journal.pone.0162625.g006

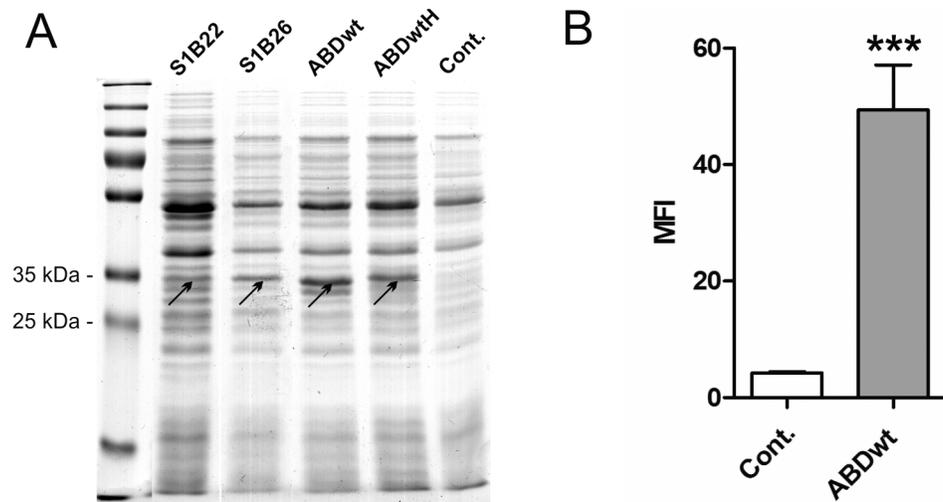


Fig 7. (A) SDS PAGE analysis of lysates of *L. lactis* cells expressing S1B22, S1B26, ABDwt and H6-ABDwt (ABDwth), all in fusion with Usp45 secretion signal and the LysM-containing cA domain, and stained with Coomassie brilliant blue. ABD fusion proteins are high-lighted with arrows. (B) Flow cytometric analysis of ABD surface display, detection with FITC-conjugated human serum albumin. The MFI value of ABDwt was compared with that of the control using Student's t test. *** $p < 0.001$. Cont.: control containing empty plasmid pNZ8148.

doi:10.1371/journal.pone.0162625.g007

surface display of target proteins in fusion with Usp45 secretion signal [41] and the surface anchoring C-terminal domain of AcmA (cA), as reported [17, 18, 20–22, 33]. Fusion proteins were expressed in *L. lactis* by induction with nisin and visualized in the cell lysates by SDS PAGE and Coomassie brilliant blue staining (Fig 7A).

Surface display of ABDs was confirmed for ABDwt and H6-ABDwt using flow cytometry. *L. lactis* cells expressing ABDwt on their surface bound FITC-conjugated HSA (Fig 7B), which also indicates the functionality of the displayed binder.

Evaluation of binding of Stx1B by recombinant *L. lactis* with surface displayed S1B binders

Binding of Stx1B by recombinant *L. lactis* with surface displayed S1B binders was evaluated by flow cytometry (Fig 8A) and whole cell ELISA (Fig 8B). With flow cytometry, we observed statistically significant binding of fluorescence-labelled Stx1B by *L. lactis* cells displaying S1B26 on their surface in comparison with control *L. lactis* cells expressing ABDwt. With whole cell ELISA binding of Stx1B by *L. lactis* cells displaying both S1B22 and S1B26 was confirmed, the strongest being with S1B26. On the basis of these results, S1B26 was selected as the most promising Stx1B binder for the display on the surface of *L. lactis*, even though S1B22 exhibited lower binding constants in SPR and MST, possibly due to the fusion with TolA-Avi and H6 in isolated S1Bs.

Conclusion

Shiga toxin receptor analogues are an attractive option for treating infections with Shiga toxin-producing bacteria [8]. They place no stress on bacteria and do not induce Shiga toxin release. They bind the toxin *in situ* in the gastrointestinal tract, thereby preventing its activity. Engineered bacteria, such as recombinant *E. coli* producing a modified lipopolysaccharide mimicking the Shiga toxin receptor [23, 24], could substitute the polymer analogs. Probiotic food-

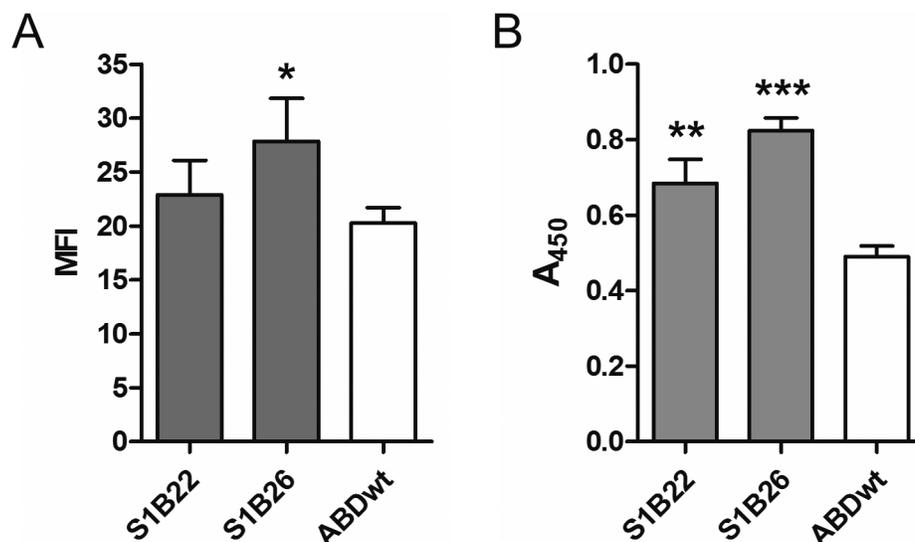


Fig 8. Flow cytometric (A) and whole-cell ELISA (B) analyses of binding of recombinant Stx1B by *L. lactis* cells displaying S1B variants or ABDwt on their surface. (A) Alexa488-conjugated Stx1B was used for detection. MFI: Mean fluorescence intensity. (B) Mouse antiStx1B antibody and HRP-conjugated anti mouse antibody were used for detection of Stx1B. A₄₅₀: Absorbance at 450 nm. Vertical bars denote standard deviation. MFI or A₄₅₀ values of S1B binders were compared to those of the ABDwt control using Student's t test. *: p<0.05, ** p<0.01, *** p<0.001.

doi:10.1371/journal.pone.0162625.g008

grade LAB were previously shown to be able to inhibit Shiga toxin-producing bacteria by the production of lactic acid [16] and this could be exploited in creating a synergistic therapeutic effect.

In the present study we demonstrated for the first time functional display of ABD proteins on the surface of LAB *L. lactis*. This represents an additional class of alternative binding proteins successfully displayed on the surface of *L. lactis*, next to Affibodies [17] and DARPin [18]. LAB *L. lactis* capable of binding Stx1B by displaying on its surface ABD-derived Stx1B binding proteins were engineered and could be used for neutralization of Shiga toxin in the human intestine in the early stages of infections with Shiga toxin producing bacteria. Additionally, novel Stx1B binders on the basis of ABD scaffold can be used for basic research as a small non-immunoglobulin alternative to antibodies and with further modification could be developed for diagnostics.

Acknowledgments

We are grateful to Prof. Roger Pain for a critical reading of the manuscript, Petra Kadlčáková for excellent technical assistance during work in Prague, and Dr. Maja Štalekar and Dr. Simona Darovic for help with HeLa cells.

Author Contributions

Conceptualization: PZ AB BŠ.

Formal analysis: PZ LM HP VH MPN GA.

Funding acquisition: AB PM BŠ.

Investigation: PZ LM HP VH MPN.

Methodology: PZ LM HP VH GA MPN AB PM.

Project administration: AB PM BŠ.

Resources: AB GA BŠ PM.

Supervision: AB PM BŠ.

Validation: PZ LM HP VH MPN.

Visualization: PZ VH.

Writing – original draft: PZ.

Writing – review & editing: PZ AB VH MPN PM BŠ.

References

1. Paton JC, Paton AW. Pathogenesis and diagnosis of Shiga toxin-producing *Escherichia coli* infections. *Clin Microbiol Rev*. 1998; 11(3):450–79. PMID: [9665978](#),
2. O'Brien AD, Holmes RK. Shiga and Shiga-Like Toxins. *Microbiol Rev*. 1987; 51(2):206–20. PMID: [3299029](#)
3. Johannes L, Römer W. Shiga toxins—from cell biology to biomedical applications. *Nat Rev Microbiol*. 2010. doi: [10.1038/nrmicro2279](#)
4. Keir LS, Marks SD, Kim JJ. Shigatoxin-associated hemolytic uremic syndrome: current molecular mechanisms and future therapies. *Drug Des Devel Ther*. 2012; 6:195–208. PMID: [22888220](#).
5. Sandvig K, van Deurs B. Endocytosis, intracellular transport, and cytotoxic action of Shiga toxin and ricin. *Physiol Rev*. 1996; 76(4):949–66. PMID: [8874490](#).
6. Sandvig K. Shiga toxins. *Toxicol*. 2001; 39(11):1629–35. doi: [10.1016/S0041-0101\(01\)00150-7](#) PMID: [11595626](#).
7. Melton-Celsa AR, O'Brien AD. New Therapeutic Developments against Shiga Toxin-Producing *Escherichia coli*. *Microbiol Spectr*. 2014; 2(5). doi: [10.1128/microbiolspec.EHEC-0013-2013](#) PMID: [26104346](#).
8. Rahal EA, Fadlallah SM, Nassar FJ, Kazzi N, Matar GM. Approaches to treatment of emerging Shiga toxin-producing *Escherichia coli* infections highlighting the O104:H4 serotype. *Front Cell Infect Microbiol*. 2015; 5:24. doi: [10.3389/fcimb.2015.00024](#) PMID: [25853096](#).
9. Skrllec K, Strukelj B, Berlec A. Non-immunoglobulin scaffolds: a focus on their targets. *Trends Biotechnol*. 2015; 33(7):408–18. doi: [10.1016/j.tibtech.2015.03.012](#) PMID: [25931178](#).
10. Gebauer M, Skerra A. Engineered protein scaffolds as next-generation antibody therapeutics. *Curr Opin Chem Biol*. 2009; 13(3):245–55. doi: [10.1016/j.cbpa.2009.04.627](#) PMID: [19501012](#).
11. Ahmad JN, Li J, Biedermannova L, Kuchar M, Sipova H, Semeradtova A, et al. Novel high-affinity binders of human interferon gamma derived from albumin-binding domain of protein G. *Proteins*. 2012; 80(3):774–89. doi: [10.1002/prot.23234](#) PMID: [22113774](#).
12. Kuchar M, Vankova L, Petrokova H, Cerny J, Osicka R, Pelak O, et al. Human interleukin-23 receptor antagonists derived from an albumin-binding domain scaffold inhibit IL-23-dependent ex vivo expansion of IL-17-producing T-cells. *Proteins*. 2014; 82(6):975–89. doi: [10.1002/prot.24472](#) PMID: [24549990](#).
13. Mareckova L, Petrokova H, Osicka R, Kuchar M, Maly P. Novel binders derived from an albumin-binding domain scaffold targeting human prostate secretory protein 94 (PSP94). *Protein Cell*. 2015. doi: [10.1007/s13238-015-0194-9](#) PMID: [26264490](#).
14. Mohsin M, Guenther S, Schierack P, Tedin K, Wieler LH. Probiotic *Escherichia coli* Nissle 1917 reduces growth, Shiga toxin expression, release and thus cytotoxicity of enterohemorrhagic *Escherichia coli*. *Int J Med Microbiol*. 2015; 305(1):20–6. doi: [10.1016/j.ijmm.2014.10.003](#) PMID: [25465158](#).
15. Reissbrodt R, Hammes WP, dal Bello F, Prager R, Fruth A, Hantke K, et al. Inhibition of growth of Shiga toxin-producing *Escherichia coli* by nonpathogenic *Escherichia coli*. *FEMS Microbiol Lett*. 2009; 290(1):62–9. doi: [10.1111/j.1574-6968.2008.01405.x](#) PMID: [19016876](#).
16. Ogawa M, Shimizu K, Nomoto K, Tanaka R, Hamabata T, Yamasaki S, et al. Inhibition of in vitro growth of Shiga toxin-producing *Escherichia coli* O157:H7 by probiotic *Lactobacillus* strains due to production of lactic acid. *Int J Food Microbiol*. 2001; 68(1–2):135–40. PMID: [11545213](#).

17. Ravnikar M, Strukelj B, Obermajer N, Lunder M, Berlec A. Engineered Lactic Acid Bacterium *Lactococcus lactis* Capable of Binding Antibodies and Tumor Necrosis Factor Alpha. *Appl Environ Microbiol*. 2010; 76(20):6928–32. doi: [10.1128/aem.00190-10](https://doi.org/10.1128/aem.00190-10) PMID: [20802083](https://pubmed.ncbi.nlm.nih.gov/20802083/)
18. Zdravec P, Strukelj B, Berlec A. Improvement of LysM-mediated surface display of designed ankyrin repeat proteins (DARPs) in recombinant and nonrecombinant strains of *Lactococcus lactis* and *Lactobacillus* Species. *Appl Environ Microbiol*. 2015; 81(6):2098–106. doi: [10.1128/AEM.03694-14](https://doi.org/10.1128/AEM.03694-14) PMID: [25576617](https://pubmed.ncbi.nlm.nih.gov/25576617/).
19. Zdravec P, Strukelj B, Berlec A. Heterologous surface display on lactic acid bacteria: non-GMO alternative? *Bioengineered*. 2015; 6(3):179–83. doi: [10.1080/21655979.2015.1040956](https://doi.org/10.1080/21655979.2015.1040956) PMID: [25880164](https://pubmed.ncbi.nlm.nih.gov/25880164/).
20. Steen A. Cell Wall Attachment of a Widely Distributed Peptidoglycan Binding Domain Is Hindered by Cell Wall Constituents. *J Biol Chem*. 2003; 278(26):23874–81. doi: [10.1074/jbc.M211055200](https://doi.org/10.1074/jbc.M211055200) PMID: [12684515](https://pubmed.ncbi.nlm.nih.gov/12684515/)
21. Buist G, Kok J, Leenhouts KJ, Dabrowska M, Venema G, Haandrikman AJ. Molecular cloning and nucleotide sequence of the gene encoding the major peptidoglycan hydrolase of *Lactococcus lactis*, a muramidase needed for cell separation. *J Bacteriol*. 1995; 177(6):1554–63. PMID: [7883712](https://pubmed.ncbi.nlm.nih.gov/7883712/).
22. Steen A, Buist G, Horsburgh GJ, Venema G, Kuipers OP, Foster SJ, et al. Acma of *Lactococcus lactis* is an N-acetylglucosaminidase with an optimal number of LysM domains for proper functioning. *FEBS J*. 2005; 272(11):2854–68. doi: [10.1111/j.1742-4658.2005.04706.x](https://doi.org/10.1111/j.1742-4658.2005.04706.x) PMID: [15943817](https://pubmed.ncbi.nlm.nih.gov/15943817/).
23. Paton AW, Morona R, Paton JC. A new biological agent for treatment of Shiga toxicogenic *Escherichia coli* infections and dysentery in humans. *Nat Med*. 2000; 6(3):265–70. PMID: [10700227](https://pubmed.ncbi.nlm.nih.gov/10700227/)
24. Pinyon RA, Paton JC, Paton AW, Botten JA, Morona R. Refinement of a therapeutic Shiga toxin-binding probiotic for human trials. *J Infect Dis*. 2004; 189(9):1547–55. doi: [10.1086/383417](https://doi.org/10.1086/383417) PMID: [15116289](https://pubmed.ncbi.nlm.nih.gov/15116289/).
25. Bondos SE, Bicknell A. Detection and prevention of protein aggregation before, during, and after purification. *Anal Biochem*. 2003; 316(2):223–31. doi: [10.1016/S0003-2697\(03\)00059-9](https://doi.org/10.1016/S0003-2697(03)00059-9) PMID: [12711344](https://pubmed.ncbi.nlm.nih.gov/12711344/).
26. Tsumoto K, Ejima D, Kumagai I, Arakawa T. Practical considerations in refolding proteins from inclusion bodies. *Protein Expr Purif*. 2003; 28(1):1–8. doi: [10.1016/S1046-5928\(02\)00641-1](https://doi.org/10.1016/S1046-5928(02)00641-1) PMID: [12651100](https://pubmed.ncbi.nlm.nih.gov/12651100/).
27. Oneda H, Inouye K. Refolding and recovery of recombinant human matrix metalloproteinase 7 (matrylsin) from inclusion bodies expressed by *Escherichia coli*. *J Biochem*. 1999; 126(5):905–11. PMID: [10544284](https://pubmed.ncbi.nlm.nih.gov/10544284/).
28. de Ruyter PG, Kuipers OP, de Vos WM. Controlled gene expression systems for *Lactococcus lactis* with the food-grade inducer nisin. *Appl Environ Microbiol*. 1996; 62(10):3662–7. PMID: [8837421](https://pubmed.ncbi.nlm.nih.gov/8837421/).
29. Kuipers OP, Beerthuyzen MM, Siezen RJ, De Vos WM. Characterization of the nisin gene cluster nisABTCIPR of *Lactococcus lactis*. Requirement of expression of the nisA and nisl genes for development of immunity. *Eur J Biochem*. 1993; 216(1):281–91. PMID: [7689965](https://pubmed.ncbi.nlm.nih.gov/7689965/).
30. Kuipers OP, de Ruyter PGG, Kleerebezem M, de Vos WM. Quorum sensing-controlled gene expression in lactic acid bacteria. *J Biotechnol*. 1998; 64(1):15–21. doi: [10.1016/S0168-1656\(98\)00100-X](https://doi.org/10.1016/S0168-1656(98)00100-X)
31. Mierau I, Kleerebezem M. 10 years of the nisin-controlled gene expression system (NICE) in *Lactococcus lactis*. *Appl Microbiol Biotechnol*. 2005; 68(6):705–17. doi: [10.1007/s00253-005-0107-6](https://doi.org/10.1007/s00253-005-0107-6) PMID: [16088349](https://pubmed.ncbi.nlm.nih.gov/16088349/)
32. Ashkenazi S, Cleary TG. Rapid method to detect shiga toxin and shiga-like toxin I based on binding to globotriosyl ceramide (Gb3), their natural receptor. *J Clin Microbiol*. 1989; 27(6):1145–50. PMID: [2666433](https://pubmed.ncbi.nlm.nih.gov/2666433/).
33. Berlec A, Malovrh T, Zdravec P, Steyer A, Ravnikar M, Sabotic J, et al. Expression of a hepatitis A virus antigen in *Lactococcus lactis* and *Escherichia coli* and evaluation of its immunogenicity. *Appl Microbiol Biotechnol*. 2013; 97(10):4333–42. doi: [10.1007/s00253-013-4722-3](https://doi.org/10.1007/s00253-013-4722-3) PMID: [23371298](https://pubmed.ncbi.nlm.nih.gov/23371298/).
34. Berlec A, Zdravec P, Jevnikar Z, Strukelj B. Identification of candidate carrier proteins for surface display on *Lactococcus lactis* by theoretical and experimental analyses of the surface proteome. *Appl Environ Microbiol*. 2011; 77(4):1292–300. doi: [10.1128/AEM.02102-10](https://doi.org/10.1128/AEM.02102-10) PMID: [21183632](https://pubmed.ncbi.nlm.nih.gov/21183632/).
35. Zdravec P, Mavric A, Bogovic Matijasic B, Strukelj B, Berlec A. Engineering BmpA as a carrier for surface display of IgG-binding domain on *Lactococcus lactis*. *Protein Eng Des Sel*. 2014; 27(1):21–7. doi: [10.1093/protein/gzt059](https://doi.org/10.1093/protein/gzt059) PMID: [24336343](https://pubmed.ncbi.nlm.nih.gov/24336343/).
36. Lindholm A, Smeds A, Palva A. Receptor binding domain of *Escherichia coli* F18 fimbrial adhesin FedF can be both efficiently secreted and surface displayed in a functional form in *Lactococcus lactis*. *Appl Environ Microbiol*. 2004; 70(4):2061–71. PMID: [15066797](https://pubmed.ncbi.nlm.nih.gov/15066797/).
37. Kim JH, Lingwood CA, Williams DB, Furuya W, Manolson MF, Grinstein S. Dynamic measurement of the pH of the Golgi complex in living cells using retrograde transport of the verotoxin receptor. *J Cell Biol*. 1996; 134(6):1387–99. PMID: [8830769](https://pubmed.ncbi.nlm.nih.gov/8830769/).

38. Neri P, Shigemori N, Hamada-Tsutsumi S, Tsukamoto K, Arimitsu H, Shimizu T, et al. Single chain variable fragment antibodies against Shiga toxins isolated from a human antibody phage display library. *Vaccine*. 2011; 29(33):5340–6. doi: [10.1016/j.vaccine.2011.05.093](https://doi.org/10.1016/j.vaccine.2011.05.093) PMID: [21664401](https://pubmed.ncbi.nlm.nih.gov/21664401/).
39. Lipovsek D, Pluckthun A. In-vitro protein evolution by ribosome display and mRNA display. *J Immunol Methods*. 2004; 290(1–2):51–67. doi: [10.1016/j.jim.2004.04.008](https://doi.org/10.1016/j.jim.2004.04.008) PMID: [15261571](https://pubmed.ncbi.nlm.nih.gov/15261571/).
40. Richter A, Eggenstein E, Skerra A. Anticalins: exploiting a non-Ig scaffold with hypervariable loops for the engineering of binding proteins. *FEBS Lett*. 2014; 588(2):213–8. doi: [10.1016/j.febslet.2013.11.006](https://doi.org/10.1016/j.febslet.2013.11.006) PMID: [24239535](https://pubmed.ncbi.nlm.nih.gov/24239535/).
41. Dieye Y, Usai S, Clier F, Gruss A, Piard JC. Design of a protein-targeting system for lactic acid bacteria. *J Bacteriol*. 2001; 183(14):4157–66. doi: [10.1128/JB.183.14.4157-4166.2001](https://doi.org/10.1128/JB.183.14.4157-4166.2001) PMID: [11418555](https://pubmed.ncbi.nlm.nih.gov/11418555/).



Optical microchips based on high-affinity recombinant protein binders—Human serum albumin detection in urine



Alena Semeradtova^a, Marcel Stofik^a, Lucie Vankova^b, Petr Maly^b, Ondrej Stanek^c, Jan Maly^{a,*}

^a Department of Biology, J.E. Purkyně University in Ústí nad Labem, 40096 Ústí nad Labem, Czech Republic

^b Laboratory of Ligand Engineering, Institute of Biotechnology of the Czech Academy of Sciences, BIOCEV Research Center, Průmyslová 595, Vestec, 252 50, Czech Republic

^c Laboratory of Molecular Biology of Bacterial Pathogens, Institute of Microbiology of the Czech Academy of Sciences, Vídeňská 1083, Prague, 142 20, Czech Republic

ARTICLE INFO

Keywords:

Microarrays
Biosensors
Protein binders
Albumine-binding domain
Protein G
Affibody
Protein A

ABSTRACT

Recent developments in molecular evolution technologies have led to novel types of high-affinity recombinant protein binders (PB) able to substitute antibodies in many diagnostic and therapeutic applications. Despite almost a decade of research, they have so far only been sporadically used for biosensor construction. Here, we present a proof-of-principle comparative study focused on the application of three types of PB recognizing human serum albumin (HSA) in the fabrication of diagnostic optical microchips detecting clinically relevant HSA levels in urine. The PB tested were: (i) biotinylated anti-HSA Affibody (AF) (IgG binding domain of protein A, *Staphylococcus aureus*); (ii) biotinylated protein construct based on albumin-binding domain (ABD) of protein G (*Streptococcus* G148) fused with long TolA spacer (6xHis-WT-ABD-TolA-AviTag) and (iii) WT-ABD-Trp leader-streptavidin tetrameric fusion protein (SA-ABD-WT). Open glass microchips with 24 independent microwells (volume 8 μ L) and micropatterned detection zones were prepared and used for oriented binding of proteins through the biotin/streptavidin chemistry. The analytical performance of the optical microchips was tested by performing direct specific detection of fluorescently labelled HSA in various environments. Results show that the length of peptide spacer present between the binding protein domain and sensor surface is a key factor influencing biosensor performance. The biosensor based on SA-ABD-WT reached the limit of detection (LOD) for HSA in urine (LOD = 0.65 μ g/ml) sufficient to identify the chronic kidney disease caused by high blood pressure or diabetes. Furthermore, it offers the highest signal intensity, low noise and significant simplification of microchip preparation due to a simple one-step immobilization procedure. Our results may be further exploited in development of diagnostic microchips dedicated to the detection of a wide range of molecular targets recognized by specific ABD protein binders.

1. Introduction

Design of the affinity binder molecules and their surface immobilization is still the crucial issue of successful introduction of new sensors into diagnostic medicine [1]. The field has been dominated by monoclonal antibodies (mAb), which are the most common biorecognizing component of the immunosensors. Despite their usefulness and widespread applicability, mAbs suffer from several drawbacks, including high molecular weight, instability and high production cost [2]. Other kinds of proteins have been tested as backbones for affinity molecules by converting them to a library of PB following randomization of amino acids at the binding surface. From this complex library of PB, a specific binder can be selected using phage, bacterial, ribosome, yeast display or other similar approaches [3]. Such novel strategies

have been shown to be effective for production of various PBs with affinities comparable or even better than mAbs. High affinity binders such as ABD, Adnectin, Affibody and Preonectin are based on simple low MW structures and share favourable structural and biochemical properties that support their use in a vast range of applications [1]. Affibodies, PBs derived from the IgG binding domain of protein A (*Staphylococcus aureus*), being also commercially available, have attracted increased attention in diagnostic and therapeutic fields during the past few years [4].

ABD is a small, three-helix bundle domain (46 amino-acid residues) which is a part of protein G (*Streptococcus* G148, PDB ID: 1GJT, residues 20–65). It naturally binds HSA with nM affinity [5]. To date, more than 100 engineered variants with altered specificity, improved affinity or stability and even new binding specificities have been reported [6].

* Corresponding author: University of J.E. Purkyně in Ústí nad Labem, Department of Biology, České mládeže 8, 40096 Ústí nad Labem, Czech Republic.
E-mail address: malyjalga@seznam.cz (J. Maly).

Their application has been demonstrated in peptide pharmacology [7], nanoparticle labelling [8] and even biosensing [9].

The immobilization of proteins on the surface of solid materials is a key step in the production of protein arrays, biosensors and microfluidic devices. For these applications, it is necessary to arrange the orientation of immobilized proteins as well as their density and surface distribution so that their function will be maintained [10]. Proteins may be immobilized by physical adsorption [11], covalent coupling [10], as a self-assembled monolayer (SAM) [12] or through affinity interactions (e.g., avidin/biotin [10], Ni-NTA (nickel-nitrilotriacetic acid)/His-tagged protein [13–15]). For practical use, the immobilization should be based on the minimized number of steps to enable the scale-up of the device production and to decrease the complexity of sensor surface preparation.

Despite their large application potential, there are only few examples of Affibody use in biosensor fabrication [16,17] and even less in the case of ABD proteins [9]. The question of an effective way of protein binder immobilization with the respect to signal intensity, sensitivity and limit of detection has not been studied in more details. In this study, we target such issues by comparison of the analytical performances of the optical microchips, based on three different recombinant PBs, all recognizing HSA as the target analyte: (i) commercially available anti-HSA Affibody; (ii) 6xHis-WT-ABD-TolA-AviTag construct and (iii) WT-ABD fusion protein with streptavidin (SA-ABD-WT).

2. Materials and methods

2.1. Chemicals and reagents

Chemical reagents obtained from commercial suppliers were used without further purification. More details about the chemicals used are available in SI.

2.2. Design and production of HSA protein binders

Anti-HSA Affibody[®] Molecule (Biotin) (ab31898) was purchased from Abcam (UK). The *in vivo* biotinylated ABD protein was designed according to Refs. [18,19], produced in the *E. Coli* BL21 (DE3) BirA strain and purified from cell extracts on Ni-NTA agarose columns according to Ref. [20]. The process of designing and construction of the SA-ABDwt protein has been described recently [8]. Detailed description of production of those proteins is available in Supplementary information (SI).

2.3. Fabrication of microchips

The microchip for assay (open glass microchip) was propounded as follows: microchips should contain 6×4 microwells (volume $8 \mu\text{L}$) with detection zones for biosensing located on their bottom, each zone should consist of 4×4 squares, $150 \times 150 \mu\text{m}$ wide with $150 \mu\text{m}$ distance between the squares. For detailed description of the whole fabrication process, please see SI.

2.4. Fluorescence-based direct assay of labelled HSA

High-affinity PBs based on biotinylated molecules (6xHis-WT-ABD-TolA-AviTag and AF) were attached to the microchip surface via streptavidin – biotin interaction. Streptavidin-fusion based variants (SA-ABD-WT) were attached directly to the biotinylated surface of the microchip via the same chemistry. Based on previous knowledge from optimization experiments, the concentration of proteins immobilized to the microchip surface was $10 \mu\text{g/ml}$ for streptavidin and SA-ABD-WT and $40 \mu\text{g/ml}$ for biotinylated proteins (6xHis-WT-ABD-TolA-AviTag and AF); incubation time was one hour at 4°C . After incubation, the microchips were rinsed several times with water. Then, fluorescently labelled HSA analyte ($0\text{--}30 \mu\text{g/ml}$) in different media (B-PBS or F-PBS

buffer) was loaded into the microwells and incubated for one hour at 4°C . Microchips were then rinsed with water and used for fluorescence measurements (please see SI for more details).

2.5. Competition assay for estimation of HSA concentration

For the competition assay, the immobilization of PBs (AF, 6xHis-WT-ABD-TolA-AviTag, SA-ABD-WT) was performed in the same way as in the previous case. For all PBs, the concentration of fluorescently labelled HSA was initially set to be $10 \mu\text{g/ml}$ to reach the saturation of the surface; for SA-ABD-WT, the concentration was then decreased to $2 \mu\text{g/ml}$. The concentration range of unlabelled HSA was kept the same as in the direct assay (i.e. $0\text{--}30 \mu\text{g/ml}$). Evaluation of the data was performed in a similar manner as in the previous case.

2.6. Data analysis and statistics

Data are presented as the mean value \pm standard deviation (error bars, S.D.). Each experiment was conducted in at least three independent runs. The statistical and data analysis was performed with GraphPad Prism 7 (GraphPad Software, Inc, USA) software. The experimental data from dose-response curves were background subtracted and normalized before non-linear regression fitting. A one-site total binding model with linear component characterizing non-specific binding was used for data fitting:

$$Y = B_{\text{max}} * X / (K_d + X) + NS * X + \text{Background} \quad (1)$$

where $X = \log$ of analyte concentration, $Y =$ normalized signal response, $K_d =$ equilibrium binding constant, NS is the slope of non-specific binding in Y units divided by X units and Background is the amount of nonspecific binding with no added analyte.

For more details about the calculation of sensitivity, limit of detection (LOD) and limit of quantitation (LOQ) used in this work, please see SI.

3. Results and discussion

3.1. Design and production of protein binders

To develop an affinity assay for HSA detection, specific PB should be immobilized on the detection platform. Here, three different PBs – anti-HSA Affibody (AF), 6xHis-WT-ABD-TolA-AviTag and SA-ABD-WT – were used in biosensor construction and their analytical performance was compared. Fig. 1 illustrates a schematic molecular design of each PB, tested in our experiments. In general, AF comprises one recognition part with a zero-length peptide spacer based on the IgG-binding domain of protein A (58 amino acids); the molecular weight is 14 kDa . On the C-terminus, the AF is chemically biotinylated through the sulfhydryl group present on the terminal cysteine. The albumin-binding domain of streptococcal protein G (wild-type G148-GA3, pdb id 1gjt), lacking disulfide bridges and naturally recognizing HSA with high affinity ($K_D = 1.2 \text{ nM}$) [5], was used in the form of an N-terminally poly-histidinylated tag (12 amino acids) fused with the ABD (46 amino acids), a helper TolA helical protein spacer (305 amino acid residues) and C-terminal AVITag sequence consensus (15 amino acids), forming a fusion protein of 378 amino acids. This 38 kDa ABD protein has recently been characterized for its stability (melting temperature $T_m = 58^\circ\text{C}$) and binding specificity [7,18–20].

The third protein (SA-ABDwt) contains a natural core of streptavidin (amino acid residues 13–139 [21]). Its C-terminal part is genetically attached to the ABD via a short linker (Trp leader; Fig. 1B) [8]. The SA-ABDwt protein was produced and isolated as a denatured monomeric form (22 kDa) and the functional tetrameric form (88 kDa), which enables high-affinity binding to biotin. The tetramer formation and its stability were verified by SDS PAGE electrophoresis.

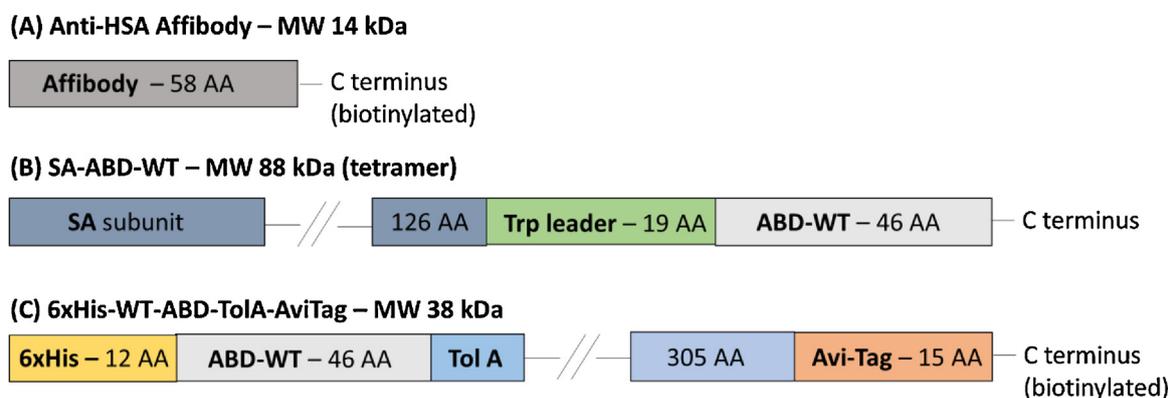


Fig. 1. Schematic drawing of the molecular design of PBs used in experiments. (A) Affibody – zero length peptide spacer; (B) SA-ABD-WT – 19 residues long spacer (Trp leader); (C) 6xHis-WT-ABD-TolA-AviTag – 305 residue long spacer (Tol A).

3.2. Design and fabrication of open glass microchip

Precise control of immobilization conditions as well as of low amount of proteins and solutions used during the assay were crucial for obtaining a sensitive response and reproducible results. Therefore, we have designed a concept of open glass microchips, comprising an array of microwells (volume 8 μ L) and the micropatterned protein binding zones at the bottom of each microwell. Several steps which combined the UV-photolithography and microabrasive approaches were used for the microchip fabrication (Figs. SI1 and 2A and B). Each detection zone at the bottom of the microwell contained 4 \times 4 silanized squares separated by a chromium layer, so both the signal from the modified glass and the background were acquired simultaneously (Fig. 2C, D).

3.3. Immobilization of binding proteins on glass microchip

The glass microchips were first optimized to deposit biotinylated surfaces in active detection zones with low non-specific protein binding. The silylation of zones with APTES followed by coupling biotin-PEG₁₁-COOH to modified surface were used (Fig. SI1B). Further on, the optimization of streptavidin-binding layers was performed with fluorescently labelled Atto488-streptavidin to achieve a protein surface saturation (results not shown).

The immobilization strategy of the PBs is depicted in Fig. 3. The two-step approach was followed in the case of AF and 6xHis-WT-ABD-TolA-AviTag (Fig. 3A, B). Both HSA binding proteins are decorated on their C-terminus part with a single biotin molecule on a zero-length

(AF) or long (6xHis-WT-ABD-TolA-AviTag) peptide spacer. Those two proteins were immobilized on streptavidin binding layers. The one-step immobilization approach was performed in the case of SA-ABD-WT. Four units of ABD-WT domains separated from the streptavidin part by the TRP leader were therefore immobilized simultaneously in one binding event. As in the case of streptavidin, binding proteins' concentrations necessary to achieve a fully saturated surface on streptavidin surfaces (AF, 6xHis-WT-ABD-TolA-AviTag) or directly on biotin layers (SA-ABD-WT) were also optimized. The detection of HSA from different solutions was then performed on such optimized binding surfaces.

3.4. Direct HSA detection with glass microchip biosensors

The analytical performances of the biosensors were tested by performing direct specific detection of fluorescently labelled HSA (HSA_{FL}) in a 0–30 μ g/ml concentration range. This was made in two different environments. First, in 1% BSA solution, an environment that is commonly used for minimizing the nonspecific binding. Second, in 6% FBS, an environment that mimics the conditions of blood plasma. Normalized dose-response curves are shown in Fig. 4.; kinetic parameters derived from the fitting model are summarized in Table 1. All biosensors show a clear concentration-dependent signal response, but differ in analytical parameters, such as K_d, LOD, level of non-specific binding at higher analyte concentration and signal intensities achieved (Fig. 5). Analytical parameters measured in 6% FBS were in most cases improved as compared to the 1% BSA environment, with lower

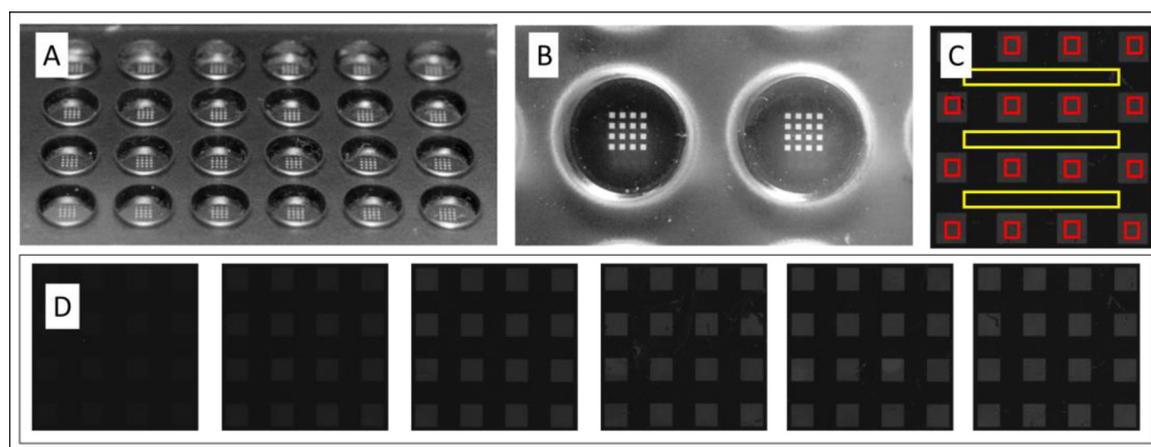


Fig. 2. Open glass microchip with microwells and micropatterned detection zones. A – fully assembled 24-well glass microchip; B – detail of the two microwells with active detection zones; C – schematic description of signal validation: signal from modified glass sensing areas (red) is corrected for the background (yellow); D – example of cropped fluorescence images of measuring zones after incubation with increasing concentration of fluorescently labelled analyte (from left to right). (For interpretation of the references to colour in this figure legend, the reader is referred to the web version of this article.)

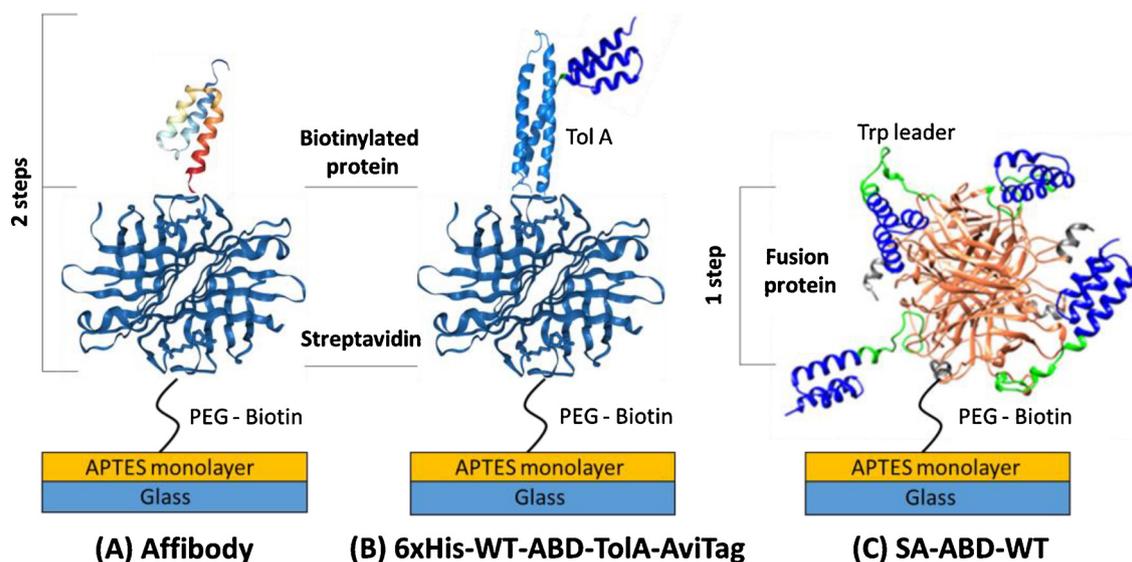


Fig. 3. Immobilization strategies of PBs. Two-step (A, B) and one-step (C) immobilization strategies of PBs were followed. The biotinylated patterned glass surface was modified with streptavidin and further with biotinylated Affibody (A) or 6xHis-WT-ABD-TolA-AviTag (B) molecules or incubated directly with streptavidin-ABD-WT fusion protein (SA-ABD-WT) (C).

standard deviations and increased reproducibility of measurements (see increased R^2 of the fit in all exp. variants performed in 6% FBS – Fig. 4; increase of overall fluorescence signal intensity in 6% FBS – Fig. 6). This suggests a more complex interaction of FBS components with the sensor surface, which may help to support the proper orientation of binding domains.

Both AF and SA-ABD-WT showed non-specific binding visible mainly at relatively high HSA_{FL} concentrations ($c > 10 \mu\text{g/ml}$ HSA_{FL}), which resulted in non-saturation binding kinetics. Therefore, the one-site total binding model with linear component characterizing non-specific binding was used for data fitting. The 6xHis-WT-ABD-TolA-AviTag followed sigmoidal saturation kinetics without the visible non-specific binding at higher HSA_{FL} concentrations. The curve fitting

was performed with the same model, showing a negligible non-specific binding kinetic component. We may hypothesize that the low non-specific binding observed in the case of 6xHis-WT-ABD-TolA-AviTag, as compared to the other two protein binders, could be connected to the existence of its long TolA peptide spacer. This spacer may increase the flexibility of the ABD-WT domain and may also function as a steric barrier which protects the interaction of HSA_{FL} with the underlying streptavidin/glass surface. On the other hand, since the clinically relevant concentration values of HSA in urine as well as of other types of potential diagnostic markers in body fluids are much less than $10 \mu\text{g/ml}$, such a level of non-specific binding should not have a significant influence on the final applicability of biosensors.

Table 1 shows significant differences in affinities (K_d values)

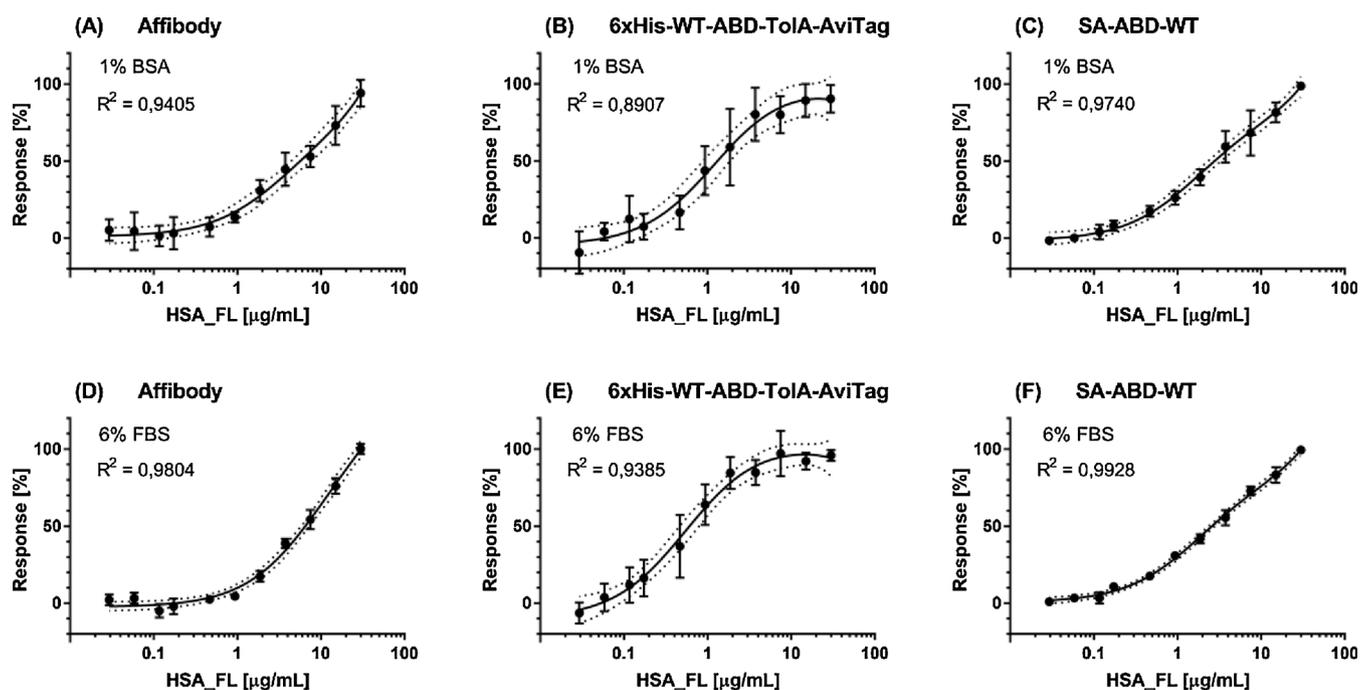


Fig. 4. Dose-response calibration curves of biosensors with fluorescently labelled HSA (HSA_{FL}). Background subtracted and normalized experimental data were fitted with a one-site total binding model with linear component characterizing non-specific binding (as described in Chapter 2.6). Data are presented as a mean value \pm SD. 95% confidence intervals are depicted as dotted lines.

Table 1
Main kinetic parameters of capture protein – HSA_FL binding derived from calibration curves.

Conditions	1% BSA			6% FBS		
	Affibody	6xHis-WT-ABD-TolA-AviTag	SA-ABD-WT	Affibody	6xHis-WT-ABD-TolA-AviTag	SA-ABD-WT
Kd [nM]	49.8	10.9	24.9	131.7	8.2	25.8
LOD (HSA) [$\mu\text{g/ml}$]	0.44	0.20	0.12	0.63	0.24	0.07
LOQ (HSA) [$\mu\text{g/ml}$]	3.10	0.72	0.96	3.55	0.65	0.72
Sensitivity (AU/ μg)	0.0016	0.0008	0.0105	0.0088	0.0054	0.0138

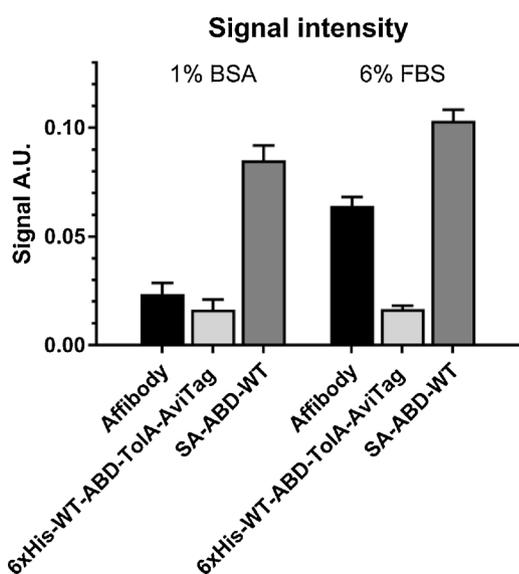


Fig. 5. Fluorescence signal intensities of biosensors. Data were collected from calibration curves at a concentration of HSA_FL 10 $\mu\text{g/ml}$ in the presence of B-PBS buffer (PBS with 1% BSA) and F-BPS (PBS buffer with 6% FBS). Mean values and SD are presented.

between AF (131.7 nM in 6% FBS) and both ABD-WT protein variants (8.2 nM for 6xHis-WT-ABD-TolA-AviTag and 25.8 nM for SA-ABD-WT in 6% FBS). In fact, the affinity of ABD-WT binding domain for HSA reported elsewhere lies in the 1–50 nM range [5,22,23]. Therefore, the calculated Kd values in our experiments fit well within this range, with slightly higher values in the case of SA-ABD-WT as compared to the TolA variant. The reported affinity of affibody for HSA is approximately

10 nM [24]. In our measurements, the Kd values in 6% FBS are significantly higher (Kd = 131.7 nM). We suggest that the binding of the affibody through a zero-length peptide spacer to streptavidin could negatively influence the properties of binding domain and limits its binding ability as compared to relatively sterically free ABDwt domains exposed on longer TolA and Trp leaders. This assumption is in good agreement with the results described for ABDwt domains coupled covalently on the surface plasmon resonance (SPR) sensor [9]. We conclude that the HSA binding domains exposed on the longer peptide spacer offer better conditions for ligand binding.

Fig. 5 shows the fluorescence intensity of biosensors under conditions where the non-specific binding is still negligible (10 $\mu\text{g/ml}$ HSA_FL). As apparent, the lowest sensitivity (see also Table 1) under both experimental conditions (1% BSA, 6% FBS) shows the 6xHis-WT-ABD-TolA-AviTag biosensor, followed by the AF biosensor. The SA-ABD-WT biosensor offered unprecedentedly highest signals which were 2–3 fold higher than AF (based on type of the solution) and more than 4–5 fold higher than 6xHis-WT-ABD-TolA-AviTag. This disproportion between experimental variants could be theoretically ascribed to a combination of two factors: (i) the different density of immobilized HSA binders achieved on the surface and (ii) the availability of proteins for binding with HSA (proper orientation, flexibility). As for the ABD-WT proteins, it does not seem that case (ii) is important since the affinity for HSA is not dramatically changed in both binders. Instead, we hypothesize that the long TolA spacer sterically prevents high surface density immobilization of the 6xHis-WT-ABD-TolA-AviTag binder. In contrast, a compact SA-ABD-WT immobilizes four ABD domains in one single immobilization event and thus would enable to reach significantly higher density of binding domains on the sensor surface.

The LOD and LOQ for HSA in all experimental variants are presented in Table 1. From these results, it is apparent that the lowest LOD in all variants was obtained with the SA-ABD-WT binder (0.07 $\mu\text{g/ml}$ in 6% FBS), followed by 6xHis-WT-ABD-TolA-AviTag (0.24 $\mu\text{g/ml}$ in 6% FBS) and AF (0.63 $\mu\text{g/ml}$ in 6% FBS). Under the experimental conditions used, both immobilized ABD-WT variants exhibit lower LOD than commercially available affibodies, with SA-ABD-WT showing the most favourable properties for further biosensor development.

3.5. Competitive assay for HSA estimation in urine

In order to demonstrate the application of presented biosensors in detection of clinically relevant concentrations of HSA in urine, we performed an additional set of experiments, focused on competitive assays between the fluorescently labelled HSA_FL and HSA in solution (1% BSA, urine). Only results with SA-ABD-WT biosensors are presented (Fig. 6). Two constant concentrations of HSA_FL in 1% BSA solution were tested (10 $\mu\text{g/ml}$ and 2 $\mu\text{g/ml}$) in competitive format and their influence on dose-response calibration curves and kinetic parameters evaluated (Fig. 6A, B). Both experimental variants resulted in a

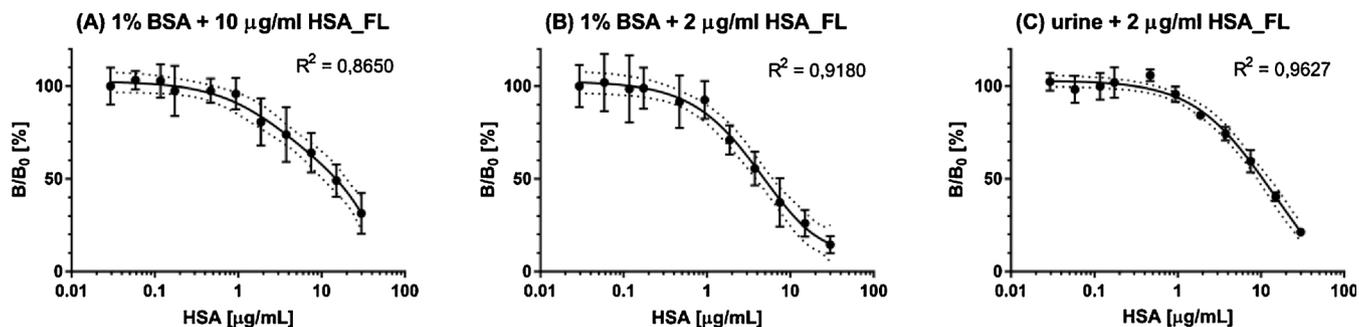


Fig. 6. Calibration curves of HSA competitive assay with SA-ABD-WT as capture protein. Data were background subtracted and expressed as percentual ratio of bound HSA_FL molecules (B) to initial conditions (B_0 = maximal amount of bound HSA_FL molecules at $c(\text{HSA}) = 0 \mu\text{g/ml}$). Experimental data were fitted with a one-site total binding model with linear component characterizing non-specific binding (as described in Chapter 2.6). Data are presented as mean values \pm SD. 95% confidence intervals are depicted as dotted lines.

Table 2
Comparison of LODs of HSA reached by various sensors/assays designs described in literature.

Author	Method	LOD
Tu et al. [28]	IgGs sandwich assay with fluorescence detection using CdSe/ZnS quantum dots	0.03 µg/ml in buffer
Ma et al. [27]	Detection of TF-SiO ₂ labelled HSA using near-infrared reflectance spectroscopy	1.89 µg/ml in urine
Li et al. [26]	Detection of fluorescently labelled HSA	1.73 µg/ml in buffer 2.71 µg/ml in urine
Ho and Chen [29]	Liquid crystal-based detection of immobilized HSA via IgGs	50 µg/ml in buffer
Wang et al. [30]	Time-resolved fluorescence energy transfer	0.004 µg/ml in buffer
Torffvit and Wieslander [31]	ELISA	0.015 µg/ml in buffer
This work	Competitive assay with fluorescently labelled HSA	0.65 µg/ml in urine

fluorescence signal decrease which was proportional to the concentration increase of unlabelled HSA in solution. In the case of 10 µg/ml HSA_{FL}, the sensitivity of the competitive assay was lower (LOQ = 5.5 µg/ml HSA) as compared to the exp. variant with 2 µg/ml HSA_{FL} (LOQ = 2.0 µg/ml). Apparently, lower (non-saturating) concentration of HSA_{FL} increased the analytical performance of the biosensor. Based on the results of such initial analysis, we also performed a similar assay in urine samples (with addition of 2 µg/ml HSA_{FL}). Morning urine was used without any pretreatment; the sample was just gently shaken to disperse sedimented parts. For the competition assay, an exact amount of unlabelled and labelled HSA was added. The concentration range was kept the same as in previous cases. As apparent from Fig. 6C, the resulting measurements were again well reproducible (similarly to 6% FBS as discussed in Chapter 3.4.) with lower SD values ($R^2 = 0.96$) as compared to the model 1% BSA solution ($R^2 = 0.91$) (see Fig. 6B, C). Again, the LOQ of the assay was estimated to be 2.0 µg/ml HSA. LOD was calculated to be 0.65 µg/ml HSA. The 2 µg/ml HSA concentration is a critical value which could indicate kidney problems when it is repeatedly exceeded [25]. In fact, the published works on biosensors for HSA detection in urine usually do not aspire to reach better sensitivity [26,27]. A comparison of optical methods published elsewhere and reached LOD is presented in Table 2. However, we are aware that not every presented method aspires to reach the lowest LOD, but rather meets clinical requirements for a given country.

4. Conclusions

In this paper, we present a proof-of-principle comparative study focused on the application of three types of high-affinity recombinant protein binders (anti-HSA Affibody; 6xHis-WT-ABD-TolA-AviTag construct; WT-ABD fusion protein with streptavidin (SA-ABD-WT)) in the fabrication of diagnostic optical microchips detecting clinically relevant HSA levels in urine. These recombinant proteins varied in the type and source of binding domains (part of protein A/G from *Staphylococcus aureus*/*Streptococcus sp.*), the length of peptide spacer used for connecting the binding domain to the surface of the chip and the number of necessary steps to immobilize the proteins on the biosensor surface. The open glass microchip biosensor platform, suitable for sensitive optical detection of analytes in an 8 µL sample volume was fabricated. Proteins were then immobilized on the microarrayed detection zones located at the bottom of each microwell present on the biosensor (24-microwell format). The analytical performances in detection of fluorescently labelled HSA in fully assembled biosensors were compared. The main conclusions are: (i) the length of peptide spacer significantly influences the kinetic parameters of HSA binding (measured affinity) – longer spacers preserve the ability to bind the analyte with high affinity and helps to minimize the non-specific binding of analyte to the sensor surface; (ii) higher signal response as well as lower LODs for the analyte can be achieved by immobilization of genetically fused protein binding domains with streptavidin (SA-ABD-WT). The biosensor based on SA-ABD-WT reached the LOD for HSA in urine (LOD = 0.65 µg/ml) sufficient to identify the chronic kidney disease caused by high blood pressure or diabetes. The results of this study can be exploited in

development of other types of biosensors/microarrays focused on different molecular targets, where ABDs will be used as active capture components of the biosensor.

Acknowledgements

This work was supported by the Ministry of Health of the Czech Republic (project No. 16-29738A), by the Ministry of Education, Youth and Sports of the Czech Republic (Research Infrastructure NanoEnviCz – project No. LM2015073) and the EU-ESIF in the frame of Operational Programme Research Development and Education (project Pro-NanoEnviCz reg. No. CZ.02.1.01/0.0/0.0/16_013/0001821 and project EATRIS-CZ reg. No. CZ.02.1.01/0.0/0.0/16_013/0001818), by the CAS (RVO: 8665206) and the ERDF (BIOCEV: CZ.1.05/1.1.00/02.0109). Authors also acknowledge the Internal grant agency of UJEP.

Appendix A. Supplementary data

Supplementary data associated with this article can be found, in the online version, at <https://doi.org/10.1016/j.snb.2018.05.180>.

References

- [1] K. Škrlec, B. Štrukelj, A. Berlec, Non-immunoglobulin scaffolds: a focus on their targets, *Trends Biotechnol.* 33 (2016) 408–418.
- [2] P. Chames, M. Van Regenmortel, E. Weiss, D. Baty, Therapeutic antibodies: successes, limitations and hopes for the future, *Br. J. Pharmacol.* 157 (2009) 220–233.
- [3] C. Gronwall, S. Stahl, Engineered affinity proteins—generation and applications, *J. Biotechnol.* 140 (2009) 254–269.
- [4] F.Y. Frejd, K.-T. Kim, Affibody molecules as engineered protein drugs, *Exp. Mol. Med.* 49 (2017) e306.
- [5] A. Jonsson, J. Dogan, N. Herne, L. Abrahmsen, P.A. Nygren, Engineering of a femtomolar affinity binding protein to human serum albumin, *Protein Eng. Des. Sel.* 21 (2008) 515–527.
- [6] J. Nilvebrant, S. Hober, The albumin-binding domain as a scaffold for protein engineering, *Comput. Struct. Biotechnol. J.* 6 (2013) e201303009.
- [7] L. Křížová, M. Kuchař, H. Petroková, R. Osička, M. Hlavničková, O. Peláček, et al., p19-targeted ABD-derived protein variants inhibit IL-23 binding and exert suppressive control over IL-23-stimulated expansion of primary human IL-17+ T-cells, *Autoimmunity* 50 (2017) 102–113.
- [8] J. Maly, O. Stanek, J. Frolík, M. Maly, F. Ennen, D. Appelhans, et al., Biocompatible size-defined dendrimer–albumin binding protein hybrid materials as a versatile platform for biomedical applications, *Macromol. Biosci.* 16 (2016) 553–566.
- [9] H. Šípová, V. Ševců, M. Kuchař, J.N. Ahmad, P. Mikulecký, R. Osička, et al., Surface plasmon resonance biosensor based on engineered proteins for direct detection of interferon-gamma in diluted blood plasma, *Sens. Actuators B* 174 (2012) 306–311.
- [10] F. Rusmini, Z. Zhong, J. Feijen, Protein immobilization strategies for protein biochips, *Biomacromolecules* 8 (2007) 1775–1789.
- [11] H. Ge, UPA, a universal protein array system for quantitative detection of protein–protein, protein–DNA, protein–RNA and protein–ligand interactions, *Nucleic Acids Res.* 28 (2000) e3-e.
- [12] D. Samanta, A. Sarkar, Immobilization of bio-macromolecules on self-assembled monolayers: methods and sensor applications, *Chem. Soc. Rev.* 40 (2011) 2567–2592.
- [13] J. Maly, C. Di Meo, M. De Francesco, A. Masci, J. Masojidek, M. Sugiura, et al., Reversible immobilization of engineered molecules by Ni-NTA chelators, *Bioelectrochemistry* 63 (2004) 271–275.
- [14] J. Maly, A. Masci, J. Masojidek, M. Sugiura, R. Pilloton, Monolayers of natural and recombinant photosystem II on gold electrodes – Potentials for use as biosensors for detection of herbicides, *Anal. Lett.* 37 (2004) 1645–1656.
- [15] J. Maly, E. Illiano, M. Sabato, M. De Francesco, V. Pinto, A. Masci, et al., Immobilisation of engineered molecules on electrodes and optical surfaces, *Mater.*

- Sci. Eng. C-Biol. S 22 (2002) 257–261.
- [16] B. Renberg, J. Nordin, A. Merca, M. Uhlén, J. Feldwisch, P.-Å. Nygren, et al., Affibody molecules in protein capture microarrays: evaluation of multidomain ligands and different detection formats, *J. Proteome Res.* 6 (2007) 171–179.
- [17] B. Renberg, I. Shiroyama, T. Engfeldt, P.-K. Nygren, A.E. Karlström, Affibody protein capture microarrays: synthesis and evaluation of random and directed immobilization of affibody molecules, *Anal. Biochem.* 341 (2005) 334–343.
- [18] J.N. Ahmad, J. Li, L. Biedermannová, M. Kuchař, H. Šípová, A. Semerádová, et al., Novel high-affinity binders of human interferon gamma derived from albumin-binding domain of protein G, *Proteins: Struct. Funct. Bioinf.* 80 (2012) 774–789.
- [19] M. Kuchař, L. Vaňková, H. Petroková, J. Černý, R. Osička, O. Pelák, et al., Human interleukin-23 receptor antagonists derived from an albumin-binding domain scaffold inhibit IL-23-dependent ex vivo expansion of IL-17-producing T-cells, *Proteins: Struct. Funct. Bioinf.* 82 (2014) 975–989.
- [20] L. Marečková, H. Petroková, R. Osička, M. Kuchař, P. Malý, Novel binders derived from an albumin-binding domain scaffold targeting human prostate secretory protein 94 (PSP94), *Protein Cell* 6 (2015) 774–779.
- [21] T. Sano, M.W. Pandori, X. Chen, C.L. Smith, C.R. Cantor, Recombinant core streptavidins. A minimum-sized core streptavidin has enhanced structural stability and higher accessibility to biotinylated macromolecules, *J. Biol. Chem.* 270 (1995) 28204–28209.
- [22] J. Hopp, N. Hornig, K.A. Zettlitz, A. Schwarz, N. Fuss, D. Muller, et al., The effects of affinity and valency of an albumin-binding domain (ABD) on the half-life of a single-chain diabody-ABD fusion protein, *Protein Eng. Des. Sel.* 23 (2010) 827–834.
- [23] J. Lofblom, J. Sandberg, H. Werner, S. Stahl, Evaluation of staphylococcal cell surface display and flow cytometry for postselection characterization of affinity proteins in combinatorial protein engineering applications, *Appl. Environ. Microbiol.* 73 (2007) 6714–6721.
- [24] H. Orelma, L.O. Morales, L.-S. Johansson, I.C. Hoeger, I. Filpponen, C. Castro, et al., Affibody conjugation onto bacterial cellulose tubes and bioseparation of human serum albumin, *RSC Adv.* 4 (2014) 51440–51450.
- [25] W.G. Miller, D.E. Bruns, G.L. Hortin, S. Sandberg, K.M. Aakre, M.J. McQueen, et al., Current issues in measurement and reporting of urinary albumin excretion, *Clin. Chem.* 55 (2009) 24–38.
- [26] H. Li, Q. Yao, J. Fan, J. Du, J. Wang, X. Peng, An NIR fluorescent probe of uric HSA for renal diseases warning, *Dyes Pigm.* 133 (2016) 79–85.
- [27] X.-X. Ma, C.-C. Wang, W.-S. Cai, X.-G. Shao, Quantification of albumin in urine using preconcentration and near-infrared diffuse reflectance spectroscopy, *Chin. Chem. Lett.* 27 (2016) 1597–1601.
- [28] M.-C. Tu, Y.-T. Chang, Y.-T. Kang, H.-Y. Chang, P. Chang, T.-R. Yew, A quantum dot-based optical immunosensor for human serum albumin detection, *Biosens. Bioelectron.* 34 (2012) 286–290.
- [29] W.-H. Ho, C.-H. Chen, Liquid crystal-based immunoassay for detecting human serum albumin, *Res. Chem. Intermed.* 40 (2014) 2229–2236.
- [30] R.E. Wang, L. Tian, Y.-H. Chang, A homogeneous fluorescent sensor for human serum albumin, *J. Pharm. Biomed. Anal.* 63 (2012) 165–169.
- [31] O. Torffvit, J. Wieslander, A simplified enzyme-linked immunosorbent assay for urinary albumin, *Scand. J. Clin. Lab. Invest.* 46 (1986) 545–548.

Alena Semerádová completed Master Study in Biology at the University Jan Evangelista Purkyně in Ústí nad Labem. She is now studying a PhD at the same university under supervision of Dr. Jan Malý and prof. Pavla Čapková. Her current research is focused on development of optical biosensors with emphasis to preparation of biorecognizing layers based on small protein binders with affinity to selected targets as are the protein markers

and cell surface receptors.

Marcel Štofík completed his PhD at Faculty of Science at the University of South Bohemia in České Budějovice. Since 2005, he has been working at the University of Jan Evangelista Purkyně in Ústí nad Labem as researcher and assistant professor at the Department of Biology. His research interests are aimed at microtechnology and microsystems application in the field of biology. He has long-term experience in the development of biosensoric analytical devices. He is currently working on a project aimed at the development of microsystem for detection and manipulation of the circulating tumor cells from the whole blood of patients with lung adenocarcinoma.

Lucie Vaňková (Marečková) is studying a PhD under supervision of Dr. Petr Malý and is working in the Laboratory of Ligand Engineering at the Institute of Biotechnology, Czech Academy of Sciences in Vestec, Czech Republic. She completed Bachelor in Science and Master Study in Cell Biology at Faculty of Science, Charles University in Prague. Her current research is focused on generation and functional characterization of small protein binders selected from highly complex combinatorial libraries derived from protein domain scaffolds. She received Best Poster Award at 12th Euro Biotechnology Congress in Alicante, Spain, 2016, and was selected for Young Scientists' Forum by FEBS, Jerusalem, Israel, 2017.

Petr Malý is head of Laboratory of Ligand Engineering at the Institute of Biotechnology, Czech Academy of Sciences in Vestec, Czech Republic. He studied at Department of Biochemistry, Faculty of Science, Charles University in Prague, Czech Republic, and completed doctorate at the Institute of Molecular Genetics ASCR (IMG) in Prague. He spent postdoctoral fellowship at Department of Pathology and Howard Hughes Medical Institute, The University of Michigan Medical School, Ann Arbor, USA, where he published several substantial papers related to *in vivo* role of mammalian glycosyltransferases. He also worked as research group leader at the IMG in Prague. As a visiting scientist he worked at Department of Biochemistry and Molecular Biology, College of Medicine, University of Oklahoma, Oklahoma City, USA, and was participating investigator of Consortium for Functional Glycomics (USA). Currently, he is Deputy Chairperson of the Supervisory Board of the Institute of Biotechnology CAS.

Ondřej Staněk finished his PhD at the Institute of Microbiology of the Czech Academy of Sciences in 2012. The topic of his research was development of the new delivery tool for direct antigen delivery into the dendritic cells based on antigen-streptavidin fusion proteins in the combination with biotinylated targeting antibodies. Currently, he is working on the development of vaccines against whooping cough.

Jan Malý is head of the Department of Biology at the University Jan Evangelista Purkyně in Ústí nad Labem. He completed doctorate in Physiology and Immunology at the Faculty of Science at the University of South Bohemia in České Budějovice and partially working at the Institute of Microbiology of the Czech Academy of Sciences. He spent the postdoctoral fellowship at the Laboratory of Biosensors at the Italian National Agency for New Technologies, Energy and Sustainable Economic Development (ENEA), Rome, Italy, working in the field of electrochemical biosensors. As a group leader he was responsible for several research projects focused on biosensors development and related nanobiotechnology topics. Currently he focuses mainly on the development of microsystems for detection and manipulation of the circulating tumor cells from the whole blood of patients with lung adenocarcinoma and other novel medical diagnostic tools based on biosensors technology.



Article

p19-Targeting ILP Protein Blockers of IL-23/Th-17 Pro-Inflammatory Axis Displayed on Engineered Bacteria of Food Origin

Katja Škrlec^{1,2}, Petra Zadavec¹, Marie Hlavničková³, Milan Kuchař³, Lucie Vaňková³, Hana Petroková³, Lucie Křížová³, Jiří Černý⁴ , Aleš Berlec^{1,5} and Petr Malý^{3,*}

¹ Department of Biotechnology, Jožef Stefan Institute, Jamova 39, SI-1000 Ljubljana, Slovenia; katja.skrlec@ijs.si (K.Š.); petrazadavec@gmail.com (P.Z.); ales.berlec@ijs.si (A.B.)

² Graduate School of Biomedicine, Faculty of Medicine, University of Ljubljana, SI-1000 Ljubljana, Slovenia

³ Laboratory of Ligand Engineering, Institute of Biotechnology of the Czech Academy of Sciences, v. v. i., BIOCEV Research Center, Průmyslová 595, 252 50 Vestec, Czech Republic; marie.hlavnickova@ibt.cas.cz (M.H.); milan.kuchar@ibt.cas.cz (M.K.); lucie.vankova@ibt.cas.cz (L.V.); hana.petrokova@ibt.cas.cz (H.P.); lucie.krizova@ibt.cas.cz (L.K.)

⁴ Laboratory of Structural Bioinformatics of Proteins, Institute of Biotechnology of the Czech Academy of Sciences, v. v. i., BIOCEV Research Center, Průmyslová 595, 252 50 Vestec, Czech Republic; jiri.cerny@ibt.cas.cz

⁵ Faculty of Pharmacy, University of Ljubljana, Aškerčeva 7, SI-1000 Ljubljana, Slovenia

* Correspondence: petr.maly@ibt.cas.cz; Tel.: +420-325-873-763

Received: 17 May 2018; Accepted: 29 June 2018; Published: 1 July 2018



Abstract: IL-23-mediated Th-17 cell activation and stimulation of IL-17-driven pro-inflammatory axis has been associated with autoimmunity disorders such as Inflammatory Bowel Disease (IBD) or Crohn's Disease (CD). Recently we developed a unique class of IL-23-specific protein blockers, called ILP binding proteins that inhibit binding of IL-23 to its cognate cell-surface receptor (IL-23R) and exhibit immunosuppressive effect on human primary blood leukocytes *ex vivo*. In this study, we aimed to generate a recombinant *Lactococcus lactis* strain which could serve as *in vivo* producer/secretor of IL-23 protein blockers into the gut. To achieve this goal, we introduced ILP030, ILP317 and ILP323 cDNA sequences into expression plasmid vector containing USP45 secretion signal, FLAG sequence consensus and LysM-containing cA surface anchor (AcmA) ensuring cell-surface peptidoglycan anchoring. We demonstrate that all ILP variants are expressed in *L. lactis* cells, efficiently transported and secreted from the cell and displayed on the bacterial surface. The binding function of AcmA-immobilized ILP proteins is documented by interaction with a recombinant p19 protein, alpha subunit of human IL-23, which was assembled in the form of a fusion with Thioredoxin A. ILP317 variant exhibits the best binding to the human IL-23 cytokine, as demonstrated for particular *L.lactis*-ILP recombinant variants by Enzyme-Linked ImmunoSorbent Assay (ELISA). We conclude that novel recombinant ILP-secreting *L. lactis* strains were developed that might be useful for further *in vivo* studies of IL-23-mediated inflammation on animal model of experimentally-induced colitis.

Keywords: lactococcus; binding protein; albumin-binding domain; cytokine; IL-23; surface display

1. Introduction

IL-23/Th17 pro-inflammatory axis plays a central role in pathogenesis of several autoimmune diseases such as psoriasis, psoriatic arthritis and rheumatoid arthritis [1,2] but it is also closely related to development of inflammatory bowel disease and Crohn's disease [3–5]. Human IL-23 cytokine, heterodimer of p19 and p40 proteins, stimulates differentiation of naive Th cells into Th17

cell population by activation of IL-23 receptor-mediated signaling, leading to secretion of a cocktail of inflammatory mediators including IL-17, IL-22 and chemokines [6,7]. Therefore, blocking of IL-23 signaling represents a crucial step in therapeutic intervention and treatment of autoimmune diseases. Recently it has been demonstrated that neutralizing antibodies targeting IL-23 such as Ustekinumab (Stelara) or IL-17A such as Secukinumab (Cosentyx) exhibit a substantial effect in the treatment of severe forms of psoriasis [8,9].

Alternatively, several laboratories develop non-immunoglobulin blockers of IL-23 or IL-23R using directed evolution based on selection of high-affinity binding proteins from highly complex combinatorial libraries derived from small protein domain scaffolds. Among them, anti-IL-23 Nanobody demonstrate anti-inflammatory effect in mouse model of contact hypersensitivity [10], anti-IL-23 Adnectin exhibit high-affinity IL-23 binding [11], anti-IL-23 Alphabody binder prevents topical inflammation in mice [12] and albumin-binding domain (ABD)-derived antagonists of IL-23 receptor (REX ligands) suppress IL-23-stimulated expansion of primary human peripheral blood mononuclear cells in vitro [13]. Recently we developed a novel collection of ABD-derived proteins called ILP binders targeting alpha subunit of IL-23, p19 protein. These proteins were shown to suppress production of primary human Th17 cells ex vivo upon stimulation with IL-23 and IL-2 [14].

Local delivery and neutralization of pro-inflammatory mediators in situ, in gastrointestinal tract, was shown to be beneficial in animal models of inflammatory bowel disease [15]. Oral administration of protein therapeutics is not feasible due to extensive protein degradation in stomach and duodenum, high dosage requirements and high price. Advanced oral protein delivery systems are therefore required [16]. Better protein stability and cost-efficiency could be achieved by using recombinant bacteria that would serve as protein producers and delivery systems, at the same time. Administration of live bacteria is associated with concerns for safety; the latter should therefore be, beside effective protein delivery, of prime importance in selection of appropriate bacterial species [17]. The bacteria should have no or minimal pathogenic potential, should produce no toxins or immune response triggers (such as lipopolysaccharide), and should preferably be of food origin.

Lactic acid bacteria (LAB) have a long history of safe usage as part of human food. LAB are Gram-positive bacteria from genera *Lactococcus*, *Lactobacillus*, *Leuconostoc*, *Pediococcus* and *Streptococcus* that produce lactic acid as an end product of carbohydrate metabolism [18]. Several of them are part of human intestinal and vaginal microbiota. Some LAB are used as probiotics that are defined as “live microorganisms that when administered in adequate quantity confer health benefit on host” [19].

Lactococcus lactis is a model lactic acid bacterium with well-developed tools for genetic engineering. It has been widely used in the food industry as a starter for the production of cheese. Apart from its industrial importance [20], *L. lactis* has also been recognized in recent years as a potential probiotic with beneficial effects in experimental colitis [21,22], which supports its role as a delivery vehicle in IBD treatment. *L. lactis* can survive passage through the intestinal tract but does not colonize it [23]. Intrinsic probiotic efficacy of *L. lactis* can be further strengthened by genetic engineering, and several proof-of-principle applications have already been developed [24–26]. Delivery of anti-TNF α Nanobody [27], anti-TNF α Affibody [28], trefoil factors [29] and elafin [30], by recombinant *L. lactis*, have demonstrated effectiveness in DSS-induced colitis animal model of IBD. Delivery of anti-inflammatory cytokine IL-10 has been tested in human clinical trial [17,31].

Therapeutic proteins can be either secreted [27,31] or displayed on the bacterial surface [32,33]. Display of binders enables removal of the targeted mediators, together with bacteria, following bacterial passage through the intestine and their excretion. Surface display can be achieved by different molecular means [34]. A well-established approach consists of fusing the protein binder with Usp45 secretion signal [35] and C-terminal part of lactococcal AcmA protein containing 3 LysM repeats that serve as surface anchor [36,37]. In our recent work we verified the function of IL-23-binding Adnectin on lactic acid bacteria [38] and we extended this study in the current work by displaying three-helix bundle ABD scaffold-derived IL-23 binders.

2. Results

2.1. Molecular Assembly of Recombinant p19 Protein

Previous studies demonstrated that p19 protein, alpha subunit of IL-23, can be produced as a recombinant protein produced in bacterial host cells and that it retains folding recognized by IL-23 receptor on THP-1 cells or by IL-23R-IgG chimera in Enzyme-Linked ImmunoSorbent Assay (ELISA). Therefore, as a molecular probe for ILP protein binder detection, we generated a p19 fusion protein using bacterial plasmid carrying sequences coding for human p19 protein (alpha subunit of IL-23), assembled in the form of a fusion with Thioredoxin A (TRX). For the construction of this protein, we used the same plasmid vector as it was used before for the generation of p19 fusion protein with maltose-binding protein (p19-MBP) [14]. The corresponding purified p19-TRX protein, produced with a double His6-tag at the N-terminus, was refolded from urea extracts and tested in ELISA for specific recognition of ILP proteins (Figure 1). This 40 kDa protein was then used as a detection tool for the surface display of ILP binders on *L. lactis*.

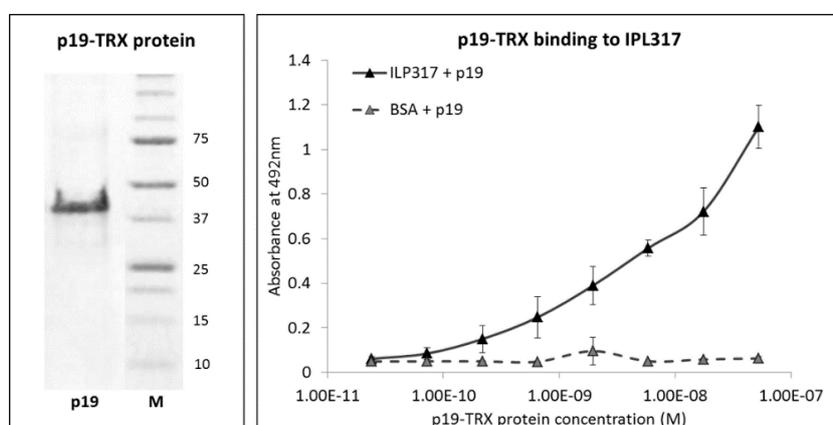


Figure 1. Binding of p19-TRX fusion protein to immobilized ILP317 variant in ELISA. Left: Recombinant p19 protein, alpha subunit of human IL-23, was produced as a fusion protein with Thioredoxin A. Protein was expressed in *E. coli* BL21(ΔDE3), purified from inclusion bodies and refolded from 8 M urea extracts. Final product of calculated molecular weight 40 kDa is shown as a stained band after SDS polyacrylamide gel electrophoresis. Right: 96-well Polysorp ELISA plate was coated with the ILP317 protein variant in the form of a fusion with TolA-Avitag protein. p19-TRX was used as an analyte, detected by anti-IL-23 (p19) polyclonal antibody and anti-mouse IgG-HRP conjugate. The result represents three individual measurements and the error bars indicate standard deviations.

2.2. Expression of ILP-Fusion Proteins in *L. lactis*

To verify whether IL-23-specific ILP protein binders can be produced in *L. lactis* host cells, DNA sequences coding for ILP proteins (ILP030, ILP317 and ILP323 variants) were genetically fused to Usp45 secretion signal and C-terminal domain of AcmA protein (cA) containing LysM repeats (LysM) for peptidoglycan anchoring. Fusion genes were under the control of inducible nisin promoter. To simplify detection of particular ILP proteins, FLAG-tag sequence consensus was added between secretion signal and ILP coding sequences. Previously reported construct for the display of IL-23-binding Adnectin variant ADN23 [38] was also modified by inserting FLAG-tag. All three ILP fusion proteins, as well as the Adnectin fusion protein, were detected in bacterial cell lysates after nisin-stimulated induction using anti-FLAG antibodies (Figure 2A). No signal could be detected in empty plasmid pNZ8148-containing control cells. Also, the fusion proteins could not be observed in Coomassie Brilliant Blue stained gel (Figure 2B). However, visualization of protein lysates demonstrates their uniform concentration. The acquired data documents that all ILP proteins are expressed. Among them, ILP317-containing fusion protein was expressed at the lowest level.

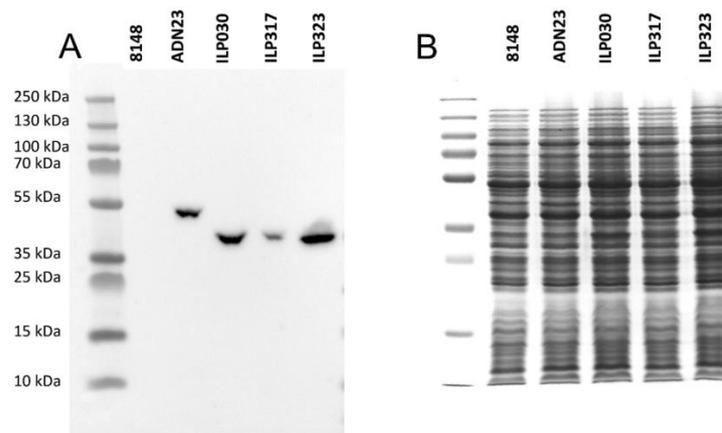


Figure 2. Analysis of protein expression by Western blot (A) and Coomassie Brilliant Blue-stained SDS PAGE gel (B) of lysates of *L. lactis* cells expressing ILP binding proteins and ADN23. All proteins are in fusion with Usp45 secretion signal, FLAG tag and LysM-containing cA surface anchor.

2.3. Display of ILP-Fusion Proteins on the Surface of *L. lactis*

To investigate a secretion efficacy of the particular ILP variants produced in lactococcal cells, cell-surface display of AcmA-anchored ILP proteins and ADN23 was used. The bound proteins were detected with anti-FLAG antibodies using flow cytometry. The data confirm that all ILP proteins as well as ADN23 Adnectin were effectively secreted and displayed in comparison to the used negative control (Figure 3A,B). However, they were displayed in different amounts. The results document that all three ILP binding proteins were displayed in higher amounts than ADN23. The best cell-surface display was achieved with ILP317 variant, followed by ILP030 and ILP323.

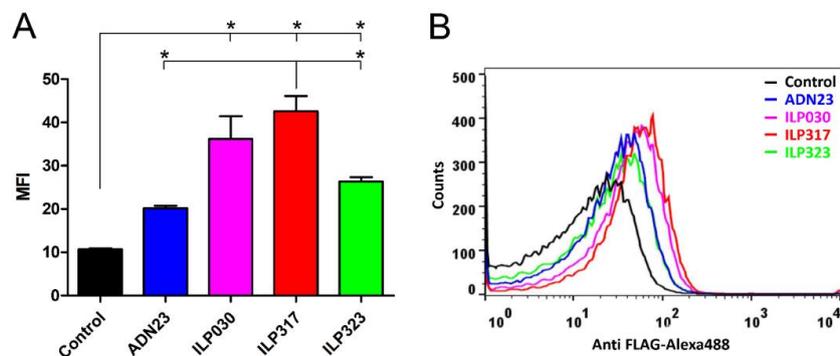


Figure 3. Flow cytometry of *L. lactis* cells displaying ILP proteins, or ADN23, detected with Anti-FLAG tag antibodies demonstrating mean fluorescence intensity (MFI; A) or a shift in fluorescence intensity (B). Vertical bars denote standard error. Significant differences ($p < 0.05$) are marked with an asterisk.

2.4. Binding of Recombinant p19 by ILP-Displaying *L. lactis*

The ability of ILP-displaying *L. lactis* to bind the p19 protein was tested by flow cytometry. To achieve this goal, a recombinant p19-TRX fusion protein was used as a useful molecular probe. The bound p19 was detected by a specific anti-human IL-23 p19 antibody. The highest binding of p19 was observed with ILP317, followed by ADN23 (without FLAG tag). Lower binding was demonstrated with ILP030 and ILP323 (Figure 4A, B). The presence of FLAG tag had a little effect on the ability of ILP proteins to bind p19. However, the binding of p19 was severely hindered when FLAG tag was attached to the ADN23 (Figure 4C, D).

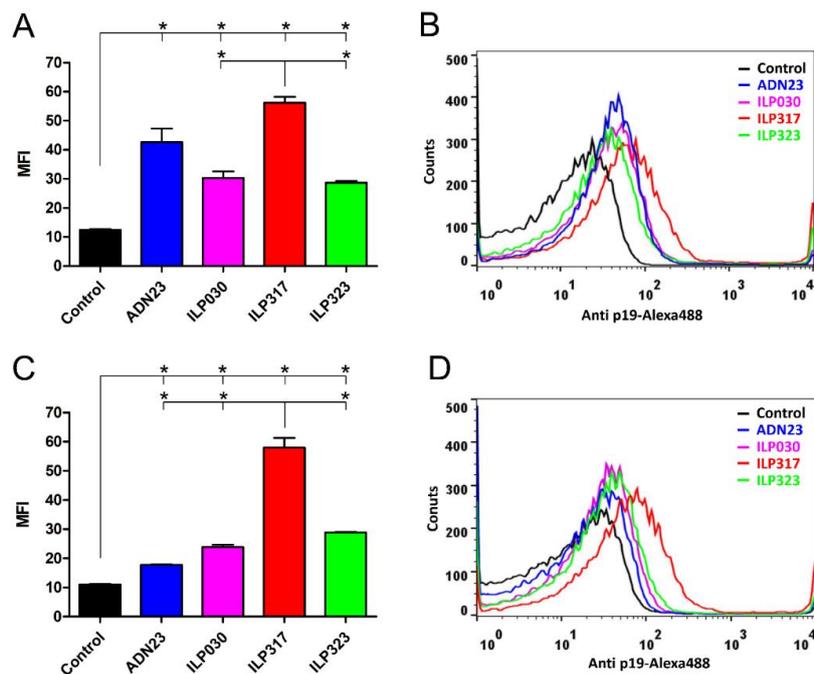


Figure 4. Flow cytometry of *L. lactis* cells displaying ILP proteins, or ADN23, without FLAG tag (A,B) or with FLAG tag (C,D) detected with recombinant p19-TRX protein. Mean fluorescence intensity (MFI; A,C) or a shift in fluorescence intensity (B,D) are depicted. Vertical bars denote standard error. Significant differences ($p < 0.05$) are marked with an asterisk.

2.5. Removal of IL-23 by ILP-Displaying *L. lactis*

To verify that ILP variants attached to *L. lactis* bacteria recognize not only recombinant p19-TRX fusion protein, but also secreted IL-23 cytokine, we performed cell-surface binding test. The binding and removal of IL-23 from the solution by 1×10^{10} ILP-displaying *L. lactis* was evaluated by ELISA and compared to ADN23-displaying *L. lactis*. The removal of IL-23 was the most effective with ADN23-displaying bacteria (Figure 5). Removal of IL-23 was more effective with ILP317-displaying bacteria than with ILP323-displaying bacteria. No significant removal of IL-23 could be observed with ILP030-displaying bacteria.

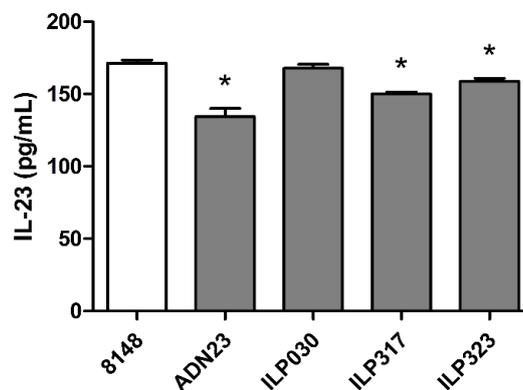


Figure 5. ELISA-determined removal of IL-23 from the solution by *L. lactis* displaying ILP binding proteins or ADN23. Concentration of remaining IL-23 is shown. Vertical bars denote standard error. Significant difference ($p < 0.05$) in comparison to control (8148) is marked with an asterisk.

3. Discussion

In the present work, we have developed a set of new recombinant bacteria of food origin with the ability to bind p19 protein, an alpha-subunit of the pro-inflammatory cytokine IL-23. IL-23/Th17 pro-inflammatory axis plays an important role in the pathogenesis of inflammatory bowel disease. It has been demonstrated that the mucosal delivery of anti-inflammatory cytokines or engineered protein blockers of pro-inflammatory cytokines can effectively decrease inflammation in the mouse models of disease, and that mucosal delivery can be achieved by recombinant bacteria, preferably of confirmed safety and of food origin. We have previously used lactic acid bacterium *Lactococcus lactis* to deliver binders of TNF α , IL-17A, IL-23 and chemokines [32,33,38]. In the present work we displayed our recently developed ILP binders of p19 subunit of IL-23 [14] on the surface of *L. lactis* and confirmed their ability to bind the p19 subunit that was isolated from *E. coli* in the form of thioredoxin fusion, as well as their ability to bind and remove IL-23 in vitro.

ILP binders were originally selected from a highly complex combinatorial library derived from albumin-binding domain (ABD) scaffold using ribosome display where the target p19 protein was produced as a bacterial fusion product of maltose-binding protein (p19-MBP) [14]. However, this soluble protein is not suitable for cell-surface competition binding assays performed with IL-23 receptor-expressing human and mouse cell lines as MBP interacts with glycans of plasma membrane receptors. As double-His6-p19 protein expression is rather poor and this protein is not sufficiently stable, we produced another type of p19 fusion protein using thioredoxin A. This p19-TRX was well produced in *E. coli* as insoluble protein and after refolding, it was recognized by anti-p19 antibody in ELISA. Stability of this product was increased further by a carrier protein added into solutions. We used, therefore, p19-TRX protein as a molecular probe for detection of ILP variants presented on the surface of *L. lactis*.

Previously developed IL-23-binding *L. lactis*, displaying Adnectin against IL-23 (ADN23) [38] was complemented with the display of three additional binders, directed against p19 subunit of IL-23, ILP030, ILP317 and ILP323. All three ILP binders were effectively displayed on the surface of *L. lactis* in the form of FLAG-tag fusion. The amount of surface display of ILP binders was higher than that of ADN23. All three ILP binders, as well as ADN23, were able to bind recombinant p19 subunit of IL-23. However, the binding depended on the presence of FLAG tag. After its removal, the binding ability of displayed ADN23 increased, probably due to the elimination of steric hindrances, as it is known that the N-terminus of ADN23 is important in the interaction with p19 [11]. Lower binding of p19 by ADN23 can also be explained by the fact that ADN23 interacts with both subunits of IL-23, p19 and p40 [11].

ILP317 emerged as the most effective binder of p19 subunit in the *L. lactis* host system. Although its expression level was lower than that of ILP030 or ILP323, it demonstrated the highest level of surface display (established by anti-FLAG antibody), as well as the highest ability to bind recombinant p19 subunit among the tested binders. The FLAG tag had a little effect on binding of p19 with ILP317-displaying lactococci. ILP317 was also the most effective ILP binder of IL-23, when displayed on the surface of lactococci. Its binding efficacy was compared to that of ADN23 (being only slightly lower). ADN23 used in this study was identified as a high-affinity human IL-23 binder which binds to the interface between p19 and p40 subunits with 2 nM K_d ([11]). This binding region is, however, far from that one essential for IL-23 recognition by a distal IgG-like domain of the IL-23 receptor (based on 5MZV crystal structure by [39]) and, therefore, is not expected to suppress IL23/IL23R interaction. In our study, ADN23 was intended as a suitable IL-23-binding probe useful for *L. lactis*-secreting ILP strains characterization. On the other hand, our results suggest that ILP317 would be a suitable candidate for future testing of the in vivo mucosal neutralization of IL-23, and possible anti-inflammatory activity in an animal model of IBD. However, relatively low amount of the in vitro removed IL-23 may require further optimization of the binder affinity or of the bacterial concentration.

ILP binding proteins were originally targeted to human p19 protein. In our previous study we identified probable binding modes for the all ILP proteins by docking to our homology model of the

human IL-23/IL-23R complex [14]. We built a homology model for IL-23R using the IL-6 receptor as a template and performed docking of p19 as well as the IL-23 cytokine with IL-23R. The results of docking suggested the most probable binding site located at the extracellular Ig-like domain and distal domain of the fibronectin-type III of IL-23R. This agrees with the recently deposited crystal structure of the human IL-23/IL-23R complex (PDB ID 5MZV [39]) shown in Figure 6A. However, the structure of mouse IL-23/IL-23R complex is still not available. We, therefore, generated a homology model of the mouse p19 and relaxed its structure using short molecular dynamics simulation. To investigate the most probable binding regions for the all ILP binding proteins, we performed docking of ILP030, ILP317, and ILP323 to the mouse p19 model. The docking revealed two principal binding regions (Figure 6B–D). While the first one overlaps with p19/p40 interaction interface in the human IL-23/IL-23R complex (Figure 6A blue/red) and is, therefore, inaccessible in IL-23 due to a steric hindrance by p40, the second one corresponds to p19/IL-23R interface (Figure 6A blue/magenta) and is exposed for binding of ILP blockers.

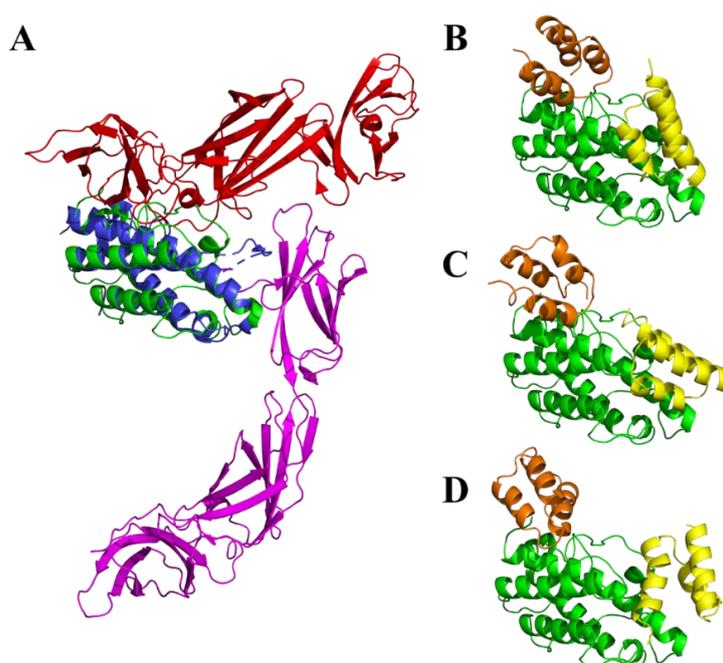


Figure 6. Modeling of p19/ILP interactions. (A) Comparison of homology model of mouse p19 protein (green) to crystal structure of human IL-23/IL-23R complex (PDB ID 5MZV [39]), with p19 (blue), p40 (red) and IL-23R (magenta). Representative binding modes from docking of ILP variants ILP030 (B), ILP317 (C) and ILP323 (D) to the homology model of the mouse p19 protein (green) are shown. Yellow and orange colors indicate common binding areas predicted on the mouse p19. The residues involved in the interaction with the orange binder overlap with p19/p40 interaction interface (Figure 6A blue/red) while the yellow binding mode corresponds to p19/IL-23R interface (Figure 6A blue/magenta).

As our intention is to verify an inhibitory potential of ILP proteins *in vivo* using mouse model of experimentally induced colitis, there is a question about the efficacy of ILP blockers on the mouse IL-23. Sequence comparison of human p19 (UniProt Q9NPF7) and mouse p19 (Q9EQ14) revealed overall protein sequence identity 71.9% and the similarity 90.4%. Based on our previously described p19-ILP complexes [14] we generated a homology model of mouse p19 complexes. This allowed us to identify 28 amino acid residues forming a “common interface” between p19 and particular ILP variants. In this amino acid stretch, only seven amino acids differ between human and mouse p19 proteins. However, six of them do not change the charge: 49-51PLV to 49-51APA, D55 to N55, S114 to A115, 159L to 160P, and 163F to 164S. The analysis of human p19-ILP complexes demonstrated that

most of the contacts between p19 and ILP proteins are mediated by charged amino acid residues. Therefore, we do not expect major changes in the binding affinity/neutralization efficacy of the used ILP protein blockers in the mouse model. Modeling of the mouse p19 suggests that sequence differences between mouse and human p19 protein cause only minor structural differences (Figure 6A, blue/green). These results support an expectation that ILP variants secreted by modified *L. lactis* cells can serve as anti-inflammatory blockers during stimulated intestinal inflammation in mouse. However, this has yet to be verified.

4. Materials and Methods

4.1. Bacterial Strains, Media and Growth Conditions

The bacterial strains used in this study are shown in Table 1. *Lactococcus lactis* NZ9000 was grown at 30 °C in M17 medium (Merck, Darmstadt, Germany) supplemented with 0.5% glucose (GM-17) without agitation or in the same medium solidified with 1.5% agar. Electroporation of *L. lactis* was performed according to [40], using Gene Pulser II apparatus (Bio-Rad, Hercules, CA, USA). To maintain selection pressure on transformation, 10 µg/mL chloramphenicol was added to the growth medium. *E. coli* strain DH5α was grown at 37 °C with agitation in lysogeny broth (LB) medium supplemented with 100 µg/mL ampicillin. For bacterial strains, plasmids and oligonucleotide primers used in the study see Table 1.

Table 1. Bacterial strains, plasmids and primers used in the study.

Strain, Plasmid, or Gene	Relevant Features or Sequence (5'–3')	Reference or Source
Strain		
<i>E. coli</i>		
DH5α	endA1 glnV44 thi-1 recA1 relA1 gyrA96 deoR F- Φ80dlacZΔM15 Δ(<i>lacZYA-argF</i>)U169, hsdR17(rK- mK+), λ-	Invitrogen
TOP10	F- mcrA Δ(<i>mrr-hsdRMS-mcrBC</i>) Φ80lacZΔM15 ΔlacX74 recA1 araD139 Δ(<i>ara</i> leu) 7697 galU galK rpsL (StrR) endA1 nupG	Life technologies
BL21 λ(D3)	<i>E. coli</i> B F – dcm ompT hsdS (rB- mB-) gal λ(DE3)	[41]
<i>L. lactis</i>		
NZ9000	MG1363 <i>nisRK ΔpepN</i>	[42]
Plasmid		
pNZ8148	pSH71 derivative, <i>PnisA</i> , CmR, nisin-controlled expression	[42]
pSDLBA3b	pNZ8148 containing gene fusion of Usp45 signal peptide, B domain and cA	[32]
pET-ILP030	pET28b containing a fusion gene of ILP030, toIA protein and AviTag consensus	[14]
pET-ILP317	pET28b containing a fusion gene of ILP317, toIA protein and AviTag consensus	[14]
pET-ILP323	pET28b containing a fusion gene of ILP323, toIA protein and AviTag consensus	[14]
pSD-ILP030	pNZ8148 containing gene fusion of Usp45 signal peptide, ILP030 and cA	This work
pSD-ILP317	pNZ8148 containing gene fusion of Usp45 signal peptide, ILP317 and cA	This work
pSD-ILP323	pNZ8148 containing gene fusion of Usp45 signal peptide, ILP323 and cA	This work
pSD-ADN23	pNZ8148 containing gene fusion of Usp45 signal peptide, ADN23 and cA	[38]
pSD-ILP030-FLAG	pNZ8148 containing gene fusion of Usp45 signal peptide, ILP030 and cA	This work
pSD-ILP317-FLAG	pNZ8148 containing gene fusion of Usp45 signal peptide, ILP317 and cA	This work
pSD-ILP323-FLAG	pNZ8148 containing gene fusion of Usp45 signal peptide, ILP323 and cA	This work
pSD-ADN23-FLAG	pNZ8148 containing gene fusion of Usp45 signal peptide, ADN23 and cA	This work
pET-DH-TRX-p19	pET28b containing a fusion gene of double-His-tag, Thioredoxin and p19 protein	This work
Primer		
ILP030-F	TGGATCCTTAGCTGAAGCTAAAGTC	This work
ILP030-R	AGAATTCAGGTAAATTAGCTAAAATACG	This work
ILP317-R	AGAATTCAGGTAAAGGAGCTAAAATACTATC	This work
ILP323-R	AGAATTCAGGTAAACGAGCTAAAATAACATC	This work
Usp1-NcoI	ATAACCATGGCTAAAAAAAAGATTATCTCAGCTATTTTAATG	[32]
FLAG_Bam_R	GGATCCTTTATCATCGTCGCTTTATAATCAGCGTAAACACCTGACAACG	This work
19-F-NheI	GGGCTAGCTAGCAGAGCTGTGCCTGGGGGC	This work
p19-R-XhoI	GCGCCTCGAGGGGACTCAGGGTTGCTGCTC	This work

4.2. DNA Manipulation and Plasmid Construction

Restriction enzymes and T4 DNA ligase were purchased from Fermentas or New England Biolabs. PCR amplifications were performed with Taq polymerase (Fermentas, Waltham, MA,

USA) or Phusion Hot Start polymerase (Thermo Fisher Scientific, Waltham, MA, USA) according to the manufacturer's protocols. PCR products were routinely introduced into pGEM-T Easy (Promega, Madison, WI, USA) or pJET1.2 (CloneJET PCR Cloning Kit, Fermentas, Waltham, MA, USA) for sequencing and further cloning. Plasmid DNA was isolated with NucleoSpin Plasmid (Macherey-Nagel, Duren, Germany), with an additional lysozyme treatment step in the case of *L. lactis*. Nucleotide sequencing was performed by GATC. Primers (IDT) and plasmids are listed in Table 1. The *ilp030*, *ilp317* and *ilp323* genes were amplified by PCR from original plasmids carrying sequences of ILP030, ILP317 and ILP323 proteins [14] using ILP030-F/ILP030-R, ILP030-F/ILP317-R and ILP030-F/ILP323-R primer pairs, respectively. All amplicons were cloned to pSDLBA3b [32] via BamHI/EcoRI restriction sites. To insert FLAG tag nucleotide sequence between *usp45* signal sequence and *ilp* sequences in pSD-ILP plasmids, the *usp45* sequence was amplified from pSDLBA3b using primers Usp1-NcoI/FLAG_Bam_R. The amplicon was digested with NcoI/BamHI and cloned into equally treated plasmids pSD-ILP030, pSD-ILP317, pSD-ILP323 and pSD-ADN23, thereby yielding plasmids pSD-ILP030-FLAG, pSD-ILP317-FLAG, pSD-ILP323-FLAG and pSD-ADN23-FLAG, respectively. The DNA sequence encoding p19 was inserted into an assembled pET28b-derived vector, carrying sequence coding for 2xHis6-TRX-TEV-MCS-TEV-His6, using primers p19-F-NheI and p19-R-XhoI. *E. coli* TOP10 (Life Technologies, Carlsbad, CA, USA) host cells were transformed with the p19-cloned vector and plated on LB-agar supplemented with 60 µg/mL kanamycin. The resulting plasmid construct contains sequences coding for the final 360 amino acids p19-TRX fusion product as follows:

```
MVPHHHHHHHSRAWRHPQFGGHHHHHHHARHMMSDKIIHLTDDSFDTDVLKADGAI
LVDFWAEWCGPCKMIAPILDEIADEYQGKLTVAKLNIDQNPGTAPKYGIRGIPTLLLFKNG
EVAATKVGALSKGQLKEFLDANLALQENLYFQGASRAVPGGSSPAWTQCQQLSQKLCCTLA
WSAHPVLGHMDLREEGDEETTNDVPHIQCGDGCDPQGLRDNSQFCLQRIHQGLIFYEKLL
GSDIFTGEPSELLPDSVPGQLHASLLGLSLLQPEGHHWETQQIPSLSPSQPWQRLLLLRFKILR
SLQAFVAVAARVFAHGAATLSPLEKKTCTSRASSTTTTTTEIRLLTKPERKF.
```

4.3. Production of p19-TRX Fusion Protein

p19 protein was produced from an engineered plasmid construct pET-DH-TRX-p19 in the form of a fusion protein with Thioredoxin A (TRX) and a double His6-tag at the N-terminus (calculated Mw 40 kDa). The p19-TRX fusion protein was produced in *E. coli* BL21(λDE3) host cells in 100 mL LB medium containing 60 µg/mL kanamycin at 37 °C and shaken at 250 RPM until the culture reached OD600 = 0.6. Subsequently, the protein production was induced with 1 mM IPTG and the culture was let to grow for 4 h at 37 °C. Cells were harvested by centrifugation (6000 × g, 20 min), washed with TN buffer (50 mM Tris-HCl and 150 mM NaCl, pH = 8) and centrifuged again (5000 × g, 10 min). For protein extraction and purification, cell pellets were re-suspended in 10 mL TN buffer and disrupted by MISONIX 3000 sonicator. The lysates were centrifuged at 40,000 × g for 20 min and the insoluble p19 protein was extracted with 10 mL of 8 M urea in TN buffer. The urea extract was left shaking for half an hour at room temperature and centrifuged at 40,000 × g for 30 min. The supernatant was applied on 1 mL Ni-NTA agarose column equilibrated with TN buffer. The washing steps were performed with 10 mL of TN buffer with 8 M urea and, subsequently, with TN buffer containing 8 M urea and 20 mM imidazole. The p19 protein was then eluted with TN buffer containing 8 M urea and 250 mM imidazole. To remove imidazole, urea and Ni-ion traces, eluted samples were dialyzed in PBS buffer or stabilized by adding (1:1) SuperBlock solution (SuperBlock® Blocking Buffer, 37515, Pierce Biotechnology, Rockford, IL, USA).

4.4. p19 Binding Assay

p19-TRX fusion protein was dialyzed into PBS or SuperBlock solution (1:1) and its binding activity was examined by ELISA. Wells of Polysorp plate (NUNC, Denmark) were coated with 10 µg/mL ILP317-TolA-Avitag protein diluted in 100 mM bicarbonate/carbonate coating buffer,

pH = 9.6, and incubated at 7 °C overnight. The following day, the plate was washed with PBS buffer containing 0.05% Tween (PBST) and blocked with 1% BSA resolved in the same solution (PBSTB). Series of diluted p19-TRX samples in PBSTB were prepared and p19 binding to the immobilized ILP317-TolA-Avitag protein was detected using mouse anti-human IL-23 polyclonal antibody (clone HLT2736, BioLegend, San Diego, CA, USA) diluted in PBSTB (1:2000) followed by goat anti-mouse IgG horseradish peroxidase (HRP) conjugate (BioLegend, San Diego, CA, USA) (1:1000). The enzymatic reaction of HRP with OPD substrate (Sigma-Aldrich, St. Louis, MO, USA) in citrate buffer (3.31% Sodium citrate tribasic dihydrate, phosphoric acid until pH = 5.0) was visualized after 5 min staining, then the reaction was stopped by 2M sulfuric acid and the absorbance was measured at 492 nm.

4.5. Expression of Cytokine Binding Fusion Proteins in *L. lactis*

Overnight cultures of *L. lactis* NZ9000 transformed with the appropriate plasmid (pSD-ILP030, pSD-ILP317, pSD-ILP323, pSD-ADN23, pSD-ILP030-FLAG, pSD-ILP317-FLAG, pSD-ILP323-FLAG, pSD-ADN23-FLAG or pNZ8148–empty plasmid control) were diluted (1:100) in 10 mL of fresh GM-17 medium and grown to optical density A600 = 0.80. Fusion protein expression was induced with 25 ng/mL nisin (Fluka Chemie AG, Buchs, Switzerland). After three hours of incubation, 1 mL of culture was stored at 4 °C for flow cytometry, and the remaining cell culture was centrifuged at 5000 × g for 10 min. The cell pellet was resuspended in 400 µL of phosphate-buffered saline (PBS, pH 7.4) and stored at –20 °C for SDS PAGE analysis or resuspended at to optical A600 = 10.0 and stored at 4 °C for enzyme-linked immunosorbent assay (ELISA).

4.6. SDS PAGE and Western Blot

SDS PAGE was performed with a Mini-Protean II apparatus (Bio-Rad, Hercules, USA). Samples were thawed in an ice bath, briefly sonicated with UPS200S sonicator (Hielscher Ultrasonics, Teltow, Germany), mixed with 2 × Laemmli sample buffer and dithiothreitol, and denatured by heating at 100 °C before loading. Page Ruler Plus pre-stained standard (Fermentas, Waltham, MA, USA) was used for molecular weight comparison. Proteins were transferred to nitrocellulose membrane (GE Healthcare Life Sciences, Marlborough, MA, USA) using wet transfer at 100 V for 90 min. Membranes were blocked in 5% non-fat dried milk in TBS with 0.05% Tween-20 (TBST; 50 mM Tris-HCl, 150 mM NaCl, 0.05% Tween 20, pH 7.5) and incubated overnight at 4 °C with mouse anti-FLAG IgG (Proteintech Group, Chicago, IL, USA; 1:1000) in 5% non-fat dried milk in TBST. Following three washes with TBST, membranes were incubated for 2 h with peroxidase conjugated secondary goat anti-mouse IgG (Jackson ImmunoResearch, West Grove, PA, USA; 1:5000) in 5% non-fat dried milk in TBST. After three further washes with TBST, membranes were incubated with Lumi-Light chemiluminescent reagent (Roche, Basel, Switzerland). Images were acquired using a ChemiDoc MP Imaging System (Bio-Rad, Hercules, CA, USA).

4.7. Flow Cytometry

For flow cytometry, 20 µL of a cell culture in the stationary phase was added to 500 µL of Tris-buffered saline (TBS; 50 mM Tris-HCl, 150 mM NaCl, pH 7.5) and centrifuged for 5 min at 5000 × g and 4 °C. The pellet was resuspended in 200 µL of dialyzed Ni-NTA purified p19-trx (50 µg/mL in PBS buffer with carrier protein SuperBlock). After 2 h of incubation at RT with constant shaking at 100 rpm, cells were washed three times with 200 µL 0.1% TBS-Tween (TBST) and resuspended in 200 µL of TBS with mouse anti-human IL-23 p19 IgG (BioLegend, San Diego, CA, USA; diluted 1:500). After 2 h of incubation at RT with constant shaking at 100 rpm, cells were washed three times with 200 µL 0.1% TBS-Tween (TBST) and resuspended in 200 µL of TBS with Alexa Fluor 488-conjugated goat anti-mouse IgG (Invitrogen, Carlsbad, CA, USA; diluted 1:500). 2 h incubation at RT was repeated and cells were washed again three times with 200 µL TBST and finally resuspended in 500 µL TBS. Samples were analyzed with a FACSCalibur flow cytometer (Becton Dickinson, Franklin Lakes, NJ, USA) using excitation at 488 nm and emission at 530 nm in the FL1 channel. The results are presented as mean

fluorescence intensity (MFI) values of at least 20,000 lactococcal cells. The result was expressed as the average of at least three independent experiments. Similar protocol was applied for the detection of FLAG-tagged ILP fusion proteins. Rabbit anti-FLAG IgG (Proteintech Group, Chicago, IL, USA; diluted 1:500) was used as primary antibody and Alexa Fluor 488-conjugated donkey anti-rabbit IgG (Invitrogen, Carlsbad, CA, USA; diluted 1:500) was used as a secondary antibody. All the experiments were performed in three biological replicates.

4.8. IL-23 Binding Assay

The concentration of IL-23 was determined with Human IL-23 ELISA development kit (HRP) from Mabtech. Different numbers of *L. lactis* cells expressing ILP fusion proteins were centrifuged ($5000 \times g$, 5 min, 4 °C) and resuspended in 200 μ L of incubation buffer (PBS with 0.05% Tween and 0.1% BSA) containing various concentrations of IL-23 standard and incubated for 2 h at room temperature (RT) with gentle shaking. Cells were then removed by centrifugation ($5000 \times g$, 5 min, 4 °C) and the concentrations of the remaining cytokines in the supernatant were determined according to the ELISA manufacturer's instructions. Briefly, Nunc Maxisorp 96-well plates were coated with recommended concentrations of IL-23-binding antibodies overnight at 4 °C. 100 μ L of samples were then added and incubated for 2 h at RT. Wells were washed five times with 200 μ L of PBS containing 0.05% Tween (PBST). 100 μ L per well of recommended concentration of biotinylated monoclonal antibodies against IL-23 were added and incubated at RT for 1 h. Wells were washed again for five times with 200 μ L of PBST. 100 μ L of streptavidin-HRP diluted 1:1000 was added to the plate and incubated for 1 h at RT. The plate was washed again for five times with PBST and 100 μ L of 3,3',5,5'-tetramethylbenzidine (TMB) substrate (Sigma-Aldrich, St. Louis, MO, USA) was added. The reaction was stopped after 15 min by the addition of 50 μ L of 2 M sulfuric acid. Absorbances were read at 450 nm using an Infinite M1000 microplate-reader (Tecan, Mannedorf, Switzerland).

4.9. Statistics

Data were analyzed with GraphPad Prism 5.0 software. Mean fluorescence intensities (MFIs), obtained by flow cytometry, were compared by ANOVA followed by post-hoc Bonferroni multiple pair comparison. Relevant pairs with significant differences ($p < 0.05$) were highlighted. Concentrations of IL-23, obtained by ELISA, were compared to control using *t*-test. Significant differences ($p < 0.05$) were highlighted.

4.10. Modeling of ILP-p19 and Interactions

The homology model of the mouse p19 was prepared using the MODELLER 9v14 suite of programs [43] based on the homologous structure of human p19 (PDB ID 3duh [44], protein sequence identity 71.9% and the similarity 90.4%), where the missing residues from the p19 loop regions were added using the loopmodel function of MODELLER. The homology model was relaxed using an implicit solvation parm96 molecular dynamics simulation. The MD parameters were assigned in Zephyr graphical interface [45] and 20 ns simulation was performed using GPU accelerated version of gromacs package [46]. The structure of studied ABD variants (ILP030, ILP317, and ILP323) was modeled based on the ABDwt structure (PDB ID 1gjt [47]). All the necessary sequence alignments were performed employing Muscle program [48]. Resulting three-dimensional structures were subjected to the flexible side chain docking performed using a local copy of the ClusPro server [49,50].

5. Conclusions

Collectively, this work contributes to development of new types of recombinant bacteria of food origin capable of displaying and secreting engineered binding proteins as non-immunoglobulin-blocking alternatives. The generated and characterized recombinant bacteria strains represent novel tools for in vivo testing of IL-23 anti-inflammatory agents that might be useful for treatment of intestinal inflammation.

Author Contributions: P.M. and A.B. designed the experiments and research project. K.Š., P.Z., M.H. and L.V. performed the experiments and analyzed the data. H.P., M.K. and L.K. also participated in experiments and manuscript preparation and J.Č. performed in silico modeling and docking. P.M. and A.B. wrote the paper. All authors read and approved the manuscript.

Funding: This work was supported by the Czech Academy of Sciences (CAS) and Slovenian Academy of Sciences and Arts (SAZU) (No. SAZU-16-01), by Czech Health Research Council, Ministry of Health of the Czech Republic (No. 16-27676A), by the Institutional Research Concept (RVO: 86652036), by European Regional Development Fund [BIOCEV CZ.1.05/1.1.00/02.0109] and by Slovenian Research Agency (ARRS; No. P4-0127).

Acknowledgments: The authors thank Michal Malý and Petra Kadlčáková for excellent experimental assistance.

Conflicts of Interest: The authors declare no conflict of interest.

References

1. Girolomoni, G.; Strohal, R.; Puig, L.; Bachelez, H.; Barker, J.; Boehncke, W.H.; Prinz, J.C. The role of IL-23 and the IL-23/TH 17 immune axis in the pathogenesis and treatment of psoriasis. *J. Eur. Acad. Dermatol. Venereol.* **2017**, *31*, 1616–1626. [[CrossRef](#)] [[PubMed](#)]
2. Razawy, W.; van Driel, M.; Lubberts, E. The role of IL-23 receptor signaling in inflammation-mediated erosive autoimmune arthritis and bone remodeling. *Eur. J. Immunol.* **2018**, *48*, 220–229. [[CrossRef](#)] [[PubMed](#)]
3. Luo, C.; Zhang, H. The Role of Proinflammatory Pathways in the Pathogenesis of Colitis-Associated Colorectal Cancer. *Mediat. Inflamm.* **2017**, *2017*, 5126048. [[CrossRef](#)] [[PubMed](#)]
4. Sarra, M.; Pallone, F.; Macdonald, T.T.; Monteleone, G. IL-23/IL-17 axis in IBD. *Inflamm. Bowel. Dis.* **2010**, *16*, 1808–1813. [[CrossRef](#)] [[PubMed](#)]
5. Siakavellas, S.I.; Bamias, G. Role of the IL-23/IL-17 axis in Crohn's disease. *Discov. Med.* **2012**, *14*, 253–262. [[PubMed](#)]
6. Floss, D.M.; Schroder, J.; Franke, M.; Scheller, J. Insights into IL-23 biology: From structure to function. *Cytokine Growth Factor Rev.* **2015**, *26*, 569–578. [[CrossRef](#)] [[PubMed](#)]
7. Gaffen, S.L.; Jain, R.; Garg, A.V.; Cua, D.J. The IL-23-IL-17 immune axis: From mechanisms to therapeutic testing. *Nat. Rev. Immunol.* **2014**, *14*, 585–600. [[CrossRef](#)] [[PubMed](#)]
8. Bilal, J.; Berlinberg, A.; Bhattacharjee, S.; Trost, J.; Riaz, I.B.; Kurtzman, D.J.B. A Systematic Review and Meta-Analysis of the Efficacy and Safety of the Interleukin (IL)-12/23 and IL-17 Inhibitors Ustekinumab, Secukinumab, Ixekizumab, Brodalumab, Guselkumab, and Tildrakizumab for the Treatment of Moderate to Severe Plaque Psoriasis. *J. Dermatol. Treat.* **2018**, 1–37. [[CrossRef](#)] [[PubMed](#)]
9. Fotiadou, C.; Lazaridou, E.; Sotiriou, E.; Ioannides, D. Targeting IL-23 in psoriasis: Current perspectives. *Psoriasis (Auckl)* **2018**, *8*, 1–5. [[CrossRef](#)] [[PubMed](#)]
10. Desmyter, A.; Spinelli, S.; Boutton, C.; Saunders, M.; Blachetot, C.; de Haard, H.; Denecker, G.; Van Roy, M.; Cambillau, C.; Rommelaere, H. Neutralization of Human Interleukin 23 by Multivalent Nanobodies Explained by the Structure of Cytokine-Nanobody Complex. *Front. Immunol.* **2017**, *8*, 884. [[CrossRef](#)] [[PubMed](#)]
11. Ramamurthy, V.; Krystek, S.R., Jr.; Bush, A.; Wei, A.; Emanuel, S.L.; Das Gupta, R.; Janjua, A.; Cheng, L.; Murdock, M.; Abramczyk, B.; et al. Structures of adnectin/protein complexes reveal an expanded binding footprint. *Structure* **2012**, *20*, 259–269. [[CrossRef](#)] [[PubMed](#)]
12. Desmet, J.; Verstraete, K.; Bloch, Y.; Lorent, E.; Wen, Y.; Devreese, B.; Vandenbroucke, K.; Loverix, S.; Hettmann, T.; Deroo, S.; et al. Structural basis of IL-23 antagonism by an Alphabody protein scaffold. *Nat. Commun.* **2014**, *5*, 5237. [[CrossRef](#)] [[PubMed](#)]
13. Kuchar, M.; Vankova, L.; Petrokova, H.; Cerny, J.; Osicka, R.; Pelak, O.; Sipova, H.; Schneider, B.; Homola, J.; Sebo, P.; et al. Human interleukin-23 receptor antagonists derived from an albumin-binding domain scaffold inhibit IL-23-dependent ex vivo expansion of IL-17-producing T-cells. *Proteins* **2014**, *82*, 975–989. [[CrossRef](#)] [[PubMed](#)]
14. Krizova, L.; Kuchar, M.; Petrokova, H.; Osicka, R.; Hlavnickova, M.; Pelak, O.; Cerny, J.; Kalina, T.; Maly, P. p19-targeted ABD-derived protein variants inhibit IL-23 binding and exert suppressive control over IL-23-stimulated expansion of primary human IL-17+ T-cells. *Autoimmunity* **2017**, *50*, 102–113. [[CrossRef](#)] [[PubMed](#)]

15. Worledge, K.L.; Godiska, R.; Barrett, T.A.; Kink, J.A. Oral administration of avian tumor necrosis factor antibodies effectively treats experimental colitis in rats. *Dig. Dis. Sci.* **2000**, *45*, 2298–2305. [[CrossRef](#)] [[PubMed](#)]
16. Pawar, V.K.; Meher, J.G.; Singh, Y.; Chaurasia, M.; Surendar Reddy, B.; Chourasia, M.K. Targeting of gastrointestinal tract for amended delivery of protein/peptide therapeutics: Strategies and industrial perspectives. *J. Control. Release* **2014**, *196*, 168–183. [[CrossRef](#)] [[PubMed](#)]
17. Braat, H.; Rottiers, P.; Hommes, D.W.; Huyghebaert, N.; Remaut, E.; Remon, J.P.; van Deventer, S.J.; Neiryneck, S.; Peppelenbosch, M.P.; Steidler, L. A phase I trial with transgenic bacteria expressing interleukin-10 in Crohn's disease. *Clin. Gastroenterol. Hepatol.* **2006**, *4*, 754–759. [[CrossRef](#)] [[PubMed](#)]
18. Douillard, F.P.; de Vos, W.M. Functional genomics of lactic acid bacteria: From food to health. *Microb. Cell Factor* **2014**, *13*. [[CrossRef](#)] [[PubMed](#)]
19. Sanders, M.E. Probiotics: Definition, sources, selection, and uses. *Clin. Infect. Dis.* **2008**, *46* (Suppl. 2), S58–S61, discussion S144–S51. [[CrossRef](#)] [[PubMed](#)]
20. Siezen, R.J.; Bayjanov, J.R.; Felis, G.E.; van der Sijde, M.R.; Starrenburg, M.; Molenaar, D.; Wels, M.; van Hijum, S.A.; van Hylckama Vlieg, J.E. Genome-scale diversity and niche adaptation analysis of *Lactococcus lactis* by comparative genome hybridization using multi-strain arrays. *Microb. Biotechnol.* **2011**, *4*, 383–402. [[CrossRef](#)] [[PubMed](#)]
21. Ballal, S.A.; Veiga, P.; Fenn, K.; Michaud, M.; Kim, J.H.; Gallini, C.A.; Glickman, J.N.; Quere, G.; Garault, P.; Beal, C.; et al. Host lysozyme-mediated lysis of *Lactococcus lactis* facilitates delivery of colitis-attenuating superoxide dismutase to inflamed colons. *Proc. Natl. Acad. Sci. USA* **2015**, *112*, 7803–7808. [[CrossRef](#)] [[PubMed](#)]
22. Kawahara, M.; Nemoto, M.; Nakata, T.; Kondo, S.; Takahashi, H.; Kimura, B.; Kuda, T. Anti-inflammatory properties of fermented soy milk with *Lactococcus lactis* subsp. *lactis* S-SU2 in murine macrophage RAW264.7 cells and DSS-induced IBD model mice. *Int. Immunopharmacol.* **2015**, *26*, 295–303. [[CrossRef](#)] [[PubMed](#)]
23. Drouault, S.; Corthier, G.; Ehrlich, S.D.; Renault, P. Survival, physiology, and lysis of *Lactococcus lactis* in the digestive tract. *Appl. Environ. Microbiol.* **1999**, *65*, 4881–4886. [[PubMed](#)]
24. Berlec, A.; Ravnikar, M.; Strukelj, B. Lactic acid bacteria as oral delivery systems for biomolecules. *Pharmazie* **2012**, *67*, 891–898. [[PubMed](#)]
25. Bermudez-Humaran, L.G.; Aubry, C.; Motta, J.P.; Deraison, C.; Steidler, L.; Vergnolle, N.; Chatel, J.M.; Langella, P. Engineering lactococci and lactobacilli for human health. *Curr. Opin. Microbiol.* **2013**, *16*, 278–283. [[CrossRef](#)] [[PubMed](#)]
26. Song, A.A.; In, L.L.A.; Lim, S.H.E.; Rahim, R.A. A review on *Lactococcus lactis*: From food to factory. *Microb. Cell Fact.* **2017**, *16*, 55. [[CrossRef](#)] [[PubMed](#)]
27. Vandenbroucke, K.; de Haard, H.; Beirnaert, E.; Dreier, T.; Lauwereys, M.; Huyck, L.; Van Huysse, J.; Demetter, P.; Steidler, L.; Remaut, E.; et al. Orally administered *L. lactis* secreting an anti-TNF Nanobody demonstrate efficacy in chronic colitis. *Mucosal. Immunol.* **2010**, *3*, 49–56. [[CrossRef](#)] [[PubMed](#)]
28. Berlec, A.; Perse, M.; Ravnikar, M.; Lunder, M.; Erman, A.; Cerar, A.; Strukelj, B. Dextran sulphate sodium colitis in C57BL/6J mice is alleviated by *Lactococcus lactis* and worsened by the neutralization of Tumor necrosis Factor alpha. *Int. Immunopharmacol.* **2017**, *43*, 219–226. [[CrossRef](#)] [[PubMed](#)]
29. Vandenbroucke, K.; Hans, W.; Van Huysse, J.; Neiryneck, S.; Demetter, P.; Remaut, E.; Rottiers, P.; Steidler, L. Active delivery of trefoil factors by genetically modified *Lactococcus lactis* prevents and heals acute colitis in mice. *Gastroenterology* **2004**, *127*, 502–513. [[CrossRef](#)] [[PubMed](#)]
30. Galipeau, H.J.; Wiepjes, M.; Motta, J.P.; Schulz, J.D.; Jury, J.; Natividad, J.M.; Pinto-Sanchez, I.; Sinclair, D.; Rousset, P.; Martin-Rosique, R.; et al. Novel role of the serine protease inhibitor elafin in gluten-related disorders. *Am. J. Gastroenterol.* **2014**, *109*, 748–756. [[CrossRef](#)] [[PubMed](#)]
31. Steidler, L.; Hans, W.; Schotte, L.; Neiryneck, S.; Obermeier, F.; Falk, W.; Fiers, W.; Remaut, E. Treatment of murine colitis by *Lactococcus lactis* secreting interleukin-10. *Science* **2000**, *289*, 1352–1355. [[CrossRef](#)] [[PubMed](#)]
32. Ravnikar, M.; Strukelj, B.; Obermajer, N.; Lunder, M.; Berlec, A. Engineered lactic acid bacterium *Lactococcus lactis* capable of binding antibodies and tumor necrosis factor alpha. *Appl. Environ. Microbiol.* **2010**, *76*, 6928–6932. [[CrossRef](#)] [[PubMed](#)]

33. Skrlec, K.; Pucer Janez, A.; Rogelj, B.; Strukelj, B.; Berlec, A. Evasin-displaying lactic acid bacteria bind different chemokines and neutralize CXCL8 production in Caco-2 cells. *Microb. Biotechnol.* **2017**, *10*, 1732–1743. [[CrossRef](#)] [[PubMed](#)]
34. Michon, C.; Langella, P.; Eijsink, V.G.; Mathiesen, G.; Chatel, J.M. Display of recombinant proteins at the surface of lactic acid bacteria: Strategies and applications. *Microb. Cell Factor.* **2016**, *15*, 70. [[CrossRef](#)] [[PubMed](#)]
35. Dieye, Y.; Usai, S.; Clier, F.; Gruss, A.; Piard, J.C. Design of a protein-targeting system for lactic acid bacteria. *J. Bacteriol.* **2001**, *183*, 4157–4166. [[CrossRef](#)] [[PubMed](#)]
36. Buist, G.; Kok, J.; Leenhouts, K.J.; Dabrowska, M.; Venema, G.; Haandrikman, A.J. Molecular cloning and nucleotide sequence of the gene encoding the major peptidoglycan hydrolase of *Lactococcus lactis*, a muramidase needed for cell separation. *J. Bacteriol.* **1995**, *177*, 1554–1563. [[CrossRef](#)] [[PubMed](#)]
37. Steen, A.; Buist, G.; Horsburgh, G.J.; Venema, G.; Kuipers, O.P.; Foster, S.J.; Kok, J. AcmA of *Lactococcus lactis* is an N-acetylglucosaminidase with an optimal number of LysM domains for proper functioning. *FEBS J.* **2005**, *272*, 2854–2868. [[CrossRef](#)] [[PubMed](#)]
38. Kosler, S.; Strukelj, B.; Berlec, A. Lactic Acid Bacteria with Concomitant IL-17, IL-23 and TNFalpha-Binding Ability for the Treatment of Inflammatory Bowel Disease. *Curr. Pharm. Biotechnol.* **2017**, *18*, 318–326. [[CrossRef](#)] [[PubMed](#)]
39. Bloch, Y.; Bouchareychas, L.; Merceron, R.; Skladanowska, K.; Van den Bossche, L.; Detry, S.; Govindarajan, S.; Elewaut, D.; Haerynck, F.; Dullaers, M.; et al. Structural Activation of Pro-inflammatory Human Cytokine IL-23 by Cognate IL-23 Receptor Enables Recruitment of the Shared Receptor IL-12Rbeta1. *Immunity* **2018**, *48*, 45–58.e6. [[CrossRef](#)] [[PubMed](#)]
40. Holo, H.; Nes, I.F. Transformation of *Lactococcus* by electroporation. *Methods Mol. Biol.* **1995**, *47*, 195–199. [[PubMed](#)]
41. Ahmad, J.N.; Li, J.; Biedermannova, L.; Kuchar, M.; Sipova, H.; Semeradtova, A.; Cerny, J.; Petrokova, H.; Mikulecky, P.; Polinek, J.; et al. Novel high-affinity binders of human interferon gamma derived from albumin-binding domain of protein G. *Proteins* **2012**, *80*, 774–789. [[CrossRef](#)] [[PubMed](#)]
42. Mierau, I.; Kleerebezem, M. 10 years of the nisin-controlled gene expression system (NICE) in *Lactococcus lactis*. *Appl. Microbiol. Biotechnol.* **2005**, *68*, 705–717. [[CrossRef](#)] [[PubMed](#)]
43. Webb, B.; Sali, A. Comparative Protein Structure Modeling Using MODELLER. *Curr. Protoc. Bioinform.* **2014**, *47*, 561–32. [[CrossRef](#)] [[PubMed](#)]
44. Lupardus, P.J.; Garcia, K.C. The structure of interleukin-23 reveals the molecular basis of p40 subunit sharing with interleukin-12. *J. Mol. Biol.* **2008**, *382*, 931–941. [[CrossRef](#)] [[PubMed](#)]
45. Eastman, P.; Pande, V.S. OpenMM: A Hardware Independent Framework for Molecular Simulations. *Comput. Sci. Eng.* **2015**, *12*, 34–39. [[CrossRef](#)] [[PubMed](#)]
46. Van Der Spoel, D.; Lindahl, E.; Hess, B.; Groenhof, G.; Mark, A.E.; Berendsen, H.J. GROMACS: Fast, flexible, and free. *J. Comput. Chem.* **2005**, *26*, 1701–1718. [[CrossRef](#)] [[PubMed](#)]
47. Johansson, M.U.; Frick, I.M.; Nilsson, H.; Kraulis, P.J.; Hober, S.; Jonasson, P.; Linhult, M.; Nygren, P.A.; Uhlen, M.; Bjorck, L.; et al. Structure, specificity, and mode of interaction for bacterial albumin-binding modules. *J. Biol. Chem.* **2002**, *277*, 8114–8120. [[CrossRef](#)] [[PubMed](#)]
48. Edgar, R.C. MUSCLE: Multiple sequence alignment with high accuracy and high throughput. *Nucleic Acids Res.* **2004**, *32*, 1792–1797. [[CrossRef](#)] [[PubMed](#)]
49. Kozakov, D.; Beglov, D.; Bohnuud, T.; Mottarella, S.E.; Xia, B.; Hall, D.R.; Vajda, S. How good is automated protein docking? *Proteins* **2013**, *81*, 2159–2166. [[CrossRef](#)] [[PubMed](#)]
50. Kozakov, D.; Brenke, R.; Comeau, S.R.; Vajda, S. PIPER: An FFT-based protein docking program with pairwise potentials. *Proteins* **2006**, *65*, 392–406. [[CrossRef](#)] [[PubMed](#)]





Article

ABD-Derived Protein Blockers of Human IL-17 Receptor A as Non-IgG Alternatives for Modulation of IL-17-Dependent Pro-Inflammatory Axis

Marie Hlavničková¹, Milan Kuchař¹, Radim Osička², Lucie Vaňková¹, Hana Petroková¹, Michal Malý¹, Jiří Černý³ , Petr Arenberger⁴ and Petr Malý^{1,*}

¹ Laboratory of Ligand Engineering, Institute of Biotechnology of the Czech Academy of Sciences, v. v. i., BIOCEV Research Center, Průmyslová 595, 252 50 Vestec, Czech Republic; marie.hlavnickova@ibt.cas.cz (M.H.); milan.kuchar@ibt.cas.cz (M.K.); lucie.vankova@ibt.cas.cz (L.V.); hana.petrokova@ibt.cas.cz (H.P.); michal.maly@ibt.cas.cz (M.M.)

² Laboratory of Molecular Biology of the Bacterial Pathogens, Institute of Microbiology, Czech Academy of Sciences, v. v. i., Vídeňská 1083, 142 20 Prague, Czech Republic; osicka@biomed.cas.cz

³ Laboratory of Structural Bioinformatics of Proteins, Institute of Biotechnology of the Czech Academy of Sciences, v. v. i., BIOCEV Research Center, Průmyslová 595, 252 50 Vestec, Czech Republic; jiri.cerny@ibt.cas.cz

⁴ Department of Dermatology and Venereology, Faculty Hospital of Královské Vinohrady, Šrobárova 50, 100 34 Prague, Czech Republic; petr.arenberger@fnkv.cz

* Correspondence: petr.maly@ibt.cas.cz; Tel.: +420-325-873-763

Received: 10 September 2018; Accepted: 6 October 2018; Published: 9 October 2018



Abstract: Interleukin 17 (IL-17) and its cognate receptor A (IL-17RA) play a crucial role in Th17 cells-mediated pro-inflammatory pathway and pathogenesis of several autoimmune disorders including psoriasis. IL-17 is mainly produced by activated Th-17 helper cells upon stimulation by IL-23 and, via binding to its receptors, mediates IL-17-driven cell signaling in keratinocytes. Hyper-proliferation of keratinocytes belongs to major clinical manifestations in psoriasis. To modulate IL-17-mediated inflammatory cascade, we generated a unique collection of IL-17RA-targeting protein binders that prevent from binding of human IL-17A cytokine to its cell-surface receptor. To this goal, we used a highly complex combinatorial library derived from scaffold of albumin-binding domain (ABD) of streptococcal protein G, and ribosome display selection, to yield a collection of ABD-derived high-affinity ligands of human IL-17RA, called ARS binders. From 67 analyzed ABD variants, 7 different sequence families were identified. Representatives of these groups competed with human IL-17A for binding to recombinant IL-17RA receptor as well as to IL-17RA-Immunoglobulin G chimera, as tested in enzyme-linked immunosorbent assay (ELISA). Five ARS variants bound to IL-17RA-expressing THP-1 cells and blocked binding of human IL-17 cytokine to the cell surface, as tested by flow cytometry. Three variants exhibited high-affinity binding with a nanomolar K_d value to human keratinocyte HaCaT cells, as measured using Ligand Tracer Green Line. Upon IL-17-stimulated activation, ARS variants inhibited secretion of Gro- α (CXCL1) by normal human skin fibroblasts in vitro. Thus, we identified a novel class of inhibitory ligands that might serve as immunosuppressive IL-17RA-targeted non-IgG protein antagonists.

Keywords: binding protein; albumin-binding domain; cytokine; IL-17 receptor; combinatorial library

1. Introduction

Interleukin 23/Interleukin 17 (IL-23/IL-17) pro-inflammatory axis plays a pivotal role in the pathogenesis of several chronic autoimmune diseases [1–3]. Heterodimer of a unique p19 subunit

and a common p40 protein, both known as α - and β -subunits of IL-23 cytokine [4], is secreted by activated dendritic cells and macrophages, and stimulates the differentiation of naive Th cells into Th17 cell population. This action is mediated via interactions with its cognate receptor complex, formed by IL-23R and IL-12R β 1 receptor units. Synergistic tethering of the IL-23 heterodimer to both receptor units leads to a receptor heterodimerization followed by a quaternary complex formation and triggering of Jak/Stat signaling cascade, involving Jak2, Tyk2, Stat1, Stat3, Stat 4, and Stat5 [5]. The activation pathway of Th17 cell stimulates transcription of several inflammatory genes, resulting in the secretion of inflammatory mediators including IL-17A/F cytokine [6,7].

IL-17 cytokine gene family consists of six members known as IL-17A, B, C, D, E, and F [8]. Among them, IL-17A and IL-17F have been described to closely associate with development of autoimmune diseases via interactions with a receptor complex formed by IL-17 receptor A and C [9]. After binding of IL-17A or IL-17F homodimers, or IL-17A/F heterodimer, to the IL-17 receptor complex composed of a heterodimer of IL-17RA and IL-17RC, Act1 associates with IL-17RA/RC through SEFIR domains and, via TRAF-6, promotes MAPK, NF- κ B and C/EBP signaling [10]. IL-17A and F are mostly secreted by activated Th17 cells and $\gamma\delta$ T cells, but can be produced also by NKT cells or iLCs [11,12].

To target IL-23/Th17 pro-inflammatory cascade, several strategies have been developed. An attention has mostly been paid to blocking of an early step of the cascade by suppression of IL-23-mediated signaling in Th cells, thus suppressing the secretion of a cocktail of IL-17A, IL-22, and several chemokines by Th17 cells [13]. For psoriasis treatment, blocking of IL-17A cytokine or its receptor function on keratinocytes or skin fibroblasts is a valuable alternative. Originally, fully human monoclonal antibodies recognizing p40 subunit of the IL-23 cytokine were generated. While ustekinumab (Stelara) [14,15], a product of Janssen Biotech Inc., has been proved to be safe and already reached the market, another one, Briakinumab, was withdrawn due to an increased risk of cardiovascular side effects [16,17]. The strategy for modulation of IL-23/Th17 axis has been changed by focusing on p19 protein with aim to increase the specificity and safety of the drugs. Currently, there are several fully human or humanized monoclonal antibodies targeting the p19 in the development. Those include Guselkumab [18,19], Tildrakizumab (MK-3222) [20,21], and Risankizumab (B1655066) [22].

Alternatively, several neutralizers of downstream pathways of the IL-23/Th17 inflammatory cascade have been developed. Among them, fully human monoclonal antibody secukinumab (Cosentyx), a product of Novartis International AG, targeting human IL-17A cytokine, is available for treatment of psoriasis, ankylosing spondylitis, and psoriatic arthritis [23–25]. Fully human monoclonal antibody ixekizumab (Taltz) by Eli Lilly and Co., blocking IL-17A-mediated signaling, is approved for treatment of moderate-to-severe forms of plaque psoriasis and psoriatic arthritis [26]. Brodalumab (Siliq, Kyntheum), a human monoclonal antibody-based antagonist of IL-17 receptor A developed by Astra Zeneca, demonstrated an excellent efficacy in treatment of moderate-to-severe forms of plaque psoriasis [27,28]. In addition to that, soluble mutants of human IL-17A receptor were also developed and they exhibited a promising therapeutic effect in mouse model of psoriasis [29].

While monoclonal antibody-based biologics still represent a major line in drug development, non-immunoglobulin binding proteins derived from small protein domain scaffolds, generated by a directed evolution approach, attract attention as next generation therapeutics [30,31]. Small binding proteins selected from highly complex combinatorial libraries to any chosen target can be further engineered for desired specificity and binding affinity by *in silico* approaches. In contrast to antibodies, they lack disulfide bridges, can be produced *in vitro* and easily modified by molecular and gene-fusion approaches. Due to a small size, they exhibit an excellent tissue penetration and, in combination with transdermal delivery systems, they can be useful for development of topically-administrated drugs. Albumin-binding domain (ABD) of streptococcal protein G belongs to the smallest protein domain scaffolds that have been successfully verified for the generation of highly complex combinatorial libraries. This scaffold of 46 amino acids is formed by a three-helix bundle (pdb id 1GJT, residues 20–65) which provides three surfaces amenable to randomization [32–34]. As the parental non-mutated

wild-type ABD scaffold does not contain cysteine residues, it can be easily refolded into a functional state, supporting its binding specificity. As the critical residues for a high-affinity binding to human serum albumin (HSA) are located on the second and third helices, we selected this surface for the randomization of 11 residues, thus disrupting the original HSA binding sites and providing a library of a theoretical complexity 2×10^{14} protein variants. The validity of the library concept has already been demonstrated by the generation of ABD-derived binders targeting human interferon- γ with a sub-nanomolar affinity [32], by immunosuppressive protein blockers of human IL-23 receptor [35], by development of ABD-derived binders of human prostate specific protein 94 (PSP94, MSMB) [36] and by Shiga toxin 1B subunit-specific binders [37], and recently by immunomodulatory binders of human IL-23 cytokine [38].

In this work we used the ABD-derived highly complex combinatorial library to generate a unique collection of high-affinity binding proteins targeting the human IL-17 receptor A. We selected 7 representatives of the found sequence families and demonstrated that 5 of them interact with a soluble IL-17RA-IgG chimera and bind to IL-17RA-expressing THP-1 cells. In correlation to a predicted blocking function by in-silico docking, these variants inhibited binding of IL-17A cytokine to the recombinant IL-17RA and exhibited an immunosuppressive potential demonstrated on normal human skin fibroblast in vitro. We, therefore, contribute to the development of novel non-IgG immunomodulatory agents that can be useful in targeting of IL-23/Th-17 pro-inflammatory axis as unique IL-17RA antagonists.

2. Results

2.1. Molecular Assembly and Production of Recombinant IL-17RA

In our previous work [35] we demonstrated that the extracellular moiety of the human IL-23 receptor gene can be successfully produced as a refolded bacterial protein, which can serve as a target for the selection of protein binders from a highly complex combinatorial library. Therefore, we used a similar approach here and cloned the cDNA sequence coding for an extracellular part of the human IL-17RA (IL-17RAex), consisting of two fibronectin-type III domains (amino acid residues 33–320), into the bacterial expression vector pET-28b. This recombinant plasmid was used for IL-17RAex production in the *E. coli* SHuffle strain upon the optimization of the induction at 18 °C. Under these conditions, the major amount of the IL-17RAex protein was produced in an insoluble fraction from which the protein was purified by affinity chromatography on a Ni-NTA-agarose column under denaturing conditions. This urea-containing solution was diluted in a coating buffer, followed by refolding on Polysorp plate using several washing steps with PBS buffer. The significant amount of IL-17RAex was also present in a soluble fraction from which the protein was purified by Ni-NTA chromatography under native conditions. The identity of the purified IL-17RAex variants was verified on SDS-PAGE, as seen in Figure S1A, and by Western blot using anti-IL-17RA polyclonal antibody. Refolded IL-17RAex product, similarly to the soluble product, bound human IL-17A cytokine in enzyme-linked immunosorbent assay (ELISA) as seen in Figure S1B. We, therefore, used the soluble IL-17RAex as well as the refolded product as target proteins for the selection of IL-17RA-targeted protein binders.

2.2. Selection of ABD-Derived Variants Producing IL-17RA-Targeted Proteins

In our previous studies [32,35,36], we used only one recombinant product as a target for the selection of high-affinity binders. In this study, we decided to independently select ligands against the IL-17RAex protein purified either from the soluble fraction or from the insoluble fraction, and to investigate whether ribosome display will generate collections of IL-17RA binding proteins of the same sequence identity. After 5-round ribosome display with the protein purified from the soluble fraction, we generated a plasmid library carrying ABD-derived sequences encoding IL-17RAex-targeted protein variants that were called ARS ligands. Similarly, using the IL-17RAex protein purified from the insoluble fraction, we generated a plasmid library encoding a collection of protein binders, called

ARU binders. Both libraries were screened for the identification of the best binding candidates using ELISA. For this screening, ARS and ARU variants were produced in the form of in vivo biotinylated His₆-ARS/ARU-TolA-AVI fusion proteins, biotinylated through the C-terminal AviTag sequence (GLNDIFEAQKIEWHE) in BirA-positive *E. coli* host cells. An example of the screening of the ARS and ARU variants is presented in Figure 1. Production of 40 kDa ARS/ARU proteins of the selected candidates was verified by Western blot using an anti-His-tag antibody.

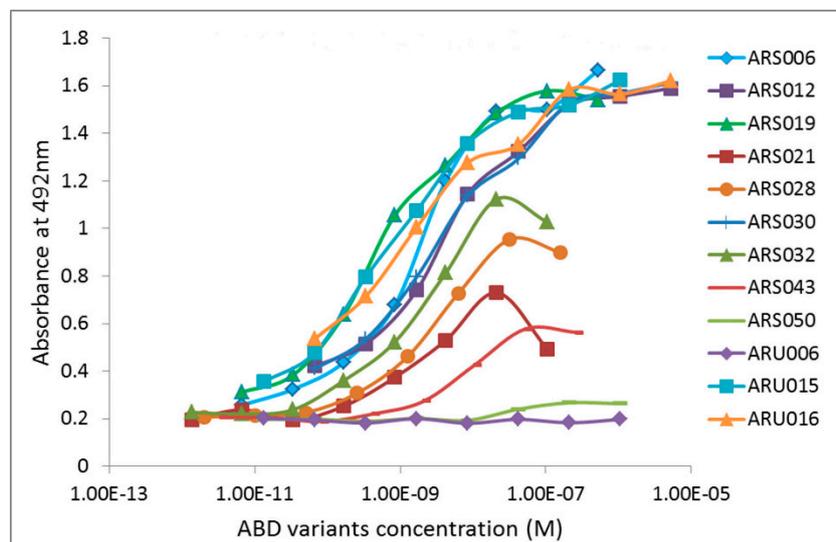


Figure 1. Screening of the interleukin 17 cognate receptor A (IL-17RA)-binding variants in enzyme-linked immunosorbent assay (ELISA). Bacterial cell lysates of individual ARS and ARU clones were screened for binding to the immobilized recombinant IL-17RA receptor. The binding proteins were produced in the form of in vivo biotinylated ARS/ARU-TolA-AVI fusion proteins and their binding to IL-17RA was visualized by streptavidin-HRP conjugate.

Following the experimental approach used previously for IL-23 receptor-targeted REX and IL-23 cytokine-targeted ILP binder selections [35,38], we identified 67 clones of ARS/ARU-producing variants that resulted from screening of both types of plasmid libraries. Plasmid DNA coding for all these clones was analyzed by sequencing, providing a final collection of all DNA sequences. Comparison of sequence similarity among all 67 tested clones and the parental non-randomized ABD was performed and this result is shown as a phylogenetic tree of 51 clones in Figure 2 (16 missing members are only sequentially redundant clones of ARS001). We found that representatives of ARU variants matched well to variants of the ARS collection, represented by the sequence identity or a high level of similarity. Contrary that, some of the ARS variants were unique (ARS002, ARS019, ARS021) or did not overlap with ARU sequences at a high similarity level (ARS043). As the ARS library represents a more complex collection, we selected ARS variants as representatives for 7 identified sequence families as seen in Figure 2. Those are ARS004 and ARS012 with many redundant clones, ARS014 with a limited sequence variability, and ARS002, ARS019, ARS021, and ARS043, each identified by one unique representative. These 7 ARS variants were selected as major candidates for further analysis.

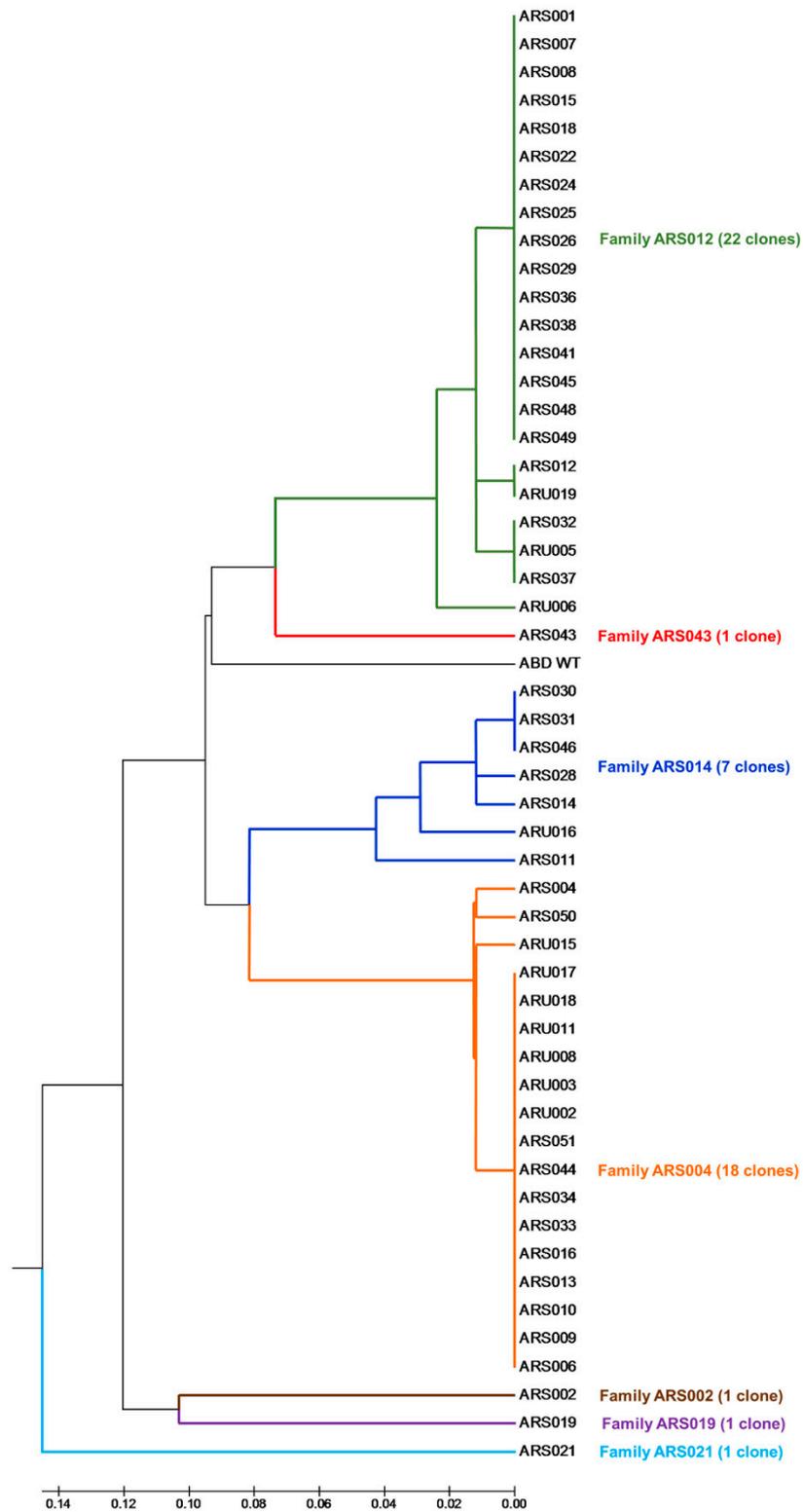


Figure 2. Comparison of a sequence similarity of the selected ARS and ARU clones. Similarity tree of polypeptide sequences of 51 analyzed ARS and ARU variants that were targeted to the recombinant extracellular IL-17RA receptor and selected by ribosome display. Sequence analysis of the ARS/ARU binders revealed 17 unique sequence variants that were clustered into 7 sequence families. For a similarity analysis, only the sequences between residues 20 and 46 were compared, as the N-terminal amino acid positions 1–19 were non-randomized.

2.3. Characterization of Binding Properties of the Selected ARS Variants

Representatives of the ARS sequencing families were produced in the form of fusion proteins containing a polyhistidinyl tag at the N-terminus and a 305 residues long helical TolA spacer protein and an Avitag consensus sequence as a target for *in vivo* biotinylation at the C-terminus (His₆-ARS-TolA-AVI). The fusion proteins were purified using affinity chromatography on a Ni-NTA agarose column and tested for binding to the IL-17 receptor. As all identified ARS and ARU clones were originally selected via targeting to the recombinant IL-17RA_{ex} protein expressed in *E. coli*, we investigated whether the selected ARS binding proteins can recognize a soluble glycosylated product of the human IL-17RA produced in the form of IL-17RA-IgG chimera. As shown in Figure 3, the ARS004, ARS012, ARS014, ARS019 and ARS043 variants in the form of His₆-ARS-TolA-AVI fusion proteins bound to the IL-17RA-IgG chimera, while no binding was observed with the ARS002 and ARS021 variants, similarly as the parental non-randomized ABD wild-type protein. These binding variants were, therefore, identified as major candidates for further studies.

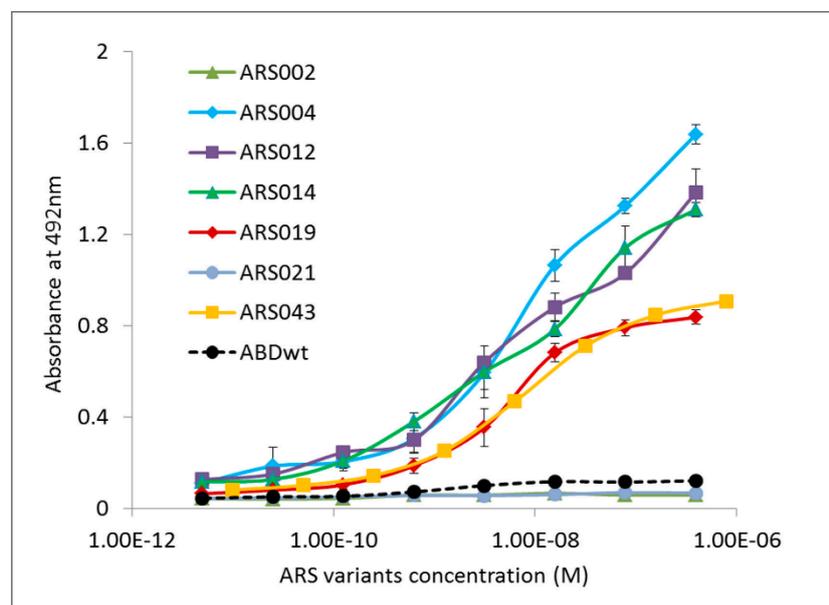


Figure 3. Binding of the selected representatives of ARS sequence families to the immobilized human IL-17RA-IgG chimera in ELISA. Purified binding proteins were produced in the form of *in vivo* biotinylated His₆-ARS-TolA-AVI fusion proteins. Binding to IL-17RA-IgG was visualized by streptavidin-HRP conjugate. Each point represents the mean value \pm standard deviation (SD).

To verify this fact, we performed the same competition ELISA experiment using the soluble IL-17RA-IgG chimera as a target. We tested all the selected ARS variants that were identified as binders of the IL-17RA-IgG chimera as seen in Figure 3. As presented in Figure 4 and Figure S2B, ARS004, ARS012, ARS014, ARS019, and ARS043 suppressed binding of IL-17A to the chimera, suggesting a blocking potential of these variants.

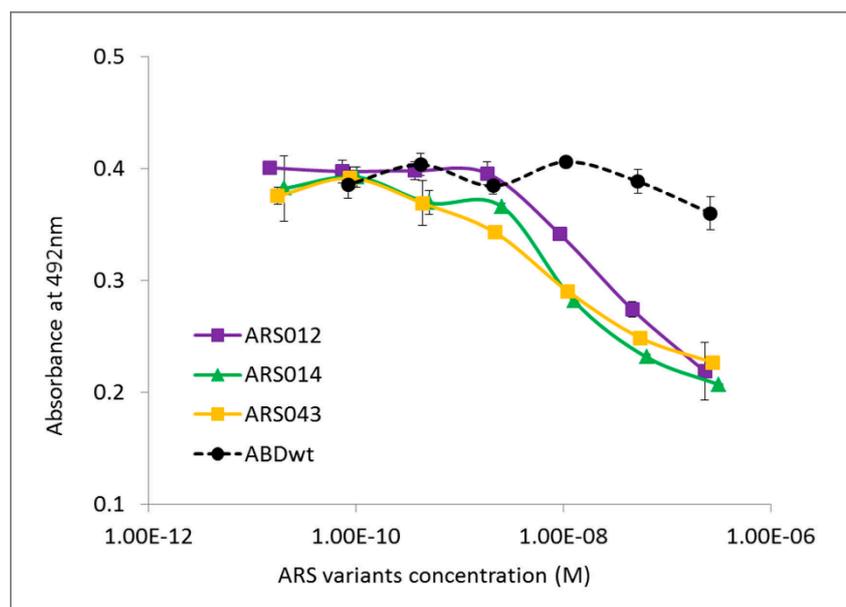


Figure 4. ARS ligands compete with IL-17A cytokine for binding to the human IL-17RA-IgG receptor chimera. The IL-17RA-IgG chimera was immobilized on an ELISA plate and serially diluted inhibitory His₆-ARS-TolA-AVI ligands were used to compete for binding with 10 nM IL-17A. Bound IL-17A was detected with anti-IL-17A polyclonal antibody in combination with secondary anti-IgG-HRP conjugate. His₆-ABDwt-TolA-AVI served as a negative control. Error bars represent standard deviations (SDs).

Protein sequences of the five ARS protein variants that bound to the soluble IL-17 receptor chimera and exhibited a blocking potential are presented in Table 1.

Table 1. Sequence comparison of the ARS binders. The non-mutated ABDwt was aligned with the randomized part of the ARS binders selected by ribosome display. Grey boxes indicate the 11 positions at which the residues of albumin-binding domain (ABD) (aa 20–46) were randomized. The non-randomized N-terminal part of ABD (aa 1–19) contain sequence LAEAKVLANRELDKYGVS D.

Protein	20	21	22	23	24	25	26	27	28	29	30	31	32	33	34	35	36	37	38	39	40	41	42	43	44	45	46
ABDwt	Y	Y	K	N	L	I	N	N	A	K	T	V	E	G	V	K	A	L	I	D	E	I	L	A	A	L	P
ARS004	V	Y	K	-	L	I	N	Y	A	C	P	V	T	W	V	K	W	V	I	D	P	I	L	A	M	L	P
ARS012	V	Y	K	-	L	I	N	M	A	L	Y	V	T	G	V	K	P	W	I	D	V	I	L	A	V	L	P
ARS014	V	Y	K	N	L	I	N	Y	A	W	L	V	M	W	V	-	-	P	I	D	A	I	L	A	L	L	P
ARS019	M	Y	K	N	V	I	N	I	A	W	W	V	S	I	V	K	Y	P	I	D	C	I	L	A	L	L	P
ARS043	L	Y	K	N	M	I	N	M	A	L	W	V	T	G	V	K	W	L	I	D	P	I	L	A	T	L	P

In our previous studies we demonstrated that the 305 residues long helical TolA protein served as a solubility- and stability-supporting moiety of the 40 kDa fusion protein, which did not interfere with the binding specificity of the tested ligands [32,36,38]. To demonstrate this fact in this study, we constructed short forms of selected ARS variants lacking the TolA protein sequence. These short variants of 8.3 kDa were produced as soluble His₆-ARS-AviTag in vivo biotinylated proteins, as seen in Figure S3A, and their binding to IL-17RA was confirmed by ELISA, shown in Figure S3B. We further used these short ARS protein forms to verify an inhibitory function of the long TolA-containing ARS forms as it has been demonstrated in Figure S2 and Figure 4. Therefore, we performed a competition ELISA experiment in which the purified short ARS variants competed with IL-17A cytokine for binding to IL-17RA. As presented in Figure S4, the short ARS variants, presented as examples of ARS012s, ARS014s and ARS043s, inhibited binding of human IL-17A, thus supporting previous conclusions done using the long His₆-ARS-TolA-AVI variants. In contrast to this, a short ARS002s protein did not exhibit an inhibitory potential shown in Figure S2 for the long His₆-ARS-TolA-AVI fusion protein.

2.4. Binding of the ARS Variants to Human Cells

Human uninduced THP-1 myelomonocytic cells are known to express the IL-17 receptor [39]. This was confirmed by flow cytometry upon staining of THP-1 cells with anti-human IL-17RA antibody as seen in Figure 5A. Thus, this cell line was used to determine, which of the seven selected representatives of the ARS sequence families bind to the IL-17RA. As shown in Figure 5B, the variants ARS002 and ARS021 exhibited only a negligible binding to THP-1 cells, which is in a good agreement with the ELISA results, where these two proteins did not significantly bind the coated IL-17RA-IgG chimera, shown in Figure 3. In contrast to that, all ARS variants found to be binders of the IL-17RA-IgG chimera, as seen in Figure 3, substantially bound to IL-17RA-expressing THP-1 cells as shown in Figure 5B.

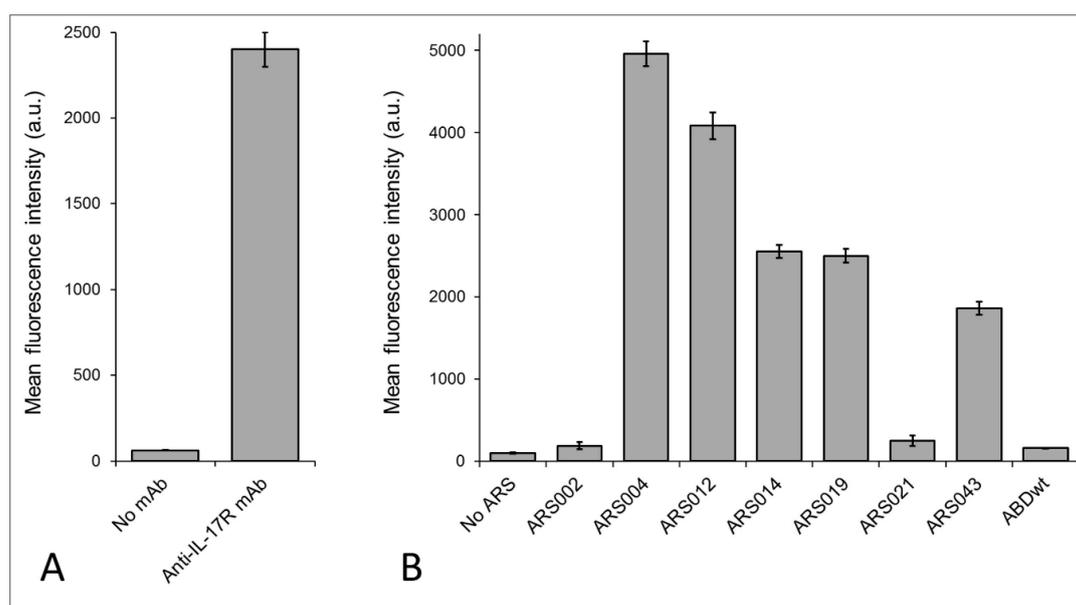


Figure 5. Binding of the ARS variants to human THP-1 cells. (A) The expression of IL-17RA on the surface of THP-1 cells was confirmed by anti-IL-17RA antibody. (B) For binding assay, 2.5×10^5 THP-1 cells were incubated with *in vivo* biotinylated His₆-ARS-TolA-AVI proteins or His₆-ABDwt-TolA-AVI negative control (10 μ g/mL) for 30 min at 4 °C. The cell-bound proteins were stained with streptavidin-PE for 30 min at 4 °C and analyzed by flow cytometry. Each bar represents the mean value \pm SD of three independent experiments.

The ARS variants confirmed to bind to THP-1 cells were used for a cell-surface competition experiment in which the ARS ligands competed with the human IL-17A cytokine for binding to IL-17RA-expressing cells. As shown in Figure S5, all five ARS variants substantially reduced binding of IL-17A to the surface of THP-1 cells.

2.5. Determination of Binding Kinetics and Affinities of the ARS Variants Using Human Cells

To investigate binding parameters of the five ARS variants that bound to human THP-1 cells, as seen in Figure 5, we used adherent IL-17RA-expressing human keratinocyte HaCaT cells [40]. Determination of binding affinities and rate-off kinetics in a real-time fluorescent mode was done using Ligand Tracer Green Line system upon detection of the bound ARS proteins to the cell surface by secondary Streptavidin-APC conjugate. To get binding curves, we used three concentrations of each ARS protein (3 nM, 30 nM, and 90 nM) and rate-off kinetics were evaluated after a saturation by measuring in medium lacking the ARS binders. As shown in Figure 6, a very slow release of the ARS014 and ARS019 variants from the cell surface was observed. This indicates high-affinity binding and corresponds to values calculated by Trace Drawer software as $K_d = 2$ nM for ARS014 and 0.7

nM for ARS019, respectively. Using this approach, we also estimated K_d value for ARS004 (1.2 nM), ARS012 (35 nM) and ARS043 (32 nM), respectively.

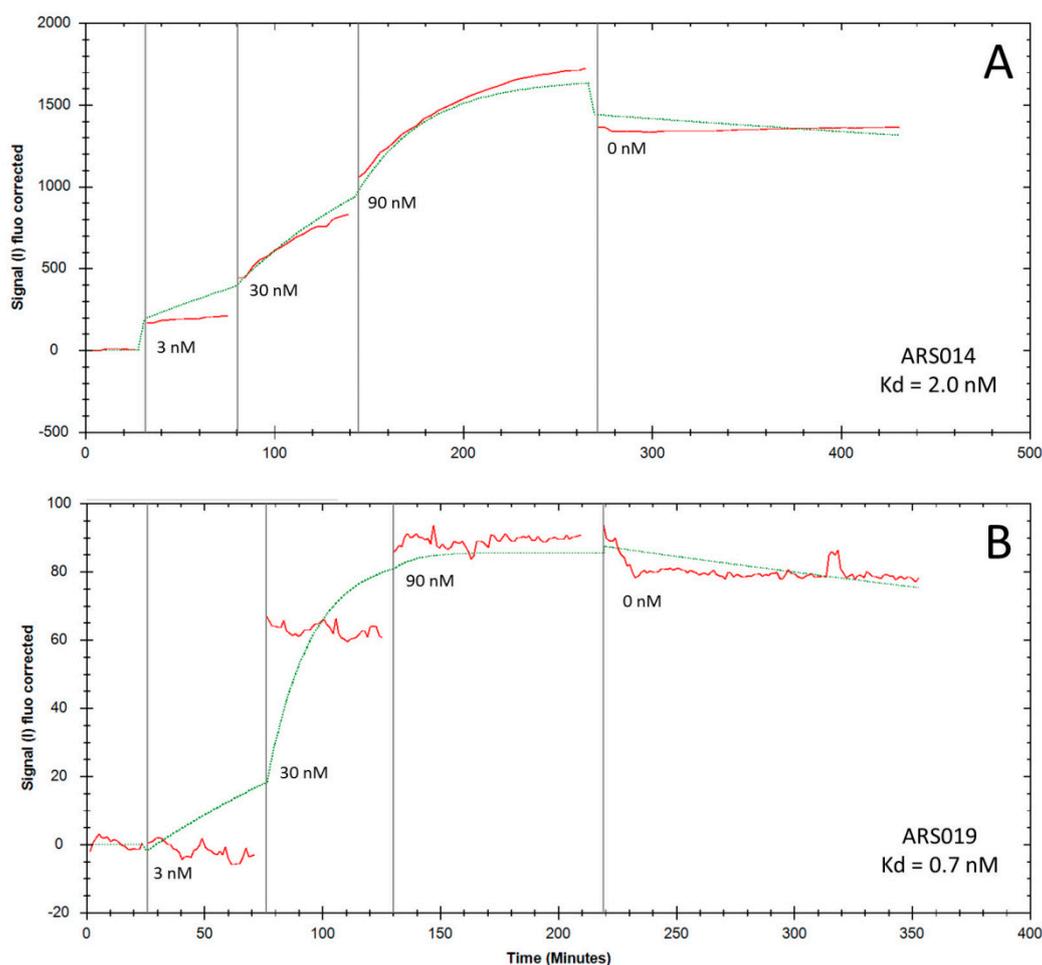


Figure 6. Binding of ARS014 (panel (A)) and ARS019 (panel (B)) to HaCaT cells tested by LigandTracer Green Line system. For binding assay, 10^6 cells were plated overnight on Petri dish and the next day, in vivo biotinylated His₆-ARS-Tola-AVI proteins were added into medium and incubated gradually at three different concentrations. Cell-bound proteins were stained with streptavidin-APC conjugate and the measured binding curve (red line) was analyzed using the TraceDrawer software (fitted curve, green line). Analysis of the binding affinities and rate-off kinetics indicated K_d values for ARS014 and ARS019 to be 2 nM and 0.7 nM, respectively.

2.6. Thermal Stability of the ARS Binding Proteins

For the analysis of thermal stability of the most promising ARS variants, we used the fluorescently-based thermal-shift assay using His₆-ARS-Tola-AVI fusion proteins. Melting temperatures (T_m) found for the ARS012, ARS014 and ARS043 variants are presented in the Figure 7. Thermal stability of the ARS019 and ARS 004 binding proteins was not determined, as the used experimental approach failed for these particular protein variants. In our previous studies [32,35,38] we measured the thermal stability of the parental ABD-wild type protein using the same approach and provided the T_m value 58 °C. Thus, our results suggest that the randomization of mutable residues of the ABD domain significantly affected the basic stability of the scaffold structure in the case of ARS012, ARS014, and ARS043.

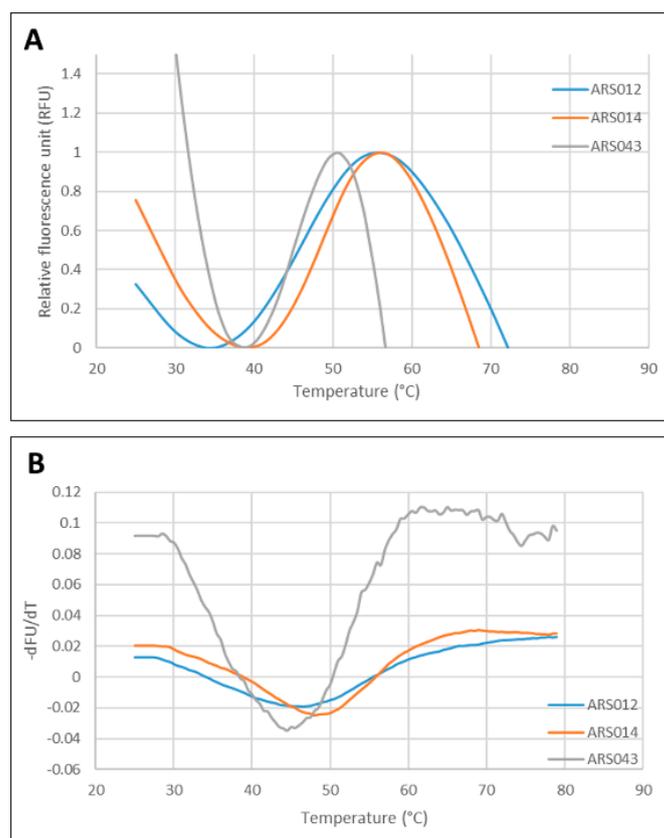


Figure 7. Analysis of thermal stability of the selected ARS binders. **(A)** Normalized thermal melting fluorescence curves of the His₆-ARS-TolA-AVI binders. **(B)** First derivative of fluorescence versus temperature of curves shown in the panel A. The melting point is given as the lowest point of the curve. All measurements were done in duplicate and averaged. Identified temperature melting (T_m) points are as follows: ARS012 T_m 45.5 °C; ARS014 T_m 48 °C; ARS043 T_m 44.5 °C.

2.7. Modeling of ARS-IL17RA Interactions

To gain a structural insight of the ARS-IL-17RA interactions, we performed modeling of the IL-17RA receptor in a complex with particular ARS variants. Therefore, we prepared homology models of the ARS binding proteins based on a three-helix bundle structure of the ABD. Then, we identified probable binding modes of the ARS binders found on the IL-17RA receptor by docking. For the ARS004, ARS012, ARS019, and ARS043 variants, binding modes are shown in Figure 8. In the case of the ARS004 variant, the most probable binding mode predicted by docking was located in the distal IL-17RA receptor domain, which is crucial for recognition by IL-17A cytokine, as shown by the crystal structure of the IL-17A/IL-17RA complex. This is well documented in Figure 8A where ARS004 binding protein clearly overlaps with IL-17A cytokine domains. For the variants ARS012 and ARS019, the same binding area on the IL-17RA domain as that found for ARS004 was predicted as the second most probable binding mode, as seen in Figure 8B,C. The same binding area on the receptor was identified by docking of the ARS043 binder as the 4th most probable binding mode, as shown in Figure 8D. These results correspond to data of competition ELISA tests where inhibitory effects of these ARS variants were demonstrated as seen in Figure 4, Figures S2 and S4.

Interestingly, docking of the ARS014 variant did not predict any binding into the identified common binding area of the receptor among 10 the most probable binding modes. However, this finding does not correspond to a demonstrated inhibitory effect of this ARS variant found in the competition ELISA tests, as seen in Figure 4, Figures S2 and S4. The ARS014 variant differs from other analyzed ARS proteins by a double deletion in positions 35–36 of the ABD sequence as shown in Table 1. This could lead to an increased probability that the used homology model does not reflect

the equilibrium structure of the binding protein. Therefore, we performed further modeling using molecular dynamics simulations looking for structural consequences of the specific combinations of amino acid alterations. Molecular dynamics simulation of the ARS004 indicates that the structure of this variant remains similar to that of an initial homology model keeping the three-helix bundle conformation of the parental ABD template. This structure we used for molecular docking to the IL-17RA. This analysis predicted the same binding mode as found for the initial unrelaxed homology model. To validate the docking prediction, we studied a possible rearrangement of the ARS004/IL-17RA complex by means of molecular dynamics. Our results supported stability of the binding mode, which was predicted by docking as seen in Figure 9A. Following this approach, we performed the molecular dynamics of the ARS014 binding protein and identified a significant structural change of the C-terminal helix resulting in a perpendicular orientation of the helix in contrast to the initial parallel orientation found in other analyzed ARS variants. This structure was used for docking to the IL-17RA. This modeling approach led to the identification of the third most probable binding mode occupying the common binding area of the IL-17RA, as seen in Figure 9B. Molecular dynamics simulation of the ARS014/IL-17RA complex revealed that both interacting interfaces undergo a mutual structural rearrangement, shown in Figure 9C, leading to a larger interacting area resulting in an increased binding affinity (K_d 2 nM) as measured experimentally and presented in Figure 6A.

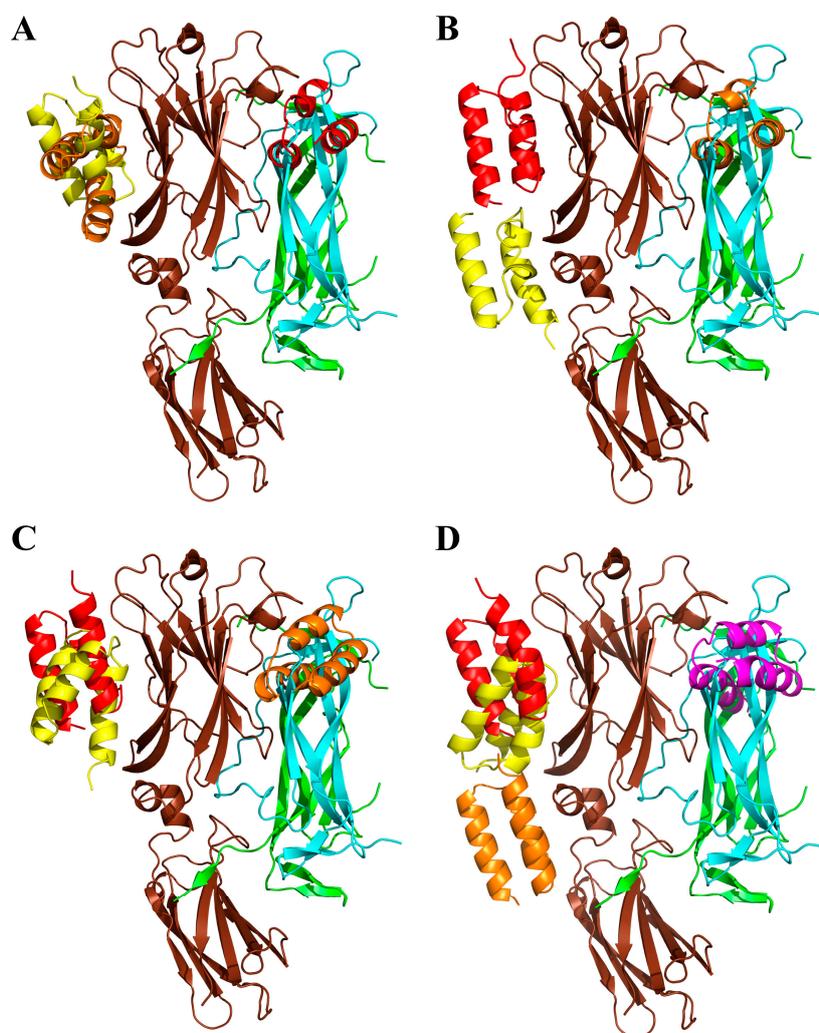


Figure 8. Modeling of ARS/IL-17RA interactions by docking. Summary of the first three poses of the ARS004 (A), ARS012 (B), ARS019 (C), and four poses of the ARS043 (D) binding to the complex of IL-17RA (brown) and dimer of human IL-17A (green/cyan), in decreasing predicted order of probability demonstrated in red (the most probable), orange, yellow and magenta, respectively.

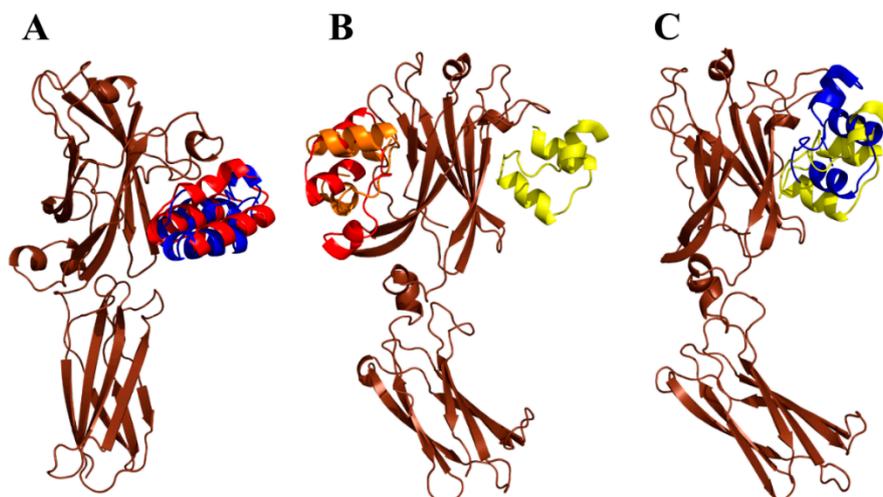


Figure 9. Structural effect of amino acid alterations in the ABD scaffold. (A) The most probable pose of the ARS004/IL-17RA interaction obtained by flexible side chain docking (red, see also Figure 7A) compared to the structure relaxed by 100 ns molecular dynamics simulation (blue). (B) Modeling of the ARS014/IL-17RA interaction by docking. The initial geometry of ARS014 was obtained from a 1 μ s molecular dynamics simulation. Summary of the first three poses of ARS014 binding to the IL-17RA (brown) is shown in decreasing predicted order of probability demonstrated in red (the most probable), orange, and yellow, respectively. (C) The third most probable pose (yellow) of the ARS014/IL-17RA interaction compared to the structure relaxed by 100 ns molecular dynamics simulation (blue).

2.8. Immunomodulatory Potential of the ARS Binding Proteins

To study an immunomodulatory potential of the particular ARS protein variants, we used normal human skin fibroblast cell line CCD-1070Sk, which has been previously described to be suitable for testing of the immunosuppressive potential of soluble IL-17 receptor mutants [29]. As a first step, we measured secretion of Gro- α (CXCL-1) released by CCD-1070Sk cells upon the activation by IL-17 cytokine using ELISA. This chemokine was significantly present in the cell medium supernatants after 6 h of activation by IL-17A, but the most suitable time period was found to be between 15 and 30 h after the activation, where levels of the secreted protein reached maximum values as seen in Figure S6. Therefore, we activated CCD-1070Sk cells by IL-17A for 24 h in the presence or absence of the five selected ARS protein variants and measured levels of secretion of the Gro- α in cell supernatants. Results of these experiments summarized in Figure 10 suggested the immunosuppressive potential for ARS004, ARS014, ARS019, and ARS043, where the inhibition of secretion of the chemokine was demonstrated. Contrary that, ARS012 protein binder did not exhibit any inhibitory function.

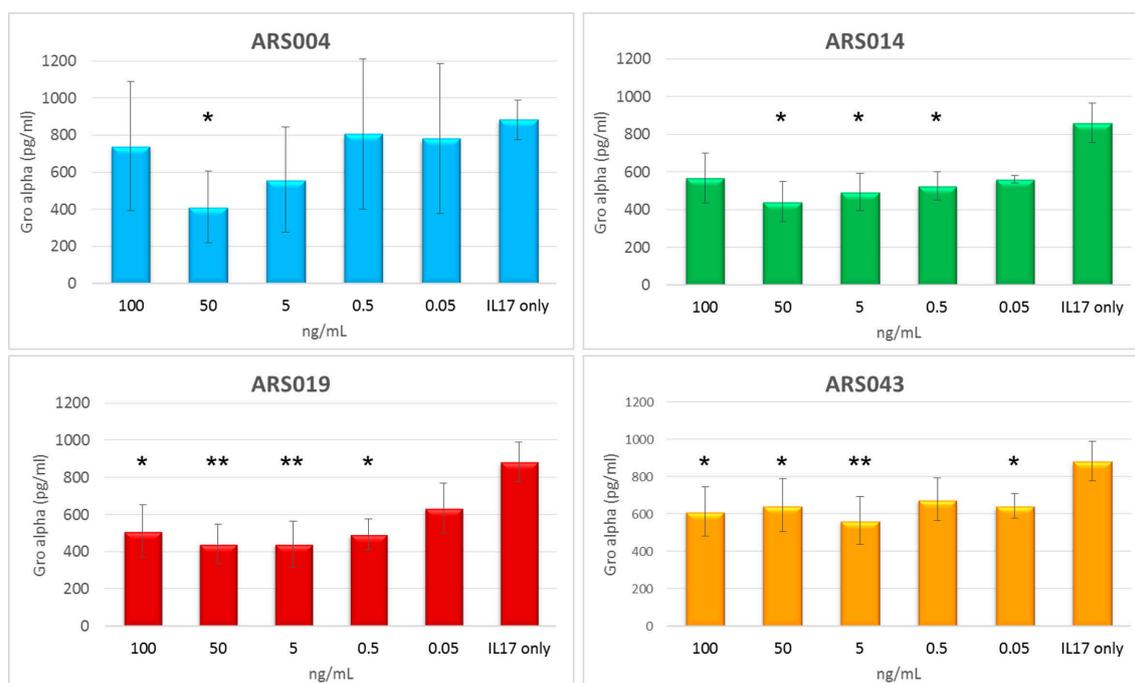


Figure 10. Test of immunomodulatory effect of the ARS ligands. The His₆-ARS-TolA-AVI fusion proteins were added in different concentrations to medium containing IL-17A cytokine. As a control, medium with cytokine but without the ARS proteins was used (IL17 only). After 24 h, levels of Gro- α (CXCL1) secreted by CCD-1070Sk cells were measured by ELISA. Each bar represents the mean value \pm SD of four (ARS019 and ARS043) or two (ARS004 and ARS014) independent experiments. Significant differences between mean values of the control (IL17 only) and the samples are shown (*, $p < 0.05$; **, $p < 0.01$; analysis of variance (ANOVA)).

3. Discussion

To interfere with IL-17-driven immunomodulation via IL-17RA-mediated cell signaling, we used a non-immunoglobulin approach. Recently we demonstrated that albumin-binding domain-derived library was successfully used for the generation of immunosuppressive binding proteins targeted to IL-23 cytokine [38] and for the development of IL-23R-targeted antagonists [35]. In these studies, we used our own concept of the highly complex ABD-derived library in which randomization of 11 residues of helix 2 and helix 3 of the ABD scaffold disrupts a parental high-affinity binding to human serum albumin [32] but also eliminates a set of crucial residues of the known human T- and B-cell epitopes carried by the parental non-mutated ABD wild-type protein [38,41].

To target the IL-17RA, soluble as well as refolded bacterial products of the extracellular receptor domains were used as capture proteins for ribosome display selection. We demonstrate that both protein variants can be used for the selection of high-affinity binders. Interestingly, the ARU collection of binders of the refolded IL-17 receptor provided variants identical, or of a high sequence similarity (1–2 amino acid alteration), to those found in the ARS protein library generated with the soluble IL-17RA. Yet the ARS library of selected variants seems to be more complex by the presence of several unique clones absent in the ARU collection. A high correlation between both libraries is rather surprising and underlines the high efficiency of ribosome display selection. Such comparison of independent selections of non-IgG binding proteins targeted to different forms of the same protein target has not been described for other known protein scaffold libraries.

Among 7 sequentially unrelated families identified by alignment and clustering, five of them are of a high interest as those represent blockers of cell-surface IL-17RA. Among them, ARS014 group is important as this family of 7 variants is formed by 5 different protein forms. As ARS014 representative belongs to the best blocking candidates, each member of this group should be analyzed

for its immunosuppressive potential. Contrary that, family of ARS004 of 18 representatives contains only 4 sequence variants, as the majority of clones is redundant. Even higher redundancy was found in the ARS012 sequence group, while families of ARS019 and ARS043 are formed by a single variant. Interestingly, only these two family representatives lack deletions in the ABD sequence, as the ARS004 and ARS012 miss the residue 23N and ARS014 is characterized by a double 35/36 deletion gap followed by the residue 37P. This unique combination alters the parental ABD three-helix bundle scaffold to a structurally more variable moiety that complicates modeling by docking. Paradoxically, this relaxed conformation may well accommodate to its receptor counterpart, providing an increased ligand stability, supported also by the highest thermal stability among the five ARS blocking candidates, and by a high binding affinity. However, ARS ligands stability is, in a broader context, significantly lower in comparison to ILP or REX immunosuppressive binders [35,38]. This might be due to the presence of proline residues found in the randomized positions of all five blocking ARS variants, thus changing the local conformation of the protein backbone or breaking the optimal three-helical structure.

Prediction of binding areas on the IL-17RA surface by docking ascribed a probable blocking potential to all five ARS ligands, yet for the ARS014 variant only upon the relaxation of its structure. The ARS004 protein was predicted as the most promising inhibitor of the cytokine IL-17A binding to its cognate receptor. This correlates with competition ELISA data but it is also strongly supported by cell-surface competition binding test on THP-1 cells and by the strong binding affinity estimated by LigandTracer on HaCaT keratinocytes. Slow dissociation of the ARS004 from the cell-surface receptor significantly contributes to the observed immunosuppressive effect on normal human IL-17A-activated skin fibroblasts. These cells were very efficiently suppressed in secretion of Gro- α by the presence of ARS014 and ARS019 variants in cell medium. This fact correlates very well with a slow dissociation of both proteins blockers from the HaCaT cell surface. In addition, an inhibitory function for both these variants was predicted by docking as highly probable, i.e., as the second (ARS019) and third (ARS014) most probable binding areas overlapping with the region known to be recognized by IL-17A [42]. Interestingly, ARS012 competed with IL-17A in vitro as shown by ELISA, as seen in Figure 4, and THP-1 cell-surface competition binding assay, shown in Figure S5, while its immunosuppressive potential has not been demonstrated in normal human skin fibroblasts. As ARS012 inhibitory potential on activated CCD-1071Sk cells is not conclusive and ARS043 exerts only a mild suppressing potential, variants ARS004, ARS014 and ARS019 are the best candidates for further development of IL-17R antagonists. However, their anti-inflammatory potential needs to be yet verified in vivo.

Although the IL-23/Th17 pro-inflammatory axis is closely linked to development of psoriasis, psoriatic arthritis and rheumatoid arthritis, a substantial role for IL-17A/F cytokine and IL-17RA in intestinal inflammation such as inflammatory bowel disease and Crohn's disease has been documented [43,44]. Recently, we described the generation of unique strains of *Lactococcus lactis* that can produce and secrete ABD-derived ILP proteins, blocking the function of human IL-23 cytokine [45]. The ILP-producing *L. lactis* cells can be used as in vivo tolerable probiotic bioreactors for the production and delivery of anti-inflammatory agents during the intestinal inflammation. In this context, a novel class of anti-IL-17RA-targeted ABD-derived blockers can be used for the development of ARS-producing *L. lactis* strains useful for in vivo suppression of experimentally induced colitis.

Anti-IL-17A inhibitors play a substantial role in development of anti-cancer drugs for colorectal cancer. Elevated levels of IL-23, IL-17, and IL-6 in early stages of colorectal cancer have been associated with adverse prognosis and more aggressive disease [46]. IL-17A is also associated with development of skin cancer via STAT3-mediating signaling in tumor and stromal cells, thus stimulating the penetration of myeloid cells into tumor environment [47,48]. Generation of non-IgG protein blockers of IL-17A-mediated signaling is, therefore, a valuable alternative in anti-cancer drug development.

4. Materials and Methods

4.1. Antibodies, Recombinant Proteins and Detection Agents

Anti-human IL-17R rabbit polyclonal antibody (H-168 clone) was purchased from Santa Cruz Biotechnology Inc., Dallas, TX, USA. Goat anti-rabbit IgG-HRP conjugate was obtained from Abcam plc., Cambridge, UK. The monoclonal anti-poly-histidine-HRP antibody produced in mouse was obtained from Sigma-Aldrich, St. Louis, MO, USA. Rabbit polyclonal to human IL17A was obtained from Abcam plc., Cambridge, UK. Cy5-conjugated goat anti-rabbit IgG F(ab')₂ fragment was obtained from Jackson ImmunoResearch Laboratories, West Grove, PA, USA.

Recombinant human IL-17 RA/IL-17 R Fc Chimera was obtained from R&D Systems, Minneapolis, MN, USA. Human IL-17A was purchased from Cell Signaling Technology, Danvers, MA, USA. Streptavidin-phycoerythrin was purchased from eBioscience, San Diego, CA, USA. Streptavidin-HRP conjugate was obtained from Thermo Scientific, Rockford, IL, USA.

4.2. Cell Lines and Growth Conditions

Cell lines used in the study were human acute monocytic leukemia cell line THP-1 (ATCC[®] TIB-202), normal human skin fibroblast CCD-1070Sk (ATCC[®] CRL-2091, ATCC, Manassas, VA, USA.), and a spontaneously transformed aneuploid immortal keratinocyte cell line from adult human skin HaCaT (330493, CLS Cell Lines Service GmbH, Eppelheim, Germany). All cell lines were grown in DMEM medium (Sigma-Aldrich, St. Louis, MO, USA) supplemented with 10% fetal calf serum (FCS) (GIBCO, Grand Island, NY, USA) and antibiotic antimycotic solution (ATB) (Sigma-Aldrich, St. Louis, MO, USA).

4.3. Molecular Assembly and Production of Recombinant IL-17RA

For IL-17A receptor (accession #: BC011624) cloning, plasmid DNA (Source BioScience, 4053746) was used. DNA sequence coding for extracellular part of IL-17R (IL-17RAex cDNA, Leu33–Trp320, 287 amino acids) was amplified by PCR using forward primer IL17RAex-F-Nco-his ATTACCATGGGCAGCAGCCACCATCATCATCATCACAGCAGCGGCCTGCGACTCCTGGACCA CC and reverse primer IL17RAex-R-Bam ATATGGATCCTCACCACAGGGGCATGTAGTCCG. The resulted PCR product was cloned in vector pET-28b using restriction sites NcoI and BamHI. Protein was produced in *E. coli* SHuffle strain (SHuffle[®] T7 Express Competent *E. coli*, New England Biolabs, Ipswich, MA, USA). Bacterial cells were grown in LB broth with kanamycin (60 µg/L) at 30 °C, protein production was induced by adding 1 mM IPTG after the culture reached the density OD₆₀₀ = 0.6. Cells were cultivated for 4 h at 30 °C or overnight at 18 °C. Cultures were collected by centrifugation, sonicated in TN buffer (50 mM Tris, 150 mM NaCl, pH = 8.0), and the disrupted cells were spun down at 40,000× *g* for 20 min. Supernatant representing the cytosolic extract was used for purification of soluble protein using Ni-NTA. The pelleted inclusion bodies were dissolved in TN buffer containing 8 M urea (50 mM Tris, 150 mM NaCl, 8 M urea, pH = 8.0), purified on Ni-NTA agarose and eluted in EB buffer containing 4 M urea (50 mM Tris, 150 mM NaCl, 250 mM imidazol, 4 M urea, pH = 8.0). Soluble as well as refolded IL-17RA forms were tested in ELISA and used for ribosome display selection.

4.4. ABD Library Construction and Ribosome Display Selection

ABD-derived DNA library was generated as described previously [32]. The library was used for the selection of binders by ribosome display [35]. Pre-selection was performed in wells of Polysorp plate (NUNC, Roskilde, Denmark) coated with His₆-TolA-AVI (Δ ABD clone) followed by blocking with 3% BSA. Unbound ribosomal complexes were used for further selection steps. For the selection, wells of Polysorp plate were coated with bacterial recombinant soluble human IL-17RA receptor or with the receptor refolded from 4 M urea solution in coating buffer, followed by blocking with 3% BSA. After five-round ribosome display selection, transcribed DNA was inserted into pET-28b-TolA-AVI

vector by digestion with restriction endonucleases NcoI and XhoI [38] and a resulted plasmid library was used to transform *E. coli* TOP10 host cells.

4.5. Production of In Vivo Biotinylated Protein Binders

ARS binders were prepared in the form His₆-ARS/ARU-TolA-AVI fusion biotinylated proteins produced in *E. coli* BL21 (DE3) BirA strain. Bacterial cells were cultivated in LB medium containing kanamycin (60 µg/mL) and chloramphenicol (30 µg/mL) and for protein biotinylation, 50 µM d-biotin was added, prepared as 5 mM solution in 10 mM bicine buffer pH = 8.3. Protein production was induced by 1.5 mM IPTG after reaching the cell density OD₆₀₀ = 0.6. Culture was harvested 4 h after the induction, then sonicated in TN buffer, centrifuged and subsequently purified on a Ni-NTA-agarose column, finally eluted with 250 mM imidazole.

4.6. Screening of IL-17RA-Targeted Binders in ELISA

Polysorp plate (NUNC, Roskilde, Denmark) was coated by IL-17RA recombinant protein (10 µg/mL, produced in *E. coli* SHuffle strain) or 5 µg/mL human IL-17RA-IgG chimera (Recombinant Human IL-17 RA/IL-17 R Fc Chimera Protein, R&D Systems, Minneapolis, MN, USA) in coating buffer (100 mM bicarbonate/carbonate solution, pH = 9.6) at 7 °C overnight. The next day, the plate was washed by PBST (PBS buffer containing 0.05% Tween, pH = 7.4) and blocked by PBSTB (1% BSA in PBST). The samples of bacterial lysates in PBSTB or purified proteins were applied as a series of different dilutions in PBSTB and bound biotinylated ARS proteins were detected using streptavidin-HRP conjugate diluted in the same buffer 1:10,000 (Pierce, Rockford, IL, USA). Results were visualized by enzymatic reaction of HRP with OPD substrate (Sigma-Aldrich, St. Luis, MO, USA) in citrate buffer (3.31% sodium citrate tribasic dihydrate, phosphoric acid until pH = 5.0), reaction was stopped by 2 M sulfuric acid and absorbance at 492 nm was measured.

4.7. Sequence Analysis and Clustering of Selected ARS and ARU Variants

DNA constructs of all selected clones expressing full-length His₆-ARS-TolA-AVI proteins were sequenced. Multiple alignments of amino acid sequences of the ARS variants and the construction of the UPGMA-based similarity tree were performed using the MEGA5 software (Molecular Evolutionary Genetics Analysis, available online: <https://www.megasoftware.net>).

4.8. Modeling of ARS-IL17RA Interactions

The structure of studied ABD variants (ARS004, ARS012, ARS014, ARS019, and ARS043) was modeled using the MODELLER 9v14 suite of programs [49] based on the ABDwt structure (pdb id 1gjt [50]). Amino acid sequences of the ABD variants were aligned with the Clustal Omega program [51]. The structure of IL-17R was obtained from the available crystal structure of the IL-17/IL-17R complex (pdb id 4hsa [42]). The flexible side chain protein-protein docking was performed using a local copy of the ClusPro server [52,53]. The GBSA implicit solvation molecular dynamics simulations were prepared using the OpenMM Zephyr graphical interface [54] with the Amber96 force field, 2 fs time step, temperature 295 K, and water collisional interval of 0.01099 ps. The calculations were performed using the GPU accelerated version of gromacs program [55] collecting geometry every 10 ps.

4.9. Competition ELISA

Polysorp plate (NUNC, Roskilde, Denmark) was coated with recombinant IL-17RA (5 µg/mL, recombinant protein produced in *E. coli* SHuffle strain) or IL-17RA-IgG (Recombinant Human IL-17 RA/IL-17 R Fc Chimera Protein, R&D Systems, Minneapolis, MN, USA) in coating buffer at 7 °C overnight and the washed plates were blocked by PBSTB. Human interleukin IL-17A cytokine (Cell Signaling Technology, Danvers, MA, USA) at the constant concentration (10 nM) presented in

serially diluted ARS variants in PBSTB as competitors were added. Binding of IL-17A to IL-17RA was detected by a primary polyclonal rabbit anti-human IL-17 antibody (1:1000, Abcam plc., Cambridge, UK) and the secondary anti-rabbit antibody conjugated with HPR (1:2000, Abcam plc., Cambridge, UK).

4.10. Fluorescence-Based Thermal-Shift Assay

Protein samples (0.1 mg/mL) in PBS and $5 \times$ Sypro Orange dye (Sigma-Aldrich, St. Luis, MO, USA) were mixed in total volume of 25 μ L. Using the real-time PCR Detection System CFX96 Touch (Bio-Rad Laboratories, Hercules, CA, USA), the proteins were incubated in a thermal gradient from 25 to 80 °C with increments of 0.5 °C and with 30 s-hold intervals. The degree of protein unfolding was monitored by the FRET (fluorescence resonance energy transfer) channel that captured the spectral properties of Sypro Orange unfolded protein complexes (excitation wavelength \sim 470 nm and emission wavelength \sim 570 nm). The data were analyzed by the CFX Manager software and the melting temperatures were determined using the first derivative spectra.

4.11. Flow Cytometry

All binding assays were performed in HEPES buffered salt solution (HBSS buffer; 10 mM HEPES, pH 7.4, 140 mM NaCl, 5 mM KCl) complemented with 2 mM CaCl₂, 2 mM MgCl₂, 1% (*w/v*) glucose and 1% (*v/v*) FCS (cHBSS) in 96-well culture plates (TPP Techno Plastic Products AG, Trasadingen, Switzerland). For ARS binding assay, 2.5×10^5 cells were incubated in 50 mL of cHBSS with or without His₆-ARS-TolA-AVI clones or His₆-ABDwt-TolA-AVI negative control (10 mg/mL) for 30 min at 4 °C. The cells were washed with cHBSS and the cell-bound proteins were stained with streptavidin–phycoerythrin (1:400 dilution) for 30 min at 4 °C. Cells were washed, resuspended in 100 mL of HBSS and analyzed by flow cytometry in a BD LSR II instrument (BD Biosciences, San Jose, CA, USA) in the presence of 1 μ g/mL of Hoechst 33258. Data were analyzed by FlowJo software (Tree Star, Ashland, OR, USA) and appropriate gatings were used to exclude cell aggregates and dead cells. Binding data were deduced from the mean fluorescence intensities (MFI).

4.12. Binding of ARS Proteins to Human Cells Analyzed by LigandTracer Green Line System

HaCaT cells were seeded in a distinct area of the cell dish and were allowed to attach firmly to the surface for at least 24 h. In vivo biotinylated His₆-ARS-TolA-AVI clones were labeled with Alexa Fluor 488 for 30 min. The cell dish with 3 mL cell culture medium or PBS (for ARS043) was placed into the LigandTracer Green Line (Ridgeview Instruments AB, Uppsala, Sweden) and the difference between the fluorescence intensity of the target cell area and the area opposite to the target cells (background signal) was measured every 70 s by rotating the dish with a detection delay 5 s. After a baseline measurement (30 min), the ARS protein was added gradually in the three (ARS012, ARS014, ARS019, ARS043) or four (ARS043) increasing concentration (3, 10, 90 nM or 3, 10, 30, 70 nM). Each concentration was incubated until the saturation was obtained. Then, the dissociation of the ligand was recorded after replacing the incubation solution with 3 ml fresh medium or PBS. Binding curves were analyzed using the TraceDrawer 1.7.1. evaluation software. All ligand-receptor interactions were analyzed using the “one-to-one” model. For ARS043, signal levels were normalized to 0% at baseline level.

4.13. Testing of the Immunomodulatory Potential of ARS Ligands

For the assay, CCD-1070Sk cells (10^4) were seeded to 24 well plate. After 24 h, 20 ng/mL IL-17A cytokine alone or in the presence of His₆-ARS-TolA-AVI clones in different concentrations (100, 50, 5, 0.5 ng/mL) were added. After 6, 15, 24, 30, and 48 h, supernatants were collected and levels of Gro- α and IL-6 were measured by Human CXCL1/GRO α DuoSet (R&D Systems, Minneapolis, MN, USA).

4.14. Statistical Analysis

Results were expressed as the arithmetic mean \pm standard deviation (SD) of the mean. Statistical analysis was performed by one-way ANOVA followed by Dunnett's post-test, comparing all the samples with the control, using GraphPad Prism 6.0 (GraphPad Software, San Diego, CA, USA). Significant differences are indicated by asterisks (*, $p < 0.05$; **, $p < 0.01$).

5. Conclusions

Collectively, this work describes the generation of a collection of unique ABD-derived proteins called ARS ligands that recognize human IL-17RA receptor with a high-binding affinity. These ARS proteins inhibit binding of human IL-17A cytokine to its cognate cell membrane receptor in vitro and exhibit an immunosuppressive potential demonstrated by suppression of Gro- α secretion from IL-17A-activated CCD-1070Sk skin fibroblasts. These ligands can be used as high-affinity non-IgG probes and can be useful in development of anti-IL-17RA-targeted antagonists with a therapeutic potential.

Supplementary Materials: Supplementary materials can be found at <http://www.mdpi.com/1422-0067/19/10/3089/s1>.

Author Contributions: P.M. and R.O. designed the experiments. M.H., M.K., L.V. and H.P. performed the experiments and analyzed the data. H.P., M.K., M.M. and R.O. participated in experiments and manuscript preparation. J.Č. performed in silico modeling and docking. P.M. and P.A. designed the research project. P.M. wrote the paper. All authors read and approved the manuscript.

Funding: This work was supported by Czech Health Research Council, Ministry of Health of the Czech Republic (No. 16-27676A), by the Institutional Research Concept (RVO: 86652036) and by European Regional Development Fund [BIOCEV CZ.1.05/1.1.00/02.0109].

Acknowledgments: The authors thank Petra Kadlčáková for excellent experimental assistance.

Conflicts of Interest: The authors declare no conflict of interest.

References

1. Cua, D.J.; Sherlock, J.; Chen, Y.; Murphy, C.A.; Joyce, B.; Seymour, B.; Lucian, L.; To, W.; Kwan, S.; Churakova, T.; et al. Interleukin-23 rather than interleukin-12 is the critical cytokine for autoimmune inflammation of the brain. *Nature* **2003**, *421*, 744–748. [[CrossRef](#)] [[PubMed](#)]
2. Langrish, C.L.; Chen, Y.; Blumenschein, W.M.; Mattson, J.; Basham, B.; Sedgwick, J.D.; McClanahan, T.; Kastelein, R.A.; Cua, D.J. IL-23 drives a pathogenic T cell population that induces autoimmune inflammation. *J. Exp. Med.* **2005**, *201*, 233–240. [[CrossRef](#)] [[PubMed](#)]
3. Duerr, R.H.; Taylor, K.D.; Brant, S.R.; Rioux, J.D.; Silverberg, M.S.; Daly, M.J.; Steinhardt, A.H.; Abraham, C.; Rugeiro, M.; Griffiths, A.; et al. A genome-wide association study identifies IL23R as an inflammatory bowel disease gene. *Science* **2006**, *314*, 1461–1463. [[CrossRef](#)] [[PubMed](#)]
4. Oppmann, B.; Lesley, R.; Blom, B.; Timans, J.C.; Xu, Y.; Hunte, B.; Vega, F.; Yu, N.; Wang, J.; Singh, K.; et al. Novel p19 protein engages IL-12p40 to form a cytokine, IL-23, with biological activities similar as well as distinct from IL-12. *Immunity* **2000**, *13*, 715–725. [[CrossRef](#)]
5. Parham, C.; Chirica, M.; Timans, J.; Vaisberg, E.; Travis, M.; Cheung, J.; Pflanz, S.; Zhang, R.; Singh, K.P.; Vega, F.; et al. A receptor for the heterodimeric cytokine IL-23 is composed of IL-12Rbeta1 and a novel cytokine receptor subunit, IL-23R. *J. Immunol.* **2002**, *168*, 5699–5708. [[CrossRef](#)] [[PubMed](#)]
6. Zheng, Y.; Danilenko, D.M.; Valdez, P.; Kasman, I.; Eastham-Anderson, J.; Wu, J.; Ouyang, W. Interleukin-22, a T(H)17 cytokine, mediates IL-23-induced dermal inflammation and acanthosis. *Nature* **2007**, *445*, 648–651. [[CrossRef](#)] [[PubMed](#)]
7. Tang, C.; Chen, S.; Qian, H.; Huang, W. Interleukin-23: As a drug target for autoimmune inflammatory diseases. *Immunology* **2012**, *135*, 112–124. [[CrossRef](#)] [[PubMed](#)]
8. Dungan, L.S.; Mills, K.H. Caspase-1-processed IL-1 family cytokines play a vital role in driving innate IL-17. *Cytokine* **2011**, *56*, 126–132. [[CrossRef](#)] [[PubMed](#)]

9. Song, X.; Qian, Y. IL-17 family cytokines mediated signaling in the pathogenesis of inflammatory diseases. *Cell. Signal.* **2013**, *25*, 2335–2347. [[CrossRef](#)] [[PubMed](#)]
10. Iwakura, Y.; Ishigame, H.; Saijo, S.; Nakae, S. Functional specialization of interleukin-17 family members. *Immunity* **2011**, *34*, 149–162. [[CrossRef](#)] [[PubMed](#)]
11. Zou, W.; Restifo, N.P. T(H)17 cells in tumour immunity and immunotherapy. *Nat. Rev. Immunol.* **2010**, *10*, 248–256. [[CrossRef](#)] [[PubMed](#)]
12. Sutton, C.E.; Mielke, L.A.; Mills, K.H. IL-17-producing gammadelta T cells and innate lymphoid cells. *Eur. J. Immunol.* **2012**, *42*, 2221–2231. [[CrossRef](#)] [[PubMed](#)]
13. Tonini, A.; Gualtieri, B.; Panduri, S.; Romanelli, M.; Chiricozzi, A. A new class of biologic agents facing the therapeutic paradigm in psoriasis: Anti-IL-23 agents. *Expert Opin. Biol. Ther.* **2018**, *18*, 135–148. [[CrossRef](#)] [[PubMed](#)]
14. Papp, K.A.; Griffiths, C.E.; Gordon, K.; Lebwohl, M.; Szapary, P.O.; Wasfi, Y.; Chan, D.; Hsu, M.C.; Ho, V.; Ghislain, P.D.; et al. Long-term safety of ustekinumab in patients with moderate-to-severe psoriasis: Final results from 5 years of follow-up. *Br. J. Dermatol.* **2013**, *168*, 844–854. [[CrossRef](#)] [[PubMed](#)]
15. Leonardi, C.L.; Kimball, A.B.; Papp, K.A.; Yeilding, N.; Guzzo, C.; Wang, Y.; Li, S.; Dooley, L.T.; Gordon, K.B. PHOENIX 1 Study Investigators. Efficacy and safety of ustekinumab, a human interleukin-12/23 monoclonal antibody, in patients with psoriasis: 76-week results from a randomised, double-blind, placebo-controlled trial (PHOENIX 1). *Lancet* **2008**, *371*, 1665–1674. [[CrossRef](#)]
16. Traczewski, P.; Rudnicka, L. Briakinumab for the treatment of plaque psoriasis. *BioDrugs* **2012**, *26*, 9–20. [[CrossRef](#)] [[PubMed](#)]
17. Gordon, K.B.; Langley, R.G.; Gottlieb, A.B.; Papp, K.A.; Krueger, G.G.; Strober, B.E.; Williams, D.A.; Gu, Y.; Valdes, J.M. A phase III, randomized, controlled trial of the fully human IL-12/23 mAb briakinumab in moderate-to-severe psoriasis. *J. Investig. Dermatol.* **2012**, *132*, 304–314. [[CrossRef](#)] [[PubMed](#)]
18. Reich, K.; Armstrong, A.W.; Foley, P.; Song, M.; Wasfi, Y.; Randazzo, B.; Li, S.; Shen, Y.K.; Gordon, K.B. Efficacy and safety of guselkumab, an anti-interleukin-23 monoclonal antibody, compared with adalimumab for the treatment of patients with moderate to severe psoriasis with randomized withdrawal and retreatment: Results from the phase III, double-blind, placebo- and active comparator-controlled VOYAGE 2 trial. *J. Am. Acad. Dermatol.* **2017**, *76*, 418–431. [[PubMed](#)]
19. Langley, R.G.; Tsai, T.F.; Flavin, S.; Song, M.; Randazzo, B.; Wasfi, Y.; Jiang, J.; Li, S.; Puig, L. Efficacy and safety of guselkumab in patients with psoriasis who have an inadequate response to ustekinumab: Results of the randomized, double-blind, phase III NAVIGATE trial. *Br. J. Dermatol.* **2018**, *178*, 114–123. [[CrossRef](#)] [[PubMed](#)]
20. Papp, K.; Thaci, D.; Reich, K.; Riedl, E.; Langley, R.G.; Krueger, J.G.; Gottlieb, A.B.; Nakagawa, H.; Bowman, E.P.; Mehta, A.; et al. Tildrakizumab (MK-3222), an anti-interleukin-23p19 monoclonal antibody, improves psoriasis in a phase IIb randomized placebo-controlled trial. *Br. J. Dermatol.* **2015**, *173*, 930–939. [[CrossRef](#)] [[PubMed](#)]
21. Reich, K.; Papp, K.A.; Blauvelt, A.; Tyring, S.K.; Sinclair, R.; Thaci, D.; Nograles, K.; Mehta, A.; Cichanowitz, N.; Li, Q.; et al. Tildrakizumab versus placebo or etanercept for chronic plaque psoriasis (reSURFACE 1 and reSURFACE 2): Results from two randomised controlled, phase 3 trials. *Lancet* **2017**, *390*, 276–288. [[CrossRef](#)]
22. Krueger, J.G.; Ferris, L.K.; Menter, A.; Wagner, F.; White, A.; Visvanathan, S.; Lalovic, B.; Aslanyan, S.; Wang, E.E.; Hall, D.; et al. Anti-IL-23A mAb BI 655066 for treatment of moderate-to-severe psoriasis: Safety, efficacy, pharmacokinetics, and biomarker results of a single-rising-dose, randomized, double-blind, placebo-controlled trial. *J. Allergy Clin. Immunol.* **2015**, *136*, 116–124. [[CrossRef](#)] [[PubMed](#)]
23. Hueber, W.; Patel, D.D.; Dryja, T.; Wright, A.M.; Koroleva, I.; Bruin, G.; Antoni, C.; Draelos, Z.; Gold, M.H.; Psoriasis Study, G.; et al. Effects of AIN457, a fully human antibody to interleukin-17A, on psoriasis, rheumatoid arthritis, and uveitis. *Sci. Transl. Med.* **2010**, *2*, 52ra72. [[CrossRef](#)] [[PubMed](#)]
24. Patel, N.U.; Vera, N.C.; Shealy, E.R.; Wetzel, M.; Feldman, S.R. A Review of the Use of Secukinumab for Psoriatic Arthritis. *Rheumatol. Ther.* **2017**, *4*, 233–246. [[CrossRef](#)] [[PubMed](#)]
25. Lubrano, E.; Perrotta, F.M. Secukinumab for ankylosing spondylitis and psoriatic arthritis. *Ther. Clin. Risk Manag.* **2016**, *12*, 1587–1592. [[CrossRef](#)] [[PubMed](#)]

26. Mease, P.J.; van der Heijde, D.; Ritchlin, C.T.; Okada, M.; Cuchacovich, R.S.; Shuler, C.L.; Lin, C.Y.; Braun, D.K.; Lee, C.H.; Gladman, D.D.; et al. Ixekizumab, an interleukin-17A specific monoclonal antibody, for the treatment of biologic-naive patients with active psoriatic arthritis: Results from the 24-week randomised, double-blind, placebo-controlled and active (adalimumab)-controlled period of the phase III trial SPIRIT-P1. *Ann. Rheum. Dis.* **2017**, *76*, 79–87. [[PubMed](#)]
27. Blair, H.A. Brodalumab: A Review in Moderate to Severe Plaque Psoriasis. *Drugs* **2018**, *78*, 495–504. [[CrossRef](#)] [[PubMed](#)]
28. Papp, K.A.; Gordon, K.B.; Langley, R.G.; Lebwohl, M.G.; Gottlieb, A.B.; Rastogi, S.; Pillai, R.; Israel, R.J. Impact of previous biologic use on the efficacy and safety of brodalumab and ustekinumab in patients with moderate-to-severe plaque psoriasis: Integrated analysis of the randomized controlled trials AMAGINE-2 and AMAGINE-3. *Br. J. Dermatol.* **2018**, *179*, 320–328. [[CrossRef](#)] [[PubMed](#)]
29. Zaretsky, M.; Etzyoni, R.; Kaye, J.; Sklair-Tavron, L.; Aharoni, A. Directed evolution of a soluble human IL-17A receptor for the inhibition of psoriasis plaque formation in a mouse model. *Chem. Biol.* **2013**, *20*, 202–211. [[CrossRef](#)] [[PubMed](#)]
30. Skrlec, K.; Strukelj, B.; Berlec, A. Non-immunoglobulin scaffolds: A focus on their targets. *Trends Biotechnol.* **2015**, *33*, 408–418. [[CrossRef](#)] [[PubMed](#)]
31. Martin, H.L.; Bedford, R.; Heseltine, S.J.; Tang, A.A.; Haza, K.Z.; Rao, A.; McPherson, M.J.; Tomlinson, D.C. Non-immunoglobulin scaffold proteins: Precision tools for studying protein-protein interactions in cancer. *New Biotechnol.* **2018**, *45*, 28–35. [[CrossRef](#)] [[PubMed](#)]
32. Ahmad, J.N.; Li, J.; Biedermannova, L.; Kuchar, M.; Sipova, H.; Semeradtova, A.; Cerny, J.; Petrokova, H.; Mikulecky, P.; Polinek, J.; et al. Novel high-affinity binders of human interferon gamma derived from albumin-binding domain of protein G. *Proteins* **2012**, *80*, 774–789. [[CrossRef](#)] [[PubMed](#)]
33. Nilvebrant, J.; Astrand, M.; Lofblom, J.; Hober, S. Development and characterization of small bispecific albumin-binding domains with high affinity for ErbB3. *Cell. Mol. Life Sci.* **2013**, *70*, 3973–3985. [[CrossRef](#)] [[PubMed](#)]
34. Nilvebrant, J.; Hober, S. The albumin-binding domain as a scaffold for protein engineering. *Comput. Struct. Biotechnol. J.* **2013**, *6*, e201303009. [[CrossRef](#)] [[PubMed](#)]
35. Kuchar, M.; Vankova, L.; Petrokova, H.; Cerny, J.; Osicka, R.; Pelak, O.; Sipova, H.; Schneider, B.; Homola, J.; Sebo, P.; et al. Human interleukin-23 receptor antagonists derived from an albumin-binding domain scaffold inhibit IL-23-dependent ex vivo expansion of IL-17-producing T-cells. *Proteins* **2014**, *82*, 975–989. [[CrossRef](#)] [[PubMed](#)]
36. Mareckova, L.; Petrokova, H.; Osicka, R.; Kuchar, M.; Maly, P. Novel binders derived from an albumin-binding domain scaffold targeting human prostate secretory protein 94 (PSP94). *Protein Cell* **2015**, *6*, 774–779. [[CrossRef](#)] [[PubMed](#)]
37. Zadavec, P.; Mareckova, L.; Petrokova, H.; Hodnik, V.; Perisic Nanut, M.; Anderluh, G.; Strukelj, B.; Maly, P.; Berlec, A. Development of Recombinant *Lactococcus lactis* Displaying Albumin-Binding Domain Variants against Shiga Toxin 1 B Subunit. *PLoS ONE* **2016**, *11*, e0162625. [[CrossRef](#)] [[PubMed](#)]
38. Krizova, L.; Kuchar, M.; Petrokova, H.; Osicka, R.; Hlavnickova, M.; Pelak, O.; Cerny, J.; Kalina, T.; Maly, P. p19-targeted ABD-derived protein variants inhibit IL-23 binding and exert suppressive control over IL-23-stimulated expansion of primary human IL-17+ T-cells. *Autoimmunity* **2017**, *50*, 102–113. [[CrossRef](#)] [[PubMed](#)]
39. Yao, Z.; Spriggs, M.K.; Derry, J.M.; Strockbine, L.; Park, L.S.; VandenBos, T.; Zappone, J.D.; Painter, S.L.; Armitage, R.J. Molecular characterization of the human interleukin (IL)-17 receptor. *Cytokine* **1997**, *9*, 794–800. [[CrossRef](#)] [[PubMed](#)]
40. Cho, K.A.; Suh, J.W.; Lee, K.H.; Kang, J.L.; Woo, S.Y. IL-17 and IL-22 enhance skin inflammation by stimulating the secretion of IL-1beta by keratinocytes via the ROS-NLRP3-caspase-1 pathway. *Int. Immunol.* **2012**, *24*, 147–158. [[CrossRef](#)] [[PubMed](#)]
41. Goetsch, L.; Haeuw, J.F.; Champion, T.; Lacheney, C.; N'Guyen, T.; Beck, A.; Corvaia, N. Identification of B- and T-cell epitopes of BB, a carrier protein derived from the G protein of *Streptococcus* strain G148. *Clin. Diagn. Lab. Immunol.* **2003**, *10*, 125–132. [[CrossRef](#)] [[PubMed](#)]
42. Liu, S.; Song, X.; Chrnyk, B.A.; Shanker, S.; Hoth, L.R.; Marr, E.S.; Griffor, M.C. Crystal structures of interleukin 17A and its complex with IL-17 receptor A. *Nat. Commun.* **2013**, *4*, 1888. [[CrossRef](#)] [[PubMed](#)]

43. Sarra, M.; Pallone, F.; Macdonald, T.T.; Monteleone, G. IL-23/IL-17 axis in IBD. *Inflamm. Bowel Dis.* **2010**, *16*, 1808–1813. [[CrossRef](#)] [[PubMed](#)]
44. West, N.R.; McCuaig, S.; Franchini, F.; Powrie, F. Emerging cytokine networks in colorectal cancer. *Nat. Rev. Immunol.* **2015**, *15*, 615–629. [[CrossRef](#)] [[PubMed](#)]
45. Skrlec, K.; Zadavec, P.; Hlavnickova, M.; Kuchar, M.; Vankova, L.; Petrokova, H.; Krizova, L.; Cerny, J.; Berlec, A.; Maly, P. p19-Targeting ILP Protein Blockers of IL-23/Th-17 Pro-Inflammatory Axis Displayed on Engineered Bacteria of Food Origin. *Int. J. Mol. Sci.* **2018**, *19*, 1933. [[CrossRef](#)] [[PubMed](#)]
46. Schetter, A.J.; Nguyen, G.H.; Bowman, E.D.; Mathe, E.A.; Yuen, S.T.; Hawkes, J.E.; Croce, C.M.; Leung, S.Y.; Harris, C.C. Association of inflammation-related and microRNA gene expression with cancer-specific mortality of colon adenocarcinoma. *Clin. Cancer Res.* **2009**, *15*, 5878–5887. [[CrossRef](#)] [[PubMed](#)]
47. Wang, L.; Yi, T.; Zhang, W.; Pardoll, D.M.; Yu, H. IL-17 enhances tumor development in carcinogen-induced skin cancer. *Cancer Res.* **2010**, *70*, 10112–10120. [[CrossRef](#)] [[PubMed](#)]
48. He, D.; Li, H.; Yusuf, N.; Elmetts, C.A.; Athar, M.; Katiyar, S.K.; Xu, H. IL-17 mediated inflammation promotes tumor growth and progression in the skin. *PLoS ONE* **2012**, *7*, e32126. [[CrossRef](#)] [[PubMed](#)]
49. Sali, A.; Blundell, T.L. Comparative protein modelling by satisfaction of spatial restraints. *J. Mol. Biol.* **1993**, *234*, 779–815. [[CrossRef](#)] [[PubMed](#)]
50. Johansson, M.U.; Frick, I.M.; Nilsson, H.; Kraulis, P.J.; Hober, S.; Jonasson, P.; Linhult, M.; Nygren, P.A.; Uhlen, M.; Bjorck, L.; et al. Structure, specificity, and mode of interaction for bacterial albumin-binding modules. *J. Biol. Chem.* **2002**, *277*, 8114–8120. [[CrossRef](#)] [[PubMed](#)]
51. Sievers, F.; Wilm, A.; Dineen, D.; Gibson, T.J.; Karplus, K.; Li, W.; Lopez, R.; McWilliam, H.; Remmert, M.; Soding, J.; et al. Fast, scalable generation of high-quality protein multiple sequence alignments using Clustal Omega. *Mol. Syst. Biol.* **2011**, *7*, 539. [[CrossRef](#)] [[PubMed](#)]
52. Kozakov, D.; Beglov, D.; Bohnuud, T.; Mottarella, S.E.; Xia, B.; Hall, D.R.; Vajda, S. How good is automated protein docking? *Proteins* **2013**, *81*, 2159–2166. [[CrossRef](#)] [[PubMed](#)]
53. Kozakov, D.; Brenke, R.; Comeau, S.R.; Vajda, S. PIPER: An FFT-based protein docking program with pairwise potentials. *Proteins* **2006**, *65*, 392–406. [[CrossRef](#)] [[PubMed](#)]
54. Eastman, P.; Pande, V.S. OpenMM: A Hardware Independent Framework for Molecular Simulations. *Comput. Sci. Eng.* **2015**, *12*, 34–39. [[CrossRef](#)] [[PubMed](#)]
55. Van Der Spoel, D.; Lindahl, E.; Hess, B.; Groenhof, G.; Mark, A.E.; Berendsen, H.J. GROMACS: Fast, flexible, and free. *J. Comput. Chem.* **2005**, *26*, 1701–1718. [[CrossRef](#)] [[PubMed](#)]



© 2018 by the authors. Licensee MDPI, Basel, Switzerland. This article is an open access article distributed under the terms and conditions of the Creative Commons Attribution (CC BY) license (<http://creativecommons.org/licenses/by/4.0/>).

8. Supplementary data

Validation report for ELISA test for detection of antibodies against rekombinant adhesins K88, K99, 987P and F41 and heat-labile toxin from *Escherichia coli*, toxins alpha, beta, beta2 and epsilon from *Clostridium perfringens* and toxin A from *Clostridium difficile*

Table of contents:

1.	Introduction.....	2
2.	Measuring range.....	2
3.	List of abbreviations and definitions.....	2
4.	Working team.....	2
5.	Process description.....	2
6.	Methodology, tools and equipment.....	3
7.	Description of the ELISA assay.....	4
8.	Tested parameters and criteria of acceptability.....	6
9.	Evaluation of validation parameters	7
9.1	Specificity	7
9.2	Precision.....	11
9.3	Linearity	20
11.	Evaluation of Validation	40
12.	Revalidation	40

Study Code:

Validation Report

1. Introduction

The validation was performed according to the directive EMEA - CVMP / VICH / 590/98 and CVMP / VICH / 591/98. The ELISA assay was validated for detection of antibodies against recombinant adhesins and heat-labile toxin from *Escherichia coli* and toxins from *Clostridium perfringens* and *Clostridium difficile*.

2. Measuring range

The validation of the method confirms that the method is suitable for verifying the efficacy of the product containing inactivated components - adhesins and recombinant heat-labile toxin of *Escherichia coli* and toxins of *Clostridium perfringens* and *Clostridium difficile*.

The scope of the validation is given by internal regulations documents, based on the instructions of state authorities and the European Medicines Agency EMA. Within this validation following parameters will be tested - the precision and accuracy of presented methodology, repeatability, reproducibility, linearity, range and selectivity.

3. List of abbreviations and definitions

Abbreviations	Definitions
RD	Recording Documentation
QA	Quality Assurance
SOP	Standard Operating Procedure
GMP	Good Manufacturing Practice
ELISA	Enzyme-Linked ImmunoSorbent Assay
LTB	Beta subunit of heat-labile toxin <i>E. coli</i>
TS	Tested serum
PS	Positive serum
NS	Negative serum
CV	Variation Coefficient
SD	Standard Deviation
ANOVA	Analysis of Variance
CPA	recombinant part of the toxin Alfa
CPB	recombinant toxin Beta
CPB2	recombinant toxin Beta 2
ETX	recombinant toxin Epsilon
TcdA	recombinant part of the toxin A

4. Working team

QA:

Head: RNDr. Petr Malý, CSc.

Members: Ing. Hana Petroková, PhD., Mgr. Lucie Marečková

5. Process description

The measurements were carried out in the Laboratory of ligand engineering at the Institute of Biotechnology AS CR.

6. Methodology, tools and equipment

The procedures were performed according to approved regulatory documentation:
RMSOP103SDX2120 – Preparation of reagents for ELISA,
RMSOP015SDX207x - Processing of the samples for serological tests.

Equipment:

Cooling device with a temperature range of 5 ± 3 ° C

Freezing device with a temperature below - 20 ° C

Spectrophotometer for measuring in microtiter plates ClarioStar

Microplate washer (Hydroflex- Schëller)

Shaker of microplates

Vortex

Laboratory with the room temperature of 20 ± 5 ° C (referred to room temperature)

Materials:

96 well microtiter plates with a flat bottom

Caps or protective adhesive film on microtiter plate

One channel and multichannel pipettes with adjustable volume

Tips

Vials of 0.5 and 1.5 ml

Stands for the vials and test tubes

Glass bottle including its sealing

A vessel for ice

Wood pulp

Stopwatch

Working protective equipment

Antigens for ELISA:

- recombinant adhesin K88 *E. coli*, 2,5 µg/ml
- recombinant adhesin K99 *E. coli*, 10 µg/ml
- recombinant adhesin 987P *E. coli*, 5 µg/ml
- recombinant adhesin F41 *E. coli*, 5 µg/ml
- recombinant part of the heat-labile toxin (LTB) *E. coli*, 5 µg/ml
- recombinant part of the toxin Alfa (CPA) *C. perfringens*, 4 µg/ml
- recombinant toxin Beta (CPB) *C. perfringens*, 5 µg/ml
- recombinant toxin Beta 2 (CPB2) *C. perfringens*, 2 µg/ml
- recombinant toxin Epsilon (ETX) *C. perfringens*, 3 µg/ml
- recombinant part of the toxin A (TcdA) *C. difficile*, 5 µg/ml

Negative standard mouse serum without specific antibodies against above mentioned antigens (Dyntec spol. s r. o.)

Positive standard mouse serum with specific antibodies against above mentioned antigens (Dyntec spol. s r. o.)

Secondary goat anti-mouse antibody conjugated to horseradish peroxidase

Substrate solution containing tetramethylbenzidine (TMB)

Listed ingredients (PS, NS, conjugate, adhesins and toxins) were aliquoted into microtubes and stored in a freezer at - 20 ° C. During dilution and handling, these ingredients were kept on ice.

Solutions:

Binding buffer, pH 9.6

Washing solution containing 0.05% Tween 20

Dilution and blocking solution containing 0.05% Tween 20 and 1% BSA

Substrate solution was stored at 5 ± 3 ° C

Sulfuric acid solution with a molar concentration of 2 mol / l

Evaluation software:

Software for the evaluation of spectrophotometric data - MARS

Software for the evaluation of biological tests Combistats

Software for the evaluation of validation - Excel 2016

7. Description of the ELISA assay
--

Vaccine efficacy is declared by the determination of antibodies against different recombinant adhesins and toxins. Before starting, all treated wells on the microplate are labelled.

Immobilization of the antigen on the microtiter plate

The antigen is diluted in the binding solution (pH 9.6) to the above mentioned concentration. Each treated well of the microtiter plate is filled with 75 µl of the diluted antigen.

The microtiter plate with the antigen is covered with a lid and incubated overnight (about 17-20 hours) at a temperature of 5 ± 3 ° C.

Removal of unbound material

After the incubation period, the unbound antigen is removed from the wells. All wells are washed 3 times with washing solution using the washing device HYDROFLEX.

Blocking

Blocking is performed using blocking solution. The incubation time for blocking is 2 hours at RT.

Removal of blocking solution

The blocking solution is removed from the wells using the washing device HYDROFLEX. In total 3 times.

Application of antibody

On each microtiter plate with tested sera in addition to the tested sera (TS), positive serum (PS) and a negative serum (NS) must be added. All sera are diluted 1000x to 64000x in dilution solution.

75 µl of the diluted sera is applied to each well of the microtiter plate.

Mouse sera are used for testing. Mice were vaccinated with the studied vaccine. Sera are diluted 1000 x - 64000 x. On each plate, diluted negative and positive standard serum control must be included.

Control wells

Control well A = without antigen, without serum, it is located in the remaining wells of the microtiter plate, the result is negative

Control well B (BLANK) = with antigen, without serum, it is located in the remaining wells of the microtiter plate, the result is negative

Study Code:
Validation Report

Control well C = without conjugate, it is located in the wells with the lowest dilution of positive and negative serum, the result is negative

The plate with the diluted sera is covered and incubated for 1 hour at RT.

Removal of unbound material

After the incubation period, the unbound serum is removed from the wells. All wells are washed 3 times with washing solution using the washing device HYDROFLEX.

Application of conjugate

The conjugate is diluted in dilution solution (8 000 x). 75 µl of the diluted conjugate is applied to each well. The plate is covered and incubated for 1 hour at RT.

Removal of unbound material

After the incubation period, the unbound conjugate is removed from the wells. All wells are washed 3 times with washing solution using the washing device HYDROFLEX.

Preparation and dosing of the substrate solution

75 µl of the substrate (TMB) is applied to each tested well.

The plate is incubated for 5 minutes at RT. During this time, in the wells containing specific antibodies against coated antigens, the color of the solution turns into blue as a result of the enzymatic reaction. With increasing content of antibodies the intensity of the staining increases.

Application of stop solution

After 5 minutes the reaction is terminated by the addition of stop solution 2M H₂SO₄. To each reaction well 75 µl of stop solution is applied to terminate the enzymatic reaction. The color of the solution changes from blue to yellow.

Evaluation of results

The color intensity is measured using a spectrophotometer at a wavelength of 450 nm.

Evaluation of the results is performed using software for processing the spectrophotometric data MARS.

8. Tested parameters and criteria of acceptability

Specificity

Negative sample should be mouse serum, where the colour reaction is not expected by any dilution (absorbance under 0.12 – quantification limit). Two negative samples in 3 days at all dilutions were tested.

Absorbance of samples without conjugate, samples without antigen and serum and samples without serum should not be higher than 0.12.

Precision

Precision describes agreement among samples and is expressed as variation coefficient.

$$CV = (SD/mean) \times 100$$

Reproducibility

Six positive samples in one day were tested. CV for reproducibility should be $\leq 15\%$ for samples with absorbance higher than 0.12.

Intermediate precision

Six or two positive samples in three days were tested. CV for reproducibility should be $\leq 15\%$ for samples with absorbance higher than 0.12.

Range

Range for the method was set from the first dilution to the last dilution, where the absorbance is higher than 0.1. Range for this validation is 1000x till 64000x or 1000x till 128000x.

Linearity

Linearity was approved by using linear regression for dependence of logarithm of absorbance on logarithm of dilution, which is usually used for ELISA method. Calculation was provided in software Combistat. Correlation coefficient should be higher than 0.95. Analysis of variance (ANOVA) was used for evaluation of regression significance and non-significance of parameter „non-linearity“. Linearity from three separate days confirmed parallelity.

Study Code:

Validation Report

9. Evaluation of validation parameters

Absorbance values were obtained by software XFLUR4. Tables and summary statistic was done in software Excel 2007. Linearity was evaluated in software QC.Expert 3.0.

9.1 Specificity*Table 1: Negative (without adhesin K88) standard serum on adhesin K88*

Dilution	Day 1		Day 2		Day 3	
	Neg. serum sample 1	Neg. serum sample 2	Neg. serum sample 1	Neg. serum sample 2	Neg. serum sample 1	Neg. serum sample 2
	Absorbance at 450nm					
1000x	0.069	0.085	0.094	0.091	0.105	0.103
2000x	0.061	0.064	0.074	0.077	0.074	0.076
4000x	0.053	0.053	0.063	0.067	0.068	0.067
8000x	0.057	0.055	0.061	0.063	0.061	0.066
16000x	0.056	0.051	0.059	0.056	0.056	0.054
32000x	0.057	0.056	0.057	0.056	0.055	0.054
64000x	0.058	0.056	0.055	0.056	0.054	0.056

Table 2: Negative (without adhesin K99) standard serum on adhesin K99

Dilution	Day 1		Day 2		Day 3	
	Neg. serum sample 1	Neg. serum sample 2	Neg. serum sample 1	Neg. serum sample 2	Neg. serum sample 1	Neg. serum sample 2
	Absorbance at 450nm					
1000x	0.068	0.066	0.075	0.074	0.083	0.080
2000x	0.061	0.063	0.067	0.074	0.078	0.073
4000x	0.055	0.058	0.060	0.062	0.064	0.065
8000x	0.057	0.060	0.061	0.060	0.060	0.062
16000x	0.057	0.058	0.059	0.060	0.058	0.058
32000x	0.058	0.059	0.059	0.059	0.057	0.058
64000x	0.058	0.059	0.058	0.060	0.057	0.060

Table 3: Negative (without adhesin 987P) standard serum on adhesin 987P

Dilution	Day 1		Day 2		Day 3	
	Neg. serum sample 1	Neg. serum sample 2	Neg. serum sample 1	Neg. serum sample 2	Neg. serum sample 1	Neg. serum sample 2
	Absorbance at 450nm					
1000x	0.087	0.088	0.104	0.098	0.103	0.099
2000x	0.072	0.074	0.083	0.082	0.083	0.076
4000x	0.061	0.061	0.068	0.066	0.069	0.070
8000x	0.069	0.059	0.066	0.065	0.067	0.064
16000x	0.058	0.055	0.061	0.059	0.062	0.059
32000x	0.062	0.056	0.061	0.061	0.061	0.057
64000x	0.058	0.056	0.060	0.059	0.060	0.057

Table 4: Negative (without adhesin F41) standard serum on adhesin F41

Dilution	Day 1		Day 2		Day 3	
	Neg. serum sample 1	Neg. serum sample 2	Neg. serum sample 1	Neg. serum sample 2	Neg. serum sample 1	Neg. serum sample 2
	Absorbance at 450nm					
1000x	0.081	0.086	0.085	0.09	0.094	0.094
2000x	0.064	0.068	0.071	0.073	0.074	0.073
4000x	0.057	0.061	0.061	0.063	0.063	0.063
8000x	0.056	0.058	0.058	0.061	0.06	0.061
16000x	0.054	0.055	0.056	0.056	0.056	0.057
32000x	0.055	0.055	0.056	0.058	0.057	0.058
64000x	0.054	0.054	0.058	0.058	0.057	0.059

Table 5: Negative (without toxin LTB) standard serum on toxin LTB

Dilution	Day 1		Day 2		Day 3	
	Neg. serum sample 1	Neg. serum sample 2	Neg. serum sample 1	Neg. serum sample 2	Neg. serum sample 1	Neg. serum sample 2
	Absorbance at 450nm					
1000x	0.081	0.086	0.098	0.102	0.104	0.102
2000x	0.064	0.068	0.080	0.080	0.083	0.080
4000x	0.057	0.061	0.065	0.068	0.071	0.066
8000x	0.056	0.058	0.064	0.065	0.064	0.063
16000x	0.054	0.055	0.059	0.061	0.059	0.059
32000x	0.055	0.055	0.062	0.060	0.060	0.060
64000x	0.054	0.054	0.059	0.060	0.060	0.060

Study Code:
Validation Report

Table 6: Negative (without toxin) standard serum on toxin CPA

Dilution	Day 1		Day 2		Day 3	
	Neg. serum sample 1	Neg. serum sample 2	Neg. serum sample 1	Neg. serum sample 2	Neg. serum sample 1	Neg. serum sample 2
	Absorbance at 450nm					
1000x	0.085	0.083	0.09	0.092	0.092	0.093
2000x	0.069	0.066	0.073	0.075	0.072	0.088
4000x	0.058	0.059	0.066	0.064	0.062	0.066
8000x	0.056	0.056	0.06	0.061	0.058	0.059
16000x	0.055	0.055	0.058	0.062	0.056	0.058
32000x	0.052	0.053	0.054	0.055	0.051	0.055
64000x	0.052	0.054	0.053	0.056	0.053	0.058
128000x	0.053	0.054	0.055	0.055	0.054	0.056

Table 7: Negative (without toxin) standard serum on toxin CPB

Dilution	Day 1		Day 2		Day 3	
	Neg. serum sample 1	Neg. serum sample 2	Neg. serum sample 1	Neg. serum sample 2	Neg. serum sample 1	Neg. serum sample 2
	Absorbance at 450nm					
1000x	0.095	0.083	0.093	0.097	0.088	0.087
2000x	0.068	0.066	0.072	0.075	0.069	0.068
4000x	0.057	0.058	0.061	0.062	0.06	0.061
8000x	0.053	0.054	0.057	0.059	0.057	0.057
16000x	0.051	0.052	0.054	0.057	0.054	0.055
32000x	0.05	0.05	0.05	0.053	0.048	0.053
64000x	0.05	0.052	0.051	0.053	0.051	0.054
128000x	0.051	0.052	0.053	0.056	0.052	0.054

Table 8: Negative (without toxin) standard serum on toxin CPB2

Dilution	Day 1		Day 2		Day 3	
	Neg. serum sample 1	Neg. serum sample 2	Neg. serum sample 1	Neg. serum sample 2	Neg. serum sample 1	Neg. serum sample 2
	Absorbance at 450nm					
4000x	0.113	0.105	0.116	0.119	0.108	0.103
8000x	0.083	0.078	0.082	0.084	0.081	0.077
16000x	0.068	0.068	0.068	0.071	0.066	0.067
32000x	0.057	0.057	0.056	0.061	0.057	0.058
64000x	0.054	0.056	0.055	0.057	0.055	0.056
128000x	0.054	0.055	0.054	0.055	0.053	0.055
256000x	0.051	0.052	0.052	0.053	0.052	0.053
512000x	0.052	0.053	0.052	0.058	0.053	0.054

Table 9: Negative (without toxin) standard serum on toxin ETX

Dilution	Day 1		Day 2		Day 3	
	Neg. serum sample 1	Neg. serum sample 2	Neg. serum sample 1	Neg. serum sample 2	Neg. serum sample 1	Neg. serum sample 2
	Absorbance at 450nm					
1000x	0.116	0.104	0.11	0.113	0.11	0.106
2000x	0.086	0.081	0.081	0.084	0.082	0.078
4000x	0.068	0.068	0.065	0.068	0.071	0.066
8000x	0.059	0.061	0.059	0.063	0.062	0.067
16000x	0.057	0.058	0.056	0.058	0.059	0.059
32000x	0.054	0.055	0.055	0.056	0.056	0.056
64000x	0.054	0.055	0.053	0.054	0.056	0.056
128000x	0.054	0.055	0.053	0.054	0.058	0.057

Table 10: Negative (without toxin) standard serum on toxin TcdA

Dilution	Day 1		Day 2		Day 3	
	Neg. serum sample 1	Neg. serum sample 2	Neg. serum sample 1	Neg. serum sample 2	Neg. serum sample 1	Neg. serum sample 2
	Absorbance at 450nm					
2000x	0.075	0.073	0.084	0.068	0.069	0.075
4000x	0.067	0.063	0.07	0.056	0.059	0.062
8000x	0.063	0.062	0.069	0.054	0.054	0.093
16000x	0.052	0.049	0.059	0.051	0.046	0.048
32000x	0.051	0.059	0.072	0.049	0.046	0.042
64000x	0.053	0.051	0.065	0.058	0.048	0.048
256000x	0.052	0.05	0.06	0.055	0.046	0.045
512000x	0.049	0.053	0.055	0.056	0.042	0.042

Colour reaction was not detected by any negative mouse sample on any dilution (absorbance value of any sample was not higher than 0.12).

Conclusion:

Method specificity was confirmed by negative samples, colour reaction was not detected by any negative mouse sample on any dilution (absorbance these samples was lower than 0.12).

9.2 Precision

Table 11: Reproducibility of positive standard serum on adhesin K88

Sample	Dilution (positive standard serum)							
	1 000x	2 000x	4 000x	8 000x	16 000x	32 000x	64 000x	128000x
1	1.011	0.78	0.513	0.305	0.192	0.122	0.087	0.071
2	0.984	0.772	0.497	0.296	0.174	0.118	0.082	0.068
3	0.963	0.667	0.389	0.223	0.144	0.100	0.087	0.064
4	1.051	0.768	0.475	0.298	0.179	0.118	0.085	0.069
5	0.931	0.694	0.417	0.258	0.154	0.105	0.082	0.067
6	0.964	0.697	0.454	0.313	0.165	0.115	0.085	0.067
Mean	0.984	0.730	0.458	0.282	0.168	0.113	0.085	0.068
SD	0.038	0.045	0.043	0.032	0.016	0.008	0.002	0.002
CV (%)	3.91	6.14	9.48	11.21	9.46	6.93	-*	-*

* CV and accuracy were not calculated for dilution, where absorbance for all samples were lower than 0.12

Table 12: Accuracy and reproducibility of positive standard serum on adhesin K99

Sample	Dilution (positive standard serum)							
	1 000x	2 000x	4 000x	8 000x	16 000x	32 000x	64 000x	128000x
1	1.608	1.262	1.059	0.721	0.419	0.27	0.18	0.118
2	1.586	1.388	1.02	0.651	0.454	0.304	0.178	0.120
3	1.512	1.265	0.966	0.602	0.388	0.237	0.147	0.102
4	1.621	1.39	1.069	0.689	0.473	0.28	0.178	0.112
5	1.498	1.19	0.929	0.549	0.367	0.222	0.157	0.099
6	1.551	1.167	0.994	0.649	0.411	0.25	0.163	0.116
Mean	1.563	1.277	1.006	0.644	0.419	0.261	0.167	0.111
SD	0.046	0.087	0.049	0.056	0.036	0.027	0.012	0.008
CV (%)	2.97	6.79	4.91	8.70	8.65	10.52	7.43	7.17

Table 13: Accuracy and reproducibility of positive standard serum on adhesin 987P

Sample	Dilution (positive standard serum)							
	1 000x	2 000x	4 000x	8 000x	16 000x	32 000x	64 000x	128000x
1	1.318	0.989	0.652	0.435	0.271	0.153	0.110	0.089
2	1.284	0.935	0.62	0.389	0.252	0.155	0.105	0.084
3	1.211	0.793	0.516	0.305	0.18	0.124	0.094	0.076
4	1.318	0.953	0.613	0.379	0.223	0.134	0.097	0.081
5	1.212	0.863	0.533	0.341	0.202	0.128	0.092	0.076
6	1.364	0.959	0.601	0.398	0.224	0.137	0.100	0.08
Mean	1.285	0.915	0.589	0.375	0.225	0.139	0.100	0.081
SD	0.057	0.067	0.049	0.042	0.030	0.012	0.006	0.005
CV (%)	4.41	7.31	8.23	11.11	13.32	8.47	6.26	-*

* CV were not calculated for dilution, where absorbance for all samples were lower than 0.12

Study Code:
Validation Report

Table 14: Accuracy and reproducibility of positive standard serum on adhesin F41

Sample	Dilution (positive standard serum)							
	1 000x	2 000x	4 000x	8 000x	16 000x	32 000x	64 000x	128000x
1	1.617	1.475	1.121	0.887	0.611	0.39	0.273	0.206
2	1.695	1.471	1.156	0.853	0.589	0.383	0.276	0.197
3	1.634	1.424	1.147	0.849	0.592	0.415	0.275	0.201
4	1.668	1.411	1.143	0.873	0.604	0.439	0.292	0.215
5	1.651	1.453	1.192	0.942	0.621	0.442	0.302	0.222
6	1.597	1.392	1.145	0.886	0.592	0.397	0.299	0.218
Mean	1.644	1.438	1.151	0.882	0.602	0.411	0.286	0.210
SD	0.032	0.031	0.021	0.031	0.012	0.023	0.012	0.009
CV (%)	1.97	2.15	1.85	3.48	1.94	5.60	4.16	4.35

Table 15: Accuracy and reproducibility of positive standard serum on toxin LTB

Sample	Dilution (positive standard serum)							
	1 000x	2 000x	4 000x	8 000x	16 000x	32 000x	64 000x	128000x
1	1.838	1.562	1.382	1.099	0.714	0.425	0.277	0.169
2	1.748	1.634	1.41	1.087	0.737	0.472	0.267	0.173
3	1.738	1.543	1.257	0.952	0.578	0.345	0.235	0.141
4	1.809	1.654	1.393	1.094	0.739	0.471	0.287	0.172
5	1.749	1.585	1.329	1.006	0.65	0.378	0.236	0.154
6	1.834	1.645	1.377	1.093	0.725	0.438	0.281	0.166
Mean	1.786	1.604	1.358	1.055	0.691	0.422	0.264	0.163
SD	0.042	0.043	0.051	0.056	0.059	0.047	0.021	0.011
CV (%)	2.36	2.66	3.79	5.32	8.48	11.06	7.92	7.06

Table 16: Accuracy and reproducibility of positive standard serum on toxin CPA

Sample	Dilution (positive standard serum)							
	1 000x	2 000x	4 000x	8 000x	16 000x	32 000x	64 000x	128000x
1	1.551	1.141	0.847	0.507	0.307	0.190	0.130	0.098
2	1.459	1.096	0.747	0.466	0.289	0.181	0.121	0.091
3	1.418	1.066	0.688	0.426	0.271	0.168	0.116	0.084
4	1.504	1.097	0.740	0.474	0.283	0.179	0.120	0.089
5	1.499	1.109	0.707	0.455	0.271	0.175	0.120	0.087
6	1.326	0.984	0.606	0.403	0.236	0.16	0.108	0.082
Mean	1.460	1.082	0.723	0.455	0.276	0.176	0.119	0.089
SD	0.072	0.049	0.072	0.033	0.022	0.010	0.007	0.005
CV (%)	4.961	4.541	10.014	7.358	7.862	5.453	-*	-*

* CV and accuracy were not calculated for dilution, where absorbance for all samples were lower than 0.12

Study Code:
Validation Report

Table 17: Accuracy and reproducibility of positive standard serum on toxin CPB

Sample	Dilution (positive standard serum)							
	1 000x	2 000x	4 000x	8 000x	16 000x	32 000x	64 000x	128000x
1	0.403	0.245	0.172	0.115	0.086	0.071	0.068	0.066
2	0.424	0.272	0.169	0.119	0.088	0.074	0.068	0.062
3	0.382	0.268	0.166	0.118	0.089	0.076	0.074	0.066
4	0.324	0.263	0.167	0.119	0.087	0.069	0.064	0.061
5	0.379	0.239	0.150	0.106	0.081	0.069	0.065	0.060
6	0.357	0.215	0.145	0.107	0.079	0.066	0.061	0.059
Mean	0.378	0.250	0.162	0.114	0.085	0.071	0.067	0.062
SD	0.032	0.020	0.010	0.005	0.004	0.003	0.004	0.003
CV (%)	8.442	7.901	6.302	-*	-*	-*	-*	-*

* CV and accuracy were not calculated for dilution, where absorbance for all samples were lower than 0.12

Table 18: Accuracy and reproducibility of positive standard serum on toxin CPB2

Sample	Dilution (positive standard serum)							
	4 000x	8 000x	16 000x	32 000x	64 000x	128000x	256000x	512000x
1	0.677	0.363	0.244	0.146	0.107	0.083	0.069	0.063
2	0.746	0.461	0.267	0.168	0.120	0.088	0.075	0.067
3	0.724	0.437	0.262	0.156	0.115	0.090	0.076	0.071
4	0.642	0.426	0.269	0.168	0.112	0.092	0.080	0.074
5	0.701	0.419	0.243	0.151	0.113	0.087	0.072	0.069
6	0.578	0.358	0.209	0.139	0.096	0.084	0.067	0.066
Mean	0.678	0.411	0.249	0.155	0.111	0.087	0.073	0.068
SD	0.056	0.038	0.021	0.011	0.008	0.003	0.004	0.004
CV (%)	8.205	9.207	8.286	6.940	-*	-*	-*	-*

* CV and accuracy were not calculated for dilution, where absorbance for all samples were lower than 0.12

Table 19: Accuracy and reproducibility of positive standard serum on toxin ETX

Sample	Dilution (positive standard serum)							
	1 000x	2 000x	4 000x	8 000x	16 000x	32 000x	64 000x	128000x
1	0.251	0.168	0.12	0.083	0.068	0.058	0.058	0.055
2	0.289	0.255	0.128	0.095	0.075	0.063	0.06	0.058
3	0.283	0.185	0.127	0.094	0.096	0.062	0.059	0.056
4	0.282	0.179	0.125	0.093	0.073	0.062	0.061	0.058
5	0.303	0.198	0.143	0.099	0.08	0.066	0.065	0.059
6	0.316	0.209	0.134	0.097	0.081	0.068	0.064	0.063
Mean	0.287	0.199	0.130	0.094	0.079	0.063	0.061	0.058
SD	0.020	0.028	0.007	0.005	0.009	0.003	0.003	0.003
CV (%)	7.014	14.204	5.653	-*	-*	-*	-*	-*

* CV and accuracy were not calculated for dilution, where absorbance for all samples were lower than 0.12

Study Code:
Validation Report

Table 20: Accuracy and reproducibility of positive standard serum on toxin TcdA

Sample	Dilution (positive standard serum)							
	2 000x	4 000x	8 000x	16 000x	32 000x	64 000x	128000x	256000x
1	0.594	0.38	0.229	0.14	0.1	0.076	0.066	0.056
2	0.711	0.419	0.273	0.166	0.119	0.084	0.07	0.065
3	0.674	0.424	0.29	0.185	0.112	0.085	0.066	0.066
4	0.621	0.439	0.258	0.156	0.117	0.088	0.071	0.058
5	0.67	0.445	0.283	0.18	0.111	0.077	0.072	0.065
6	0.57	0.334	0.232	0.153	0.105	0.086	0.071	0.063
Mean	0.640	0.407	0.261	0.163	0.111	0.083	0.069	0.062
SD	0.049	0.039	0.024	0.016	0.007	0.005	0.002	0.004
CV (%)	7.674	9.498	9.049	9.548	-*	-*	-*	-*

* CV and accuracy were not calculated for dilution, where absorbance for all samples were lower than 0.12

Reproducibility was fulfilled criteria CV (%) is lower than 15 %.

Table 21: Intermediate precision of positive standard serum on adhesin K88

	Sample	Dilution (positive standard serum)							
		1 000x	2 000x	4 000x	8 000x	16 000x	32 000x	64 000x	128000x
Day 1	1	1.011	0.78	0.513	0.305	0.192	0.122	0.087	0.071
	2	0.984	0.772	0.497	0.296	0.174	0.118	0.082	0.068
	3	0.963	0.667	0.389	0.223	0.144	0.1	0.087	0.064
	4	1.051	0.768	0.475	0.298	0.179	0.118	0.085	0.069
	5	0.931	0.694	0.417	0.258	0.154	0.105	0.082	0.067
	6	0.964	0.697	0.454	0.313	0.165	0.115	0.085	0.067
Day 2	1	1.026	0.856	0.568	0.36	0.221	0.137	0.101	0.082
	2	0.99	0.665	0.495	0.287	0.208	0.136	0.092	0.079
Day 3	1	0.94	0.634	0.404	0.27	0.151	0.109	0.08	0.068
	2	0.926	0.635	0.395	0.245	0.157	0.106	0.082	0.073
	Mean	0.979	0.717	0.461	0.286	0.175	0.117	0.086	0.071
	SD	0.040	0.070	0.056	0.037	0.024	0.012	0.006	0.005
	CV (%)	4.05	9.73	12.20	12.87	13.93	10.18	6.84	7.63

Study Code:

Validation Report

Table 22: Intermediate precision of positive standard serum on adhesin K99

	Sample	Dilution (positive standard serum)							
		1 000x	2 000x	4 000x	8 000x	16 000x	32 000x	64 000x	128000x
Day 1	1	1.608	1.262	1.059	0.721	0.419	0.27	0.18	0.118
	2	1.586	1.388	1.02	0.651	0.454	0.304	0.178	0.120
	3	1.512	1.265	0.966	0.602	0.388	0.237	0.147	0.102
	4	1.621	1.39	1.069	0.689	0.473	0.28	0.178	0.112
	5	1.498	1.19	0.929	0.549	0.367	0.222	0.157	0.099
	6	1.551	1.167	0.994	0.649	0.411	0.25	0.163	0.116
Day 2	1	1.651	1.393	1.117	0.828	0.499	0.367	0.231	0.141
	2	1.569	1.278	1.105	0.773	0.469	0.322	0.208	0.141
Day 3	1	1.499	1.408	1.099	0.752	0.480	0.317	0.207	0.135
	2	1.403	1.331	1.078	0.769	0.500	0.305	0.200	0.130
	Mean	1.550	1.307	1.044	0.698	0.446	0.287	0.185	0.121
	SD	0.070	0.083	0.060	0.082	0.044	0.042	0.025	0.014
	CV (%)	4.50	6.38	5.79	11.73	9.97	14.58	13.45	11.75

Table 23: Intermediate precision of positive standard serum on adhesin 987P

	Sample	Dilution (positive standard serum)							
		1 000x	2 000x	4 000x	8 000x	16 000x	32 000x	64 000x	128000x
Day 1	1	1.318	0.989	0.652	0.435	0.271	0.153	0.110	0.089
	2	1.284	0.935	0.62	0.389	0.252	0.155	0.105	0.084
	3	1.211	0.793	0.516	0.305	0.18	0.124	0.094	0.076
	4	1.318	0.953	0.613	0.379	0.223	0.134	0.097	0.081
	5	1.212	0.863	0.533	0.341	0.202	0.128	0.092	0.076
	6	1.364	0.959	0.601	0.398	0.224	0.137	0.100	0.08
Day 2	1	1.239	0.853	0.653	0.429	0.257	0.164	0.116	0.090
	2	1.196	0.889	0.627	0.353	0.242	0.157	0.111	0.082
Day 3	1	1.229	0.914	0.541	0.341	0.25	0.149	0.098	0.082
	2	1.141	0.894	0.534	0.372	0.245	0.14	0.103	0.08
	Mean	1.251	0.904	0.589	0.374	0.235	0.144	0.103	0.082
	SD	0.065	0.055	0.050	0.039	0.026	0.013	0.007	0.004
	CV (%)	5.16	6.12	8.49	10.33	11.13	8.82	7.27	-*

* CV were not calculated for dilution, where absorbance for all samples were lower than 0.12

Table 24: Intermediate precision of positive standard serum on adhesin F41

	Sample	Dilution (positive standard serum)							
		1 000x	2 000x	4 000x	8 000x	16 000x	32 000x	64 000x	128000x
Day 1	1	1.617	1.475	1.121	0.887	0.611	0.39	0.273	0.206
	2	1.695	1.471	1.156	0.853	0.589	0.383	0.276	0.197
	3	1.634	1.424	1.147	0.849	0.592	0.415	0.275	0.201
	4	1.668	1.411	1.143	0.873	0.604	0.439	0.292	0.215
	5	1.651	1.453	1.192	0.942	0.621	0.442	0.302	0.222
	6	1.597	1.392	1.145	0.886	0.592	0.397	0.299	0.218
Day 2	1	1.656	1.448	1.238	0.952	0.674	0.43	0.294	0.206
	2	1.646	1.42	1.197	0.926	0.637	0.427	0.309	0.213
Day 3	1	1.534	1.385	1.103	0.8	0.542	0.358	0.237	0.175
	2	1.476	1.292	1.003	0.753	0.498	0.326	0.235	0.169
	Mean	1.617	1.417	1.145	0.872	0.596	0.401	0.279	0.202
	SD	0.063	0.051	0.060	0.059	0.046	0.036	0.024	0.017
	CV (%)	3.89	3.59	5.26	6.77	7.74	8.92	8.76	8.31

Table 25: Intermediate precision of positive standard serum on toxin LTB

	Sample	Dilution (positive standard serum)							
		1 000x	2 000x	4 000x	8 000x	16 000x	32 000x	64 000x	128000x
Day 1	1	1.838	1.562	1.382	1.099	0.714	0.425	0.277	0.169
	2	1.748	1.634	1.41	1.087	0.737	0.472	0.267	0.173
	3	1.738	1.543	1.257	0.952	0.578	0.345	0.235	0.141
	4	1.809	1.654	1.393	1.094	0.739	0.471	0.287	0.172
	5	1.749	1.585	1.329	1.006	0.65	0.378	0.236	0.154
	6	1.834	1.645	1.377	1.093	0.725	0.438	0.281	0.166
Day 2	1	1.73	1.696	1.507	1.216	0.864	0.55	0.355	0.197
	2	1.769	1.614	1.536	1.086	0.849	0.52	0.342	0.193
Day 3	1	1.849	1.702	1.483	1.19	0.85	0.521	0.323	0.186
	2	1.887	1.718	1.505	1.248	0.882	0.528	0.315	0.199
	Mean	1.795	1.635	1.418	1.107	0.759	0.465	0.292	0.175
	SD	0.052	0.057	0.084	0.086	0.096	0.065	0.039	0.018
	CV (%)	2.92	3.48	5.95	7.78	12.59	13.90	13.42	10.27

Study Code:
Validation Report

Table 25: Intermediate precision of positive standard serum on toxin CPA

	Sample	Dilution (positive standard serum)							
		1 000x	2 000x	4 000x	8 000x	16 000x	32 000x	64 000x	128 000x
Day 1	1	1.551	1.141	0.847	0.507	0.307	0.190	0.130	0.098
	2	1.459	1.096	0.747	0.466	0.289	0.181	0.121	0.091
	3	1.418	1.066	0.688	0.426	0.271	0.168	0.116	0.084
	4	1.504	1.097	0.740	0.474	0.283	0.179	0.120	0.089
	5	1.499	1.109	0.707	0.455	0.271	0.175	0.120	0.087
	6	1.326	0.984	0.606	0.403	0.236	0.16	0.108	0.082
Day 2	1	1.258	0.86	0.634	0.351	0.22	0.139	0.100	0.078
	2	1.315	0.946	0.634	0.375	0.235	0.147	0.102	0.078
Day 3	1	1.349	0.967	0.646	0.386	0.254	0.155	0.111	0.086
	2	1.247	0.931	0.561	0.347	0.222	0.140	0.101	0.083
	Mean	1.393	1.020	0.681	0.419	0.259	0.163	0.113	0.086
	SD	0.103	0.089	0.079	0.052	0.028	0.017	0.010	0.006
	CV (%)	7.377	8.743	11.542	12.496	10.989	10.441	-*	-*

* CV were not calculated for dilution, where absorbance for all samples were lower than 0.12

Table 27: Intermediate precision of positive standard serum on toxin CPB

	Sample	Dilution (positive standard serum)							
		1 000x	2 000x	4 000x	8 000x	16 000x	32 000x	64 000x	128 000x
Day 1	1	0.403	0.245	0.172	0.115	0.086	0.071	0.068	0.066
	2	0.424	0.272	0.169	0.119	0.088	0.074	0.068	0.062
	3	0.382	0.268	0.166	0.118	0.089	0.076	0.074	0.066
	4	0.324	0.263	0.167	0.119	0.087	0.069	0.064	0.061
	5	0.379	0.239	0.15	0.106	0.081	0.069	0.065	0.06
	6	0.357	0.215	0.145	0.107	0.079	0.066	0.061	0.059
Day 2	1	0.357	0.22	0.139	0.100	0.078	0.066	0.062	0.06
	2	0.322	0.199	0.134	0.116	0.088	0.075	0.063	0.062
Day 3	1	0.317	0.195	0.122	0.094	0.076	0.063	0.06	0.06
	2	0.291	0.193	0.131	0.085	0.072	0.064	0.061	0.061
	Mean	0.356	0.231	0.150	0.108	0.082	0.069	0.065	0.062
	SD	0.040	0.029	0.017	0.011	0.006	0.004	0.004	0.002
	CV (%)	11.236	12.608	11.458	-*	-*	-*	-*	-*

* CV were not calculated for dilution, where absorbance for all samples were lower than 0.12

Study Code:
Validation Report

Table 28: Intermediate precision of positive standard serum on toxin CPB2

	Sample	Dilution (positive standard serum)							
		4 000x	8 000x	16 000x	32 000x	64 000x	128 000x	256 000x	512 000x
Day 1	1	0.677	0.363	0.244	0.146	0.107	0.083	0.069	0.063
	2	0.746	0.461	0.267	0.168	0.120	0.088	0.075	0.067
	3	0.724	0.437	0.262	0.156	0.115	0.090	0.076	0.071
	4	0.642	0.426	0.269	0.168	0.112	0.092	0.080	0.074
	5	0.701	0.419	0.243	0.151	0.113	0.087	0.072	0.069
	6	0.578	0.358	0.209	0.139	0.096	0.084	0.067	0.066
Day 2	1	0.581	0.363	0.201	0.132	0.098	0.077	0.066	0.061
	2	0.811	0.434	0.303	0.174	0.124	0.088	0.073	0.067
Day 3	1	0.788	0.473	0.262	0.159	0.12	0.085	0.072	0.067
	2	0.695	0.39	0.254	0.156	0.107	0.083	0.073	0.067
	Mean	0.694	0.412	0.251	0.155	0.111	0.086	0.072	0.067
	SD	0.074	0.040	0.028	0.013	0.009	0.004	0.004	0.003
	CV (%)	10.720	9.601	11.188	8.163	-*	-*	-*	-*

* CV were not calculated for dilution, where absorbance for all samples were lower than 0.12

Table 29: Intermediate precision of positive standard serum on toxin ETX

	Sample	Dilution (positive standard serum)							
		1 000x	2 000x	4 000x	8 000x	16 000x	32 000x	64 000x	128 000x
Day 1	1	0.251	0.168	0.12	0.083	0.068	0.058	0.058	0.055
	2	0.289	0.255	0.128	0.095	0.075	0.063	0.06	0.058
	3	0.283	0.185	0.127	0.094	0.096	0.062	0.059	0.056
	4	0.282	0.179	0.125	0.093	0.073	0.062	0.061	0.058
	5	0.303	0.198	0.143	0.099	0.08	0.066	0.065	0.059
	6	0.316	0.209	0.134	0.097	0.081	0.068	0.064	0.063
Day 2	1	0.239	0.167	0.121	0.087	0.076	0.067	0.064	0.064
	2	0.277	0.202	0.135	0.098	0.081	0.069	0.065	0.059
Day 3	1	0.266	0.168	0.122	0.081	0.075	0.059	0.059	0.053
	2	0.307	0.196	0.127	0.090	0.074	0.062	0.059	0.056
	Mean	0.023	0.025	0.007	0.006	0.007	0.004	0.003	0.003
	SD	0.281	0.193	0.128	0.092	0.078	0.064	0.061	0.058
	CV (%)	8.229	13.128	5.345	-*	-*	-*	-*	-*

* CV were not calculated for dilution, where absorbance for all samples were lower than 0.12

Table 30: Intermediate precision of positive standard serum on toxin TcdA

		Dilution (positive standard serum)							
	Sample	2 000x	4 000x	8 000x	16 000x	32 000x	64 000x	128000x	256000x
Day 1	1	0.594	0.38	0.229	0.14	0.1	0.076	0.066	0.056
	2	0.711	0.419	0.273	0.166	0.119	0.084	0.07	0.065
	3	0.674	0.424	0.29	0.185	0.112	0.085	0.066	0.066
	4	0.621	0.439	0.258	0.156	0.117	0.088	0.071	0.058
	5	0.67	0.445	0.283	0.18	0.111	0.077	0.072	0.065
	6	0.57	0.334	0.232	0.153	0.105	0.086	0.071	0.063
Day 2	1	0.656	0.384	0.256	0.198	0.108	0.093	0.074	0.06
	2	0.612	0.396	0.273	0.176	0.119	0.084	0.081	0.072
Day 3	1	0.579	0.500	0.274	0.172	0.125	0.086	0.063	0.052
	2	0.615	0.380	0.320	0.173	0.106	0.077	0.060	0.052
	Mean	0.630	0.410	0.269	0.170	0.112	0.084	0.069	0.061
	SD	0.043	0.043	0.026	0.016	0.007	0.005	0.006	0.006
	CV (%)	6.898	10.598	9.524	9.415	-*	-*	-*	-*

* CV were not calculated for dilution, where absorbance for all samples were lower than 0.12

Intermediate precision was fulfilled criteria CV (%) is lower than 15 %.

Study Code:

Validation Report

9.3 Linearity

Linearity was confirmed by linear regression of logarithm of absorbance on logarithm of dilution. Results of linearity on adhesin K88 see tables 31 till 33 a figures 1 and 2.

Table 31: Linearity on adhesin K88 - data

Doses	Day 1						Day 2		Day 3	
	1	2	3	4	5	6	1	2	1	2
1 000x	1.011	0.984	0.963	1.051	0.931	0.964	1.026	0.990	0.940	0.926
2 000x	0.780	0.772	0.667	0.768	0.694	0.697	0.856	0.665	0.634	0.635
4 000x	0.513	0.497	0.389	0.475	0.417	0.454	0.568	0.495	0.404	0.395
8 000x	0.305	0.296	0.223	0.298	0.258	0.313	0.360	0.287	0.270	0.245
16 000x	0.192	0.174	0.144	0.179	0.154	0.165	0.221	0.208	0.151	0.157
32 000x	0.122	0.118	0.100	0.118	0.105	0.115	0.137	0.136	0.109	0.106
64 000x	0.087	0.082	0.087	0.085	0.082	0.085	0.101	0.092	0.080	0.082
128000x	0.071	0.068	0.064	0.069	0.067	0.067	0.082	0.079	0.068	0.073

Linearity was calculated from dilution 2 000x till 32 000x, absorbance absorbance for lower dilution was not linear and for higher dilution was lower than 0.11.

Table 32: Linearity on adhesin K88 - model

Model	paralell lines
Design:	completly randomised
Transformace:	$y'=\log(y)$
Odchylka:	Observed residuals
Nalezená směrnic:	0.288578
Korelace R	0.991103

Correlation coefficient is higher than 0.95.

Table 33: Linearity on adhesin K88 - ANOVA

Source of variation	Degrees of freedom	Sum of squares	Mean square	F-ratio	Probability
Preparations	2	0.0606484	0.0303242	17.360	0.000 [****]
Regression	1	4.00109	4.00109	>1000	0.000 [****]
Non-parallelism	2	0.00520388	0.00260194	1.490	0.239
Non-linearity	9	0.00690592	0.000767325	0.439	0.904
Standard	3	0.00374589	0.00124863	0.715	0.550
Sample 1	3	0.00146912	0.000489708	0.280	0.839
Sample 2	3	0.00169091	0.000563638	0.323	0.809
Quadratic curvature	1	0.000817377	0.000817377	0.468	0.498
Lack of quadratic fit	8	0.00608855	0.000761068	0.436	0.891
Treatments	14	4.07385	0.290989	166.581	0.000 [****]
Residual error	35	0.0611391	0.00174683		
Total	49	4.13499	0.0843876		

Figure 1: Linearity on adhesin K88

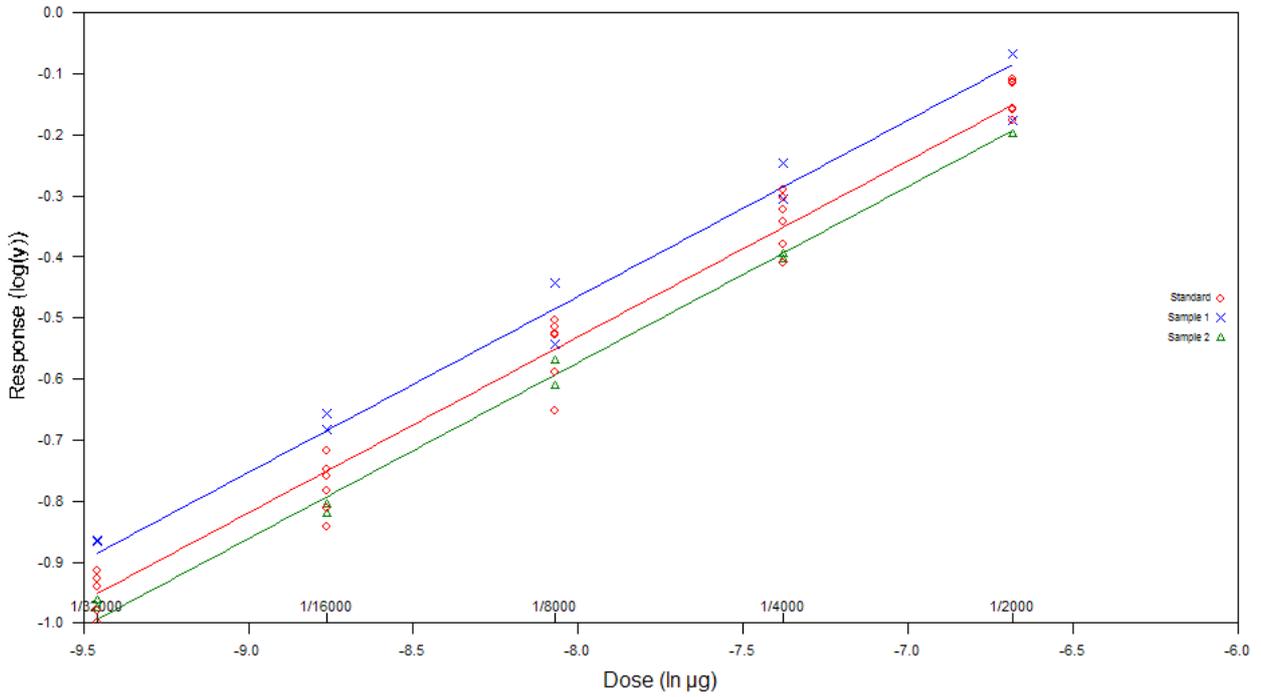
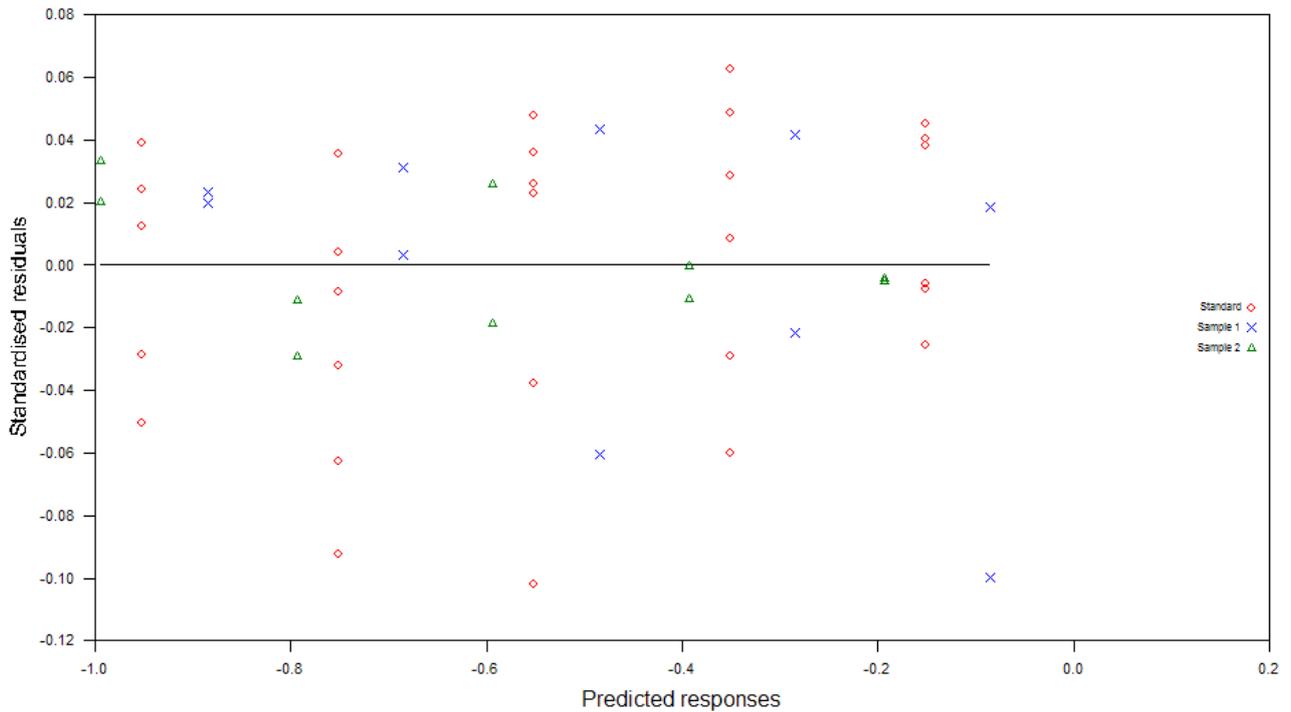


Figure 2: Linearity on adhesin K88 – residuals



Study Code:
Validation Report

Results of linearity on adhesin K99 see tables 34 till 36 a figures 3 and 4.

Table 34: Linearity on adhesin K99 - data

Doses	Day 1						Day 2		Day 3	
	1	2	3	4	5	6	1	2	1	2
1 000x	1.608	1.586	1.512	1.621	1.498	1.551	1.651	1.569	1.499	1.403
2 000x	1.262	1.388	1.265	1.390	1.190	1.167	1.393	1.278	1.408	1.331
4 000x	1.059	1.020	0.966	1.069	0.929	0.994	1.117	1.105	1.099	1.078
8 000x	0.721	0.651	0.602	0.689	0.549	0.649	0.828	0.773	0.752	0.769
16 000x	0.419	0.454	0.388	0.473	0.367	0.411	0.499	0.469	0.480	0.500
32 000x	0.270	0.304	0.237	0.280	0.222	0.250	0.367	0.322	0.317	0.305
64 000x	0.180	0.178	0.147	0.178	0.157	0.163	0.231	0.208	0.207	0.200
128000x	0.118	0.120	0.102	0.112	0.099	0.116	0.141	0.141	0.135	0.130

Linearity was calculated from dilution 4 000x till 128 000x, absorbance for lower dilution was not linear.

Table 35: Linearity on adhesin K99 - model

Model	paralell lines
Design:	completely randomised
Transformace:	$y'=\log(y)$
Odchylka:	Observed residuals
Nalezená směrnice:	0.272470
Korelace R	0.995380

Correlation coefficient is higher than 0.95.

Table 36: Linearity on adhesin K99 - ANOVA

Source of variation	Degrees of freedom	Sum of squares	Mean square	F-ratio	Probability
Preparations	2	0.0972815	0.0486408	41.430	0.000 (****)
Regression	1	6.24202	6.24202	>1000	0.000 (****)
Non-parallelism	2	0.00450185	0.00225093	1.917	0.160
Non-linearity	12	0.00517006	0.000430838	0.367	0.968
Standard	4	0.00138586	0.000346466	0.295	0.880
Sample 1	4	0.00270208	0.000675521	0.575	0.682
Sample 2	4	0.00108211	0.000270528	0.230	0.920
Quadratic curvature	1	1.97840E-05	1.97840E-05	0.017	0.897
Lack of quadratic fit	11	0.00515028	0.000468207	0.399	0.949
Treatments	17	6.34897	0.373469	318.107	0.000 (****)
Residual error	42	0.0493095	0.00117404		
Total	59	6.39828	0.108445		

Figure 3: Linearity on adhesin K99

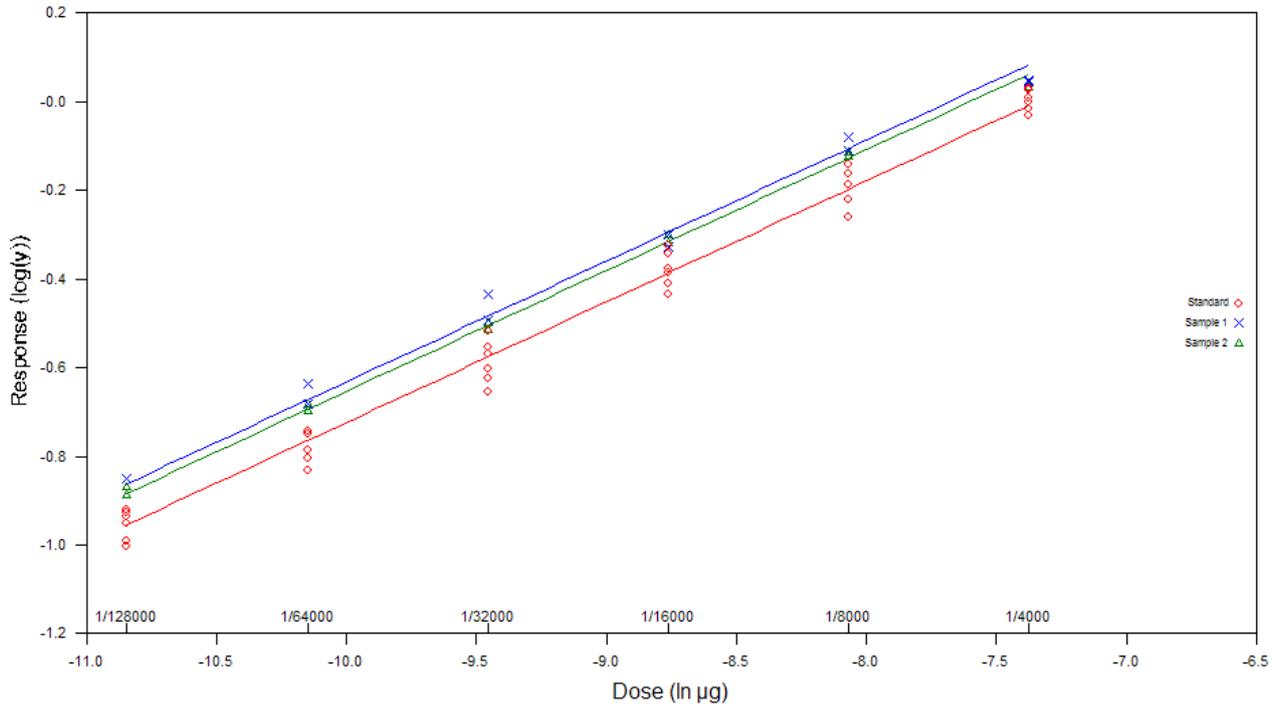
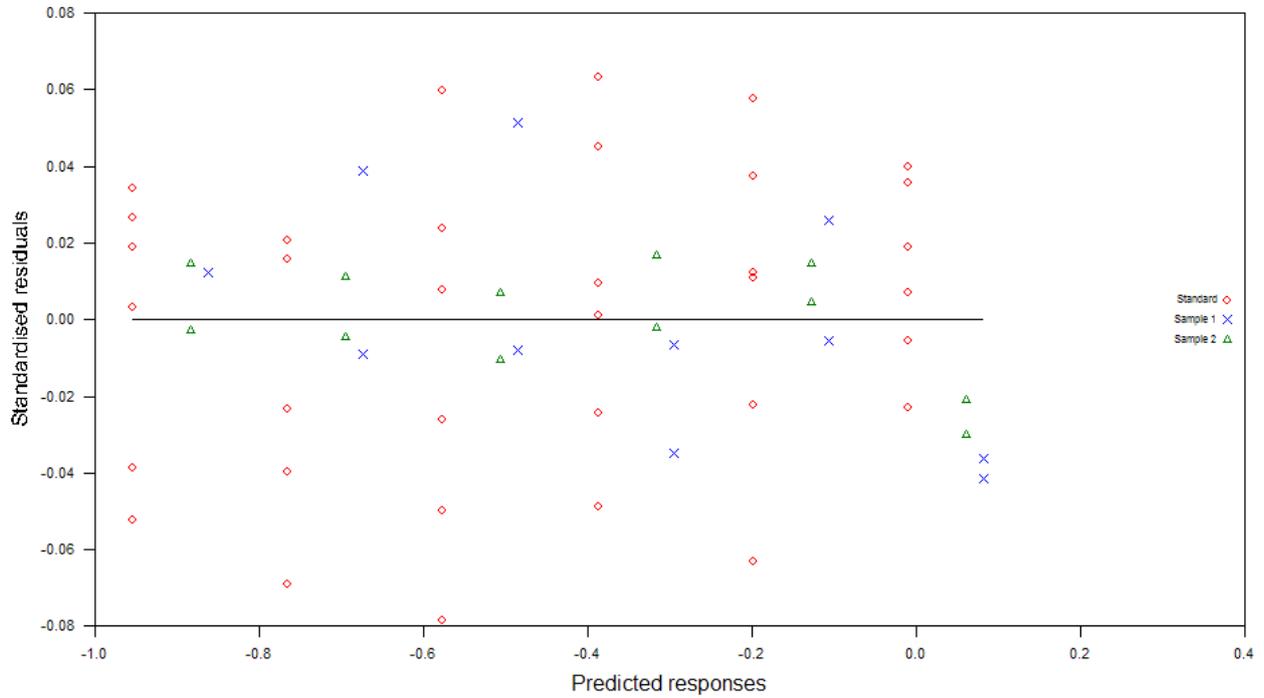


Figure 4: Linearity on adhesin K99 – residuals



Study Code:
Validation Report

Results of linearity on adhesin 987P see tables 37 till 39 a figures 5 and 6.

Table 37: Linearity on adhesin 987P - data

Doses	Day 1						Day 2		Day 3	
	1	2	3	4	5	6	1	2	1	2
1 000x	1.318	1.284	1.211	1.318	1.212	1.364	1.239	1.196	1.229	1.141
2 000x	0.989	0.935	0.793	0.953	0.863	0.959	0.853	0.889	0.914	0.894
4 000x	0.652	0.620	0.516	0.613	0.533	0.601	0.653	0.627	0.541	0.534
8 000x	0.435	0.389	0.305	0.379	0.341	0.398	0.429	0.353	0.341	0.372
16 000x	0.271	0.252	0.180	0.223	0.202	0.224	0.257	0.242	0.250	0.245
32 000x	0.153	0.155	0.124	0.134	0.128	0.137	0.164	0.157	0.149	0.140
64 000x	0.110	0.105	0.094	0.097	0.092	0.100	0.116	0.111	0.098	0.103
128000x	0.089	0.084	0.076	0.081	0.076	0.080	0.090	0.082	0.082	0.080

Linearity was calculated from dilution 2 000x till 64 000x, absorbance for lower dilution was not linear and absorbance for higher dilution was lower than 0.11.

Table 38: Linearity on adhesin 987P - model

Model	paralell lines
Design:	completely randomised
Transformace:	$y'=\log(y)$
Odchylka:	Observed residuals
Nalezená směrnice:	0.278858
Korelace R	0.992959

Correlation coefficient is higher than 0.95.

Table 39: Linearity on adhesin 987P - ANOVA

Source of variation	Degrees of freedom	Sum of squares	Mean square	F-ratio	Probability
Preparations	2	0.0112394	0.00561971	3.469	0.040 (*)
Regression	1	6.53817	6.53817	>1000	0.000 (****)
Non-parallelism	2	0.00592852	0.00296426	1.830	0.173
Non-linearity	12	0.0192442	0.00160368	0.990	0.474
Standard	4	0.0116094	0.00290235	1.792	0.149
Sample 1	4	0.00398309	0.000995772	0.615	0.654
Sample 2	4	0.00365173	0.000912933	0.564	0.690
Quadratic curvature	1	0.00264179	0.00264179	1.631	0.209
Lack of quadratic fit	11	0.0166024	0.00150931	0.932	0.520
Treatments	17	6.57458	0.386740	238.730	0.000 (****)
Residual error	42	0.0680394	0.00161999		
Total	59	6.64262	0.112587		

Figure 5: Linearity on adhesin 987P

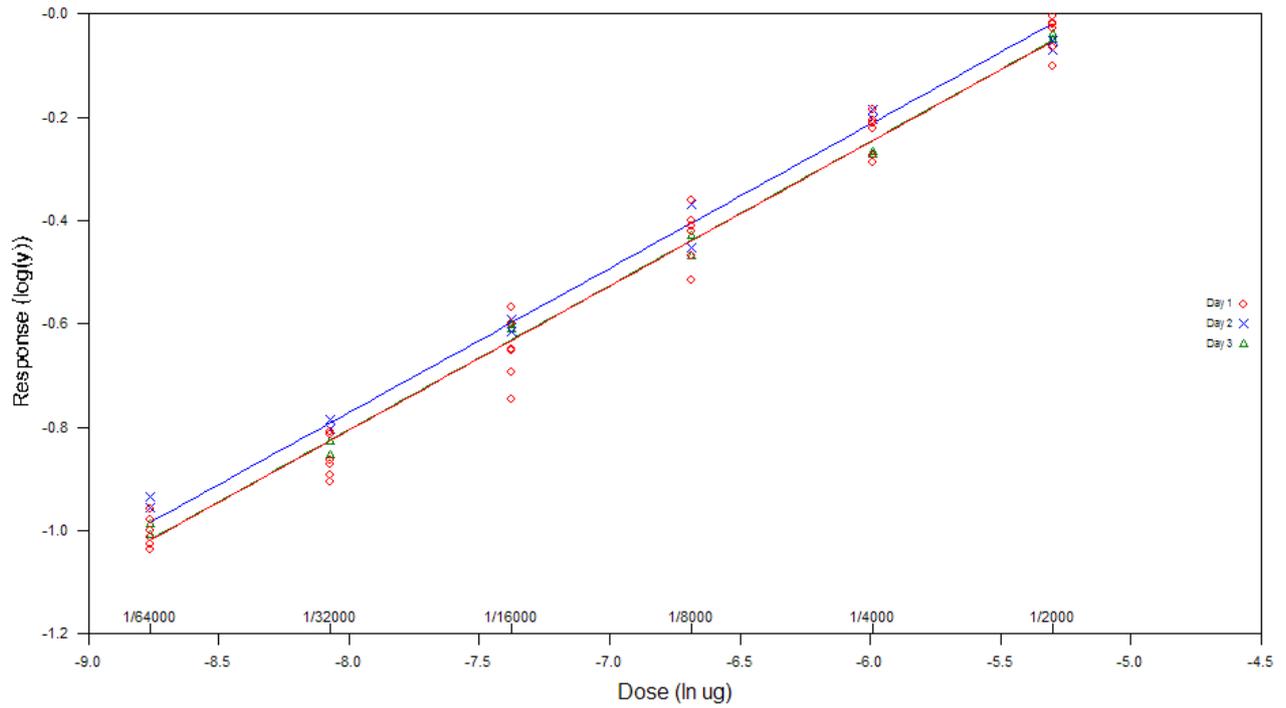
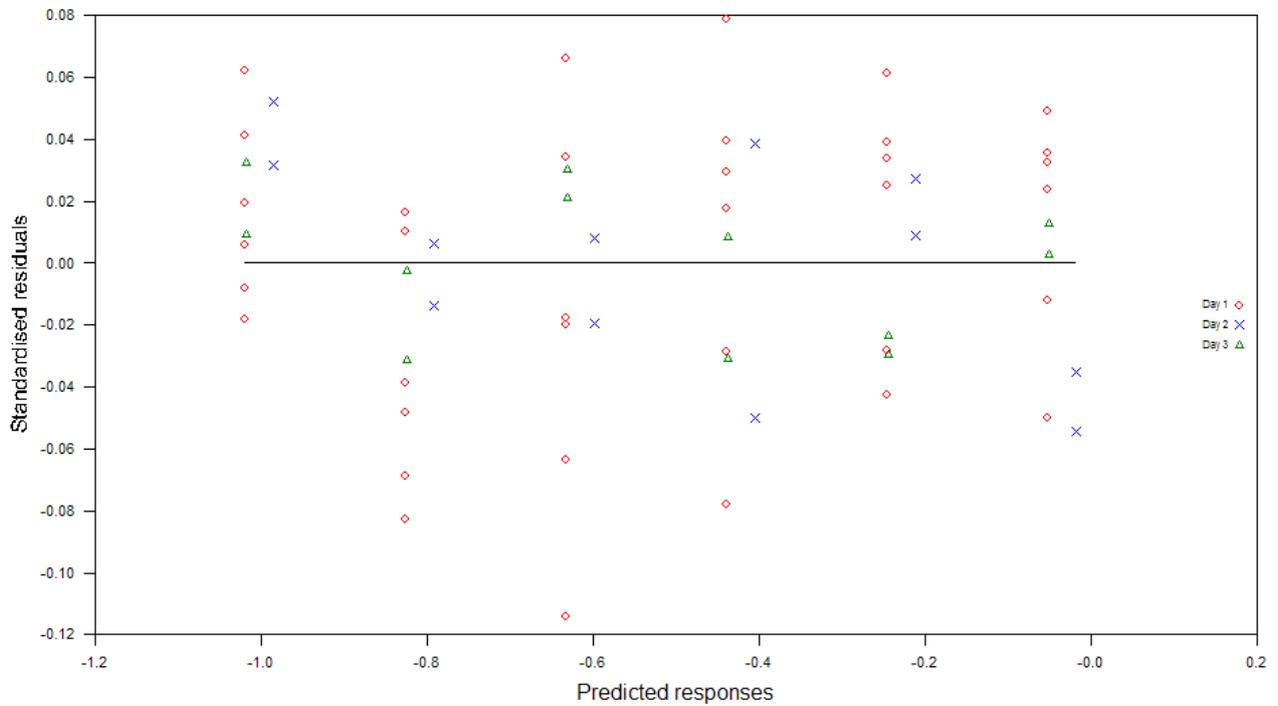


Figure 6: Linearity on adhesin 987P – residuals



Study Code:
Validation Report

Results of linearity on adhesin F41 see tables 40 till 42 a figures 7 and 8.

Table 40: Linearity on adhesin F41 - data

Doses	Day 1						Day 2		Day 3	
	1	2	3	4	5	6	1	2	1	2
1 000x	1.617	1.695	1.634	1.668	1.651	1.597	1.656	1.646	1.534	1.476
2 000x	1.475	1.471	1.424	1.411	1.453	1.392	1.448	1.420	1.385	1.292
4 000x	1.121	1.156	1.147	1.143	1.192	1.145	1.238	1.197	1.103	1.003
8 000x	0.887	0.853	0.849	0.873	0.942	0.886	0.952	0.926	0.800	0.753
16 000x	0.611	0.589	0.592	0.604	0.621	0.592	0.674	0.637	0.542	0.498
32 000x	0.390	0.383	0.415	0.439	0.442	0.397	0.430	0.427	0.358	0.326
64 000x	0.273	0.276	0.275	0.292	0.302	0.299	0.294	0.309	0.237	0.235
128000x	0.206	0.197	0.201	0.215	0.222	0.218	0.206	0.213	0.175	0.169

Linearity was calculated from dilution 8 000x till 128 000x, absorbance for lower dilution was not linear.

Table 41: Linearity on adhesin F41 - model

Model	paralell lines
Design:	completely randomised
Transformace:	$y'=\log(y)$
Odchylka:	Observed residuals
Nalezená směrnice:	0.230936
Korelace R	0.996593

Correlation coefficient is higher than 0.95.

Table 42: Linearity on adhesin F41 - ANOVA

Source of variation	Degrees of freedom	Sum of squares	Mean square	F-ratio	Probability
Preparations	2	0.0531238	0.0265619	77.201	0.000 (****)
Regression	1	2.56233	2.56233	>1000	0.000 (****)
Non-parallelism	2	0.00137685	0.000688426	2.001	0.150
Non-linearity	9	0.00449299	0.000499222	1.451	0.205
Standard	3	0.00250017	0.000833391	2.422	0.082
Sample 1	3	0.000485679	0.000161893	0.471	0.705
Sample 2	3	0.00150714	0.000502381	1.460	0.242
Quadratic curvature	1	0.00327558	0.00327558	9.520	0.004 (**)
Lack of quadratic fit	8	0.00121741	0.000152176	0.442	0.887
Treatments	14	2.62132	0.187237	544.196	0.000 (****)
Residual error	35	0.0120422	0.000344062		
Total	49	2.63336	0.0537421		

Figure 7: Linearity on adhesin F41

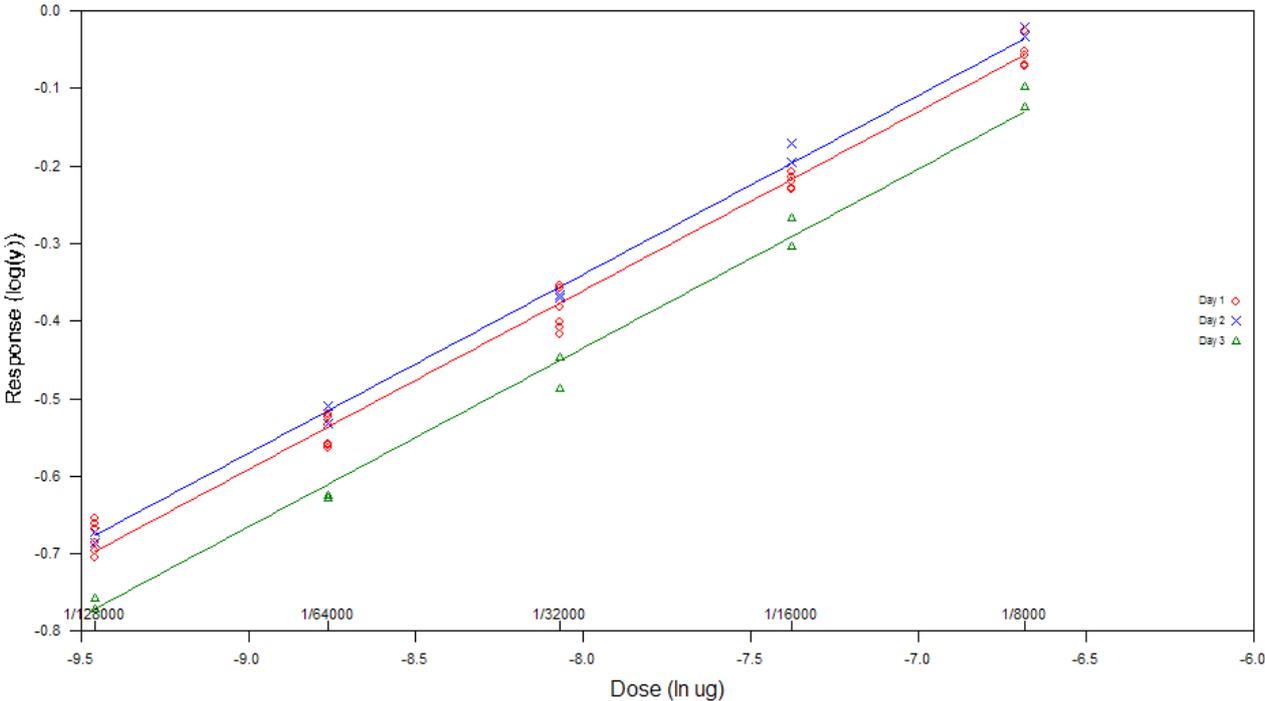
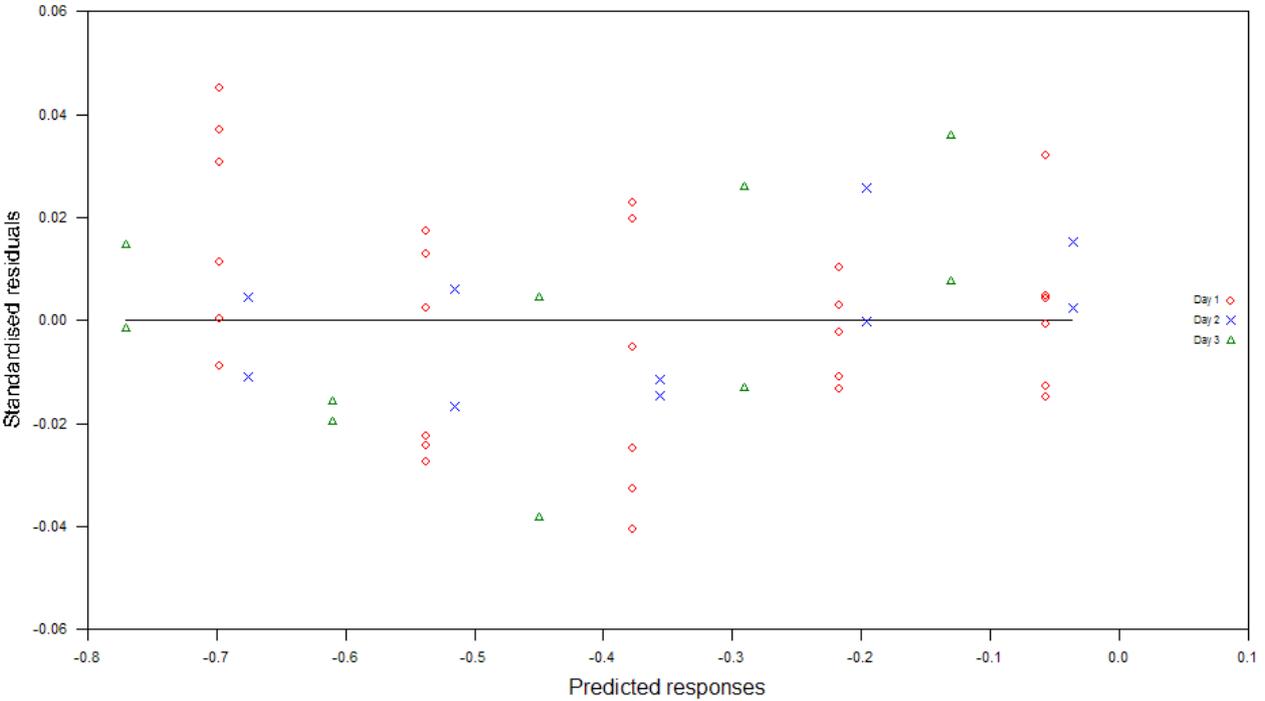


Figure 8: Linearity on adhesin F41 – residuals



Study Code:
Validation Report

Results of linearity on toxin LTB see tables 43 till 45 a figures 9 and 10.

Table 43: Linearity on toxin LTB - data

Doses	Day 1						Day 2		Day 3	
	1	2	3	4	5	6	1	2	1	2
1 000x	1.838	1.748	1.738	1.809	1.749	1.834	1.730	1.769	1.849	1.887
2 000x	1.562	1.634	1.543	1.654	1.585	1.645	1.696	1.614	1.702	1.718
4 000x	1.382	1.410	1.257	1.393	1.329	1.377	1.507	1.536	1.483	1.505
8 000x	1.099	1.087	0.952	1.094	1.006	1.093	1.216	1.086	1.190	1.248
16 000x	0.714	0.737	0.578	0.739	0.650	0.725	0.864	0.849	0.850	0.882
32 000x	0.425	0.472	0.345	0.471	0.378	0.438	0.550	0.520	0.521	0.528
64 000x	0.277	0.267	0.235	0.287	0.236	0.281	0.355	0.342	0.323	0.315
128000x	0.169	0.173	0.141	0.172	0.154	0.166	0.197	0.193	0.186	0.199

Linearity was calculated from dilution 8 000x till 128 000x, absorbance for lower dilution was not linear.

Table 44: Linearity on toxin LTB - model

Model	paralell lines
Design:	completely randomised
Transformace:	$y'=\log(y)$
Odchylka:	Observed residuals
Nalezená směrnice:	0.291393
Korelace R	0.993027

Correlation coefficient is higher than 0.95.

Table 45: Linearity on toxin LTB - ANOVA

Source of variation	Degrees of freedom	Sum of squares	Mean square	F-ratio	Probability
Preparations	2	0.0890004	0.0445002	36.080	0.000 [***]
Regression	1	4.07952	4.07952	>1000	0.000 [***]
Non-parallelism	2	0.00196243	0.000981214	0.796	0.459
Non-linearity	9	0.0136184	0.00151315	1.227	0.311
Standard	3	0.00123528	0.000411759	0.334	0.801
Sample 1	3	0.00853217	0.00284406	2.306	0.094
Sample 2	3	0.00385093	0.00128364	1.041	0.387
Quadratic curvature	1	0.00660932	0.00660932	5.359	0.027 (*)
Lack of quadratic fit	8	0.00700906	0.000876133	0.710	0.681
Treatments	14	4.18410	0.298864	242.313	0.000 [***]
Residual error	35	0.0431684	0.00123338		
Total	49	4.22727	0.0862708		

Figure 9: Linearity on toxin LTB

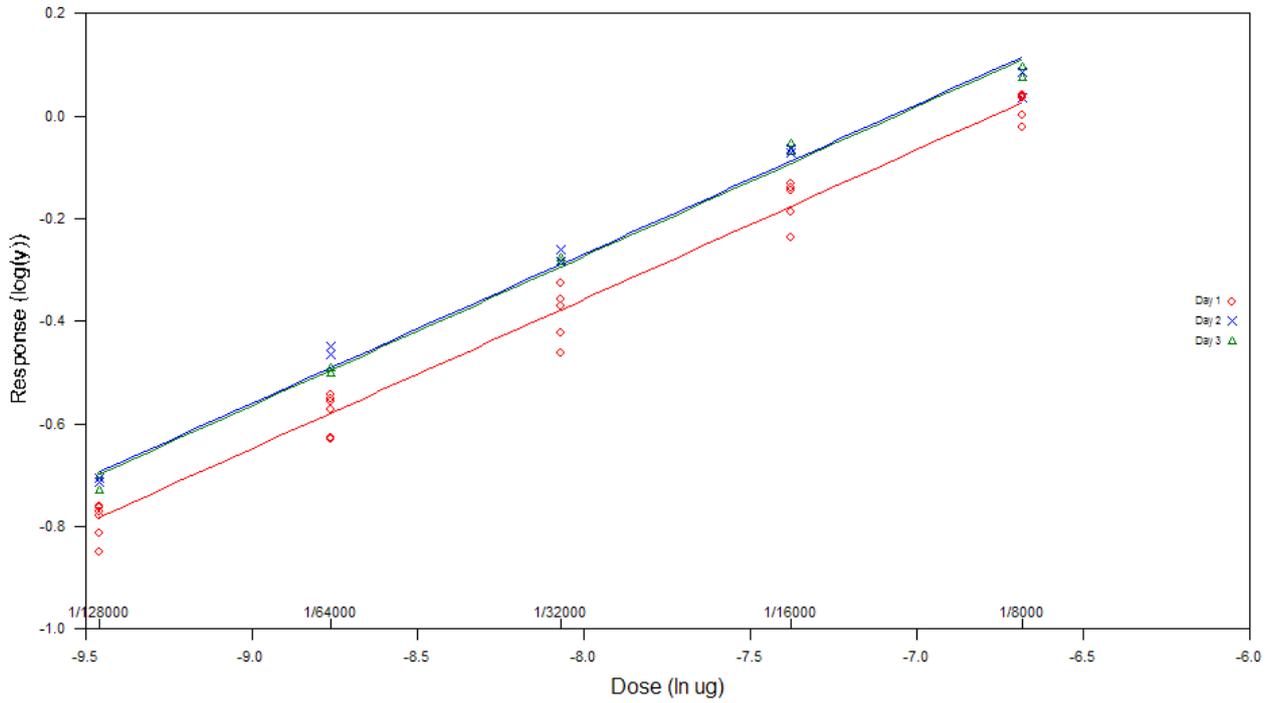
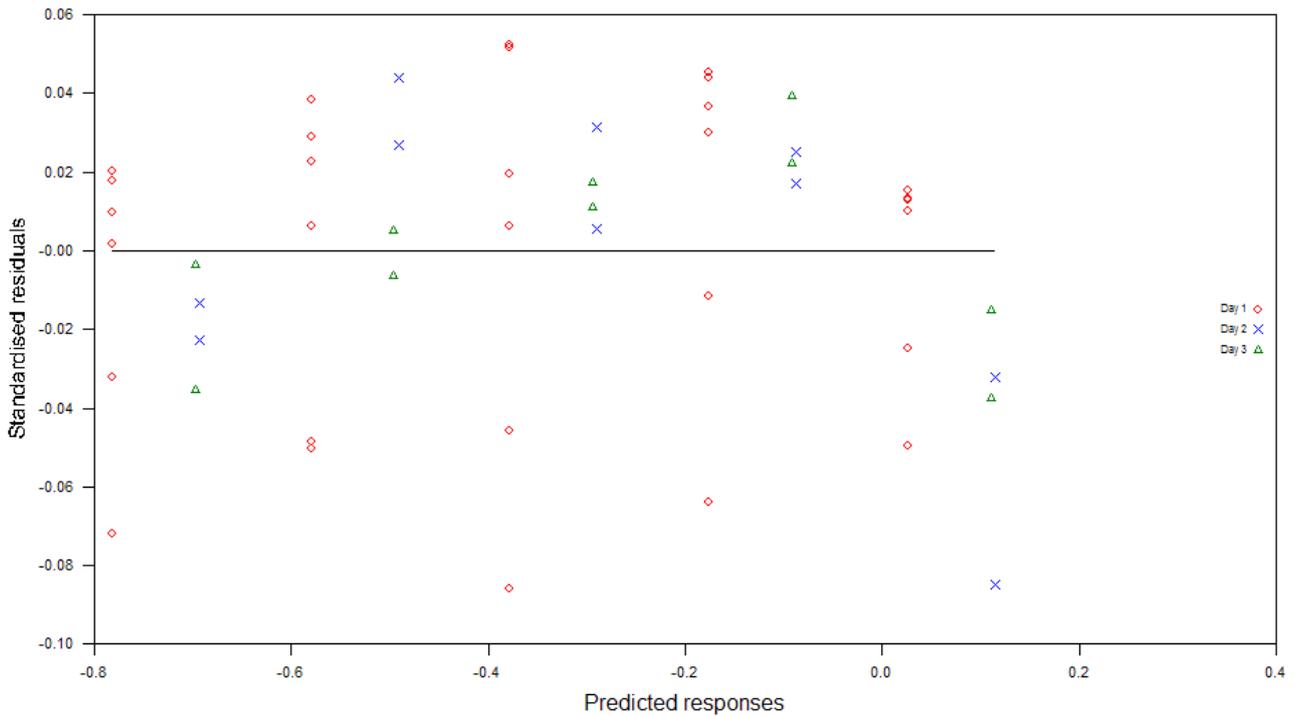


Figure 10: Linearity on toxin LTB – residuals



Study Code:
Validation Report

Results of linearity on toxin CPA see tables 46 till 48 a figures 11 and 12.

Table 46: Linearity on toxin CPA - data

Doses	Day 1						Day 2		Day 3	
	1	2	3	4	5	6	1	2	1	2
1 000x	1.551	1.459	1.418	1.504	1.499	1.326	1.258	1.315	1.349	1.247
2 000x	1.141	1.096	1.066	1.097	1.109	0.984	0.860	0.946	0.967	0.931
4 000x	0.847	0.747	0.688	0.740	0.707	0.606	0.634	0.634	0.646	0.561
8 000x	0.507	0.466	0.426	0.474	0.455	0.403	0.351	0.375	0.386	0.347
16 000x	0.307	0.289	0.271	0.283	0.271	0.236	0.220	0.235	0.254	0.222
32 000x	0.190	0.181	0.168	0.179	0.175	0.160	0.139	0.147	0.155	0.140
64 000x	0.130	0.121	0.116	0.120	0.120	0.108	0.100	0.102	0.111	0.101
128000x	0.098	0.091	0.084	0.089	0.087	0.082	0.078	0.078	0.086	0.083

Linearity was calculated from dilution 2 000x till 64 000x, absorbance for lower dilution was not linear and absorbance for higher dilution was lower than 0.11.

Table 47: Linearity on toxin CPA - model

Model	paralell lines
Design:	completely randomised
Transformace:	$y'=\log(y)$
Odchylka:	Observed residuals
Nalezená směrnice:	0.282157
Korelace R	0.995812

Correlation coefficient is higher than 0.95.

Table 48: Linearity on toxin CPA - ANOVA

Source of variation	Degrees of freedom	Sum of squares	Mean square	F-ratio	Probability
Preparations	2	0.0798485	0.0399242	39.008	0.000 (***)
Regression	1	6.69377	6.69377	>1000	0.000 (***)
Non-parallelism	2	0.000188532	9.42661E-05	0.092	0.912
Non-linearity	12	0.0139128	0.00115940	1.133	0.361
Standard	4	0.00487567	0.00121892	1.191	0.329
Sample 1	4	0.00550169	0.00137542	1.344	0.270
Sample 2	4	0.00353549	0.000883872	0.864	0.494
Quadratic curvature	1	0.00206487	0.00206487	2.017	0.163
Lack of quadratic fit	11	0.0118480	0.00107709	1.052	0.421
Treatments	17	6.78772	0.399277	390.113	0.000 (***)
Residual error	42	0.0429867	0.00102349		
Total	59	6.83070	0.115775		

Figure 11: Linearity on toxin CPA

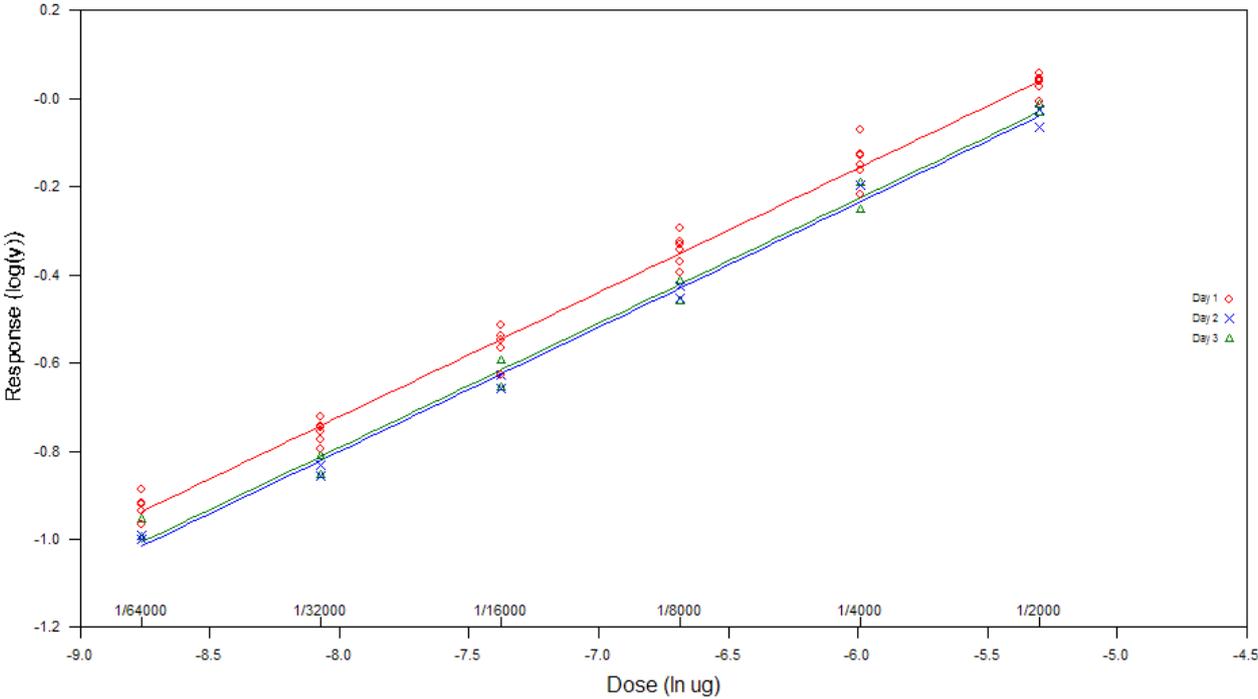
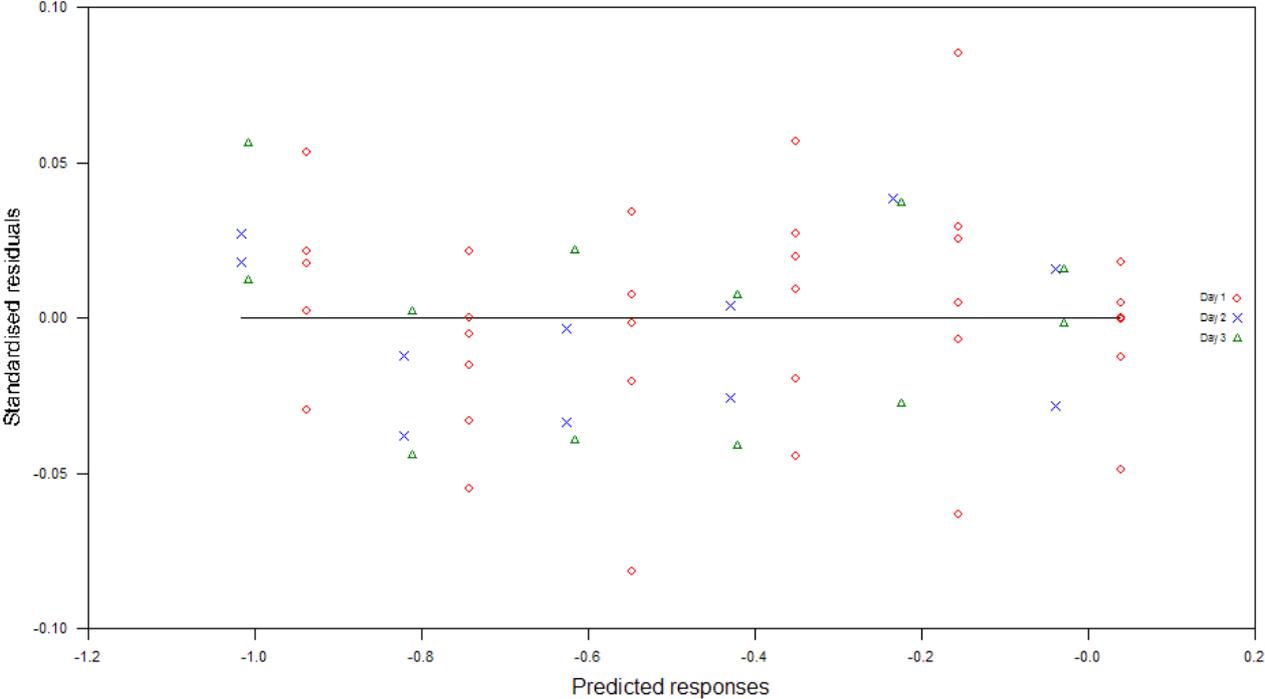


Figure 12: Linearity on toxin CPA – residuals



Study Code:
Validation Report

Results of linearity on toxin CPB see tables 49 till 51 a figures 13 and 14.

Table 49: Linearity on toxin CPB - data

Doses	Day 1						Day 2		Day 3	
	1	2	3	4	5	6	1	2	1	2
1 000x	0.403	0.424	0.382	0.324	0.379	0.357	0.357	0.322	0.317	0.291
2 000x	0.245	0.272	0.268	0.263	0.239	0.215	0.220	0.199	0.195	0.193
4 000x	0.172	0.169	0.166	0.167	0.150	0.145	0.139	0.134	0.122	0.131
8 000x	0.115	0.119	0.118	0.119	0.106	0.107	0.100	0.116	0.094	0.085
16 000x	0.086	0.088	0.089	0.087	0.081	0.079	0.078	0.088	0.076	0.072
32 000x	0.071	0.074	0.076	0.069	0.069	0.066	0.066	0.075	0.063	0.064
64 000x	0.068	0.068	0.074	0.064	0.065	0.061	0.062	0.063	0.060	0.061
128000x	0.066	0.062	0.066	0.061	0.060	0.059	0.060	0.062	0.060	0.061

Linearity was calculated from dilution 1 000x till 8 000x, absorbance for higher dilution was lower than 0.11.

Table 50: Linearity on toxin CPB - model

Model	paralell lines
Design:	completly randomised
Transformace:	$y'=\log(y)$
Odchylka:	Observed residuals
Nalezená směrnice:	0.251204
Korelace R	0.987891

Correlation coefficient is higher than 0.95.

Table 51: Linearity on toxin CPB - ANOVA

Source of variation	Degrees of freedom	Sum of squares	Mean square	F-ratio	Probability
Preparations	2	0.0694449	0.0347224	32.914	0.000 (****)
Regression	1	1.51592	1.51592	>1000	0.000 (****)
Non-parallelism	2	0.000543840	0.000271920	0.258	0.775
Non-linearity	6	0.00902018	0.00150336	1.425	0.240
Standard	2	0.00192761	0.000963803	0.914	0.413
Sample 1	2	0.00604699	0.00302350	2.866	0.074
Sample 2	2	0.00104558	0.000522788	0.496	0.614
Quadratic curvature	1	0.00553313	0.00553313	5.245	0.030 (*)
Lack of quadratic fit	5	0.00348705	0.000697410	0.661	0.656
Treatments	11	1.59493	0.144993	137.444	0.000 (****)
Residual error	28	0.0295380	0.00105493		
Total	39	1.62446	0.0416529		

Figure 13: Linearity on toxin CPB

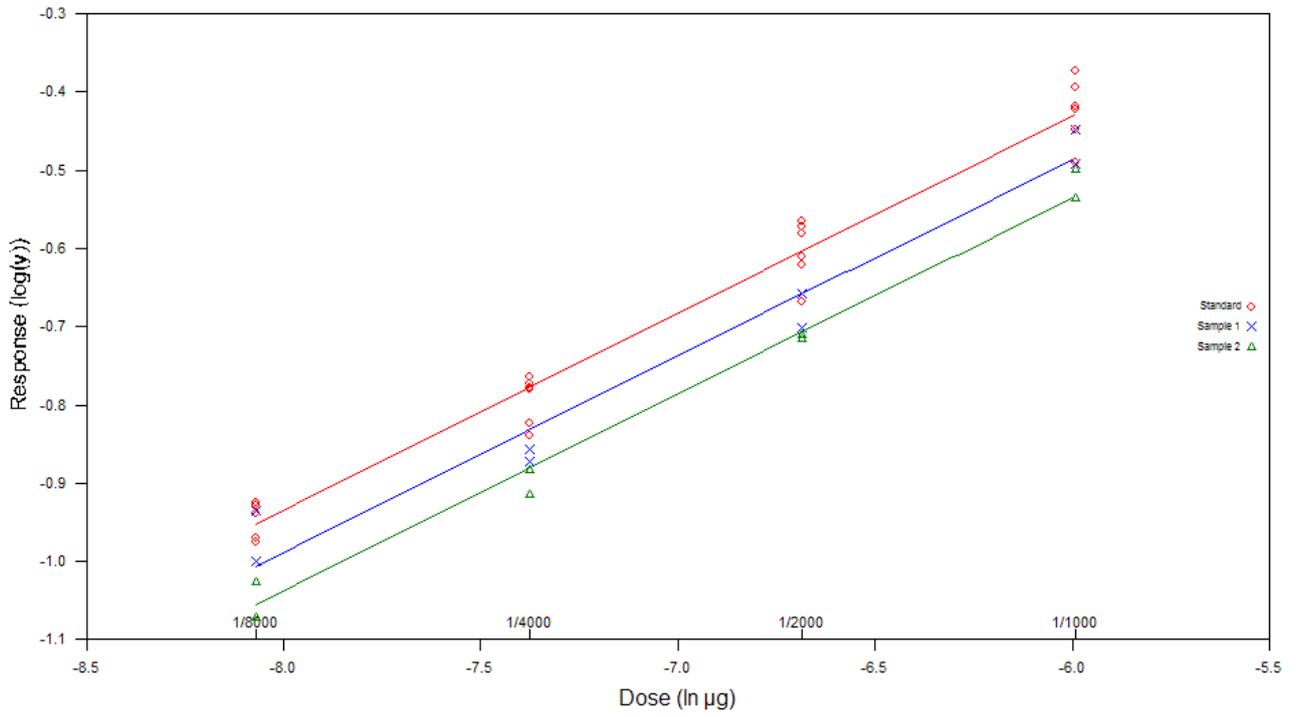
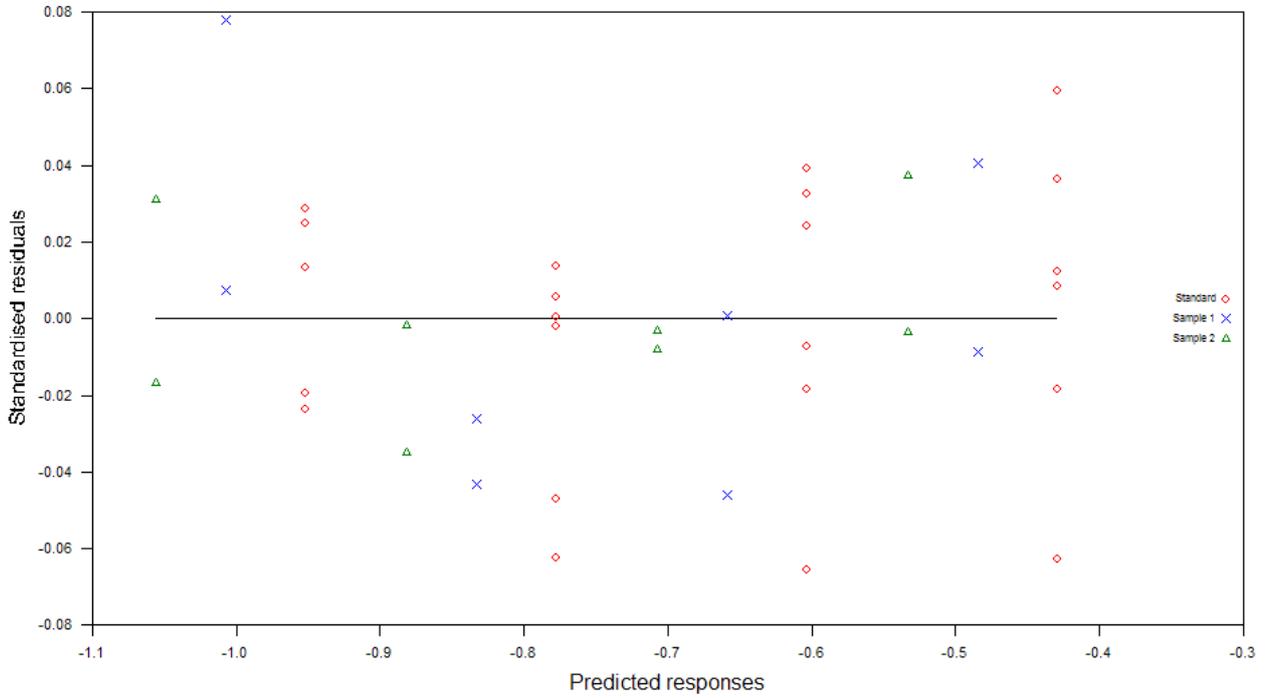


Figure 14: Linearity on toxin CPB– residuals



Study Code:
Validation Report

Results of linearity on toxin CPB2 see tables 52 till 54 a figures 15 and 16.

Table 52: Linearity on toxin CPB2 - data

Doses	Day 1						Day 2		Day 3	
	1	2	3	4	5	6	1	2	1	2
4 000x	0.677	0.746	0.724	0.642	0.701	0.578	0.581	0.811	0.788	0.695
8 000x	0.363	0.461	0.437	0.426	0.419	0.358	0.363	0.434	0.473	0.390
16 000x	0.244	0.267	0.262	0.269	0.243	0.209	0.201	0.303	0.262	0.254
32 000x	0.146	0.168	0.156	0.168	0.151	0.139	0.132	0.174	0.159	0.156
64 000x	0.107	0.120	0.115	0.112	0.113	0.096	0.098	0.124	0.120	0.107
128 000x	0.083	0.088	0.090	0.092	0.087	0.084	0.077	0.088	0.085	0.083
256 000x	0.069	0.075	0.076	0.080	0.072	0.067	0.066	0.073	0.072	0.073
512 000x	0.063	0.067	0.071	0.074	0.069	0.066	0.061	0.067	0.067	0.067

Linearity was calculated from dilution 4 000x till 64 000x, absorbance for higher dilution was lower than 0.11.

Table 53: Linearity on toxin CPB2 - model

Model	paralell lines
Design:	completely randomised
Transformace:	$y'=\log(y)$
Odchylka:	Observed residuals
Nalezená směrnice:	0.290458
Korelace R	0.986558

Correlation coefficient is higher than 0.95.

Table 54: Linearity on toxin CPB2 - ANOVA

Source of variation	Degrees of freedom	Sum of squares	Mean square	F-ratio	Probability
Preparations	2	0.00345730	0.00172865	0.705	0.501
Regression	1	4.05338	4.05338	>1000	0.000 (****)
Non-parallelism	2	0.000696226	0.000348113	0.142	0.868
Non-linearity	9	0.0247635	0.00275150	1.122	0.374
Standard	3	0.0125079	0.00416930	1.700	0.185
Sample 1	3	0.00610950	0.00203650	0.830	0.486
Sample 2	3	0.00614612	0.00204871	0.835	0.484
Quadratic curvature	1	0.0207495	0.0207495	8.460	0.006 (**)
Lack of quadratic fit	8	0.00401406	0.000501757	0.205	0.988
Treatments	14	4.08230	0.291593	118.886	0.000 (****)
Residual error	35	0.0858447	0.00245271		
Total	49	4.16814	0.0850641		

Figure 15: Linearity on toxin CPB2

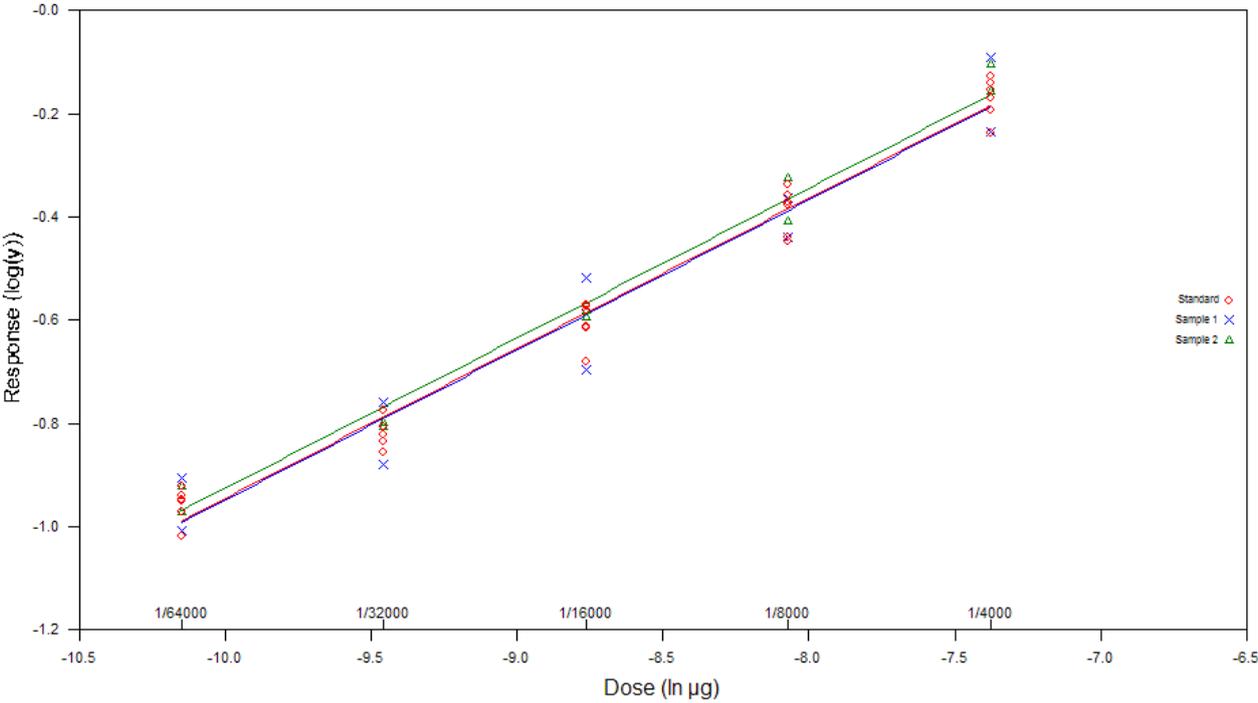
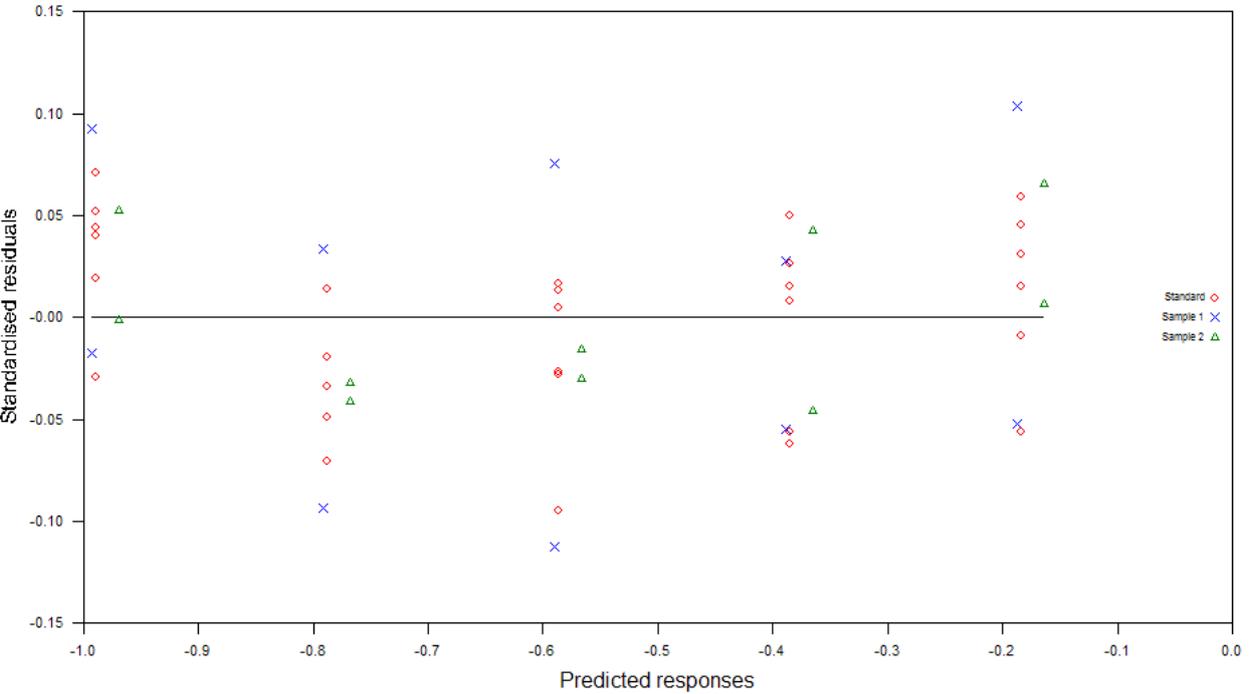


Figure 16: Linearity on toxin CPB2 – residuals



Study Code:
Validation Report

Results of linearity on toxin EXT see tables 55 till 57 a figures 17 and 18.

Table 55: Linearity on toxin EXT - data

Doses	Day 1						Day 2		Day 3	
	1	2	3	4	5	6	1	2	1	2
1 000x	0.251	0.289	0.283	0.282	0.303	0.316	0.239	0.277	0.266	0.307
2 000x	0.168	0.255	0.185	0.179	0.198	0.209	0.167	0.202	0.168	0.196
4 000x	0.120	0.128	0.127	0.125	0.143	0.134	0.121	0.135	0.122	0.127
8 000x	0.083	0.095	0.094	0.093	0.099	0.097	0.087	0.098	0.081	0.090
16 000x	0.068	0.075	0.096	0.073	0.080	0.081	0.076	0.081	0.075	0.074
32 000x	0.058	0.063	0.062	0.062	0.066	0.068	0.067	0.069	0.059	0.062
64 000x	0.058	0.060	0.059	0.061	0.065	0.064	0.064	0.065	0.059	0.059
128000x	0.055	0.058	0.056	0.058	0.059	0.063	0.064	0.059	0.053	0.056

Linearity was calculated from dilution 1 000x till 4 000x, absorbance for higher dilution was lower than 0.11.

Table 56: Linearity on toxin EXT - model

Model	paralell lines
Design:	completely randomised
Transformace:	$y'=\log(y)$
Odchylka:	Observed residuals
Nalezená směrnice:	0.235571
Korelace R	0.980977

Correlation coefficient is higher than 0.95.

Table 57: Linearity on toxin EXT - ANOVA

Source of variation	Degrees of freedom	Sum of squares	Mean square	F-ratio	Probability
Preparations	2	0.00486412	0.00243206	1.458	0.250
Regression	1	1.33310	1.33310	799.414	0.000 (***)
Non-parallelism	2	0.00310481	0.00155241	0.931	0.406
Non-linearity	6	0.00259609	0.000432681	0.259	0.951
Standard	2	0.00183368	0.000916841	0.550	0.583
Sample 1	2	8.84537E-05	4.42269E-05	0.027	0.974
Sample 2	2	0.000673954	0.000336977	0.202	0.818
Quadratic curvature	1	0.00103815	0.00103815	0.623	0.437
Lack of quadratic fit	5	0.00155794	0.000311588	0.187	0.965
Treatments	11	1.34367	0.122152	73.250	0.000 (***)
Residual error	28	0.0466928	0.00166760		
Total	39	1.39036	0.0356503		

Figure 17: Linearity on toxin EXT

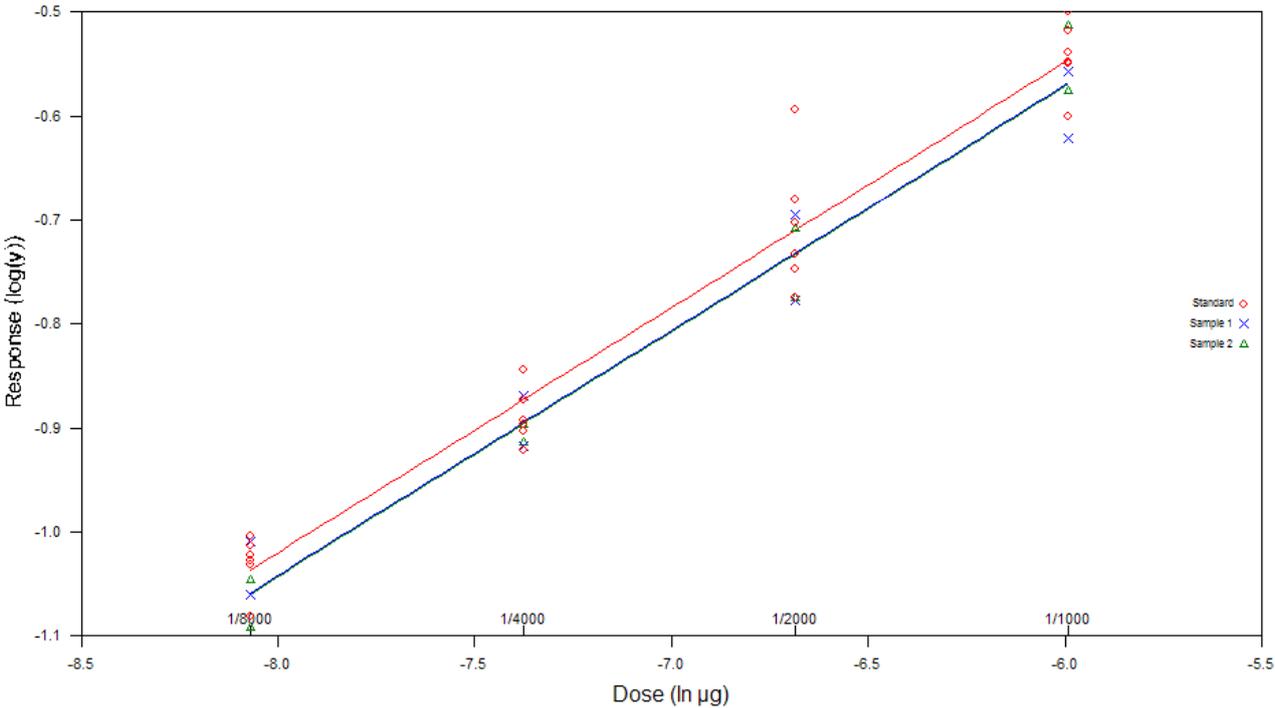
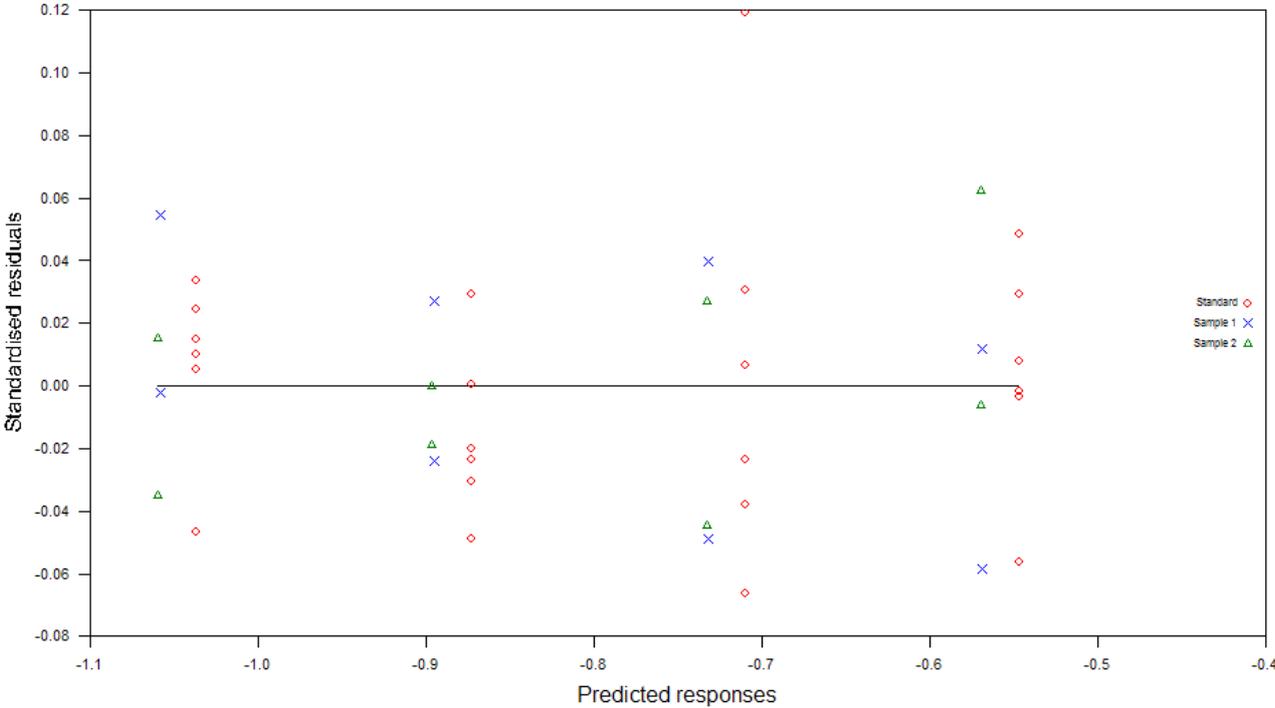


Figure 18: Linearity on toxin EXT – residuals



Study Code:
Validation Report

Results of linearity on toxin TcdA see tables 58 till 60 a figures 19 and 20.

Table 58: Linearity on toxin TcdA - data

Doses	Day 1						Day 2		Day 3	
	1	2	3	4	5	6	1	2	1	2
2 000x	0.594	0.711	0.674	0.621	0.670	0.570	0.656	0.612	0.579	0.615
4 000x	0.380	0.419	0.424	0.439	0.445	0.334	0.384	0.396	0.500	0.380
8 000x	0.229	0.273	0.290	0.258	0.283	0.232	0.256	0.273	0.274	0.320
16 000x	0.140	0.166	0.185	0.156	0.180	0.153	0.198	0.176	0.172	0.173
32 000x	0.100	0.119	0.112	0.117	0.111	0.105	0.108	0.119	0.125	0.106
64 000x	0.076	0.084	0.085	0.088	0.077	0.086	0.093	0.084	0.086	0.077
128 000x	0.066	0.070	0.066	0.071	0.072	0.071	0.074	0.081	0.063	0.060
256 000x	0.056	0.065	0.066	0.058	0.065	0.063	0.060	0.072	0.052	0.052

Linearity was calculated from dilution 2 000x till 32 000x, absorbance for higher dilution was lower than 0.11.

Table 59: Linearity on toxin TcdA - model

Model	paralell lines
Design:	completly randomised
Transformace:	$y'=\log(y)$
Odchylka:	Observed residuals
Nalezená směrnice:	0.271375
Korelace R	0.990339

Correlation coeficient is higher than 0.95.

Table 60: Linearity on toxin TcdA - ANOVA

Source of variation	Degrees of freedom	Sum of squares	Mean square	F-ratio	Probability
Preparations	2	0.00357088	0.00178544	1.088	0.348
Regression	1	3.53827	3.53827	>1000	0.000 (***)
Non-parallelism	2	0.00225428	0.00112714	0.687	0.510
Non-linearity	9	0.00972676	0.00108075	0.658	0.740
Standard	3	0.00191716	0.000639055	0.389	0.761
Sample 1	3	0.00241541	0.000805137	0.490	0.691
Sample 2	3	0.00539418	0.00179806	1.095	0.364
Quadratic curvature	1	1.45689E-06	1.45689E-06	0.001	0.976
Lack of quadratic fit	8	0.00972530	0.00121566	0.740	0.656
Treatments	14	3.55383	0.253845	154.617	0.000 (***)
Residual error	35	0.0574617	0.00164176		
Total	49	3.61129	0.0736997		

Figure 19: Linearity on toxin TcdA

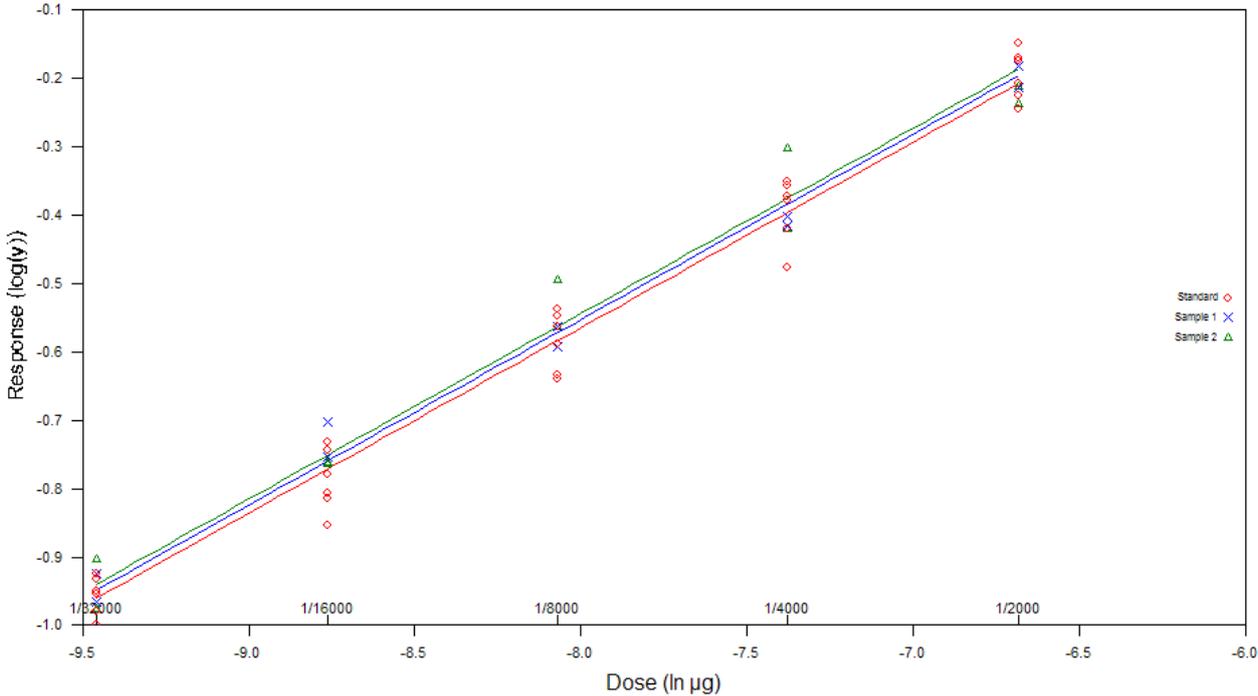
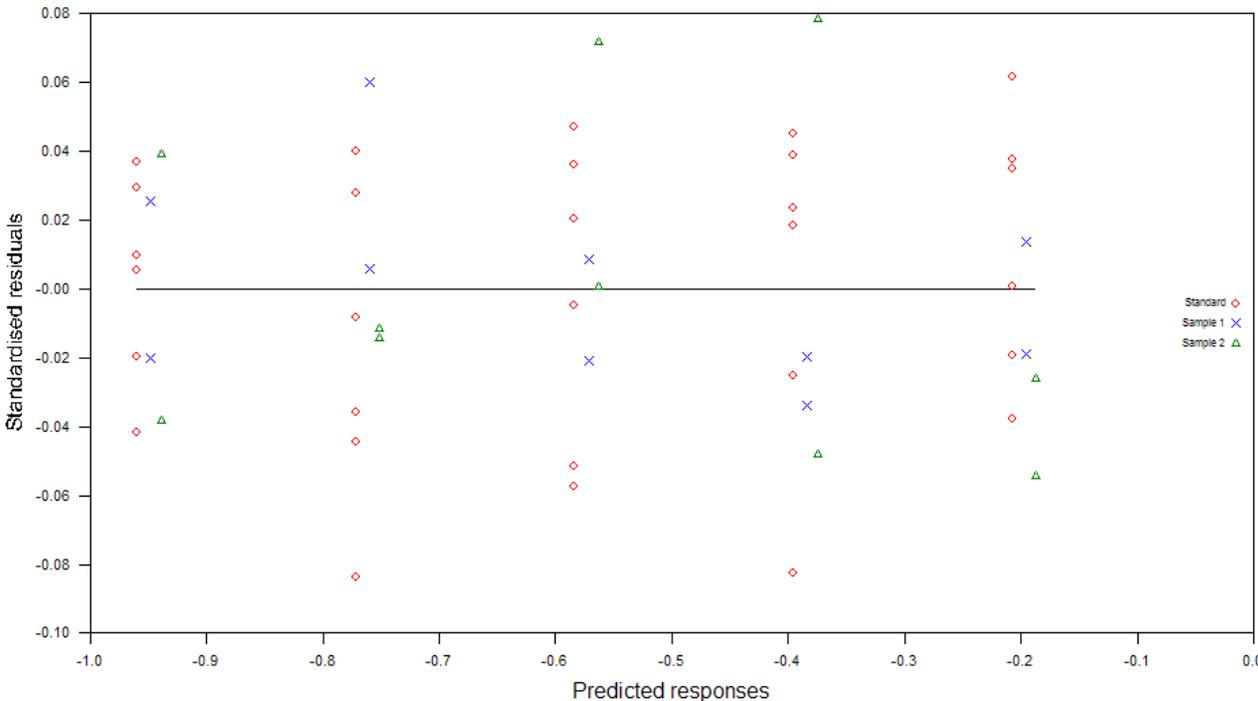


Figure 20: Linearity on toxin TcdA – residuals



11. Evaluation of Validation

Validation results were evaluated in software Excel 2016 and Combistat. All criteria were fulfilled. Validation was evaluated based on specificity, precision and linearity.

ELISA method is suitable for detection of antibodies against the *E. coli* adhesins and heat-labile toxin and toxins from *Clostridium perfringens* and *Clostridium difficile*.

12. Revalidation

Revalidation is necessary to done with each significant changes in ELISA test (e.g. ingrediencies, materials or software).